Molecules during Stellar Formation and Death

Li, X.

Molecules during Stellar Formation and Death

Universiteit Leiden

Molecules during Stellar Formation and Death

Proefschrift

ter verkrijging van
de graad van Doctor aan de Universiteit Leiden,
op gezag van de Rector Magnificus prof. mr. C. J. J. M. Stolker,
volgens besluit van het College voor Promoties
te verdedigen op donderdag 12 februari 2015
klokke 13.45 uur

door

Xiaohu Li

李小虎

geboren te Pingliang, P.R. China
in 1983

Promotiecommissie

Promotor:	Prof. dr. E. F. van Dishoeck	
Co-promotor:	Dr. A. N. Heays	
Overige leden:	Prof. dr. A. G. G. M. Tielens	
	Prof. dr. H. J. A. Röttgering	
	Prof. dr. T. J. Millar	Queen's University Belfast
	Prof. dr. G. C. Groenenboom	Radboud Universiteit
	Prof. dr. L. Decin	Universiteit Leuven
	Prof. dr. K. Han	Dalian Institute of Chemical Physics, Chinese Academy of Sciences

To those who strive, seek, find, and never really give up

Front Cover: An evolved star surrounded by molecular gas and dust. *Image*: V838 Monocerotis (Hubble Heritage Release). *Molecule*: N_2.

Back Cover. A molecular cloud where stars are born. *Image*: Horsehead Nebula (Hubble Heritage Release).

Molecules during Stellar Formation and Death

Thesis Universiteit Leiden - Written in English - Illustrated with Summary in Dutch and Chinese - With references

ISBN 978-94-6259-537-8

Printed by Ipskamp Drukkers

Cover by Changchun Song and Author

ISBN 978-94-6259-537-8

9 789462 595378 >

若無夢想 何必遠方

Table of contents

Chapter 1

Introduction

THE universe is *huge*, but many of the objects that we see on the night sky —planets, stars, galaxies— actually have their origin in microscopic processes between atoms and molecules. These species also emit many lines that can be detected by sensitive telescopes, so nowadays astronomers explore much of the universe through the *small*—at the scale of molecules and their interactions. This requires knowledge from both *astronomy* and *chemical physics*, stimulating the rapid progress in *astrochemistry* which, in principle, can answer our questions about the universe from the level of *quantum mechanics*—How fascinating! The nature of the universe might be quantum.

1.1 Understanding the universe via astrochemistry

1.1.1 The molecular universe

We live in an interesting universe, a 'molecular universe' (Tielens 2013). To date, nearly 180 different molecules (not counting isotopologues) have been identified in space via their rotational, vibrational and electronic spectra[a], including small molecules like CO and H_2O, and large molecules such as polycyclic aromatic hydrocarbons (PAHs), and fullerenes, e.g., C_{60}^+, C_{60}, and C_{70}. Molecules are known to be abundant and widespread in all phases of the neutral interstellar medium, from diffuse clouds to dense star- and planet-forming regions, and from the envelopes of dying stars to the central regions of galaxies. The very rich chemistry of these species opens a window for exploring the history and future of stars, star clusters, galaxies, and interstellar matter, both chemically and physically. This is because the excitation and abundances of species are determined by collisions, which in turn are sensitive to gas density and temperature, as well as to the radiation field induced by their surroundings (van Dishoeck 2014). Thus, molecules can be used as 'dyes' of specific processes or conditions.

Complex, prebiotic interstellar molecules may represent the first steps toward life elsewhere in the universe. Human beings are not alone in the universe—at least from the perspective of their composition, since there is no big difference between the molecules that make us and those that make up the molecular clouds, planets, stars, nebulae, and many other objects in the universe. Astrochemistry can therefore help to better understand the origin and evolution of our own planet and Solar system, and ultimately 'us', thereby attracting an increasing research interest in recent years.

1.1.2 The golden time for astrochemistry

Astrochemistry, also known as molecular astrophysics, is the study of the rich and diverse chemistry that occurs throughout the universe (Herbst & Yates 2013). Specifically, it is the study of 'the formation, destruction and excitation of molecules in astronomical environments and their influence on the structure, dynamics and evolution of astronomical objects' (Dalgarno 2008). Thanks to the rapid progress in science and technology, we are now living in a golden time for studying astrochemistry.

Observationally, significant progress has been driven by new telescopes. For example, velocity-resolved spectra of many molecules, especially H_2O, at far-infrared wavelengths that are not accessible from the ground have recently been provided by the Heterodyne Instrument for the Far-Infrared (HIFI) aboard the Herschel Space Observatory (Pilbratt et al. 2010; de Graauw et al. 2010). The Atacama Large Millimeter/submillimeter Array (ALMA), is expected to lead to a brand new decade of astrochemistry due to an enormous increase in sensitivity and spatial resolution compared with earlier facilities. Together with other space missions, such as the James Webb Space Telescope (JWST), and, further into the future, 30–40m class telescopes such as the European Extremely Large Telescope (E-ELT), these facilities will allow for directly imaged astrochemistry on the relevant physical scales, both spatially and spectrally. There is no doubt that some progress will exceed our current imaginations, and one such an example is the Rosetta mission.

[a] `http://www.astro.uni-koeln.de/cdms/molecules/`

Rosetta provides a milestone in astronomy that has been written into history. Rosetta is a robotic space probe built and launched by the European Space Agency, which is now performing a detailed study of comet 67P/Churyumov–Gerasimenko and sending back images and data on its composition, including the presence of complex organic molecules. Even expert astronomers were only convinced of Rosetta's success when they saw the clear video and images made by the satellite and its lander Philae. Rosetta provides a unique view on the most primitive material in our solar system, and thus its origins.

From a chemical-physical perspective, accurate rate coefficients for many important reactions are needed by astronomers and these have been either measured experimentally and/or calculated theoretically. Computational methods include (quasi-)classical and quantum mechanical methods (or mixed methods), based on high accuracy *ab initio* potential energy surfaces. They have benefited enormously from the increase in computer power and availability of powerful (super) computers, as well as from new numerical methods.

Various chemical databases aimed at supporting different kinds of astrochemical models are now available online and are being kept up to date. For instance, the fifth release of the UMIST Database for Astrochemistry (UDfA, McElroy et al. 2013), hereafter RATE12, now contains 6173 gas-phase reactions involving 467 species. These kinds of databases are valuable for simulating the chemistry in different physical environments, such as dark clouds, protoplanetary disks and circumstellar envelopes.

Modern chemical physics and astrochemistry are actually supporting and inspiring each others progress, leading to a very bright and promising future for both fields.

1.1.3 The formation, evolution, and fate of stars

Stars are known to be formed in cool and dense molecular clouds. However, to form a normal star these clouds must collapse, which may be induced either by external forces or by their own gravity. For instance, if the cloud is close enough to a giant supernova the external pressure may lead to its collapse. Or two dense molecular clouds can collide with each other due to gravity. Several stars may be born immediately following the collision of two galaxies.

Fig. 1.1 shows a general picture for the evolution of a star. Once formed, its fate largely depends on the initial mass. Low-mass (small) stars, especially those with mass less than 8 $M_{\odot}$, go through the red giant and planetary nebula phase before ending up as a white dwarf. High-mass (big) stars proceed through the red super-giant phase and end as supernova producing a neutron star or black hole. There are many questions surrounding these scenarios, especially about the route of high-mass star evolution which is known to occur in clustered environments. The discussion of this thesis is centered on the chemistry of molecules during the birth and death of low mass stars, which are better understood.

It is understood that the formation of low-mass star can be divided into four observationally defined 'Classes', which roughly correspond to various evolutionary stages (Robitaille et al. 2006; Evans et al. 2009). In the Class 0 phase, the parent molecular cloud fragments due to gravity or external forces, and forms first a prestellar core which then collapses into a protostar at its center. As the star-formation process continues, a disk of gas and dust forms around the protostar within the core (Class I object) and which conserves the initial angular momentum of the collapsing cloud. Meanwhile, out-

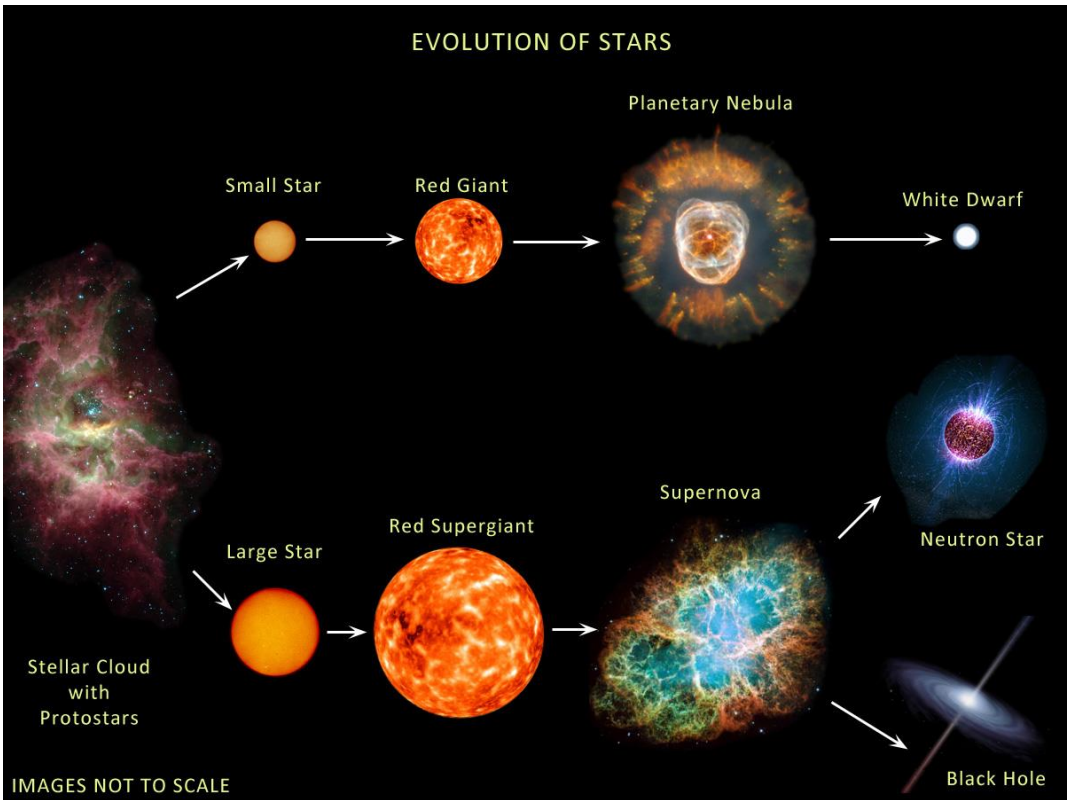

Figure 1.1 — The evolution of a star, determined largely by its mass. A low mass star eventually ends up as a white dwarf whereas a high mass one evolves to a neutron star or a black hole. Figure from E. Moravveji.

flows from the stellar poles eject material from the protostellar system and sweep up the surrounding cloud. Next, the envelope is dispersed and the dust grains stick together more and more, and grow to form pebbles, small rocks and eventually planetesimals in the disks (Class II object). Finally, a planetary system is born around a main sequence star after the remaining disk has been largely dispersed, with only some debris dust left (Class III). Basically, it takes about 10 million years to reach Class III from Class 0. Our solar system has gone through these phases and now, about 4.6 billion years later, still carries the memory of some of these processes.

The gravitational collapse of the cloud liberates heat that increases the temperature of the protostar and induces deuterium nuclear fusion (fast, a short time, $\sim$ 1000 years), which is followed by hydrogen nuclear fusion (much later, $>$ few million yr) which keeps the star on the main sequence for a long period of stability. Low mass stars finally end up as a white dwarf after the material for nuclear fusion is exhausted. One of the most important phases during the late stages of evolution is the asymptotic giant branch (AGB) phase. AGB stars are of particular interest because they eject material into their surroundings, forming a warm and dense circumstellar envelope (CSE). This process leads to the formation of new molecules and the cores of dust grains, and recycles gas and dust to the ISM again for the next loop of star formation (Fig. 1.2).

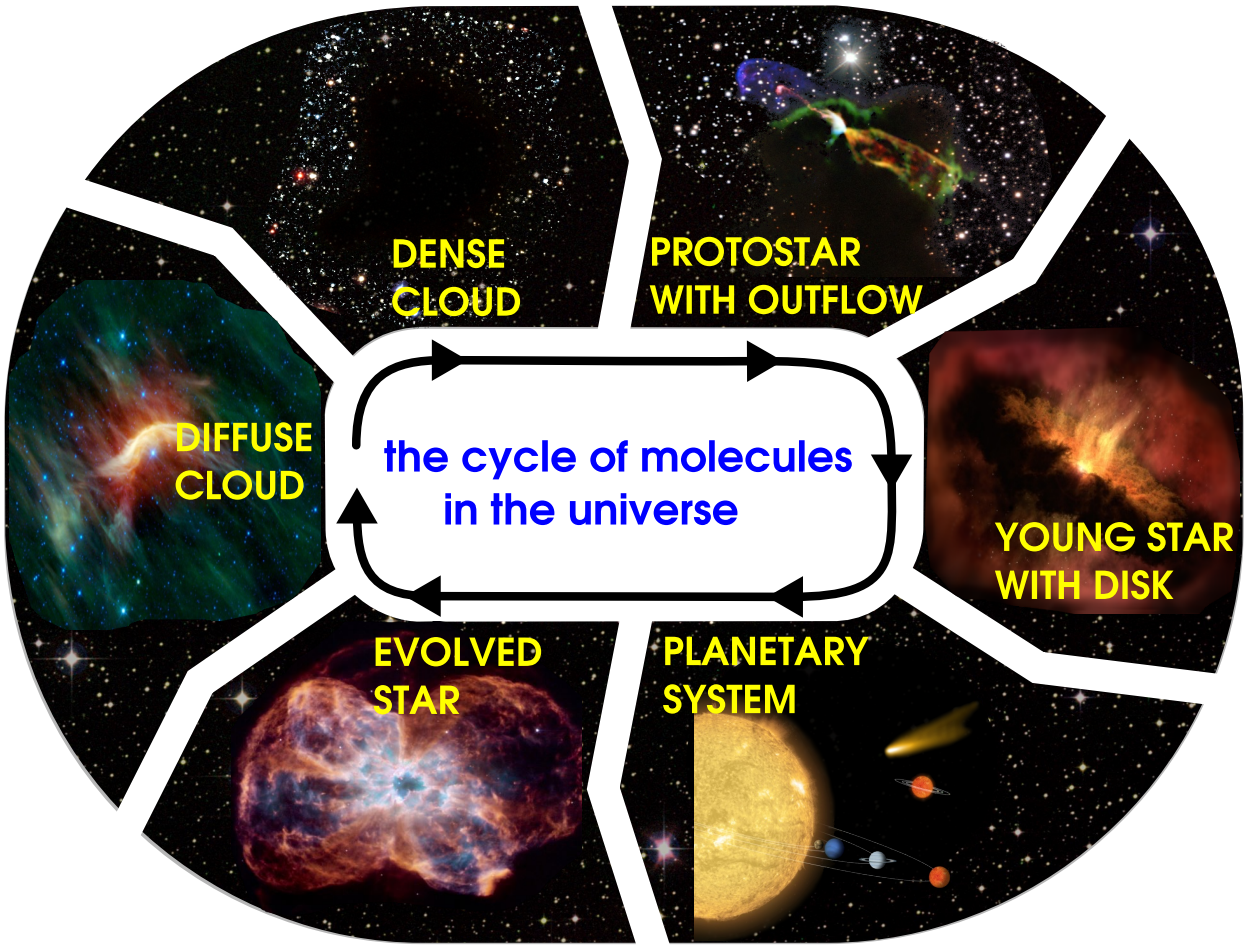

Figure 1.2 — The life cycle of molecules in the universe. Figure by M. Persson, adapted from van Dishoeck (2014).

1.2 The physical-chemical structure during star birth and death

1.2.1 Diffuse + translucent clouds

Denser concentrations in the ISM are called clouds. Key parameters, such as typical densities, temperatures and visual extinctions, of the various types of clouds studied in this thesis are summarized in Table 1.2 (van Dishoeck et al. 2013).

For a diffuse cloud, the gas density (mostly H_2) is rather low, around 10^2 cm^{-3}, with visual extinctions less than 1 mag, and temperatures between 30 and 100 K. Therefore, UV radiation can readily penetrate this kind of cloud and destroy many molecules, increasing the abundances of atoms and ions. The chemistry and physics of translucent clouds is similar to that of diffuse clouds. They have somewhat higher gas densities, around 10^3 cm^{-3}, larger visual extinctions (between 1 to 5 mag), and lower temperatures ($15 - 50$ K). Again, photodissociation is important in these clouds.

An example of a well-studied diffuse cloud is that toward the bright star ζ Oph, whereas the HD 124314 cloud studied in Chapter 2 is a borderline translucent cloud. Nowadays, these objects can be well-modelled and observed, therefore these clouds are very good candidates for testing and illustrating the importance of new improvements in

Table 1.1 — Different astrochemical environments and their typical physical parameters, adapted from van Dishoeck et al. (2013).

Name	Density (cm^{-3})	Temperature (K)	A_V (mag)	Examples
Diffuse cloud	10^2	30–100	≤ 1	ζ Oph
Translucent cloud	10^3	15–50	1–5	HD 124314
Dense PDR	$10^4 - 10^5$	50–500	< 10	Orion bar
Cold dense cloud	$10^4 - 10^5$	10–20	> 10	Taurus cloud
Prestellar core	$\geq 10^5$	8–15	10–100	L1544
Protostellar envelope				
Cold outer	$10^4 - 10^7$	8–100	10–100	NGC 1333 IRAS4A
Warm inner / hot core	$10^7 - 10^9$	$\geq$100	100–1000	W3 IRS5 / Orion hot core
Shock	$10^4 - 10^5$	200–2000	$\leq$ few	L1157 B1
Protoplanetary disk				
Outer	$10^6 - 10^{10}$	10–500	1–100	TW Hya HD 100546
Inner	$10^9 - 10^{15}$	100–3000	1–1000	AS 205
AGB envelope				
Outer	$\leq 10^8$	10–100	1–50	IRC+10216(C-rich)
Inner	$10^{10} - 10^{13}$	100–2000	50–1000	VW CMa(O-rich)

astrochemical models.

1.2.2 Photodissociation regions (PDRs)

Photodissociation regions (PDRs), also called photon-dominated regions, are defined as any interstellar cloud in which UV radiation dominates the chemistry and temperature structure. Traditionally, the term PDR refers to dense clouds located close to a bright star (such as in Orion) but the definition includes the diffuse and translucent clouds discussed above. All of the neutral atomic and most of the molecular gas in the Milky Way galaxy and external galaxies is in PDRs. Moreover, most of the non-stellar infrared and the millimeter ^{12}CO emission from a galaxy originates in PDRs (Hollenbach & Tielens 1997). Thus, the study of PDRs can help us to understand the structure, chemistry, thermal balance, and evolution of the neutral interstellar medium of galaxies illuminated by far-ultraviolet (FUV, 6 eV $< h\nu <$ 13.6 eV) photons.

One of the most important chemical processes in PDRs is photodissociation, which is sensitive to the extinction of UV radiation by dust grains. Astronomers use the extinction at visual wavelengths, A_V, as a reference point to quantify the decrease of the UV radiation with depth into a cloud. Therefore, A_V can be used to characterize the physical structure of PDRs, as illustrated in Fig. 1.3. In this figure, the ultraviolet flux from the interstellar radiation field (ISRF) or nearby hot stars is incident on one side of a cloud, and the physical conditions and chemical composition then depend on visual extinction. For example, at the surface where $A_V < 1$ mag, the temperature is between $10^2 - 10^3$ K. Atoms and ions are dominant, among which H, C^+, O, N are the most abundant, whereas ices cannot survive.

Deeper into the cloud, e.g., $1 < A_V < 10$ mag the temperature is within $10 - 10^2$ K,

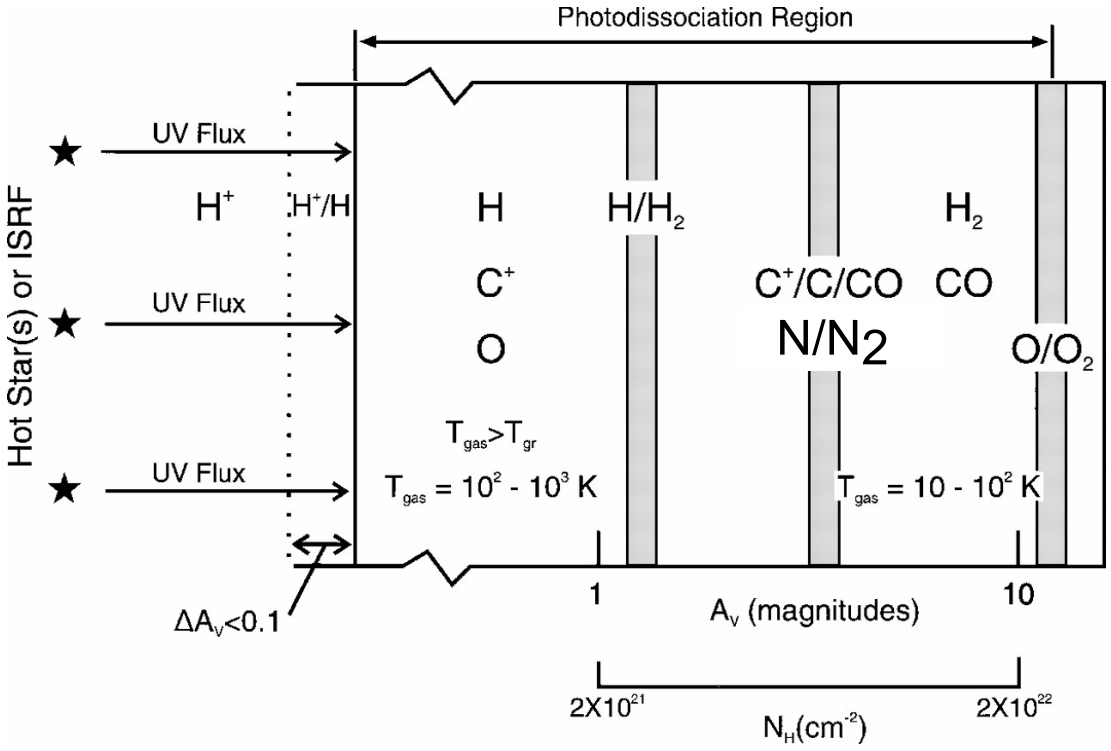

Figure 1.3 — A schematic view of a photodissociation or photon-dominated region. The PDR is illuminated from the left by a strong FUV field. The PDR extends from the H^+/H transition region through the H/H_2, $C^+/C/CO$ and N/N_2 transitions, until the O/O_2 boundaries. It thus includes the predominantly neutral atomic surface layer as well as large columns of molecular gas. Figure adapted from Hollenbach & Tielens (1997).

and a transition from atoms/ions enriches the fractional abundances of molecules. The transitions forming the most abundant molecular species are $H \rightarrow H_2$, $C^+ \rightarrow C \rightarrow CO$, and $N \rightarrow N_2$. Ices start to form on grains in this zone. In the innermost region of the cloud where $A_V > 10$ mag, the temperature falls to 10 K, the transition of atoms/ions to molecules is complete, and gas-phase molecules and ices are abundant.

In cold and shielded cloud regions, chemistry is stopped in the gas-phase but can continue in the ice phase when triggered by UV photons penetrating from outside the cloud or produced internally by the interaction of cosmic rays with H_2. Large PAH molecules can also survive in PDRs (Visser et al. 2007). The highest extincted objects are called dark clouds.

PDRs occur almost everywhere during stellar evolution. For instance at the surface of protoplanetary disks, at the edge of circumstellar envelopes around AGB stars, and elsewhere. Therefore it is of particular importance to understand the chemistry in PDRs, especially photodissociation of some key species like H_2, CO, and N_2.

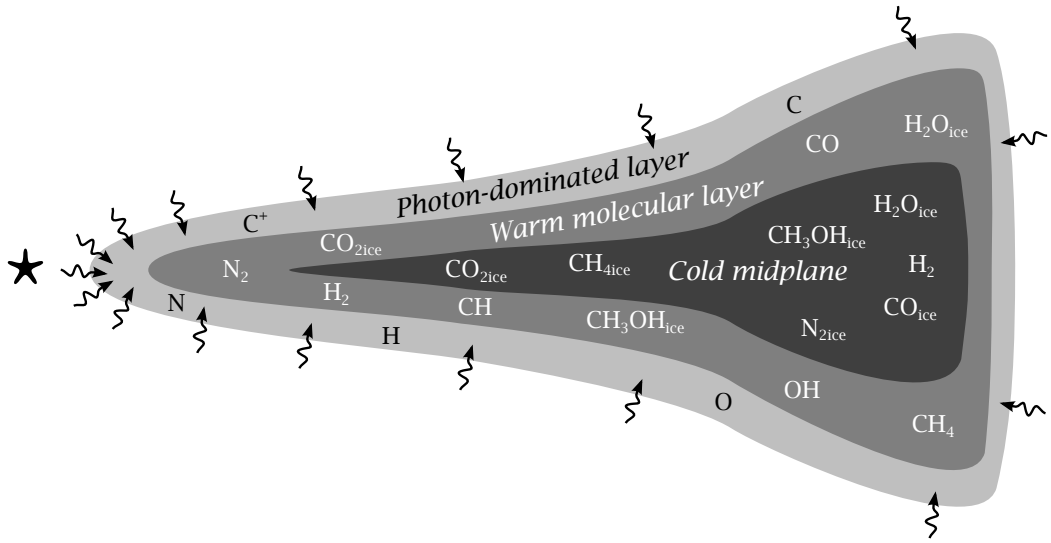

Figure 1.4 — Schematic representation of the three chemical regimes in a circumstellar disk: the photon-dominated layer (irradiated by the protostar and the interstellar UV field), the warm molecular layer, and the cold midplane. Typical species for each regime are indicated. Figure from Visser et al. (2009).

1.2.3 Protoplanetary disks

Disks around young stars are the birthplace of planets and are therefore particularly important targets for astrochemistry. Disks that are rich in gas and dust are called protoplanetary disks, in contrast with the gas-poor debris disks which represent a later evolutionary stage. As shown in Fig. 1.4, a circumstellar disk consists of three different chemical layers: the photon-dominated layer, the warm molecular layer, and the cold midplane (Aikawa et al. 2002; Bergin et al. 2007; Henning & Semenov 2013). The surface of the disk is heated by the protostar and the interstellar radiation field, therefore it forms a PDR with a strong UV field where molecules are dissociated into atoms. Deeper in the disk, molecules are shielded enough from the UV to survive in a warm layer where they are not frozen out. CO, H_2O and other species start to stick to dust grains and form icy layers when the dust temperature drops, leading to 'snow-lines'. A snow-line is an annulus in a protoplanetary disk where molecules freeze-out from the gas (Sasselov & Lecar 2000). Deep in the cold disk midplane most molecules except H_2, H_3^+ and their isotopologs are frozen out onto grains. No single instrument or wavelength regime probes the entire and variable disk reservoir. A combination of near-, mid-, and far-infrared spectroscopy combined with spatially resolved interferometric data is needed to explore the physics and chemistry in these objects.

Photodissociation plays an important role in controlling the chemistry of the molecules that are observed in the upper and midplane layers of disks. Moreover, isotope-selective processes have been invoked to explain some of the anomalies found in meteorites formed in the early solar nebula disk (Lyons & Young 2003).

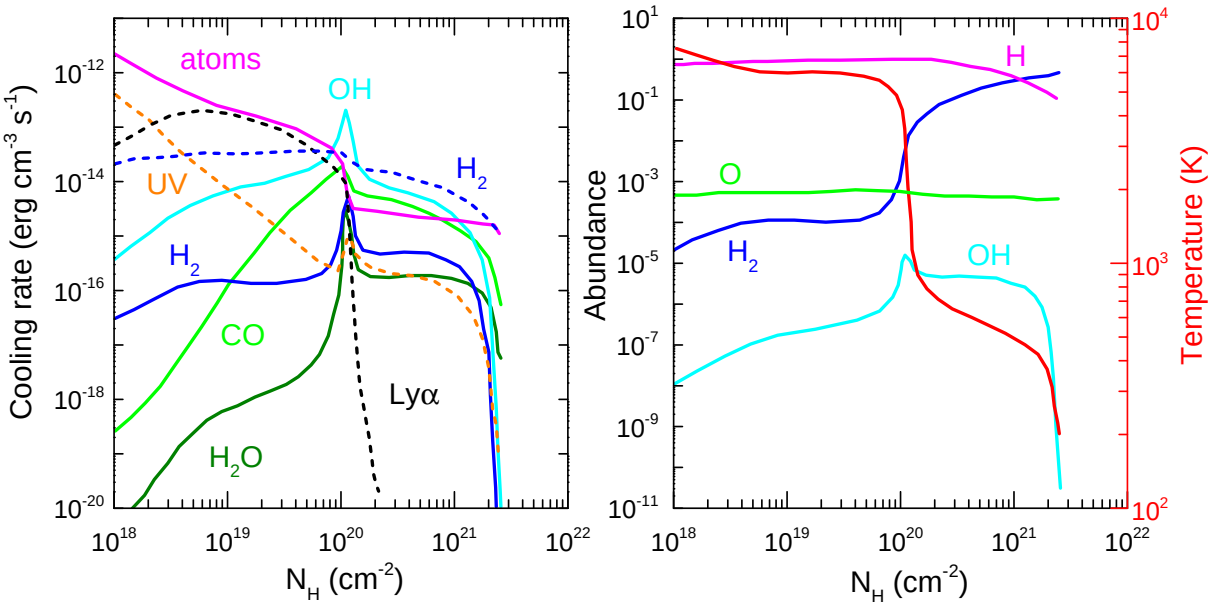

Figure 1.5 — Left panel: Rates of heating and cooling processes in dissociative shocks for a few species. Solid lines, cooling processes; dashed lines, heating processes. Right panel: Abundance profiles of H, OH, O, and H_2, as well as the temperature profile. For both panels, the shock velocity is 80 km s^{-1}, and the preshock density is 10^5 cm^{-3}. Data extracted from Neufeld & Dalgarno (1989).

1.2.4 Shocks

Shock waves provide another interesting observational signal for astrochemists, and occur in compressible media when pressure gradients are large enough to generate supersonic motions. Shocks compress, heat, and accelerate the ISM material. Most shocks in the ISM are thought to be produced by stellar winds or outflows and the strongest originate from supernovae. Interstellar shocks can also result from the collision of two interstellar clouds. Detailed discussions on shocks can be found in reviews, e.g., McKee & Hollenbach (1980).

Generally, shocks are divided into two types: C-type and J-type. For a C-type shock, the shock velocity is less than $\sim$ 50 km s^{-1} (value depending on the magnetic field strength) (Neufeld & Dalgarno 1989), which is not fast enough to dissociate molecules. Because ions couple with the magnetic field, they receive information about the shock ahead of time and can transmit this information to neutral species. Thus, physical parameters (e.g., temperature, gas density, etc.) in the shocked gas change gradually or 'continuously' across the shock front. For a J-type shock, the shock velocity is greater than $\sim$ 50 km s^{-1}, which results in such high temperatures that molecules are destroyed. They are, therefore, also called dissociative shocks or fast molecular shocks. The temperature and density in this kind of shock changes discontinuously at the shock front, like a 'jump'. J-type shocks may be generated during the birth, throughout the life, and by the explosive death of stars.

Dissociative shocks can be subdivided into two regions: a hotter region ($T > \sim 10^4$ K) containing atoms and ions, and a cooler region ($\sim 10^2$ K $< T < \sim 10^4$ K) containing atoms, ions, and molecules. The heating of gas in shocks is initially dominated by the

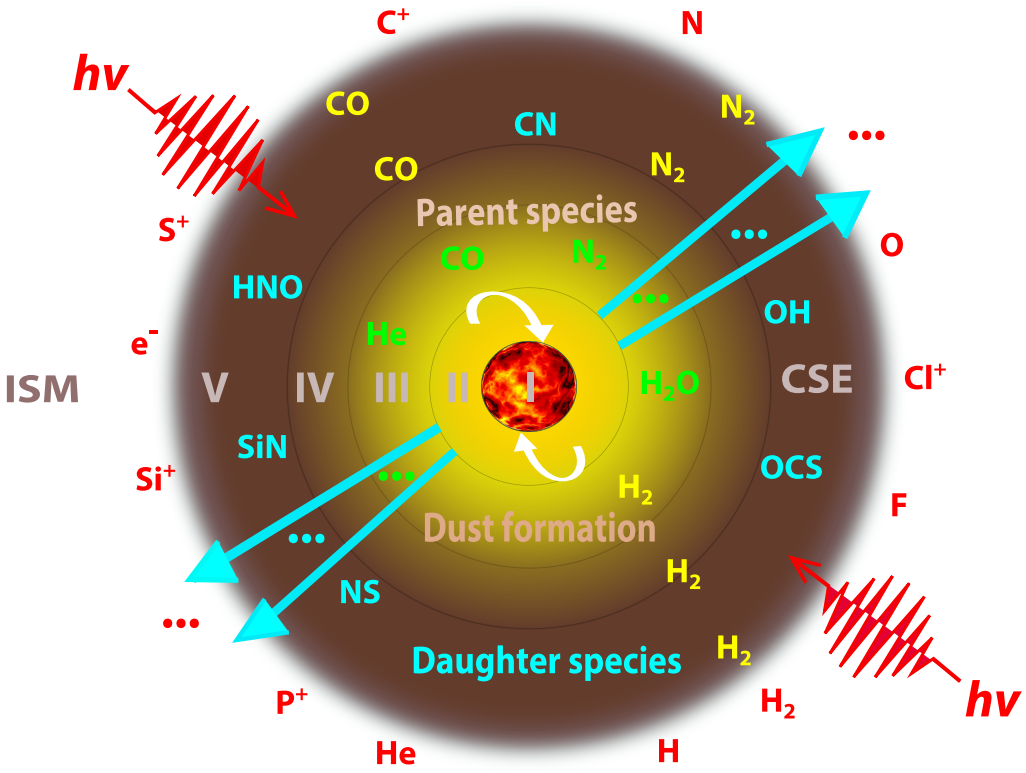

Figure 1.6 — Schematic structure of the CSE for an O-rich AGB star, which is divided into 6 regions for modelling purposes. (I): A degenerate C/O core and He/H burning shell, (II): A convective shell, (III): A stellar atmosphere in which parent species are formed, (IV): A dust formation shell with an expanding envelope, (V): An outer CSE where daughter species are formed primarily by photodissociation, (VI): The interstellar medium (ISM).

conversion of kinetic energy into heat, but absorption of radiation emitted by warmer upstream gas, and the release of chemical energy during the (re-)formation of molecules also play a role. Cooling of the hottest shocked gas is controlled by the excitation and subsequent emission from electronic levels of the most abundant atoms, and by ro-vibrational emission of molecules further downstream where the shock has cooled. Here we address the importance of molecular reactions during the cooling process.

Fig. 1.5 presents the cooling rates and abundances of a few key species in a dissociative J-type shock. Initially the gas is cooled by atoms, until the temperature decreases to about 3×10^3 K. Then, it is the excitation of molecules that contributes most to the cooling, e.g., H_2, H_2O, CO, and OH. Among these molecules, OH has the initially-largest cooling rate. In shocked layers, atomic H is more abundant than H_2 until the temperature of the gas decreases to 500 K. Collisions between H and OH in various ro-vibrational states is therefore one of the key processes affecting the chemistry and cooling, and state-selective rate constants between them, as calculated in Chapter 5, are of particular importance.

1.2.5 AGB stars

AGB stars are dying stars of low- to intermediate-mass (from 0.8 $M_{\odot}$ to $\sim$ 8 $M_{\odot}$). These stars are in the last nuclear-burning phase having exhausted their supply of H and He, and eject dust and molecules into the surrounding region, creating CSEs. These gas and dust envelopes eventually merge with the ISM and enrich molecular clouds in which new stars may be born. What remains after the AGB phase is a hot C/O core, which illuminates the expanding CSE for a short while and forming a proto-planetary nebula (Fig. C.1). AGB and post-AGB stars, in addition to proto-planetary nebulae, are important sources of dust and several elements and isotopes in the universe. Therefore understanding the composition and evolution of the material they emit is of wide interest.

There are three types of AGB stars: C-rich (C/O $>$ 1), O-rich (M-type) (C/O $<$ 1), and S-type (C/O $\approx$ 1). The Sun will eventually become an O-rich AGB star. As shown in Fig. 1.6, the molecules in the outer expanding envelopes are called 'daughter' species, which are driven by hot (1000 $-$ 2000 K) and shocked processes in the inner CSE where 'parent' species are formed. The composition of the parent molecules depends on the C/O ratio and is thus different for the various types of AGB stars. This in turn leads to rather different distributions and chemistry of the corresponding daughter species.

Generally, C-bearing molecules are abundant in C-rich AGB stars, from simple CO to large polycyclic aromatic hydrocarbons (PAHs, e.g., Boersma et al. 2006; Cherchneff 2011). The best-investigated AGB star both observationally and theoretically is the nearest C-rich star, IRC +10216 (e.g., Cordiner & Millar 2009; Decin et al. 2010; De Beck et al. 2012; McElroy et al. 2013; Li et al. 2014). To date, nearly half of the 180 identified species in inter- or circumstellar media have been detected around this star, with some being the first detections in any astrophysical environment, e.g., the cyanide anion CN^- (Agúndez et al. 2010b) and FeCN (Zack et al. 2011).

A relatively small, but increasing, number of investigations have been made into S-type AGB stars (e.g., Schöier et al. 2011; Danilovich et al. 2014). The central star in S-type AGB objects is undergoing a transition from an O-rich to a C-rich phase, therefore a mixed chemistry may occur because O-rich material is stored in a stable disk around the central star for some period of time (Willems & de Jong 1986; Szczerba et al. 2007). This interesting dual chemistry may continue to post-AGB stars and even proto-planetary nebulae (see Gielen et al. 2011,and the references therein).

For the case of O-rich AGB stars, OH and H_2O are the dominant species and important progress has been driven by new telescopes (Tenenbaum et al. 2010; Decin 2012), especially the HIFI instrument aboard Herschel (de Graauw et al. 2010), which could provide velocity-resolved spectra at far-infrared wavelengths. Not only 'small' and 'common' species have been observed, e.g., CO, H_2O, HCN, HNC, CN, OH, NO, SiS, and SiO (e.g., Decin et al. 2010a), but also inorganic molecules, e.g., AlO and AlOH (Tenenbaum & Ziurys 2010). Moreover, surprising emission from PAHs and fullerenes, e.g., C_{60}, have also been found in O-rich post-AGB sources (Gielen et al. 2011).

The outer region of the CSE around an AGB star is a PDR, where photodissociation is important. Therefore, as demonstrated in Chapters 3 and 4, treating properly the photodissociation of parent species is necessary when modelling the distributions and chemistry of daughter species, especially for high-abundance parent species, like CO and

Table 1.2 — Important molecular processes (van Dishoeck 1998).

Bond formation processes	
Radiative association	$X + Y \longrightarrow XY + h\nu$
Grain surface formation	$X + Y{:}g \longrightarrow XY + g$
Associative detachment	$X^- + Y \longrightarrow XY + e$
Bond destruction processes	
Photodissociation	$XY + h\nu \longrightarrow X + Y$
Dissociative recombination	$XY^+ + e \longrightarrow X + Y$
Collisional dissociation	$XY + M \longrightarrow X + Y + M$
Bond rearrangement processes	
Ion-molecule exchange	$X^+ + YZ \longrightarrow XY^+ + Z$
Charge-transfer	$X^+ + YZ \longrightarrow X + YZ^+$
Neutral-neutral	$X + YZ \longrightarrow XY + Z$

N_2.

1.3 Astrochemical models

1.3.1 Types of reactions: photodissociation

Astrochemical models may include thousands of reactions, but which belong to only a few different types of processes as summarised in Table 1.2. Understanding the mechanisms behind these basic processes is very important for determining the nature and abundance of molecules observed in the ISM. Detailed discussion on these processes can be found in many reviews (e.g., Smith 2011; van Dishoeck 2014). Among the different types of reactions, photodissociation is the dominant destruction process of molecules in any region exposed to intense UV radiation.

Simply speaking, photodissociation is a process in which a molecule absorbs a UV photon into an excited electronic state and then dissociates to smaller molecules or atoms. Here we take a diatomic molecule AB as an example, see Fig. 1.7. If AB absorbs a photon into an excited electronic state that is repulsive with respect to the nuclear coordinate, then the molecule simply breaks into two atoms, A + B. This kind of process is called *direct photodissociation*, and results in a broad cross section as a function of photon energy, with the width of the cross section determined by the steepness of the repulsive potential: the steeper the curve, the broader the cross section.

If AB is excited into a bound electronic state which couples with a nearby repulsive electronic state and then dissociates to atomic form along the repulsive state, the process is called *predissociation*. This kind of photodissociation produces a cross section consisting of a series of discrete peaks or lines, the width of which depends on the sum of the radiative and predissociation rates. If AB is excited into an upper electronic state which does not couple with a lower-lying repulsive state or the vibrational continuum of the ground electronic state, spontaneous emission of photons into the ground state continuum

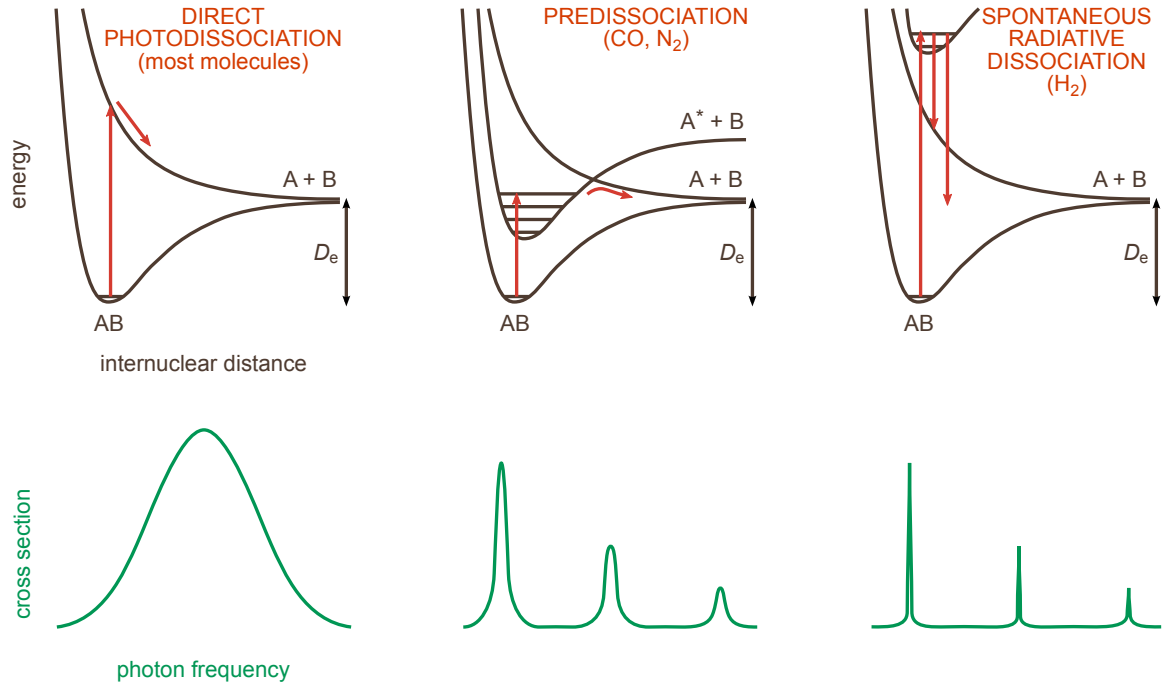

Figure 1.7 — Three types of molecular photodissociation, together with their corresponding cross sections, adapted from van Dishoeck & Visser (2011).

can occur leading to dissociation to A + B. This process is called *spontaneous radiative dissociation*. Photodissociation of most molecules, e.g., H_2O, OH, CH^+, and NH, goes through direct photodissociation. The photodissociation of CO and N_2 is dominated by predissociation. Spontaneous radiative dissociation is important for H_2. A more detailed discussion of these processes can be found in van Dishoeck & Visser (2011).

Accurate photodissociation rates of molecules are hard to obtain because a molecule can be excited to many electronic states but only some of these states lead to photodissociation. Furthermore, the photodissociation rate depends on the intensity and shape of the radiation field in PDRs. Moreover, there are many possible photodissociation product channels, but their branching ratios are not straightforward to determine. Therefore, it may take a long time to finally fully understand the photodissociation of a molecule. For example, the photodissociation of even the simple diatomic molecule N_2 took more than two decades to finally fully understand, as summarised in Chapter 2. The situation is similar for CO (Visser et al. 2009).

The photodissociation rate of a molecule decreases with depth into a cloud due to UV extinction by dust. For abundant molecules whose photodissociation is dominated by discrete absorption, the UV lines can become saturated for sufficiently large column densities. Thus, molecules lying deeper into clouds are shielded from the dissociating radiation. This 'self-shielding' is particularly important for H_2 and CO, and, as shown in Chapter 2, also for N_2. In the inner planet-forming regions of disks around young stars (inside the H_2O snow-line), the column densities of H_2O become so high that this molecule also becomes self-shielding even though its photodissociation is controlled by broad absorptions due to direct photodissociation (Bethell & Bergin 2009).

1.3.2 Astrochemical models

Astrochemical models are used to simulate the abundances of molecules in various astrophysical environments, including their variation as a function of time or distance. In the ISM, the chemistry is governed by gas-phase reactions together with interactions on grain surfaces. The development of these models started with relatively simple and small chemical networks of gas-phase reactions and was then extended piece-by-piece, taking into account more complex factors step-by-step. Nowadays, both gas-phase and grain-surface reactions are considered in many models.

Depending on the lifetime of the physical environment, models may assume equilibrium chemistry or include its time-dependence. The physical conditions in models can also vary with time. In some cases the main physical conditions are temperature, gas density, and visual extinction, and are held fixed while considering the chemistry as it evolves with time, e.g., in so-called single-point models. It is possible to obtain a full picture of the possible range of chemical evolution by running single-point models for many different fixed physical conditions. Models which consider a gradient of temperature, density, or visual extinction as a function of distance and time, or include dynamical movement, are more realistic but more complex. A detailed discussion of these matters centered on dark cloud models can be found in a recent review (Agúndez & Wakelam 2013).

It is primarily the physical conditions of the object under study that determine the requirements of an astrochemical model. The model is just a tool. The aim of using it is to understand the chemistry of the environment without delving into the maximum-possible complexity. For example, grain-surface reactions are very important in simulating the processes in protoplanetary disks because there is a large amount of ice-coated dust there. However, in hot CSEs the dust temperature is high in the inner shells and the radiation field strong enough in the outer CSE so that it is hard for ice to survive. Therefore, pure gas-phase chemical modeling can already give good predictions. Nevertheless, since the gas density is relative high at the inner radii of CSEs, the interaction of gas and bare-grains could potentially play a minor role there.

Another very important point in astrochemical simulations is the description of the radiation field, which depends on the location of interest. In the CSEs of AGB stars, the photospheres of the central stars typically have effective temperatures around 3000 K and cannot cause the photodissociation of molecules, thus one only has to take into account photons from the ISM. However, in post-AGB or protoplanetary nebulae, the central stars are very hot, up to $T_{\rm eff} \approx 100\,000$ K, and their radiation can destroy molecules rapidly, therefore one must consider these effects. Cosmic ray interactions with H_2 lead to another, weaker source of radiation which is important in the most shielded parts of dark cloud cores and protoplanetary disks.

Once the physics of the environment are well understood and the basic model has been built, the chemical evolution is modelled through reaction networks and a reliable chemical database is needed. To prevent the use of inappropriate or obsolete data and extrapolations, the best way is for experts to build such a database, and more importantly, maintain it. This in turn requires close interaction between astrochemists and chemical physicists. Fortunately, much hard work has already been done by some pioneer astrochemists. Three main chemical databases currently exist for interstellar gas-phase

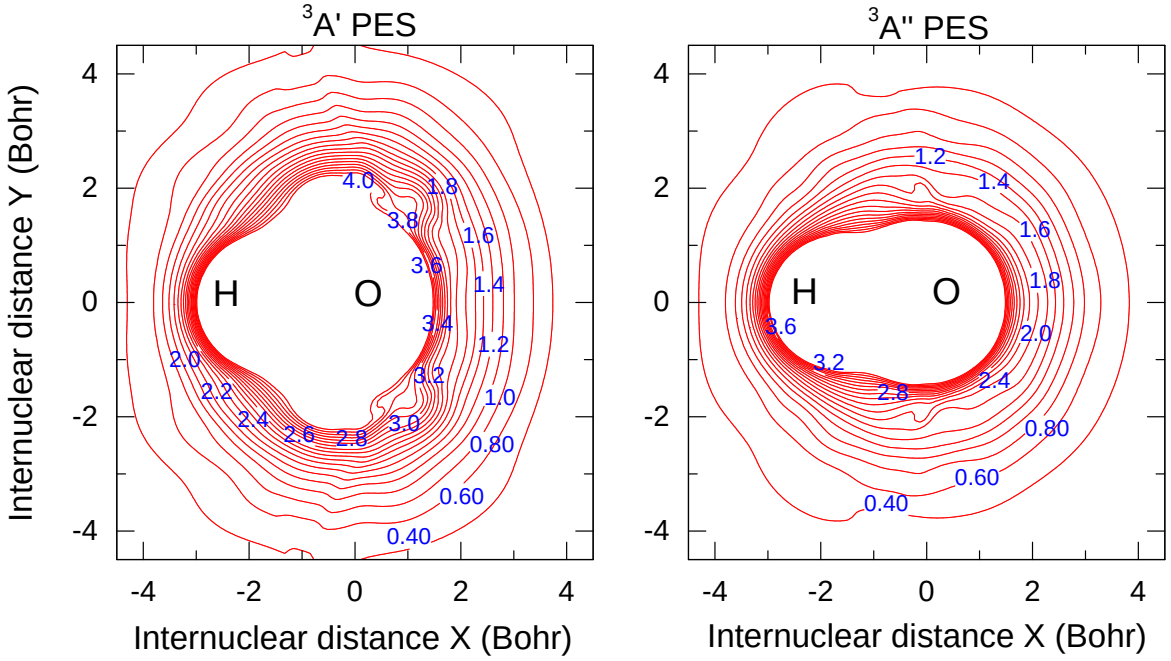

Figure 1.8 — Potential energy surface of the O(^{3}P) + H_2 system. Atomic O and H are fixed at the (X, Y) positions of (0, 0) and (-2, 0), whereas another H is free to approach them from all directions, causing different total potential energies (in units of eV). Figure from Li et al. (2014).

chemistry. The UDfA (UMIST Database for Astrochemistry) database (previously called the UMIST database, created by Tom Millar) is the best-known and most widely used. A second is the OSU database initially developed by Prasad & Huntress (1980), updated by Chun Leung and Eric Herbst, and then revised over the last twenty years by Herbst and collaborators. Recently, a third, the KInetic Database for Astrochemistry (KIDA, see Wakelam et al. 2012), has been built and is starting to be used. The simulated results may be different depending on the database used in the model calculation. A comparison between the results obtained by using UDfA and KIDA is included in the review by Agúndez & Wakelam (2013). In this thesis, we employ the UDfA database for our astrochemical simulations.

1.4 Basic chemical physics

The molecular data used in astrochemical models, such as collision rates, reaction rate coefficients and photodissociation cross sections, come from chemical physics (sometimes called physical chemistry) and are studied both experimentally and theoretically. Experimental techniques, which have heavily relied on lasers over the past 50 years, can provide information on the reaction cross sections, products and their energetics, branching ratios, and reaction mechanisms, amongst other things. These experiments, such as those using crossed molecular beams with mass spectrometric detection, chemiluminescence, and laser induced fluorescence, are very expensive and time consuming, and sometimes dangerous or difficult to conduct. Alternatively, computational chemistry, which is based on strict quantum mechanics or classical approximations, can provide similar or even

more-accurate information on chemical properties and molecular processes than can experiments, especially for radicals and ions which are difficult to prepare in the lab. This is thanks to the progress with multicore (super-)computers. Data from experiments can then be used to benchmark the chemical-physics models.

Within the Born-Oppenheimer approximation, it takes two steps to model a molecular process such as photodissociation or a collision. First, one needs to solve for the eigenvalues of the electronic Hamiltonian while keeping the nuclear positions fixed. For a diatomic system, this results in a potential energy curve for each bound or unbound electronic state (see Fig. 1.7), whereas for a tri- or poly-atomic molecule, the solutions are depicted as potential energy surfaces (PES). These PESs can be determined by first computing the energy of a large number of geometrical configurations using *ab initio* calculations from first principles of quantum mechanics or some approximate method. These points are then fitted to a convenient functional form. For a polyatomic system, accurate potential energy surfaces are very hard to compute and impossible to derive from experiments. The computation of the many excited electronic states of a triatomic molecule, or the ground electronic state of a polyatomic system typically takes years of hard work before the construction of reliable PESs.

After the calculation of a PES, the dynamics of the nuclei on it need to be solved, with the specific method depending on the application. In this thesis, the main applications are photodissociation and state-to-state reaction rates. Obtaining photodissociation cross sections may involve solving the coupled-channels nuclear Schrödinger equations, whereas other techniques may be more appropriate for solving the dynamics on the ground state potential surface to determine inelastic collision rates or reaction rate coefficients. Despite the differences between employed methods, such as for these two processes, the underlying idea is the same.

Taking the reaction between H and OH as an example, a high-accuracy potential energy surface for the reaction between O(^{3}P) and H_2, constructed by Rogers et al. (2000b), is shown in Fig. 1.8. These same PESs can also be used to study its reverse reaction, H + OH, which is experimentally difficult to measure because it is hard to prepare coincident beams of pure OH and H. To accurately evaluate a thermal rate coefficient of a reaction theoretically one has to know the contributions from the most important reactant rovibrational states. This requires individual state-to-state cross sections and reaction rates, each of which may take a long time to calculate. Full quantum mechanical calculations (QM) provide the most accurate method when solving the nuclear equations, but become computationally prohibitive at high temperatures. For the case of H + OH, the best compromise solution are Quasi-Classical Trajectory calculations (QCT), which are based on Newton's equations of motion and are more efficient than QM. Transition State Theory (TST) is another useful tool for calculating approximate rate constants for reactions occurring in the gas phase and in the condensed phases (Truhlar & Garrett 1984) and assumes that a reaction proceeds along the path of least potential energy. This method becomes especially important when the reaction system is large.

1.5 Contents of this thesis and outlook

This thesis explores the chemistry of interstellar and circumstellar molecules during star formation and death. The subjects of the next four chapters and the main questions they address are outlined below. From the perspective of chemical physics, the most important outcome of this thesis lies in that the rates for two important reactions are determined accurately for the first time: N_2 photodissociation and reaction rates (both state-to-state and thermal) of OH with H.

In Chapter 2, the photodissociation rate of interstellar N_2 is determined. Nitrogen is one of the most abundant elements in the universe, and the partitioning of nitrogen between N and N_2 controls the formation of more complex prebiotic nitrogen-containing species. Photodissociation is the primary destruction route of N_2 in any region where UV photons are present. Based on a highly-accurate spectroscopic model of the molecule, new photodissociation rates and shielding functions for N_2 are computed. The N $\rightarrow$ N_2 transition in PDRs and other astrophysical environments is then modeled, and some interesting questions are raised about a previous marginal detection of N_2 in the absorption spectrum of a translucent cloud.

In Chapter 3, the newly derived N_2 photodissociation rates from Chapter 2 are applied to the chemistry in the circumstellar envelope of a C-rich AGB stars, IRC +10216. This source is the nearest asymptotic giant branch star and the brightest object in the sky at far-infrared wavelengths, and one of the richest molecular sources in the sky. According to a sensitivity analysis of the entire chemical network, the process $N_2 + h\nu \rightarrow N + N$ is one of the most significant reactions in the outer CSEs, but has never been treated properly. In addition to using the latest reported photodissociation rates and shielding functions of N_2 and CO in our models, a new fully-3D spherical model of an isotropic interstellar radiation field has been employed. Using the RATE12 gas-phase reaction network with our improved photodissociation treatment, it is found that the abundances of many N- and C-bearing species are affected. The new results are compared with observational data.

In Chapter 4, the chemistry of O-rich AGB stars is studied using a similar approach as in Chapter 3, with our updated photodissociation treatment of N_2 and CO. The specific CSE modeled is that of the AGB star IK Tau for which many new data exist. Our improved model of CSE chemistry from Chapter 3 is combined with a new appraisal of the critical 'parent species', i.e., the products of high-temperature and shocked chemistry in the inner CSE which seed our model of the cooling outer-CSE. The important formation and destruction pathways of molecules in IK Tau are identified, this time finding higher abundances of O-bearing species relative to Chapter 3, such as H_2O, OH, and NO. The appearance of several species formed in the outer-CSE model can be linked to the abundances of parent species, and can thus put constraints on their abundances through comparison with observations of IK Tau.

In Chapter 5, state-dependent rate coefficients for the experimentally-difficult reaction, $H + OH \longrightarrow O + H_2$, are computed. The reverse O (^{3}P) + H_2 system has attracted interest for more than half a century since it is known to be a participant in combustion processes and plays an important role in warm interstellar gas such as shocks, clouds exposed to intense UV radiation, and the inner regions of protoplanetary disks. Despite

extensive theoretical and experimental investigations on O (^{3}P) + H_2, few studies have been done for the forward reaction, H + OH $(v, j) \rightarrow$ O + H_2. In particular, accurate state-specific rate constants of this reaction, which are needed in astrochemical models of dissociative shocks and disks, are lacking. In this chapter, highly-accurate *ab initio* potential energy surfaces are used to perform quasi-classical trajectory calculations as well as transition-state theory methods. The computed state-to-state cross sections over a range of collision energies and internal ro-vibrational excitation states are then used to determine state-to-state and thermal rate constants, including their temperature dependencies.

The main results of this thesis are:

- Chapter 2. The new interstellar N_2 photodissociation rate has been determined with an uncertainty of only 10%, down by an order of magnitude compared with the previous uncertainty. Self-shielding and shielding by H_2 and dust are more effective than that by H and CO. The transition of N $\rightarrow$ N_2 occurs at nearly the same depth into a cloud as that of $C^+ \rightarrow$ C $\rightarrow$ CO.
- Chapter 3. N_2 and CO are more abundant at the edge of a circumstellar envelope than predicted by previous models due to a proper treatment of their self- and mutual shielding. The new photodissociation treatment induces large changes in the predicted column densities (factor of 10) and peak radii of some species (e.g., C_nN and $C_n N^-$ carbon chains) in the IRC +10216 carbon-rich AGB star model. The new models can be tested directly by future ALMA observations.
- Chapters 4. The most abundant daughter species suitable as targets for future observations in the AGB star IK Tau were identified, quantified, and analysed, including all C-, N-, O-, Si-, S-, P-, Cl-, and F- bearing molecules. Key molecular processes in O-rich AGB envelopes are photoionization/photodissociation, ion-molecule reactions, and dissociative recombination. The upper limit on the potential parent species CH_4 is $< 2.5 \times 10^{-6}$, based on the observed upper-limits of two daughter species, C_2H and CH_3OH. Future observations of NS and N_2H^+ can be used to constrain the abundances of parent species S and N_2. Finally, the stellar mass-loss rate has a large impact on the calculated abundances, which is usually difficult to obtain from observations directly.
- Chapters 5. Rate constants for OH in excited vibrational and rotational states are orders of magnitude larger than the thermal rate constants, which needs to be taken into account in astrochemical models. An effective barrier may be induced by the rotational excitation at lower collision energies (< 0.6 eV).

The future outlook of astrochemistry is bright. This is evident in the rapid progression of observational techniques as well as theoretical and laboratory physics and chemistry, and their combination into sophisticated models of real astrochemical objects. This thesis attempts to cover a range of these astrochemical aspects. There are many interesting topics which are the subject of ongoing efforts in the field of astrochemistry. Here, I would like to mention a few possible projects that are a natural extension of current work in the coming years. Evolved stars are of particular interest and raise a few important questions which are yet to be solved. For example, what is the chemistry in S-type AGB stars? How to correctly simulate the chemistry in post-AGB objects like protoplanetary nebulae with increased central UV radiation? Which of the predictions made in this

thesis will stand up best to future observational tests made possible by spatially resolved observations with ALMA? Questions also remain about the parent species in AGB CSEs, including the abundances of elemental N and S: how well are those predicted by shock-induced non-LTE chemical models? In a broader context, in what form do the gas and dust ejected from evolved stars eventually get transferred to another generation of forming stars? More observations will raise even more questions, and with improved models some will also be answered. But, understanding these observations will undoubtedly require further efforts from chemists determining accurate rate coefficients.

One also needs to look much further into the future. Take again the Rosetta mission as an example. Planned more than 30 years ago, this mission not only helped in answering many interesting astrochemical questions but it also proved that (nearly) anything is possible in the future as long as one has a long-term vision! This holds in particular for the field of astrochemistry.

Chapter 2

Photodissociation of N_2 during stellar formation

Abstract.
Context. Molecular nitrogen is one of the key species in the chemistry of interstellar clouds and protoplanetary disks, but its photodissociation under interstellar conditions has never been properly studied. The partitioning of nitrogen between N and N_2 controls the formation of more complex prebiotic nitrogen-containing species.
Aims. The aim of this work is to gain a better understanding of the interstellar N_2 photodissociation processes based on recent detailed theoretical and experimental work and to provide accurate rates for use in chemical models.
Methods. We used an approach similar to that adopted for CO in which we simulated the full high-resolution line-by-line absorption + dissociation spectrum of N_2 over the relevant 912–1000 Å wavelength range, by using a quantum-mechanical model which solves the coupled-channels Schrödinger equation. The simulated N_2 spectra were compared with the absorption spectra of H_2, H, CO, and dust to compute photodissociation rates in various radiation fields and shielding functions. The effects of the new rates in interstellar cloud models were illustrated for diffuse and translucent clouds, a dense photon dominated region and a protoplanetary disk.
Results. The unattenuated photodissociation rate in the Draine (1978, ApJS, 36, 595) radiation field assuming an N_2 excitation temperature of 50 K is 1.65×10^{-10} s^{-1}, with an uncertainty of only 10%. Most of the photodissociation occurs through bands in the 957–980 Å range. The N_2 rate depends slightly on the temperature through the variation of predissociation probabilities with rotational quantum number for some bands. Shielding functions are provided for a range of H_2 and H column densities, with H_2 being much more effective than H in reducing the N_2 rate inside a cloud. Shielding by CO is not effective. The new rates are 28% lower than the previously recommended values. Nevertheless, diffuse cloud models still fail to reproduce the possible detection of interstellar N_2 except for unusually high densities and/or low incident UV radiation fields. The transition of $N \rightarrow N_2$ occurs at nearly the same depth into a cloud as that of $C^+ \rightarrow C \rightarrow CO$. The orders-of-magnitude lower N_2 photodissociation rates in clouds exposed to black-body radiation fields of only 4000 K can qualitatively explain the lack of active nitrogen chemistry observed in the inner disks around cool stars.
Conclusions. Accurate photodissociation rates for N_2 as a function of depth into a cloud are now available that can be applied to a wide variety of astrophysical environments.

X. Li, A. N. Heays, R. Visser, W. Ubachs, B. R. Lewis, S. T. Gibson, and E. F. van Dishoeck
A&A, **555** , A14 (2013)

2.1 Introduction

Nitrogen is one of the most abundant elements in the universe and an essential ingredient for building prebiotic organic molecules. In interstellar clouds, its main gas-phase reservoirs are N and N_2, with the balance between these species determined by the balance of the chemical reactions that form and destroy N_2. If nitrogen is primarily in atomic form, a rich nitrogen chemistry can occur leading to ammonia, nitriles and other nitrogen compounds. On the other hand, little such chemistry ensues if nitrogen is locked up in the very stable N_2 molecule. The latter situation is similar to that of carbon with few carbon-chain molecules being produced when most of the volatile carbon is locked up in CO (Langer & Graedel 1989; Bettens et al. 1995).

Direct observation of extrasolar N_2 is difficult because, unlike CO, it lacks strong pure rotational or vibrational lines. N_2 is well studied at various locations within our solar system through its electronic transitions at ultraviolet wavelengths (e.g., Strobel 1982; Meier et al. 1991; Wayne 2000; Liang et al. 2007) and a detection in interstellar space has been claimed through UV absorption lines in a diffuse cloud toward the bright background star HD 124314 (Knauth et al. 2004). In dense clouds well shielded from UV radiation, most nitrogen is expected to exist as N_2 (e.g., Herbst & Klemperer 1973; Woodall et al. 2007) but can only be detected indirectly through the protonated ion N_2H^+ (Turner 1974; Herbst et al. 1977) or its deuterated form N_2D^+. N_2H^+ emission is indeed widely observed in dense cores (e.g., Bergin et al. 2002; Crapsi et al. 2005), star-forming regions (Fontani et al. 2011; Tobin et al. 2012), protoplanetary disks (Dutrey et al. 2007; Öberg et al. 2010) and external galaxies (Mauersberger & Henkel 1991; Meier & Turner 2005; Muller et al. 2011).

Photodissociation is the primary destruction route of N_2 in any region where UV photons are present. Current models of diffuse and translucent interstellar clouds are unable to reproduce the possible detection of N_2 for one such cloud (Knauth et al. 2004). One possible explanation is that the adopted N_2 photodissociation rate is incorrect. Even in dense cores, not all nitrogen appears to have been transformed to molecular form (Maret et al. 2006; Daranlot et al. 2012). Observations of HCN in the surface layers of protoplanetary disks suggest that the nitrogen chemistry is strongly affected by whether or not a star has sufficiently hard UV radiation to photodissociate N_2 (Pascucci et al. 2009). Thus, not only the absolute photodissociation rate but also its wavelength dependence is relevant. All of these astronomical puzzles make a thorough study of the interstellar N_2 photodissociation very timely.

In contrast with many other simple diatomic molecules, the photodissociation of interstellar N_2 has never been properly studied (van Dishoeck 1988; van Dishoeck et al. 2006). The reason for this is that the photodissociation of N_2, similarly to CO, is initiated by line absorptions at wavelengths below 1000 Å (1100 Å for CO), where high-resolution laboratory spectroscopy has been difficult. To compute the absolute rate and to treat the depth dependence of the photodissociation correctly, the full high-resolution spectrum of the dissociating transitions needs to be known. Because the absorbing lines become optically thick for modest N_2 column densities, the molecule can shield itself against the dissociating radiation deeper into the cloud. Moreover, these lines can be shielded by lines of more abundant species such as H, H_2 and CO. Until recently, accurate N_2 molecular

data to simulate these processes were not available. Thanks to a concerted laboratory (e.g., Ajello et al. 1989; Helm et al. 1993; Sprengers et al. 2003, 2004, 2005; Stark et al. 2008; Lewis et al. 2008b; Heays et al. 2009, 2011) and theoretical (e.g., Spelsberg & Meyer 2001; Lewis et al. 2005a,b; Haverd et al. 2005; Lewis et al. 2008a,c; Ndome et al. 2008) effort over the last two decades, this information is now available.

In this chapter, we use a high resolution model spectrum of the absorption and dissociation of N_2 together with simulated spectra of H, H_2 and CO to determine the interstellar N_2 photodissociation rate and its variation with depth into a cloud. The effect of the new rates on interstellar N_2 abundances is illustrated through a few representative cloud models. In particular, the N_2 abundance in diffuse and translucent clouds is revisited to investigate whether the new rates alleviate the discrepancy between models and the possible detection of N_2 in one cloud (Knauth et al. 2004). The data presented here can be applied to a wide range of astrochemical models, including interstellar clouds in the local and high redshift universe, protoplanetary disks and exo-planetary atmospheres. The $^{14}N^{15}N$ photodissociation rate and isotope selective interstellar processes will be discussed in an upcoming paper (Heays et al. in prep.) and have been discussed in the context of the chemistry of Titan by Liang et al. (2007).

2.2 Photodissociation processes of N_2

2.2.1 Photoabsorption and photodissociation spectrum

The closed-shell diatomic molecule N_2 has a dissociation energy of 78 715 cm^{-1} (9.76 eV, 1270 Å) (Huber & Herzberg 1979), making it one of the most stable molecules in nature. Electric-dipole-allowed photoabsorption and predissociation in N_2 starts only in the extreme ultraviolet spectral region, at wavelengths shorter than 1000 Å. The molecular-orbital (MO) configuration of the $X\,^1\Sigma_g^+$ ground state of N_2 is

$$(1\sigma_g)^2(1\sigma_u)^2(2\sigma_g)^2(2\sigma_u)^2(1\pi_u)^4(3\sigma_g)^2. \tag{2.1}$$

Electric-dipole-allowed transitions from the ground state access only states of $^1\Pi_u$ and $^1\Sigma_u^+$ symmetry. In the region below the cutoff energy of the interstellar radiation field of 110 000 cm^{-1} (13.6 eV, 912 Å), five such states are accessible: the c' and $b'\,^1\Sigma_u^+$ states, and the c, o, and $b\,^1\Pi_u$ states. The c', c, and o states (sometimes labelled c'_4, c_3, and o_3; respectively) have Rydberg character, the relevant transitions corresponding to single-electron excitations from the $3\sigma_g$ or $1\pi_u$ orbitals into a Rydberg orbital. On the other hand, the b' and b states are valence states of mixed MO configurations accessed by transitions in which one or two electrons are excited into antibonding orbitals. The relevant potential-energy curves (PECs) for these $^1\Pi_u$ and $^1\Sigma_u^+$ states are shown in Fig. 2.1, in blue and black, respectively. The c' and c states, whose PECs have the smallest equilibrium internuclear distance in Fig. 2.1, are the first members of Rydberg series converging on the ground state of the N_2^+ ion, $X^2\Sigma_g^+$, while the o state is the first member of the series converging on the first ionic excited state, $A^2\Pi_u$. In the case of the b' and b valence states, the extended widths of the corresponding PECs in Fig. 2.1 are due to the aforementioned configurational mixing. In addition, there are significant electrostatic interactions within the manifolds of a given symmetry, Rydberg-valence for $^1\Sigma_u^+$, and Rydberg-valence and Rydberg-Rydberg for $^1\Pi_u$, since the MO configurations of all of the

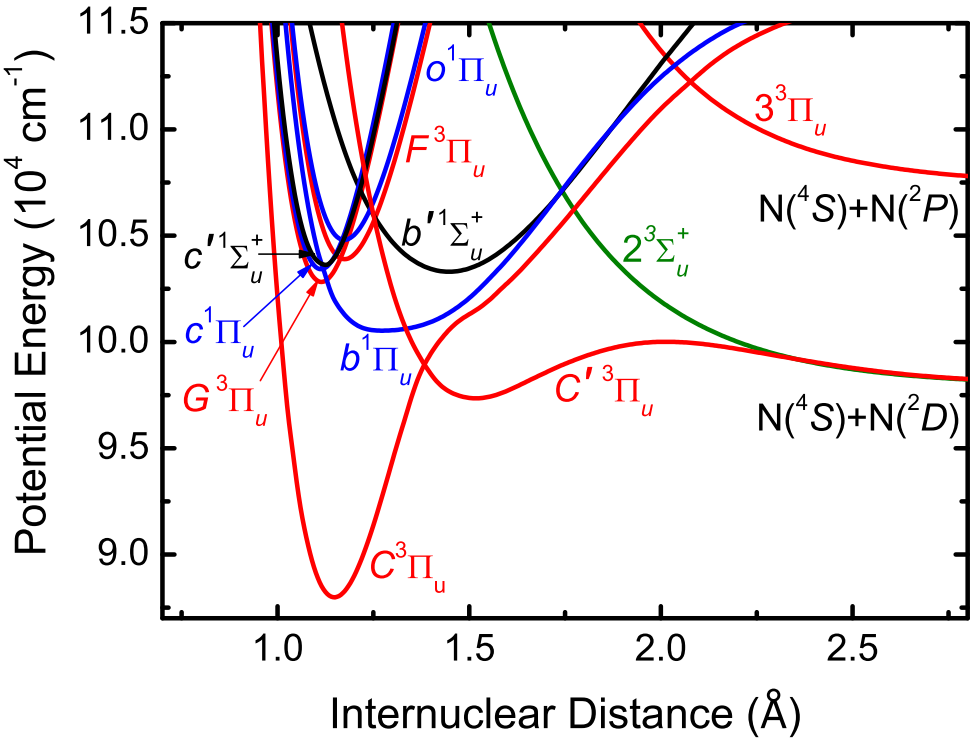

Figure 2.1 — Diabatic-basis potential-energy curves for electronic states of N_2 relevant to interstellar photodissociation. Blue curves: $^1\Pi_u$ states. Black curves: $^1\Sigma_u^+$ states. Red curves: $^3\Pi_u$ states. Green curve: $2\,^3\Sigma_u^+$ state. The energy scale is referenced to the $v = 0, J = 0$ level of the $X\,^1\Sigma_g^+$ ground state (not shown). The lowest dissociation limit, N(^4S)+N(^4S) at $\sim 78\,715$ cm^{-1} (9.76 ev), is beyond the scale of the figure. The H ionization potential of 13.6 eV provides an upper limit to the interstellar radiation field and corresponds to 109691 cm^{-1}.

isosymmetric states differ in exactly two of the occupied electron orbitals (Lefebvre-Brion & Field 2004). The PECs in Fig. 1 are shown in the diabatic (crossing) representation.

Most of the rovibrational levels of the singlet excited states are predissociated, i.e., the molecule is initially bound following photoabsorption, but then dissociates on timescales of a nanosecond or less due to direct or indirect coupling to a dissociative continuum. For the $^1\Pi_u$ states considered here, spin-orbit coupling to the strongly-coupled and -predissociated $^3\Pi_u$ manifold (red PECs in Fig. 2.1), with ultimate dissociation via the C' state, provides the predissociation mechanism (Lewis et al. 2005a; Lewis et al. 2008c), with a minor contribution from a crossing by the $2\,^3\Sigma_u^+$ state (green PEC in Fig. 2.1) at higher energies. For the $^1\Sigma_u^+$ states, two mechanisms are important (Heays 2011): first, a similar spin-orbit coupling to the $^3\Pi_u$ manifold, solely responsible for predissociation in the absence of rotation, and second, rotational coupling between the $^1\Sigma_u^+$ and $^1\Pi_u$ manifolds, followed by the $^1\Pi_u$ predissociation described above. For the wavelengths considered here, as implied by Fig. 2.1, these mechanisms result in primarily N(^4S)+N(^2D) dissociation products, i.e., one of the nitrogen atoms is formed in an excited electronic state which decays on a timescale of 17 h into the ground state N(^4S). This is consistent with the observations of Walter et al. (1993) who failed to detect direct N(^4S)+N(^4S) dissociation products.

The line-by-line models previously used to compute the N_2 photodissociation rate require knowledge of the wavelengths, oscillator strengths, lifetimes, and predissociation probabilities of (transitions to) all rovibrational levels associated with the coupled excited singlet states. For the case of the isoelectronic molecule CO, molecular models have been built previously by specifying the term values, rotational and vibrational constants, oscillator strengths, Einstein A coefficients, and predissociation probabilities for each excited electronic state (e.g., van Dishoeck & Black 1988; Viala et al. 1988; Lee et al. 1996; Visser et al. 2009). These have allowed the rotationally-resolved absorption spectra of CO and its isotopologues to be constructed using simple scaling relations. Such models must be validated by a large quantity of laboratory data and have been shown to be incorrect when strong interactions occur between electronic states and their differing energetics. For the case of N_2, it is known that there are many wide-scale perturbations, together with rapid dependences of oscillator strengths and predissociation linewidths on rotational quantum number J, and strong, irregular isotopic effects. It is impossible to fully reproduce these effects using only a few spectroscopic constants.

The best way to simulate the N_2 spectrum, and the method employed here, is, at each energy, to solve the full radial diabatic coupled-channel Schrödinger equation (CSE) for the coupled electronic states described above, including all electrostatic, spin-orbit, and rotational couplings, using the quantum-mechanical methods of van Dishoeck et al. (1984). This is a *physically-based* technique, with great predictive powers which enables confidence in the computed spectrum in regions lacking experimental confirmation, even where perturbations are present. Furthermore, computations of isotopic spectra require only the change of a single parameter, i.e., the reduced molecular mass, in the molecular model: the results can be guaranteed since the underlying physics is the same for all isotopologues. The same cannot be said for the line-by-line models such as those employed for CO, which would also benefit from a CSE approach. The detailed CSE model for N_2 employed here has been described in Heays (2011),[a] incorporates earlier models of the $^1\Pi_u$ (Lewis et al. 2005a; Haverd et al. 2005) and $^3\Pi_u$ states (Lewis et al. 2008c) and has been tested extensively against laboratory data, including high-resolution spectra obtained at the SOLEIL synchrotron facility (Heays 2011; Heays et al. 2011). A complete discussion of the CSE model and a full listing of computed spectroscopic data is deferred to Heays et al. (in prep.).

For a given rotational-branch transition, combining the excited-state coupled-channel wavefuction with the X-state radial wavefunction and appropriate diabatic allowed transition-moment components yields the corresponding (continuous with wavelength) photoabsorption cross section, with the computed linewidths providing the required predissociation lifetime information. Total cross sections for a given temperature, assuming local thermodynamic equilibrium, are formed by summing the individual branch cross sections, weighted by appropriate Boltzmann and Hönl-London factors, and including rotational levels with J as high as 50.

CSE photoabsorption cross sections, $\sigma_{\rm abs}$, are computed here over the wavelength range 912–1000 Å with a step size of 0.0001 Å, and for temperatures of 10, 50, 100, 500, and 1000 K. The Doppler broadening of the spectral lines is taken into account by convolution

[a] Available on-line at `http://hdl.handle.net/1885/7360`

with a Gaussian profile having a thermal line width.

A 10% uncertainty is estimated for the total magnitude of the photoabsorption cross section and principally arises from the absolute uncertainty of the calibrating laboratory spectra (Haverd et al. 2005; Heays 2011). The laboratory measurements in question were recorded at 300 K or below, so the uncertainty may be somewhat larger for calculations employing an extrapolation to 1000 K. Additionally, 3% of the 1000 K ground state population will be in the first vibrational level, leading to a slight redistribution of the absorption cross section into hot bands. This is considered in the model calculations.

Photodissociation cross sections, $\sigma_{\rm pd}{=}\eta \times \sigma_{\rm abs}$, are obtained from the photoabsorption cross sections by comparing the predissociation and radiative lifetimes for each rovibrational level. The predissociation efficiency η is then given by $\eta = 1 - \tau_{\rm tot}/\tau_{\rm rad}$, where $\tau_{\rm tot}$ is the inverse of the sum of the radiative and predissociation rates. For almost all transitions, $\eta \simeq 1$: significant corrections for partial dissociation are needed only for the $b - X(1,0)$ and $c' - X(0,0)$ bands near 986 and 959 Å, respectively (Lewis et al. 2005b; Liu et al. 2008; Sprengers et al. 2004; Wu et al. 2012). For example, the top panel of Fig. 2.2 illustrates the CSE-computed branching ratio between spontaneous emission back to the ground state and dissociation as a function of rotational level for $c' - X(0,0)$. Such calculations were performed for all bands appearing between 955 and 991 Å. The difference between calculated absorption and dissociation cross sections for the very-strongly absorbing $c' - X(0,0)$ band is demonstrated in Fig. 2.3, revealing a significant alteration of the band profile once the dissociation efficiency is considered.

The bottom panel of Fig. 2.2 shows the thermal population for various J levels of the ground vibrational state, assuming several temperatures. By comparing this with the top panel of Fig. 2.2 it can be seen that the dissociation fraction for this band will depend significantly on the temperature.

2.2.2 Photodissociation rates

The photodissociation rate, $k_{\rm pd}$, of N_2 exposed to UV radiation can be calculated according to

$$k_{\rm pd} = \int \sigma_{\rm pd}(\lambda) I(\lambda) d\lambda \ \ {\rm s}^{-1}, \tag{2.2}$$

where the photodissociation cross section, $\sigma_{\rm pd}$, is in units of cm^2 and I is the mean intensity of the radiation in photons cm^{-2} s^{-1} Å^{-1} as a function of wavelength, λ, in units of Å. The unattenuated interstellar radiation field according to Draine (1978) is used in most of the following calculations and is given by

$$I(\lambda) = 3.2028 \times 10^{15}\lambda^{-3} - 5.1542 \times 10^{18}\lambda^{-4} + 2.0546 \times 10^{21}\lambda^{-5}. \tag{2.3}$$

Inside a cloud, self-shielding, shielding by H, H_2, CO and other molecules, and continuum shielding by dust all reduce the photodissociation rate below its unattenuated value k^0. The shielding function is defined to be

$$\Theta = k/k^0 \tag{2.4}$$

and can be split into a self-shielding,

$$\Theta_{SS} = \frac{\int I(\lambda) \exp\left[-N({\rm N_2})\sigma_{\rm abs}(\lambda)\right] \sigma_{\rm pd}(\lambda)\, d\lambda}{\int I(\lambda)\, \sigma_{\rm pd}(\lambda)\, d\lambda}, \tag{2.5}$$

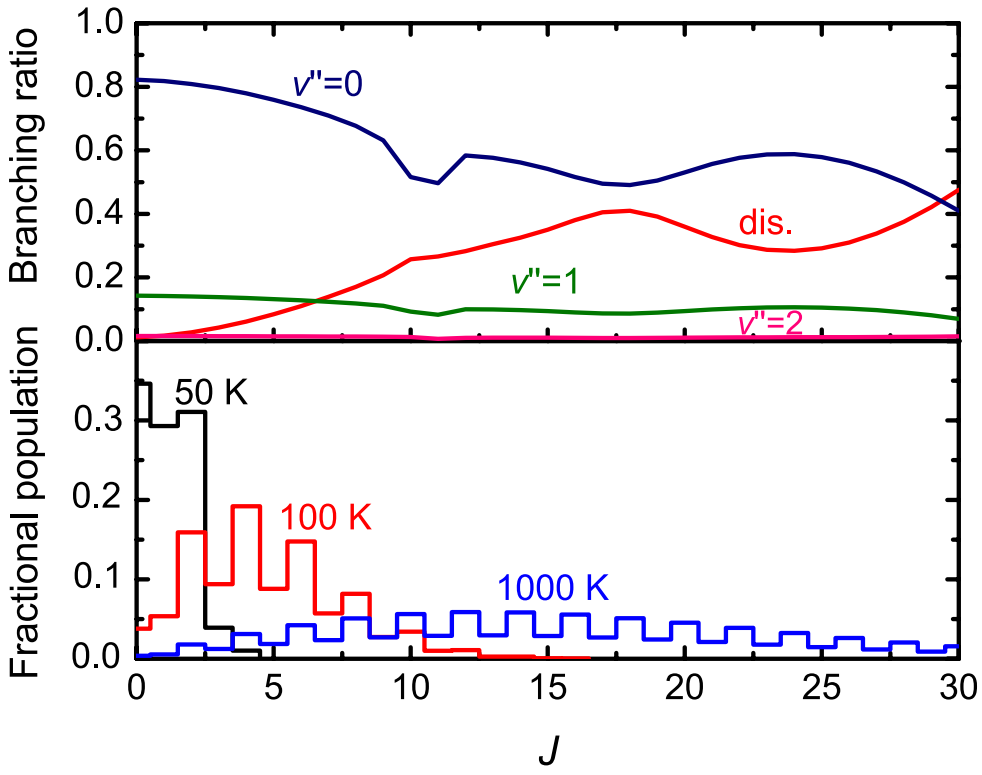

Figure 2.2 — *Top:* The branching to various decay channels of the $c'(v'=0)$ excited-state of N_2 as a function of total rotational quantum number, J. The figure includes spontaneous emission to several non-dissociative ground state vibrational levels ($v''=0, 1$ and 2) and decay due to predissociation (dis.). *Bottom:* Fractional population of the N_2 ground state in its lowest vibrational level as a function of J and for several excitation temperatures. The 2:1 ratio of populations for even:odd J levels arises from the combined rotational and nuclear spin statistics.

and a mutual-shielding part,

$$\Theta_{MS} = \frac{\int I(\lambda) \exp\left[-N(X)\sigma_{\rm X}(\lambda)\right] \sigma_{\rm pd}(\lambda)\, d\lambda}{\int I(\lambda)\, \sigma_{\rm pd}(\lambda)\, d\lambda} \tag{2.6}$$

Here, X=H, H_2 or CO and N is the column density of the various species. A dust extinction term, $\exp(-\gamma A_{\rm V})$, can be written in place of the exponential term in Eq. (6) where $A_{\rm V}$ is the optical depth in magnitudes and γ depends on the assumed properties of the dust. This is further discussed in § 2.3.3. In all cases, the integrals above are computed between 912 and 1000 Å.

2.3 Accurate N_2 photodissociation rate and shielding functions

2.3.1 Unattenuated interstellar rate

Figure 2.4 shows model spectra of N_2 and $H_2 + H$ absorption for excitation temperatures of 50 and 1000 K. At 50 K the N_2 spectrum is made up of prominent well-separated bands. These represent excitation to a range of vibrational levels attributable to the five accessible electronic states. In contrast, the spectrum simulating a temperature of

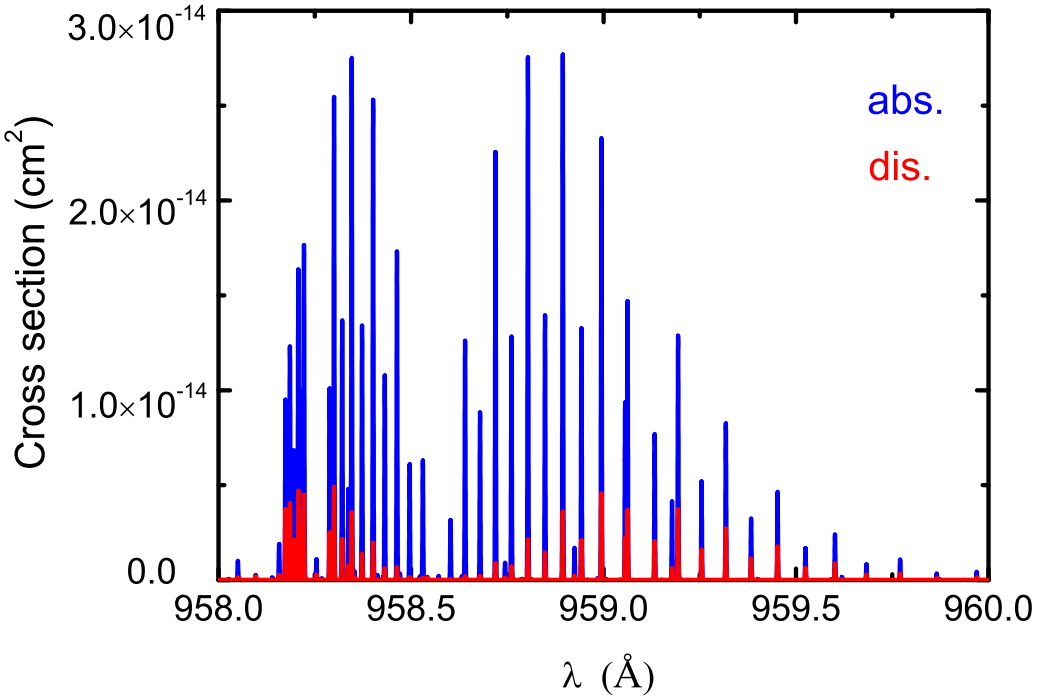

Figure 2.3 — The CSE-calculated absorption cross section (blue) of the $c'(v'=0)$ level of N_2 assuming an excitation temperature of 300 K. Also shown is a dissociation cross section (red) which has been corrected for the non-unity dissociation efficiency, η_J, of this band (see Fig. 2.2).

1000 K includes the excitation of many more rotational levels and has few sizable windows between bands.

Unshielded photodissociation rates of N_2 immersed in a Draine (1978) field were calculated from the model photodissociation cross section using Eqs. (2.2) and (2.3), and assuming a range of excitation temperatures. These are plotted in Fig. 2.5 and listed in Table 2.1. The rate at 50 K is $1.65 \times 10^{-10}\,\mathrm{s}^{-1}$, where the uncertainty of 10% only reflects the uncertainty in the cross sections, not the radiation field (see below). This new value is 28% lower than the value of $2.30 \times 10^{-10}\,\mathrm{s}^{-1}$ recommended by van Dishoeck (1988). The latter estimate was based on the best available N_2 spectroscopy at the time, and has an order-of-magnitude uncertainty. For comparison, the unshielded photodissociation rate of N_2 at low T is around 35% smaller than that of CO computed by Visser et al. (2009).

Table 2.2 summarizes the contributions of individual bands to the total unattenuated dissociation rate. It is seen that the main contributions arise from bands 12, 21, 22, 23 and 24. Hence, the key wavelength ranges responsible for the photodissociation of N_2 are around 940 Å and between 957–980 Å.

The calculated unattenuated rate of N_2 increases with increasing temperature so that the value at 1000 K, $1.86 \times 10^{-10}\,\mathrm{s}^{-1}$, is 15% higher than for 10 K. This is largely due to a variable but overall increase with rotational quantum number J of the photodissociation branching ratios of the $c'(v=0)$ and $b(v=1)$ states. This can be seen in Fig. 2.2 for the $c'(v'=0)$ state, where at 10 K all of the excited population is in levels with $J = 0-3$. These levels have a low predissociation probability and hardly contribute to the photodissociation rate. At higher temperatures, the excited population shifts to higher

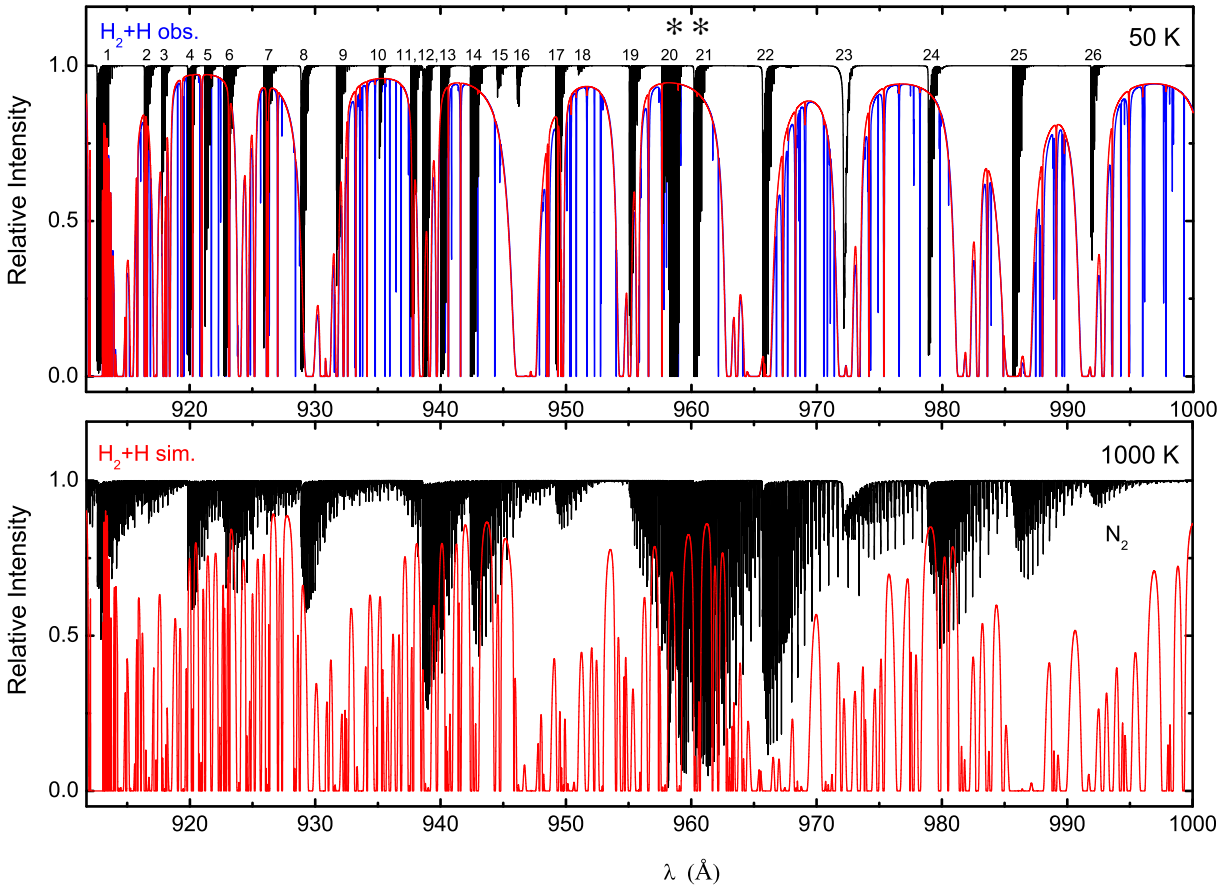

Figure 2.4 — Simulated absorption spectra for N_2 (black) and $H_2 + H$ (red) in the wavelength range 912–1000 Å assuming thermal excitation temperatures of 50 (top) and 1000 K (bottom). The column density of N_2 is 10^{15} cm^{-2} and values for H_2 and H are taken to be half of the observed column densities in the well-studied diffuse cloud toward ζ Oph, as is appropriate for the center of the cloud: $N(H_2)$=2.1×10^{20} and $N(H)$=2.6×10^{20} cm^{-2}. The model H_2 Doppler width is 3 km s^{-1}. Also shown is the $H_2 + H$ absorption spectrum (blue) towards ζ Oph using the observed column densities for individual J levels, showing enhanced non-thermal excitation of H_2 in the higher J levels. The asterisks indicate the $c'(0)$ (Band 20) and $c(0)$ (Band 21) bands, respectively, detected in absorption towards HD 124314.

J, and at 1000 K the distribution maximum occurs around $J = 15 - 20$ for which the branching ratio to dissociation is much higher.

The rate obviously depends on the choice of radiation field. For the alternative formulations of Habing (1968), Gondhalekar et al. (1980) and Mathis et al. (1983), the unattenuated rates are 1.45, 1.34 and 1.51×10^{-10} s^{-1} at 50 K, respectively. Additionally, Table 2.1 considers the unattenuated rates of N_2 assuming different blackbody radiation fields. In these calculations, the intensities have been normalized such that the integrated values from 912–2050 Å are the same as those of the Draine (1978) field. The adopted dilution factors are 1.9×10^{-9}, 3.4×10^{-12}, 1.2×10^{-13}, 1.6×10^{-14}, and 1.6×10^{-16} for blackbody temperatures of 4000, 6000, 8000, 10 000 and 20 000 K, respectively. The value of the unattenuated rate of N_2 at 4000 K (cool star) is 6 orders of magnitude smaller than that at 20 000 K (hot star), and increases steeply with stellar effective temperature. The photodissociation rate of N_2 at 20 000 K is comparable to that in the Draine interstellar

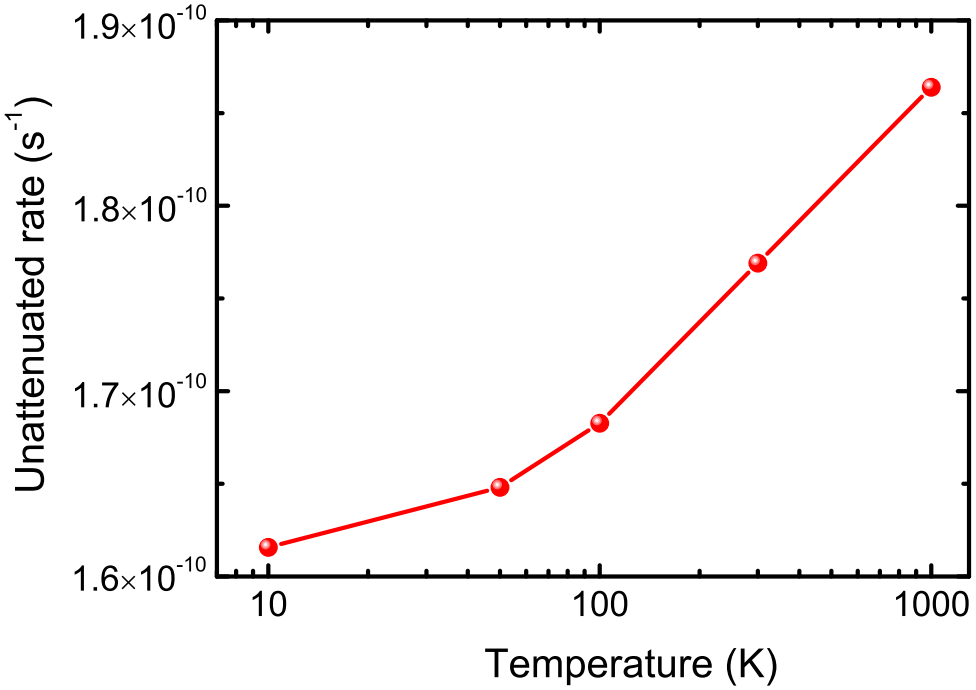

Figure 2.5 — The unattenuated photodissociation rates of N_2 immersed in a Draine (1978) field at various excitation temperatures.

Table 2.1 — The unattenuated photodissociation rates of N_2 (excitation temperature 50 K) in a blackbody radiation field at various temperatures, T_{BB}.

T_{BB}(K)	k_{pd}^{0} [a] (s^{-1})	Previous
4 000	2.18(-16)	3.0(-16)[b]
6 000	9.96(-14)	-
8 000	1.90(-12)	-
10 000	1.03(-11)	1.4(-11)[b]
20 000	1.97(-10)	-
Draine	1.65(-10)	2.3(-10)[c]

[a]All radiation fields have been normalised to a Draine (1978) field over the interval 912–2050 Å.
[b]van Dishoeck et al. (2006).
[c]van Dishoeck (1988).

field, $1.65 \times 10^{-10}\,s^{-1}$. The calculated photodissociation rates for temperatures of 4000 and 10 000 K are close to those recommended by van Dishoeck et al. (2006).

2.3.2 Self-shielding

Although self-shielding is generally less important than mutual shielding for the case of N_2 (see §3.3), it is potentially important in protoplanetary disks and has been proposed to be responsible for the enrichment of ^{15}N in bulk chondrites and terrestrial planets (Lyons 2009, 2010). In this work, we compute the self-shielding functions of N_2 at excitation

Table 2.2 — Contributions of different bands to N_2 photodissociation at 50 K at the edge (unattenuated photodissociation) and in the center of the ζ Oph diffuse cloud.

Band	Excited state[a]	λ (Å)	Edge (%)	Center (%)	Shielding
1	$o(2)$	911.7-915.1	2.41	0.07	0.01
2	$b(11)$	915.1-917.4	0.58	0.47	0.34
3	$b'(7)$	917.4-919.0	0.09	0.06	0.30
4	$c(2)$	919.0-920.8	1.63	3.65	0.95
5	$c'(2)$	920.8-922.4	0.22	0.51	0.97
6	$b(10)$	922.4-924.7	1.74	3.73	0.91
7	$b'(6)$	924.7-927.7	0.33	0.66	0.84
8	$o(1) + b(9)$	927.7-930.8	3.65	2.31	0.27
9	$b'(5)$	930.8-933.9	0.23	0.10	0.18
10	$b(8)$	933.9-936.6	0.10	0.22	0.96
11	$b'(4)$	936.6-938.5	0.47	0.52	0.47
12	$c(1)$	938.5-939.6	9.31	5.28	0.24
13	$c'(1)$	939.6-941.5	1.67	3.47	0.88
14	$b(7)$	941.5-944.1	5.01	11.04	0.93
15	$b'(3)$	944.1-945.7	0.03	0.05	0.77
16	$o(0)$	945.7-947.9	0.05	0.00	0.00
17	$b(6)$	947.9-950.6	1.23	2.00	0.69
18	$b'(2)$	950.6-953.1	0.01	0.02	0.93
19	$b(5)$	953.1-956.8	1.04	0.41	0.17
20	$c'(0) + b'(1)$	956.8-959.5	2.79	6.21	0.94
21	$c(0)$	959.5-962.9	17.00	36.80	0.92
22	$b(4) + b'(0)$	962.9-969.4	22.51	2.02	0.04
23	$b(3)$	969.4-976.2	16.05	0.51	0.01
24	$b(2)$	976.2-983.1	9.28	19.83	0.91
25	$b(1)$	983.1-988.9	1.34	0.00	0.00
26	$b(0)$	988.9-1000.0	1.24	0.05	0.02

[a]The b, c, and o levels have $^1\Pi_u$ symmetry; b' and c'_4 have $^1\Sigma_u^+$ symmetry.

temperatures of 10, 100 and 1000 K using the model absorption spectrum. Since this spectrum is constructed using thermal line widths and no turbulent broadening, it provides the maximum amount of shielding. For reference, the thermal widths of N_2 at 10, 100 and 1000 K correspond to full widths at half maximum of 0.1, 0.3 and 1.0 km s^{-1}.

As can be seen in Fig. 2.6, the photodissociation of N_2 is free of self-shielding up to a column density of around 10^{12} cm^{-2}, but is fully shielded by 10^{18} cm^{-2}. For intermediate N_2 column densities the self-shielding function increases with increasing excitation temperature. There are two reasons for this (Visser et al. 2009). First, the optical depth of each line increases linearly with the thermal population of its corresponding lower-state rotational level, but the self-shielding increases nonlinearly according to Eq. (2.5). Then, because the ground state population at higher temperatures is distributed over more levels (see Fig. 2.2) there is an overall decrease in the effectiveness of self-shielding. The second effect arises from the individual line profiles, which are constructed to have ther-

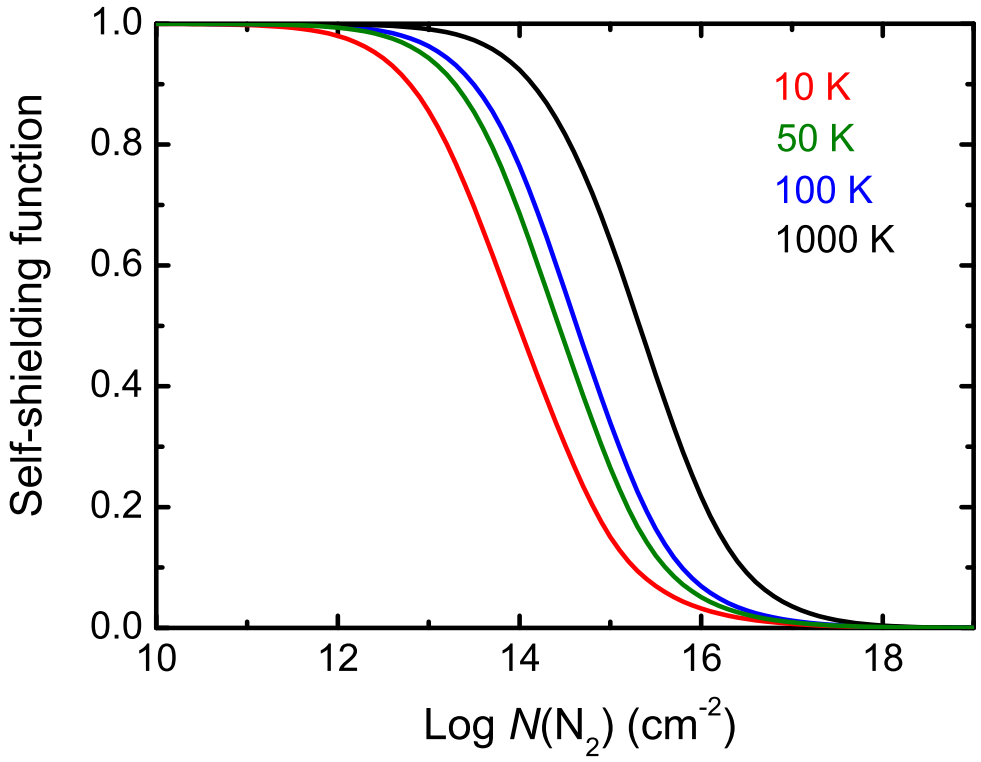

Figure 2.6 — N_2 self-shielding as a function of column density, $N(N_2)$, for excitation temperatures of 10, 50, 100 and 1000 K.

mal broadening. Those lines appearing in the 1000 K spectrum are then 10 times broader than those at 10 K, leading to decreased peak optical depth at the line center and less effective self-shielding over the whole line profile.

2.3.3 Shielding by H_2, H and CO

The wavelength range over which N_2 can be photodissociated is exactly the same range over which H_2, H and CO absorb strongly. The amount by which N_2 is shielded depends on the column densities of each of these species and is characterized by the shielding function of Eq. (2.6).

Figure 2.4 overlays absorption spectra for N_2 and H+H_2 combined. Two forms of the latter are included: a representative example spectrum deduced from observations of $H_2(J)$ and H column densities of the well-studied and commonly-referenced diffuse cloud toward ζ Oph; and a simulated spectrum using column densities of 2.1×10^{20} and $2.6 \times 10^{20}\,\mathrm{cm}^{-2}$ for H_2 and H, respectively, and assuming purely thermal excitation of H_2. The H_2 molecular data adopted for the synthetic spectra are those of Abgrall et al. (1993a,b) and were obtained from the Meudon PDR code website (Le Petit et al. 2006). The assumed column densities were taken to be half those of the observed ζ Oph cloud, as is appropriate for radiation penetrating to its center, and an excitation temperature of 50 K was used for the H_2+H and N_2 thermal models. The principal difference between observed and thermal H_2+H spectra is the appearance of additional lines in the observed spectrum from non-thermally populated higher-J levels. Thermal

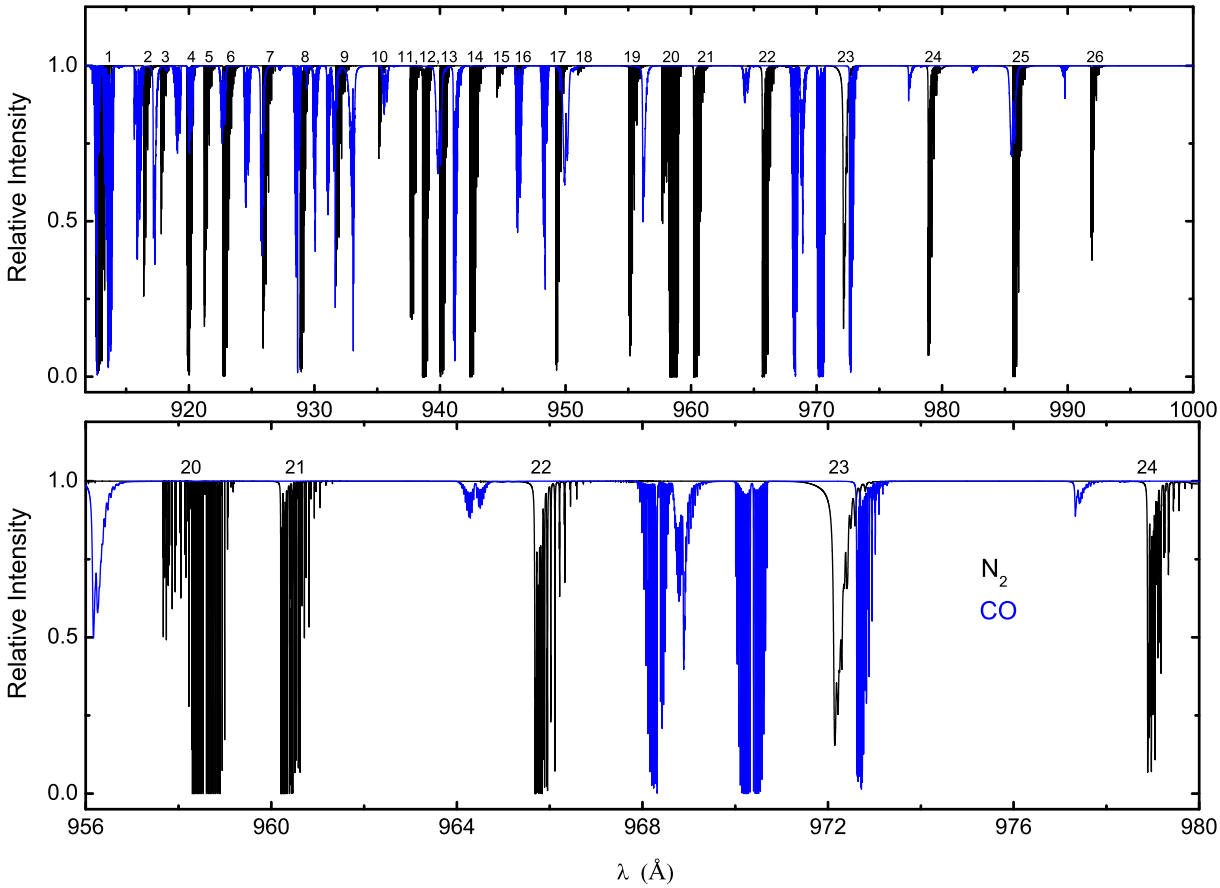

Figure 2.7 — *Top*: Comparison of N_2 (black) and CO (blue) model absorption spectra between 912 and 1000 Å assuming an excitation temperature of 50 K for both molecules. The N_2 and CO column densities are both 10^{15} cm^{-2}. *Bottom*: Blow-up of the above spectra for the wavelength region 956 – 980 Å.

excitation H_2 spectra are used throughout the following mutual-shielding calculations, and do not include extrathermal excitations such as UV pumping. This negligence leads to a slight (approximately 3%) underestimate of shielding for the case of the ζ Oph cloud. A magnified version of the spectra in Fig. 2.4 is included in the online appendix, and it is apparent that the ranges containing significant N_2 absorption and minimal shielding by H and H_2 are 919.8–920.2, 921.2–921.6, 922.6–923.1, 925.8–926.1, 935.1-935.4, 939.9–940.3, 942.3–942.8, 958.1–958.9, 959.0–959.1, 960.1–960.8 and 978.8–979.5 Å.

The calculated N_2 photodissociation rate at the centre of the ζ Oph cloud is 6.96×10^{-11} s^{-1}, corresponding to 58% shielding by H_2+H. Table 2.2 summarizes the contributions to the photodissociation rate of individual bands at the edge of the cloud (unshielded) and at its center. The pattern of increasing and decreasing significance of individual N_2 bands under the influence of shielding is easily matched to the occurrence of overlapping features in Fig. 2.4(a). The heavy shielding of bands 22 and 23 has a particularly large effect on the total photodissociation rate, the relative importance of the lightly shielded band 14 increases significantly in the center, and the 957 – 980 Å wavelength range remains particularly important for photodissociation throughout the cloud.

A similar investigation was performed considering the shielding of N_2 by CO. Simulated

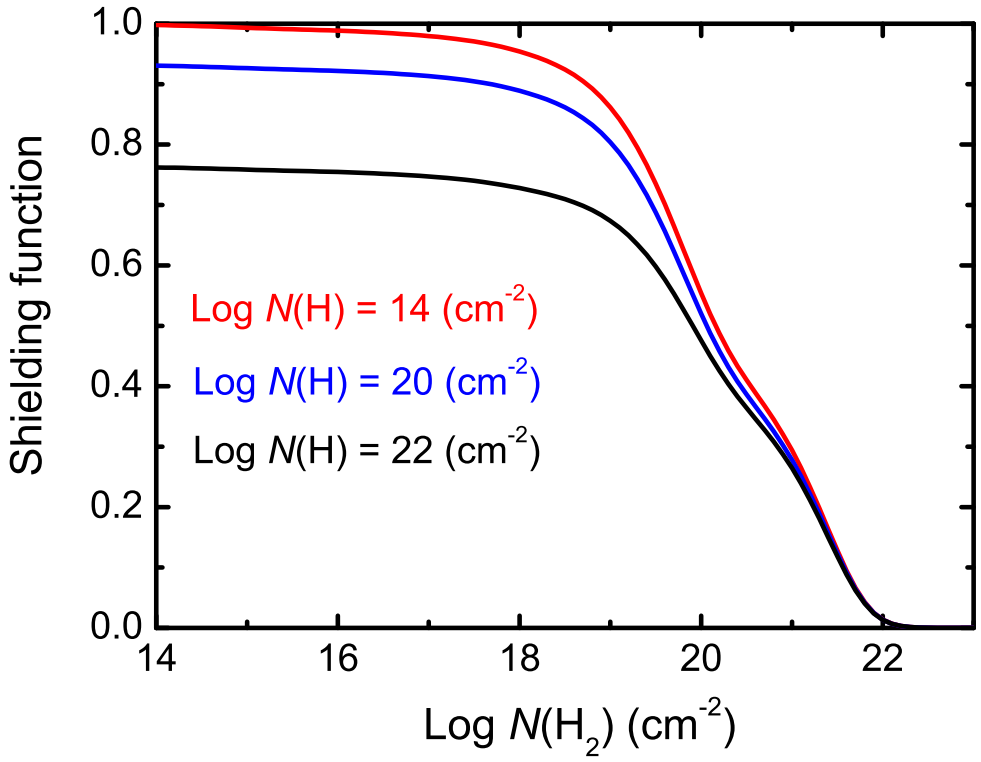

Figure 2.8 — Shielding of N_2 by $H_2 + H$ as a function of H_2 column density, $N(H_2)$, for three different values of $N(H)$. An excitation temperature of 50 K is adopted for both N_2 and H_2.

absorption spectra for both molecules are shown in Fig. 2.7, where the CO spectrum was generated by the photoabsorption model of Visser et al. (2009) assuming a column density of $10^{15}\,\mathrm{cm}^{-2}$, close to half of the observed ζ Oph value. Both spectra exhibit a complex pattern of bands so that overlaps are infrequent and do not occur at all in the most important photodissociation range, 957–980 Å. In this range CO hardly affects N_2 and, in general, shielding by H_2 and H is sufficiently dominant that the additional influence of CO can be neglected.

Two-dimensional shielding functions for a range of H_2 and H column densities have been calculated. These are tabulated in Table 2.3 and shown graphically in Fig. 2.8. For these calculations an excitation temperature of 50 K was assumed for both N_2 and H_2, and $b(H_2)$ (the nonthermal broadening) was set to $3\,\mathrm{km\,s}^{-1}$. Obviously, the shielding function decreases with increasing $N(H_2)$ and $N(H)$, but H_2 plays the more important role (as is the case for the shielding of CO; Visser et al. 2009). Specifically, N_2 is close to fully shielded ($\Theta < 2\%$) when $N(H_2) = 10^{22}\,\mathrm{cm}^{-2}$, and totally shielded by $10^{23}\,\mathrm{cm}^{-2}$. Electronic tables of the calculated shielding functions can be obtained from `www.strw.leidenuniv.nl/~ewine/photo`.

Since N_2 does not possess a permanent dipole moment, radiative decay from excited rotational levels of its electronic-vibrational ground state is slow. Then, the excitation temperature of N_2 is likely to be higher than that of CO and other molecules, and closer to the kinetic temperature. The effect of temperature on shielding by H_2+H was investigated and is illustrated in Fig. 2.9. The same excitation temperatures are adopted for H_2 and

Table 2.3 — Two-dimensional shielding functions $\Theta[N(\mathrm{H}),\ N(\mathrm{H_2})]$ assuming an excitation temperature of 50 K. The notation $x(-y)$ indicates $x \times 10^{-y}$.

log $N(\mathrm{H_2})$	log $N(\mathrm{H})$ ($\mathrm{cm^{-2}}$)		
($\mathrm{cm^{-2}}$)	14	20	22
14.0	9.979(-1)	9.307(-1)	7.621(-1)
14.2	9.972(-1)	9.301(-1)	7.617(-1)
14.4	9.964(-1)	9.293(-1)	7.610(-1)
14.6	9.955(-1)	9.284(-1)	7.603(-1)
14.8	9.945(-1)	9.274(-1)	7.595(-1)
15.0	9.934(-1)	9.264(-1)	7.586(-1)
15.2	9.923(-1)	9.254(-1)	7.577(-1)
15.4	9.913(-1)	9.245(-1)	7.569(-1)
15.6	9.904(-1)	9.237(-1)	7.562(-1)
15.8	9.896(-1)	9.228(-1)	7.555(-1)
16.0	9.885(-1)	9.219(-1)	7.546(-1)
16.2	9.873(-1)	9.207(-1)	7.536(-1)
16.4	9.859(-1)	9.193(-1)	7.524(-1)
16.6	9.841(-1)	9.177(-1)	7.509(-1)
16.8	9.821(-1)	9.157(-1)	7.492(-1)
17.0	9.797(-1)	9.134(-1)	7.472(-1)
17.2	9.767(-1)	9.105(-1)	7.447(-1)
17.4	9.729(-1)	9.069(-1)	7.418(-1)
17.6	9.681(-1)	9.023(-1)	7.380(-1)
17.8	9.619(-1)	8.964(-1)	7.335(-1)
18.0	9.541(-1)	8.890(-1)	7.280(-1)
18.2	9.443(-1)	8.800(-1)	7.217(-1)
18.4	9.319(-1)	8.685(-1)	7.141(-1)
18.6	9.154(-1)	8.534(-1)	7.046(-1)
18.8	8.927(-1)	8.326(-1)	6.916(-1)
19.0	8.615(-1)	8.040(-1)	6.738(-1)
19.2	8.198(-1)	7.658(-1)	6.496(-1)
19.4	7.663(-1)	7.164(-1)	6.175(-1)
19.6	7.012(-1)	6.563(-1)	5.766(-1)
19.8	6.281(-1)	5.887(-1)	5.280(-1)
20.0	5.540(-1)	5.201(-1)	4.758(-1)
20.2	4.875(-1)	4.583(-1)	4.259(-1)
20.4	4.333(-1)	4.078(-1)	3.830(-1)
20.6	3.886(-1)	3.660(-1)	3.457(-1)
20.8	3.446(-1)	3.251(-1)	3.081(-1)
21.0	2.940(-1)	2.781(-1)	2.645(-1)
21.2	2.327(-1)	2.213(-1)	2.113(-1)
21.4	1.630(-1)	1.561(-1)	1.497(-1)
21.6	9.495(-2)	9.178(-2)	8.843(-2)
21.8	4.260(-2)	4.164(-2)	4.030(-2)
22.0	1.375(-2)	1.359(-2)	1.320(-2)
22.2	3.210(-3)	3.200(-3)	3.120(-3)
22.4	5.737(-4)	5.734(-4)	5.600(-4)
22.6	6.110(-5)	6.108(-5)	5.969(-5)
22.8	2.146(-6)	2.146(-6)	2.094(-6)
23.0	1.151(-8)	1.151(-8)	1.118(-8)

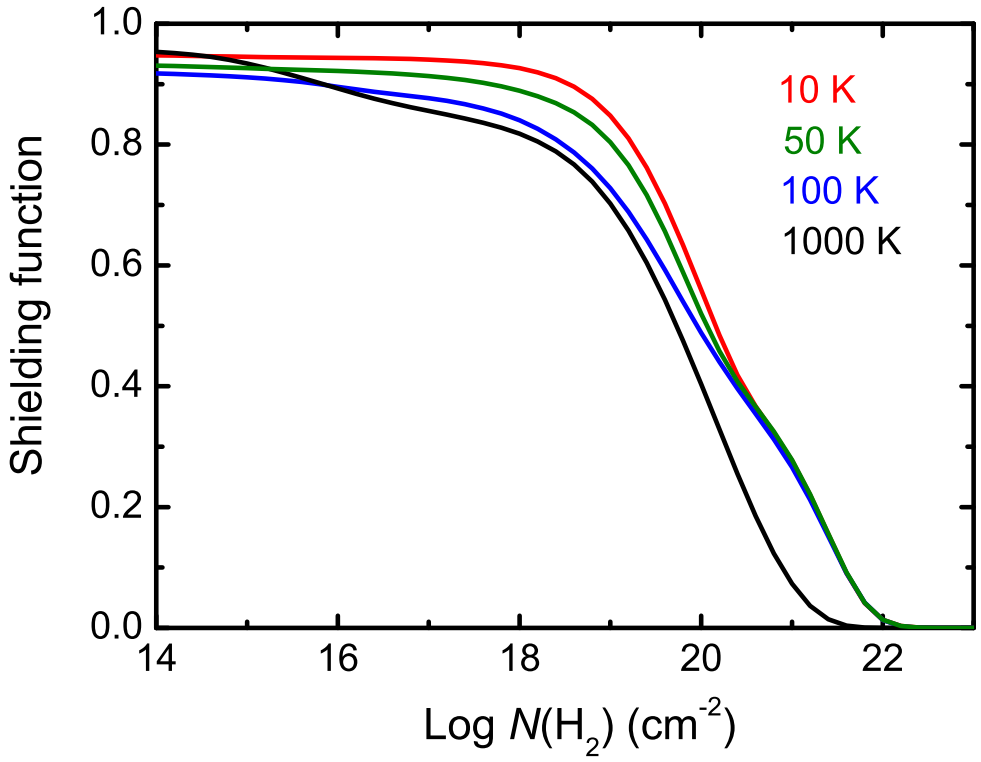

Figure 2.9 — Shielding of N_2 by $H_2 + H$ as a function of H_2 column density $N(H_2)$, for N_2 and H_2 excitation temperatures of 10, 50, 100 and 1000 K. The column-density of H is set to $10^{20}\,\mathrm{cm}^{-2}$ in all cases.

N_2 because both are zero-dipole-moment molecules. The calculated shielding functions are somewhat erratic, and even show a peculiar non-monotonic temperature dependence at low H_2 column density. This arises from the small degree of overlap occurring between atomic H lines and N_2 bands. The distribution of N_2 lines over additional rotational transitions at higher temperatures leads to the variability of Fig. 2.9 and illustrates the need for high-resolution reference spectra in these kinds of applications. For significant H_2 column densities, and in contrast with N_2 self-shielding, the amount of shielding increases with increasing temperature. This results from a H_2 population that is spread over more rotational levels at higher temperatures, leading to an absorption spectrum featuring more lines available to shield N_2. This is clearly evident when comparing the various curves in Fig. 2.4.

Table 2.4 compares the H+H_2 shielding of N_2 with the CO shielding calculations of Visser et al. (2009). The two molecules follow a similar pattern, within 50%, up to $N(H_2) = 10^{22}\,\mathrm{cm}^{-2}$. This difference becomes more significant when $N(H_2) = 10^{23}\,\mathrm{cm}^{-2}$, but photodissociation has long ceased to be important as an N_2 destruction mechanism by then.

2.3.4 Shielding by dust

Dust grains compete with molecules in the cloud by also absorbing UV photons. For the 912–1000 Å wavelength range, the attenuation by dust is largely independent of

Table 2.4 — Comparison of the shielding of $^{14}N_2$ and ^{12}CO by $H_2 + H$ and dust for a range of extinction, A_V, at 10 K and taking $N(H) = 5 \times 10^{20}\,cm^{-2}$.[a]

	Shielding due to $H_2 + H$			Shielding due to dust	
A_V	$\log N(H_2)$ (cm^{-2})	$^{14}N_2$	^{12}CO[b]	Interstellar	Protoplanetary
0.31	0	8.916(-1)	0.9	3.318(-1)	8.290(-1)
0.32	19	8.098(-1)	8.176(-1)	3.175(-1)	8.228(-1)
0.44	20	5.543(-1)	7.223(-1)	2.134(-1)	7.691(-1)
1.56	21	2.759(-1)	3.260(-1)	4.023(-3)	3.916(-1)
12.8	22	1.346(-2)	1.108(-2)	0	4.585(-4)
125.3	23	2.343(-8)	3.938(-7)	0	0

[a]The unattenuated photodissociation rates of $^{14}N_2$ and ^{12}CO are 1.65×10^{-10} and 2.59×10^{-10} s^{-1}, respectively.

[b]The CO values are from Visser et al. (2009).

wavelength and can be taken into account by an additional shielding term $\exp(-\gamma A_V)$ (van Dishoeck et al. 2006). For the wavelength range appropriate for N_2, a value of $\gamma = 3.53$ is found, using the method of Roberge et al. (1981) and standard diffuse-cloud grain properties of Roberge et al. (1991). For larger dust grains of a few μm in size, such as is appropriate for protoplanetary disks, $\gamma \approx 0.6$ (van Dishoeck et al. 2006). The visual extinction A_V is computed from the total hydrogen column N_H=N(H) + 2N(H_2) through the relation $A_V = N_H/1.6 \times 10^{21}$, based on Savage et al. (1977).

For diffuse clouds with total visual extinctions around 1 mag, radiation from the other side of the cloud may result in a shallower depth dependence than given by the above single exponential form. In such cases, a bi-exponential form $\exp(-\alpha A_V + \beta A_V^2)$ may be more appropriate (van Dishoeck & Dalgarno 1984; van Dishoeck 1988). For A_V^{tot}=1 mag, $\alpha = 7.25$ and $\beta = 6.92$ are found.

The shielding of N_2 by dust under various conditions is listed in Table 2.4. This shows that shielding by normal interstellar dust is larger than that by H_2 and H for any A_V and implies that the 'smoke screen' by dust also plays a significant role in diffuse and translucent clouds and photon-dominated regions. However, in protoplanetary disks where the larger dust particles absorb and scatter less efficiently, the effects of H_2 and H shielding become comparable, or even dominant, at large A_V.

2.4 New chemistry in diffuse and translucent clouds, PDRs, and circumstellar disks

As an example of how to apply the new photodissociation rates, we ran chemical models for a set of diffuse and translucent clouds, a photon-dominated region (PDR), and a vertical cut through a circumstellar disk. The models use the UMIST06 chemical network (Woodall et al. 2007), stripped down to species containing only H, He, C, N and O. Species containing more than two C, N or O atoms are also removed since they are not relevant for our purposes. Freeze-out and thermal evaporation are added for all neutral species, but no grain-surface reactions are included other than H_2 formation according to Black & van Dishoeck (1987). Self-shielding of CO is computed using the shielding

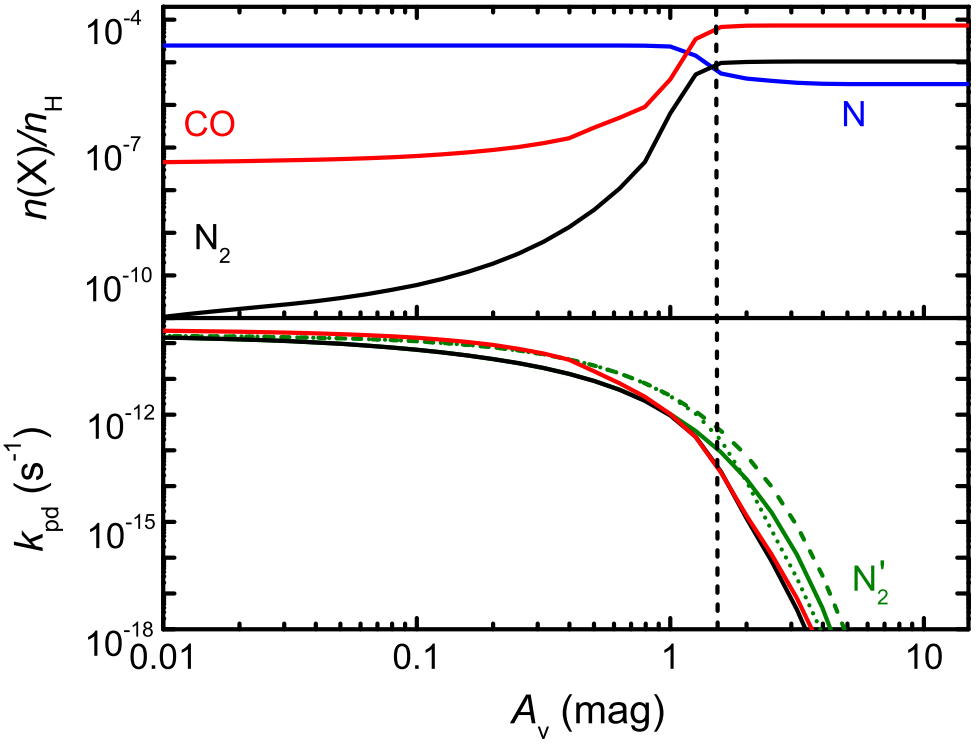

Figure 2.10 — *Top*: Relative abundances of N, N_2 and CO as a function of depth into a translucent cloud with $\chi = 1$, $T = 30$ K and $n_H = 10^3\,cm^{-3}$. *Bottom*: Photodissociation rates of N_2 (black) and CO (red) as functions of depth. Alternative photodissociation rate curves (N_2', green) consider shielding by dust alone (dashed), dust + self-shielding (dotted), and dust + H + H_2 (solid). The conversion from N to N_2 occurs at $A_V \simeq 1.5$ mag, as shown by the vertical dashed line.

functions of Visser et al. (2009); for N_2, we use the self-shielding functions calculated here at 50 K. The elemental abundances relative to H are 0.0975 for He, 7.86×10^{-5} for C, 2.47×10^{-5} for N and 1.80×10^{-4} for O (Aikawa et al. 2008). Enhanced formation of CH^+ (and thus also CO) at low A_V is included following Visser et al. (2009) by supra-thermal chemistry, boosting the rate of ion-neutral reactions by setting the Alfvén speed to $3.3\,km\,s^{-1}$ for column densities less than 4×10^{20} cm^{-2}. Unless stated otherwise, the model of impinging UV flux is the Draine field of Eq. (2.3) modified by a scaling factor, χ. In all cases, the abundances of N, N_2 and CO reach steady state after ∼1 Myr, regardless of whether the gas starts in atomic or molecular form.

2.4.1 Diffuse and translucent clouds

A set of diffuse and translucent cloud models was run for central densities $n_H = n(H) + 2n(H_2) = 100, 300$ and 10^3 cm^{-3}, at a temperature of 30 K, and assuming scaling factors of the UV flux of $\chi = 0.5, 1$ and 5. Figure 2.10 shows the abundances of N, N_2 and CO and the photodissociation rates of N_2 and CO as functions of depth into the cloud (measured in A_V) for the $n_H = 10^3$ and χ=1 model. Both CO and N_2 are rapidly photodissociated in the limit of low extinction and carbon and nitrogen are primarily in atomic form. Some CO is formed in a series of (supra-thermal) ion-molecule reactions starting with C^+ at the edge (Visser et al. 2009). Since the ionization potential of atomic N lies just above that

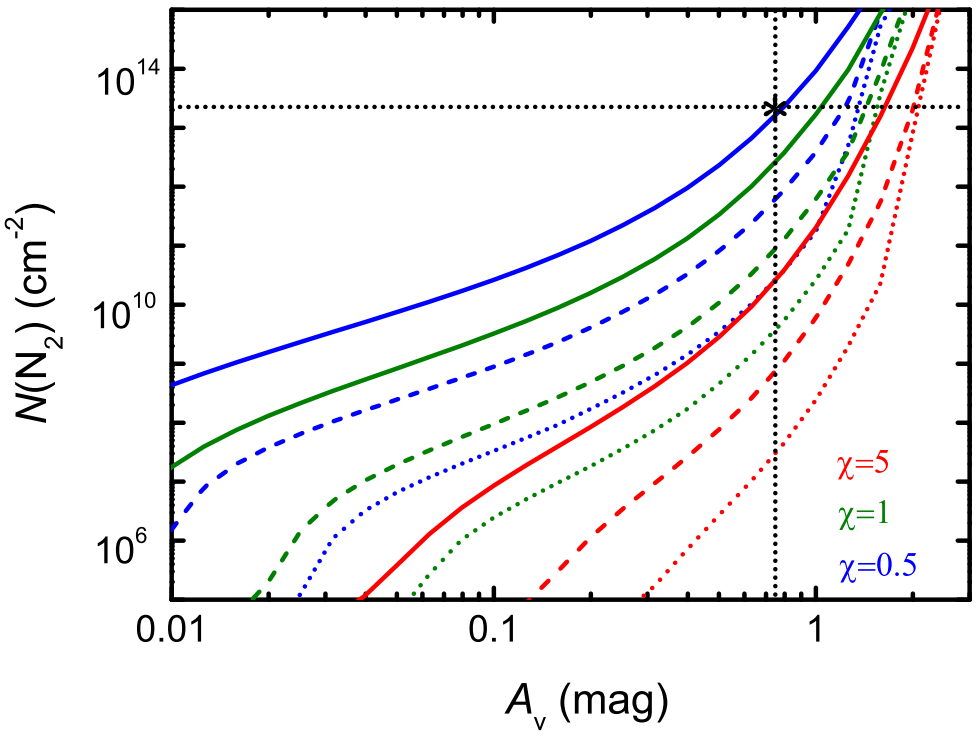

Figure 2.11 — Cumulative column density of N_2 as a function of extinction, A_V, at an excitation temperature of 30 K. Curves are shown for several different models: dotted, dashed, and solid lines indicate $n_H = 100$, 300 and 1000 cm^{-3}, respectively; blue, green and red lines scale the radiation field by $\chi = 0.5$, 1 and 5, respectively. The asterisk indicates half the N_2 column density and half the extinction observed by Knauth et al. (2004) in the diffuse cloud toward HD 124314.

of H, preventing the formation of N^+, N_2 can only form through slower neutral-neutral reactions. As a result, the abundance of N_2 is three orders of magnitude lower than that of CO at the edge of the cloud. The conversion from N to N_2 occurs at an A_V of 1.5 mag, at which point CO has become the main form of carbon. The bottom panel of Figure 2.10 illustrates that self-shielding and mutual shielding by H and H_2 significantly reduce the photodissociation rate relative to dust alone. The column densities of N_2 and CO at A_V=1.5 mag are 1.5×10^{15} and 1.3×10^{16} cm^{-2}. At high A_V, atomic N is maintained at an abundance of 3×10^{-6} by the dissociative recombination of N_2H^+, which in turn is formed from the reaction between N_2 and cosmic-ray-produced H_3^+.

To investigate the role of turbulence or non-thermal motions on the results, a model has been run in which the Doppler width of the N_2 lines in the self-shielding calculation was increased to 3 km s^{-1} rather than the thermal width at low temperatures. The resulting N_2 abundance as a function of depth is nearly identical to that presented in Fig. 2.10.

Absorption bands of N_2 have possibly been detected in observations of the diffuse cloud toward HD 124314 (Knauth et al. 2004). The two relevant bands, indicated in Fig. 2.4, are particularly strongly absorbing, and are relatively unshielded by hydrogen. The depth of the observed absorption indicates a total N_2 column density of $(4.6 \pm 0.8) \times 10^{13}$ cm^{-2} and the stellar reddening of HD 124314 provides an estimate of the cloud's extinction, $A_V = 1.5$ mag. Figure 2.11 shows the cumulative N_2 column density calculated for a range

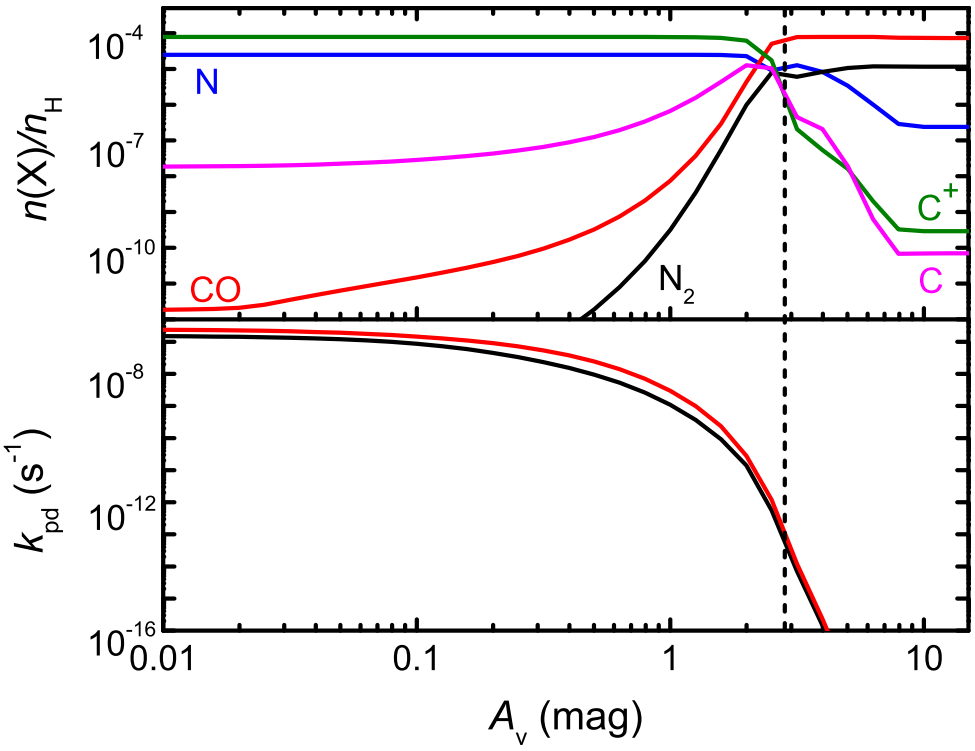

Figure 2.12 — *Top*: Relative abundances of N (blue), N_2 (black), C (magenta), C^+ (green) and CO (red) as functions of depth into a dense PDR. *Bottom*: Photodissociation rates of N_2 and CO as functions of depth into a dense PDR. The vertical dashed line indicates where He^+ and H_3^+ take over from photodissociation as the main destruction mechanism for N_2.

of radiation field intensities and n_H densities as a function of A_V. For comparison with the model, which considers only half of the cloud from edge to center and is irradiated from one side only, the observed A_V and N_2 column density must be halved. These models use the single exponential dust continuum shielding function; if the bi-exponential formulation were used, the model N_2 column densities would be even lower for small A_V. The maximum calculated column density occurs where the radiation field is weakest ($\chi = 0.5$) and for the highest density ($n_H = 10^3\,cm^{-3}$). These are extreme physical conditions for a cloud like HD 124314 and inconsistent with its relatively high H/H_2 column density ratio (André et al. 2003) and low CO column density (Sheffer et al. 2008). An independent conformation of the N_2 detection is warranted. Observed upper limits toward other diffuse clouds with lower A_V are a few$\times 10^{12}\,cm^{-2}$ (Lutz et al. 1979), which are consistent with the current models for typical densities of a few hundred cm^{-3} and $\chi \geq 1$.

2.4.2 Photon-dominated region

The PDR model is run assuming an n_H density of $10^5\,cm^{-3}$, a temperature of 100 K, and a UV flux of $\chi = 10^3$. Figure 2.12 shows the resulting abundances of N, N_2, C, C^+ and CO and the relevant photodissociation rates as functions of A_V.

The calculated abundances of both N_2 and CO at low A_V are lower in the PDR model compared with the diffuse and translucent clouds, because of the stronger UV field. For all models, the abundance of N_2 is several orders of magnitude lower than that of CO.

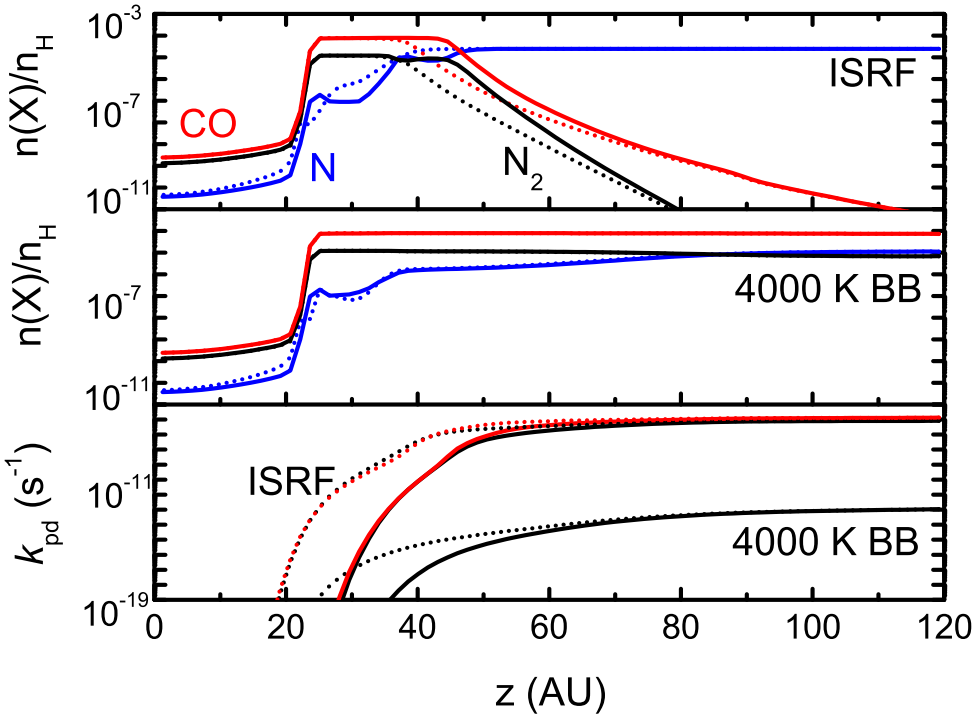

Figure 2.13 — *Top* and *Middle*: Relative abundances of N (blue), N_2 (black) and CO (red) as a function of height in a slice through a circumstellar disk exposed to the interstellar radiation field (ISRF) scaled by a factor χ =516 and a 4000 K black body field. *Bottom* The relevant photodissociation rates of CO and N_2. Solid lines are for a grain size of 0.1 μm, dotted lines for 1 μm.

Also, because of the increased radiation, the transition from N to N_2 occurs deeper into the PDR: at an A_V of about 3 mag. The column densities of N_2 and CO at this point are 6×10^{15} and 3×10^{16} cm^{-2}. The minor wiggle in the atomic N abundance profiles at $A_V = 2$–3 mag is due to the abundance patterns of CH and OH. CH is the main destroyer of N at $A_V = 2$ mag but its abundance drops going into the cloud because its main precursor, C^+, disappears. The simultaneously increasing extinction allows for an increase in the OH abundance, so that this becomes the main destroyer of N for $A_V > 3$ mag. Interestingly, the transition from N→N_2 occurs at nearly the same depth into the cloud than that of C^+ →C→CO.

2.4.3 Circumstellar disk

The fourth model simulates a vertical slice through a circumstellar disk and its setup is identical to that of Visser et al. (2009). The slice is located at a radius of 105 AU in the standard model of D'Alessio et al. (1999), which supposes a disk of 0.07 $M_\odot$ and 400 AU radius surrounding a T Tauri star of 0.5 $M_\odot$ and 2 $R_\odot$ radius. The surface of the slice, at a height of 120 AU, is illuminated by the Draine (1978) field with $\chi = 516$. We ran the model assuming dust grain sizes of 0.1 and 1 μm. The results are plotted in Fig. 2.13.

Starting from the disk surface (high z) and moving inwards, the abundance profiles of N, N_2 and CO show the same qualitative trends as they do for the translucent cloud and PDR models. The main difference arises from freeze-out of N_2 and CO for z below 25 AU,

at which point the dust temperature drops below ∼20 K. The depletion of N_2 also drives down the abundance of N_2H^+ which, in turn, restricts the abundance of atomic N. In the models presented here, nitrogen is fully converted into N_2 at heights where no freeze-out occurs.

Increasing the grain size from 0.1 to 1 μm allows the UV field to penetrate to heights of about 35 instead of 45 AU. The abundances of N_2 and CO are then a factor of 10–100 lower in the intervening zone, while that of atomic N is a factor of a few higher. Since atomic N is a prerequisite for an active nitrogen chemistry leading to species like HCN, this result illustrates that larger column densities of nitrogen-containing molecules can be expected in disks with grain growth.

The column densities integrated from surface to midplane are 2×10^{17} cm^{-2} for N_2 and 1.2×10^{18} cm^{-2} for CO, regardless of the grain size, since the bulk of the N_2 and CO are at high densities where UV photodissociation is negligible. The total column of N is 5×10^{16} cm^{-2} for 0.1 μm grains and 8×10^{16} cm^{-2} for 1 μm grains.

The models discussed above use a scaled Draine (1978) radiation field. A much cooler radiation field was also considered by assuming a 4000 K blackbody source scaled to the same flux between 912 and 2050 Å. Then, both carbon and nitrogen are fully molecular at the disk surface since photodissociation of both CO and N_2 is negligible. A smaller amount of atomic N is maintained by chemical reactions for active nitrogen chemistry. This result is qualitatively consistent with the observation of Pascucci et al. (2009) that the color of the radiation field affects the nitrogen chemistry, although that study applied to the inner rather than the outer disk.

2.5 Concluding remarks

In this work, we compute accurate N_2 photodissociation rates in the interstellar medium for the first time by employing new molecular data on its electronic transitions. The calculated N_2 photodissociation rate in an unattenuated interstellar radiation field is 1.65×10^{-10} s^{-1} (50 K), ∼28% lower than the previously recommended value. This rate increases somewhat with temperature due to $J-$dependent predissociation rates.

The simulated spectra reveal that the most important range for photodissociation is 957–980 Å, where H_2 and H absorption significantly overlap with N_2 absorption. In contrast, CO only weakly shields N_2. Self-shielding and mutual shielding functions have been computed for a range of N_2, H_2 and H column densities. For interstellar grains, shielding by dust is also effective. In protoplanetary disks, where dust particles have grown to μm size, the dust shielding becomes less than that of H_2.

The new rates have been incorporated into models of diffuse and translucent clouds, of a dense PDR, and a protoplanetary disk. The translucent cloud models show that the observed column of interstellar N_2 in a translucent cloud with $A_V = 1.5$ mag can only be reproduced if the density n_H is higher than 1000 cm^{-3} and the radiation field has an intensity of less than half of the Draine (1978) field. For dense PDRs, the N_2 abundance only becomes significant at extinctions of more than 3 mag into the cloud but the transition of N → N_2 occurs at nearly the same depth as that of $C^+ \rightarrow C \rightarrow$ CO. Disk models show that nitrogen is fully converted into N_2 at heights before freeze-out occurs, irrespective of grain size. However, an active nitrogen chemistry can take

place in the upper layers of a disk where not all nitrogen is locked up in N_2, except for very cool radiation fields. Altogether, data are now available to accurately model N_2 photodissociation in a wide variety of interstellar and circumstellar media.

Acknowledgements

Astrochemistry in Leiden is supported by the Netherlands Research School for Astronomy (NOVA), by a Spinoza grant and grant 648.000.002 from the Netherlands Organisation for Scientific Research (NWO), and by the European Community's Seventh Framework Programme FP7/2007-2013 under grant agreements 291141 (CHEMPLAN) and 238258 (LASSIE). Calculations of the N_2 photodissociation cross sections were supported by the Australian Research Council Discovery Program, through Grant Nos. DP0558962 and DP0773050.

2.6 Appendix: Self-shielding functions

In this section, we provide a table containing the self-shielding functions of N_2 at 10, 100 and 1000 K (data for Fig. 2.6).

Table 2.5 — N_2 self-shielding as a function of column density, $N(N_2)$, for excitation temperatures of 10, 100 and 1000 K. The notation $x(-y)$ indicates $x \times 10^{-y}$.

log $N(N_2)$	Temperature (K)		
(cm^{-2})	10	100	1000
10.0	9.998(-1)	1.000(0)	1.000(0)
10.2	9.997(-1)	9.999(-1)	1.000(0)
10.4	9.995(-1)	9.999(-1)	1.000(0)
10.6	9.991(-1)	9.998(-1)	1.000(0)
10.8	9.986(-1)	9.997(-1)	9.999(-1)
11.0	9.979(-1)	9.996(-1)	9.999(-1)
11.2	9.966(-1)	9.994(-1)	9.999(-1)
11.4	9.947(-1)	9.990(-1)	9.998(-1)
11.6	9.917(-1)	9.984(-1)	9.996(-1)
11.8	9.870(-1)	9.974(-1)	9.994(-1)
12.0	9.798(-1)	9.960(-1)	9.991(-1)
12.2	9.691(-1)	9.936(-1)	9.986(-1)
12.4	9.533(-1)	9.900(-1)	9.977(-1)
12.6	9.305(-1)	9.844(-1)	9.964(-1)
12.8	8.985(-1)	9.757(-1)	9.943(-1)
13.0	8.554(-1)	9.627(-1)	9.910(-1)
13.2	8.001(-1)	9.436(-1)	9.859(-1)
13.4	7.333(-1)	9.163(-1)	9.781(-1)
13.6	6.579(-1)	8.785(-1)	9.662(-1)
13.8	5.778(-1)	8.282(-1)	9.486(-1)
14.0	4.967(-1)	7.643(-1)	9.235(-1)
14.2	4.169(-1)	6.877(-1)	8.891(-1)
14.4	3.400(-1)	6.022(-1)	8.440(-1)
14.6	2.680(-1)	5.130(-1)	7.875(-1)
14.8	2.037(-1)	4.244(-1)	7.197(-1)
15.0	1.505(-1)	3.394(-1)	6.412(-1)
15.2	1.100(-1)	2.609(-1)	5.546(-1)
15.4	8.073(-2)	1.928(-1)	4.641(-1)
15.6	5.945(-2)	1.384(-1)	3.747(-1)
15.8	4.374(-2)	9.802(-2)	2.911(-1)
16.0	3.214(-2)	6.920(-2)	2.175(-1)
16.2	2.361(-2)	4.886(-2)	1.567(-1)
16.4	1.731(-2)	3.454(-2)	1.100(-1)
16.6	1.267(-2)	2.441(-2)	7.613(-2)
16.8	9.250(-3)	1.717(-2)	5.229(-2)
17.0	6.720(-3)	1.199(-2)	3.557(-2)
17.2	4.870(-3)	8.280(-3)	2.387(-2)
17.4	3.510(-3)	5.640(-3)	1.574(-2)
17.6	2.520(-3)	3.810(-3)	1.013(-2)
17.8	1.790(-3)	2.570(-3)	6.340(-3)
18.0	1.270(-3)	1.740(-3)	3.850(-3)
18.2	8.906(-4)	1.190(-3)	2.280(-3)
18.4	6.247(-4)	8.066(-4)	1.310(-3)
18.6	4.359(-4)	5.425(-4)	7.183(-4)
18.8	2.998(-4)	3.613(-4)	3.737(-4)
19.0	2.031(-4)	2.386(-4)	1.820(-4)

2.7 Appendix: High resolution spectra

In this section, we provide the high resolution spectra of N_2 at 50 K (zoom in for Fig. 2.4). The H_2 and H column densities are the same as those used in Figure 2.4.

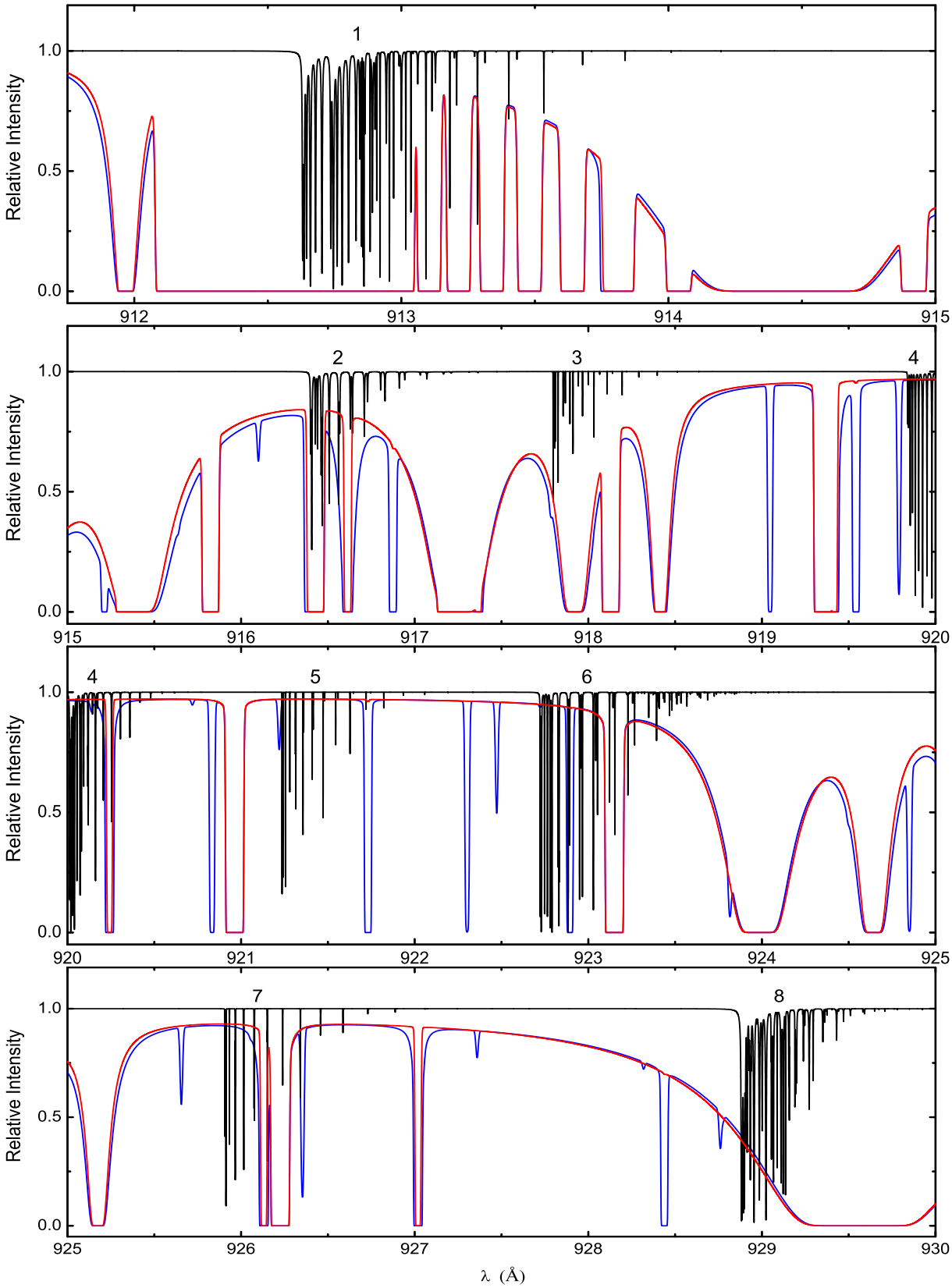

Figure 2.1 — Zoom-in of the high-resolution spectra of N_2 (black line) and H plus H_2 (red line) in the wavelength range of 911.75–930 Å for a thermal excitation temperature of 50 K. The column density of N_2 is $10^{15}\,\mathrm{cm}^{-2}$ and values for H_2 and H are taken to be half of the observed column densities in the well-studied diffuse cloud toward ζ Oph, as is appropriate for the center of the cloud: $N(H_2)=2.1\times10^{20}$ and $N(H)=2.6\times10^{20}\,\mathrm{cm}^{-2}$. The model H_2 Doppler width is $3\,\mathrm{km\,s}^{-1}$. Also shown is the H_2+H absorption spectrum (blue) towards ζ Oph using the observed column densities for individual J levels, showing non-thermal excitation of H_2.

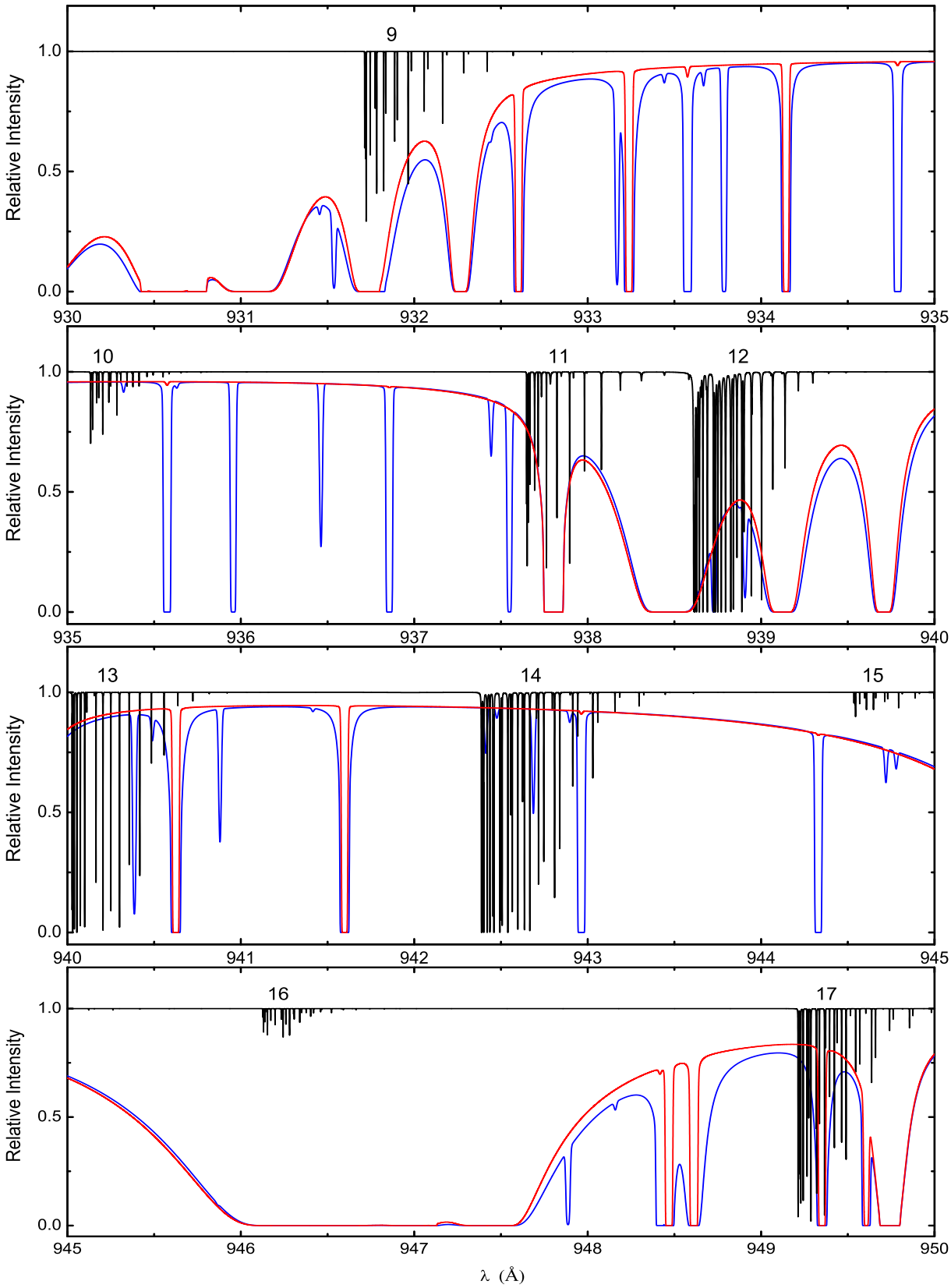

Figure 2.2 — As Fig. 2.1, but for 930–950 Å.

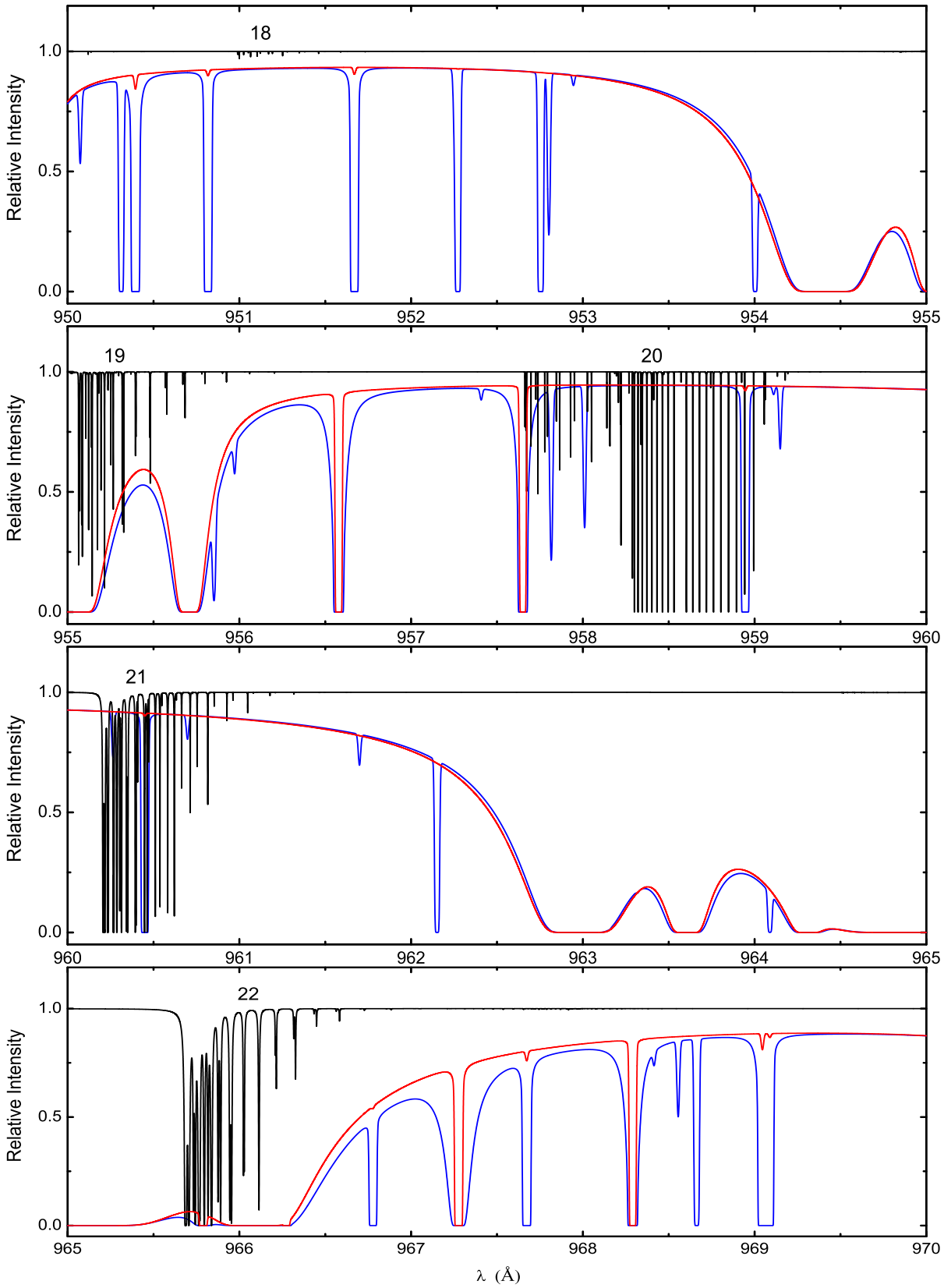

Figure 2.3 — As Fig. 2.1, but for 950–970 Å.

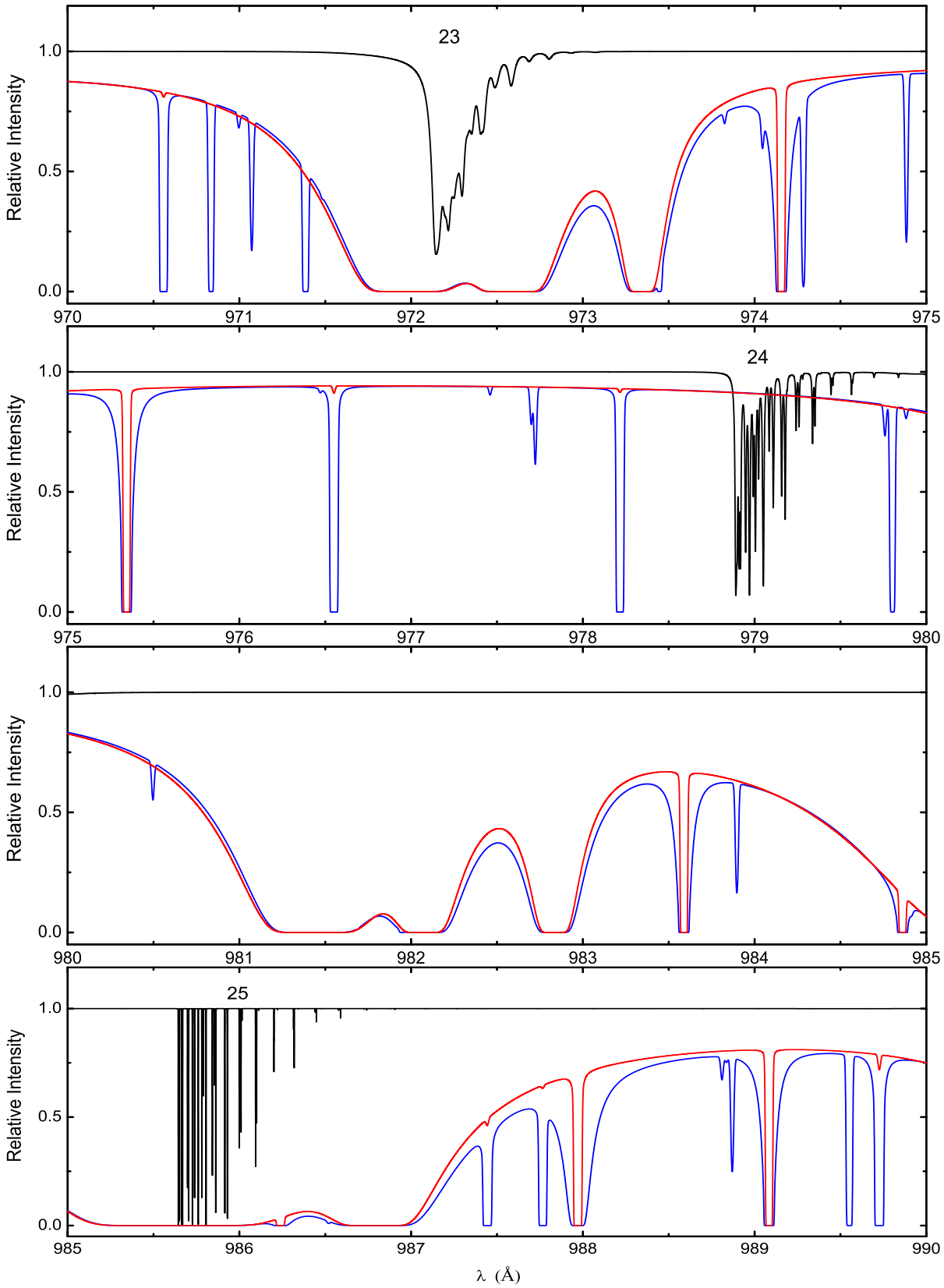

Figure 2.4 — As Fig. 2.1, but for 970–990 Å

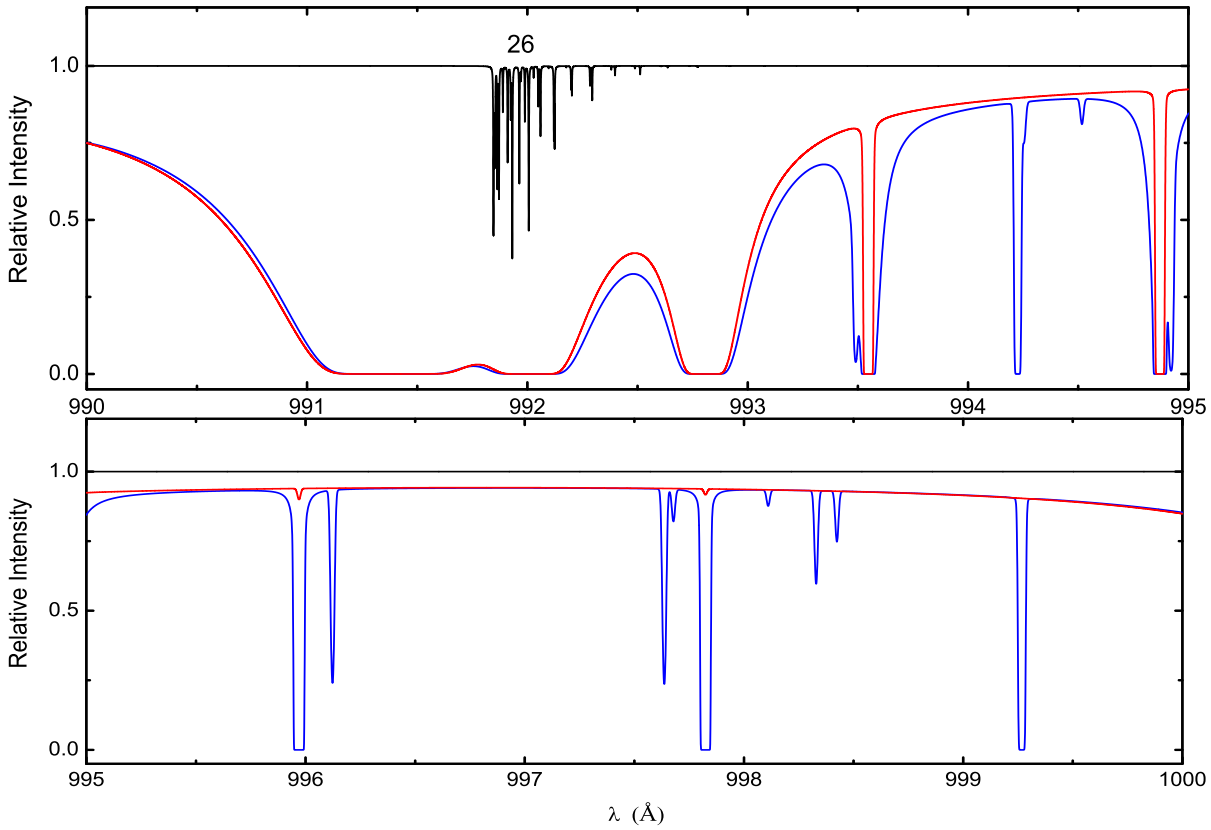

Figure 2.5 — As Fig. 2.1, but for 990–1000 Å.

Chapter 3

New chemistry in C-rich AGB stars

Abstract.
Context. The envelopes of AGB stars are irradiated externally by ultraviolet photons; hence, the chemistry is sensitive to the photodissociation of N_2 and CO, which are major reservoirs of nitrogen and carbon, respectively. The photodissociation of N_2 has recently been quantified by laboratory and theoretical studies. Improvements have also been made for CO photodissociation.
Aims. For the first time, we use accurate N_2 and CO photodissociation rates and shielding functions in a model of the circumstellar envelope of the carbon-rich AGB star, IRC +10216.
Methods. We use a state-of-the-art chemical model of an AGB envelope, the latest CO and N_2 photodissociation data, and a new method for implementing molecular shielding functions in full spherical geometry with isotropic incident radiation. We compare computed column densities and radial distributions of molecules with observations.
Results. The transition of $N_2 \rightarrow N$ (also, $CO \rightarrow C \rightarrow C^+$) is shifted towards the outer envelope relative to previous models. This leads to different column densities and radial distributions of N-bearing species, especially those species whose formation/destruction processes largely depend on the availability of atomic or molecular nitrogen, for example, C_nN (n=1, 3, 5), C_nN^- (n=1, 3, 5), HC_nN (n=1, 3, 5, 7, 9), H_2CN and CH_2CN.
Conclusions. The chemistry of many species is directly or indirectly affected by the photodissociation of N_2 and CO, especially in the outer shell of AGB stars where photodissociation is important. Thus, it is important to include N_2 and CO shielding in astrochemical models of AGB envelopes and other irradiated environments. In general, while differences remain between our model of IRC +10216 and the observed molecular column densities, better agreement is found between the calculated and observed radii of peak abundance.

X. Li, T. J. Millar, C. Walsh, A. N. Heays, and E. F. van Dishoeck
A&A, **568** , A111 (2014)

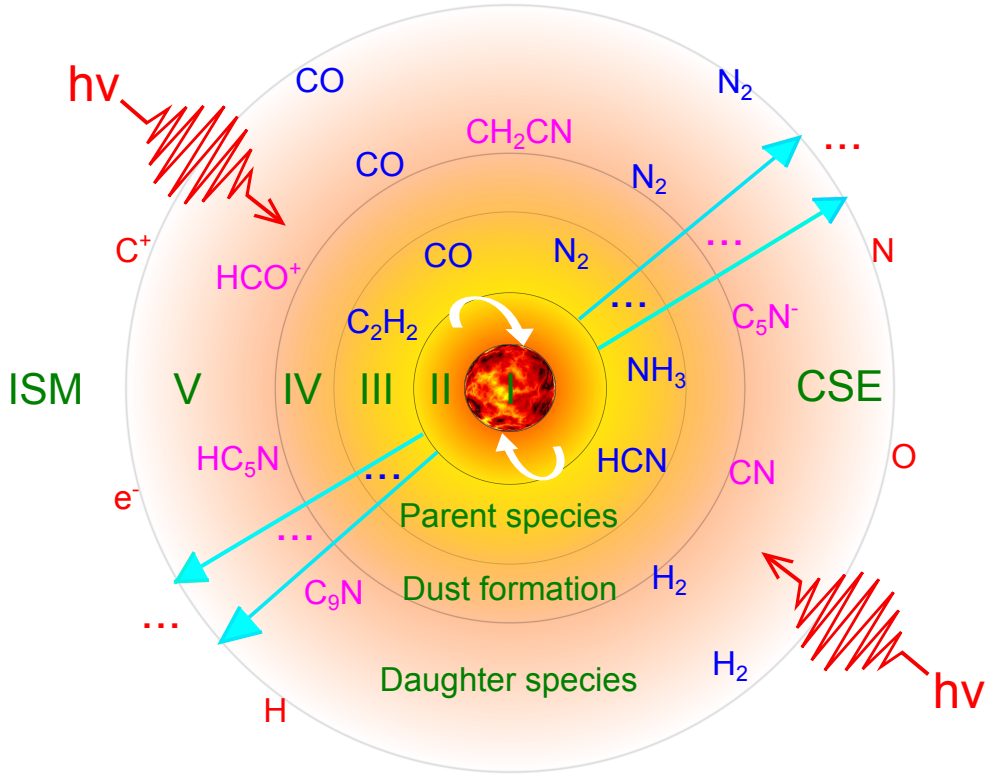

Figure 3.1 — Schematic structure of the CSE for a C-rich AGB star, which is divided into 6 regions for modelling purposes. (I): a degenerate C/O core and He/H burning shell, (II): a convective shell, (III): a stellar atmosphere in which parent species are formed, (IV): a dust formation shell with an expanding envelope, (V): an outer CSE where daughter species are formed primarily by photodissociation, (VI): the interstellar medium (ISM). This study focusses on the outer CSE where chemistry is mainly driven by the photodissociation of molecules.

3.1 Introduction

The asymptotic giant branch (AGB) is the last nuclear-burning phase for low- to intermediate-mass stars (from 0.8 $M_\odot$ to $\sim$ 8 $M_\odot$), where the core of the star evolves into an inert and degenerate C-O core (Herwig 2005). AGB stars can be classified by the elemental C/O ratio, namely, C-rich AGB stars (C/O $>$ 1), M-type AGB stars (C/O $<$ 1) and S-type AGB stars (C/O $\approx$ 1). Our own Sun will become an M-type AGB star. Generally, the envelopes of C-rich stars contain CO plus C-bearing molecules, such as C_2, CN, HCN, and C_2H_2, while O-rich stars contain CO plus O-bearing molecules such as H_2O, TiO, and VO (Le Bertre 1997). AGB stars undergo considerable mass loss and eject dust and molecules into the surrounding regions, creating circumstellar envelopes (CSEs). These gas and dust envelopes eventually merge with the interstellar medium (ISM), enriching molecular clouds in which new stars may be born. Furthermore, CSEs are one of the richest sources for detecting new molecules. The study of AGB stars is of particular interest and importance for our understanding of molecular formation, destruction, and the recycling of material between star birth and star death. The schematic structure of the CSE of an AGB star is shown in Fig. 4.1.

IRC +10216 (CW Leonis), the brightest object in the sky at mid-infrared wavelengths

outside the solar system, is the nearest C-rich AGB star and attracts intensive theoretical and observational study (e.g., Morris 1975; Bieging & Rieu 1988; Glassgold 1996; Mauron & Huggins 1999; Millar et al. 2000; Cernicharo et al. 2000; Woods et al. 2003; Cordiner & Millar 2009; De Beck et al. 2012; Agúndez et al. 2012; McElroy et al. 2013). More importantly, it is one of the richest molecular sources in the sky. To date, around 180 molecular species, not counting isotopologues, have been identified in the interstellar medium or CSEs[a] while more than 80 of them have been detected in IRC +10216. Among these, more than 30 nitrogen-bearing species have been identified, including HCN, CN, SiN, PN, HNC, MgCN, NaCN, NH_3, HC_7N, and C_5N^-, amongst others (Wakelam et al. 2010). Even water, which was thought unlikely to form in C-rich AGB envelopes, has been detected here (Melnick et al. 2001; Decin et al. 2010). Some molecular detections in IRC +10216 were their first discoveries in astrophysical environments, for example, the first detection of the cyanide anion CN^- (Agúndez et al. 2010b), and FeCN (Zack et al. 2011).

Most of the detected species in IRC +10216 are found in the cool, expanding outer CSE, where photodissociation processes dominate the destruction of molecules. The investigation of 'key' reactions, which might affect the entire chemical network and therefore the comparison of simulations and observations, is an important topic. According to a systematic sensitivity study using a large chemical network, the reaction

$$N_2 + h\nu \rightarrow N + N \tag{3.1}$$

is one of the most significant reactions in the outer CSE, which directly affects the abundances of many N-bearing species, such as N, N_2, HC_2N, C_3N, C_3N^- and C_2N (Wakelam et al. 2010). Eq. (3.1) is the primary destruction route of N_2 in any region where UV photons are present. From an observational point of view, the direct detection of N_2 is very challenging because it has no permanent electric dipole and thus possesses no electric-dipole-allowed pure rotational spectrum. The only reported detection of molecular nitrogen is via its far-UV electronic transitions observed in the interstellar medium (Knauth et al. 2004). One can infer N_2 indirectly through the protonated ion, N_2H^+ (Turner 1974; Herbst et al. 1977) or its deuterated form, N_2D^+. However, neither N_2H^+ nor N_2D^+ have been identified in IRC +10216. From the simulation point of view, Eq. (3.1) has usually not been treated properly in models because these have not included N_2 self-shielding. The importance of self-shielding of molecules in CSEs was first noticed for CO some 30 years ago (Morris & Jura 1983). Even with an approximate treatment of CO self-shielding (the 'one-band approximation'), much better agreement was obtained between simulations and observations.

We here employ the latest reported photodissociation rate and shielding functions for N_2 (Li et al. 2013; Heays et al. 2014) to investigate the effects in a chemical model of the CSE of IRC +10216. These are based on a concerted laboratory (e.g., Ajello et al. 1989; Helm et al. 1993; Sprengers et al. 2004; Stark et al. 2008; Lewis et al. 2008b; Heays et al. 2011) and theoretical (e.g., Spelsberg & Meyer 2001; Lewis et al. 2005b; Lewis et al. 2008c; Ndome et al. 2008) effort over the last two decades. An update was also made to the photodissociation of CO using the self-shielding functions from Visser et al. (2009)

[a] `http://www.astro.uni-koeln.de/cdms/molecules/`

Table 3.1 — Envelope parameters and assumptions for IRC +10216 in this study.[a]

1. Shape	Spherical
2. Mass-loss rate	1.5(-5) $M_\odot$ yr^{-1}
3. Envelope expansion velocity	14.5 km s^{-1}
4. Radiation field	Draine (1978) field, isotropic incidence
5. Dust and gas shells in the outflow	Ignored
6. Grain surface reactions	Ignored
7. Polycyclic aromatic hydrocarbons (PAHs)	Ignored
8. Gas density distribution	Falls as r^{-2}, where r is radius
9. Chemical evolution	Kinetic equations solved as a function of r
10. H_2	Fully self-shielded, no photodissociation
11. Parent species	See Table 3.2
12. T, A_V , and gas density	See Fig. 3.2
13. Distance	150 pc (De Beck et al. 2012)

[a] a(b)=$a \times 10^b$

following a similarly large experimental effort over the past decades. While the absolute unshielded rates of both N_2 and CO are changed only at the level of $\sim 30\%$ with respect to the previous values (van Dishoeck 1988), it is important to realize that the uncertainty in the photorates is reduced by an order of magnitude. Also, we develop and employ a new fully spherically-symmetric (SS) model that computes the self-shielding of molecules in an isotropic interstellar radiation field, rather than the usual plane-parallel (PP) geometry.

The paper is organised as follows: the CSE model, the improvements in N_2 and CO photodissociation, as well as the theory and details for the evaluation of photodissociation rates for the SS model are described in Sect. 4.2. The results and discussion can be found in Sect. 4.3, followed by the concluding remarks in Sect. 4.4. The impact of these improvements on the molecular abundances in the CSE of IRC +10216 are discussed. Special attention is given to those species which have already been detected and those which may be detectable in the near future, e.g., using the Atacama Large Millimeter/submillimeter Array (ALMA). A full description of the SS model used for calculating the photodissociation rates of CO and N_2, together with the proposed numerical methods for implementing molecular shielding functions, are included in Appendices 3.5 and 3.6.

3.2 Improvements in our models

3.2.1 CSE Model

The CSE model described in McElroy et al. (2013) was employed and extended in the present work. Specific details can be found in Millar et al. (2000) and Cordiner & Millar (2009). Improvements in the model are summarised in Sect. 3.2.2. The latest (fifth) release of the UMIST Database for Astrochemistry (UDfA), McElroy et al. (2013), hereafter Rate12, was adopted in all of the calculations. Rate12 contains 6173 gas-phase reactions involving 467 species. McElroy et al. (2013) tested this network in a dark cloud model and in a CSE model of IRC +10216 and compared the results with previous models and observations.

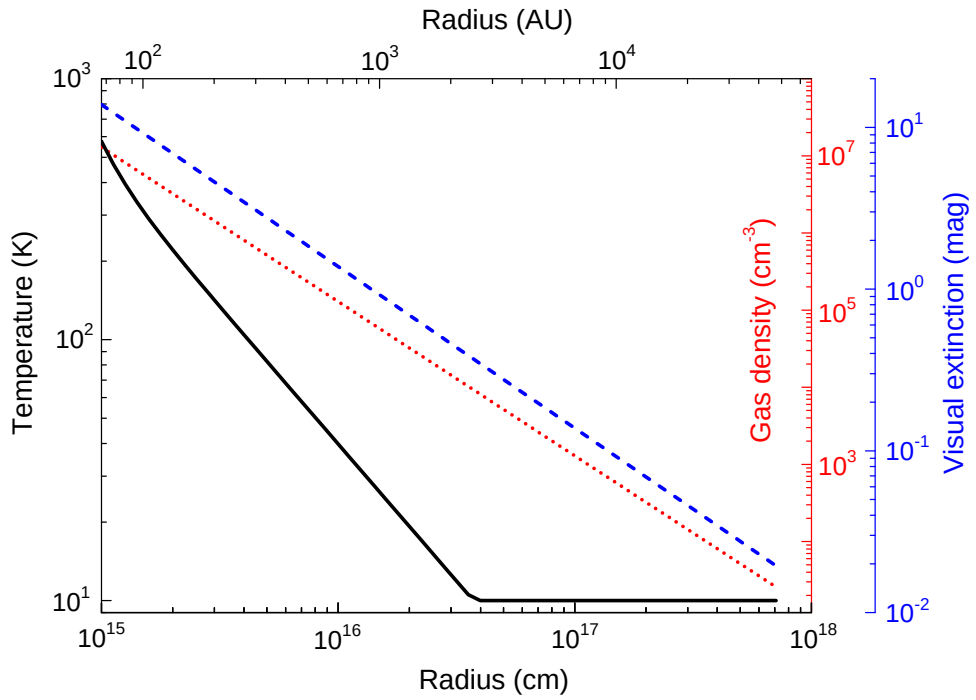

Figure 3.2 — Gas density, visual extinction, and gas temperature as functions of radius for the CSE of IRC +10216 from the center of the star towards the outside of the envelope. For clarity, the radius is given in units of 'cm' and 'AU'.

Table 3.2 — Initial abundances of parent species, relative to H_2, at the inner radius.[a]

Species	Abundance	Species	Abundance
N_2	2.0(-4)	SiS	1.3(-6)
NH_3	2.0(-6)	CH_4	3.5(-6)
HCN	2.0(-5)	H_2O	1.0(-7)
He	1.0(-1)	Mg	1.0(-5)
HF	8.0(-9)	C_2H_4	2.0(-8)
C_2H_2	8.0(-5)	SiH_4	2.2(-7)
CO	6.0(-4)	HCl	1.0(-7)
H_2S	4.0(-9)	HCP	2.5(-8)
CS	7.0(-7)	SiC_2	2.0(-7)
SiO	1.8(-7)		

[a]Same as those adopted in the model of McElroy et al. (2013).

The main assumptions and key parameters adopted in our model of IRC +10216 are summarised in Table 3.1. Parent species that are injected at the inner radius of the envelope are listed in Table 3.2. The simulations start at the inner envelope with the following set of parameters: the radius, molecular hydrogen number density, visual extinction, and kinetic temperature of the gas are $r_1 = 1.0 \times 10^{15}$ cm, $n(H_2) = 1.3 \times 10^7 \mathrm{cm}^{-3}$, $A_V = 13.8$ mag, and $T = 575$ K, respectively. The outer radius of the envelope is set to $r_f = 7 \times 10^{17}$ cm, where the density has decreased to $n(H_2) = 26$ cm^{-3}, the

temperature to $T = 10\,\mathrm{K}$, and the visual extinction to $A_\mathrm{V} = 0.02$ mag. We pay particular attention to the chemistry in the outer CSE where photodissociation is an important process. For all photoreactions, species are destroyed by photons from all directions, i.e., the radiation field is isotropic. For IRC +10216, one has to only take into account photons that come from the interstellar medium. The star, with a temperature of ~ 2330 K (De Beck et al. 2012), is too cool to generate photons that could lead to the photodissociation of molecules.

3.2.2 What's new

Our aim is to improve the treatment of N_2 and CO photodissociation. In the work of McElroy et al. (2013), they employed the following parameters and methods:

1. Unshielded photodissociation rates
   CO: 2.0×10^{-10} s^{-1}, from van Dishoeck (1988)
   N_2: 2.0×10^{-10} s^{-1}, from van Dishoeck (1988)
2. Shielding functions
   CO: dust + self-shielding, from Morris & Jura (1983), neither taking into account all lines for CO self-shielding nor shielding from H_2
   N_2: dust shielding only
3. Method for implementing self-shielding functions
   The 'one-band approximation' (Morris & Jura 1983)

In this work, we employ the most accurate molecular data to date and develop a new method for implementing molecular shielding functions in the SS model:

1. Unshielded photodissociation rates
   CO: 2.6×10^{-10} s^{-1}, 30% higher, from Visser et al. (2009)
   N_2: 1.65×10^{-10} s^{-1}, 28% lower, from Li et al. (2013)
2. Shielding functions
   CO: dust + self- + H + H_2 shielding, from Visser et al. (2009)
   N_2: dust + self- + H + H_2 shielding, from Li et al. (2013)
3. Method for implementing self-shielding functions
   By iterating the calculations to get converged results for the column densities in spherical symmetry for an isotropic radiation field. Details of this method are described in Sect. 3.2.3 and Appendix 3.6.

3.2.3 Photodissociation rate and shielding function

The definitions of the photodissociation rate, k, unshielded rate, k^0, and shielding function, Θ, appropriate for a plane-parallel model (only considering photons from the normal direction) are the same as those described in our recent paper (Li et al. 2013). In this work, we consider photons from all directions in space (SS model) for photoreactions that occur in the outer CSE. Suppose an incident ray, inclined with angle ϑ to the outward normal direction, arrives at a specific radius, r_i. The total column density of H_2 integrated from this point along the ray to infinity can be written as (Jura & Morris 1981; Morris & Jura 1983)

$$N_{\mathrm{H_2}}(r_i, \vartheta) = N_{\mathrm{H_2}}(r_i, 0)\ \vartheta / \sin\vartheta \ \ \mathrm{cm}^{-2}\ . \tag{3.2}$$

This expression diverges for ϑ close to zero and π. In practice, the value of $\vartheta/\sin\vartheta$ equals 1 if $\vartheta = 0$. For the case of $\vartheta = \pi$, its value is obtained using a linear extrapolation from the preceding data points on our angular grid.

In the CSE of IRC +10216, most hydrogen is locked in H_2 due to self-shielding. Thus, the corresponding visual extinction, $A_V(r_i, \vartheta)$, is

$$A_V(r_i, \vartheta) = 2N_{H_2}(r_i, \vartheta)/(1.87 \times 10^{21}) \text{ mag} , \tag{3.3}$$

with the conversion factor based on the observations of Bohlin et al. (1978) and Rachford et al. (2009). The photodissociation rates of most interstellar species are mainly attenuated by dust, which is characterised by dust shielding functions given by

$$\Theta_{dust}(r_i, \vartheta) = e^{-\gamma A_V(r_i, \vartheta)} , \tag{3.4}$$

where γ is the parameter used to estimate the increased dust extinction at ultraviolet wavelengths. In general, the contribution of a specific ray of interstellar photons to the overall photodissociation rate at r_i may be calculated using

$$k(r_i, \vartheta) = k^0 \, \Theta_{dust}(r_i, \vartheta) \text{ s}^{-1} . \tag{3.5}$$

However, the photodissociation rates of N_2, CO, and H_2 are more complex due to self- and mutual-shielding by H, H_2, CO, and other molecules (which are wavelength and column density dependent) and also continuum shielding by dust. A convenient way to take these effects into account in models is by use of molecular shielding functions that are calculated from high accuracy wavelength-dependent absorption cross sections. There is no need to consider H_2 photodissociation in the current study because it is fully shielded everywhere in the CSE. For N_2 and CO, one must consider self-shielding and mutual-shielding by H_2. The photodissociation rate of N_2 is calculated by

$$k_{N_2}(r_i, \vartheta) = k^0_{N_2} \Theta_{dust}(r_i, \vartheta) \, \Theta_{mol}[N_{H_2}(r_i, \vartheta), N_{N_2}(r_i, \vartheta)] \text{ s}^{-1}, \tag{3.6}$$

where $k^0_{N_2}$ is the unshielded photodissociation rate of N_2, and $N_{N_2}(r_i, \vartheta)$ is the column density of N_2 at radius r_i, integrated from this point along angle ϑ to infinity. $\Theta_{mol}[N_{H_2}(r_i, \vartheta), N_{N_2}(r_i, \vartheta)]$ is the molecular shielding function that is responsible for the multiple shielding effects caused by N_2 (self-) and H_2. It can be obtained via a bi-linear interpolation of N_2 and H_2 shielding functions that depend only on their column densities.

Correspondingly, the CO photodissociation rate is calculated using

$$k_{CO}(r_i, \vartheta) = k^0_{CO} \Theta_{dust}(r_i, \vartheta) \Theta_{mol}[N_{H_2}(r_i, \vartheta), N_{CO}(r_i, \vartheta)] \text{ s}^{-1}, \tag{3.7}$$

where k^0_{CO} is the CO unshielded photodissociation rate, and $N_{CO}(r_i, \vartheta)$ is the column density of CO at radius r_i, integrated along angle ϑ to infinity. Atomic hydrogen can also shield N_2 and CO, although in practice this is unimportant for the case of CSEs because the majority of hydrogen is locked in H_2.

A full description of the SS model and the numerical method for the computation of $N(r_i, \vartheta)$ can be found in Appendix 3.5. The implementation of N_2 and CO shielding functions in the SS model is not straightforward. This is because before starting the evolution

of the chemistry, one needs to know in advance the abundances of N_2 and CO at each radius to evaluate their column densities, and to compute the molecular shielding functions. However, these data are generated from the output of the model. One approximate solution is to assume that the N_2 and CO number densities are a constant proportion of H_2, which falls as r^{-2} (Jura & Morris 1981), then work out the corresponding column densities. This assumption is inaccurate in the photon-dominated regions where N_2 and CO densities are no longer constant with respect to H_2. In this study, we propose a new procedure which gives more accurate and convergent results by iterating the computation of the chemistry. This method is described in Appendix 3.6.

The photodissociation of N_2 and CO becomes considerable at the edge of the CSE, where the visual extinction is less than 1.0 mag and the temperature is around 10 K, as can be seen in Fig. 3.2. When calculating the N_2 shielding functions, the excitation temperature for both H_2 and N_2 are chosen to be 10 K. The Doppler widths of N_2, H_2, and H are 0.2, 3, and 5 km s^{-1}, respectively. The column density of atomic hydrogen is taken to be 1.0×10^{14} cm^{-2}. For CO shielding, the excitation temperature for H_2 and CO are chosen to be 11 and 5 K, respectively. At the low densities in the outer CSE, CO is subthermally excited. The Doppler widths of CO, H_2, and H are 0.3, 3, and 5 km s^{-1}. Electronic tables of the N_2 and CO shielding functions are available online.[b] Note that these shielding functions were calculated by considering (H_2, H, and self-) shielding at various temperatures for a few typical column densities. Shielding functions for other temperatures and column densities can be obtained by interpolation. In practice, the uncertainties in the shielding functions over a temperature variation of a few degrees are negligible, see Li et al. (2013). The parameter γ used to account for the dust extinction at ultraviolet wavelengths for N_2 and CO was taken to be 3.9 and 3.5, respectively.

Finally, the radial photodissociation rate in a spherical geometry with isotropic incident radiation is evaluated by

$$k(r_i) = \frac{1}{2} \int_0^{\pi} k(r_i, \vartheta) \sin\vartheta \, \mathrm{d}\vartheta \quad \mathrm{s}^{-1}. \tag{3.8}$$

3.3 Results

3.3.1 Improvements in N_2 and CO photodissociation

Figure 3.3 compares the calculated column densities and photodissociation rates for the spherically-symmetric and plane-parallel models. For the PP case, we consider photons from the radial direction only but the full shielding (dust + self- + H + H_2) was included. The envelope was illuminated by a Draine (1978) field, extended to wavelengths longer than 2000 according to van Dishoeck & Black (1988) and with a scaling factor, χ. In the SS model, photons from all directions in space were considered with $\chi = 1$ and the angular weighting scheme is given by Eq. (3.8). For the PP model, radiation from one side was taken into account explicitly with $\chi = 0.5$ and radiation from the far side assumed completely attenuated. Hence, in the absence of the envelope the same unattenuated Draine (1978) radiation field is recovered as for the SS model. Indeed, for $\chi = 0.5$, the N_2 photodissociation rates in the SS and PP cases are very similar (middle panel Fig. 3.3),

[b] `http://home.strw.leidenuniv.nl/~ewine/photo/`

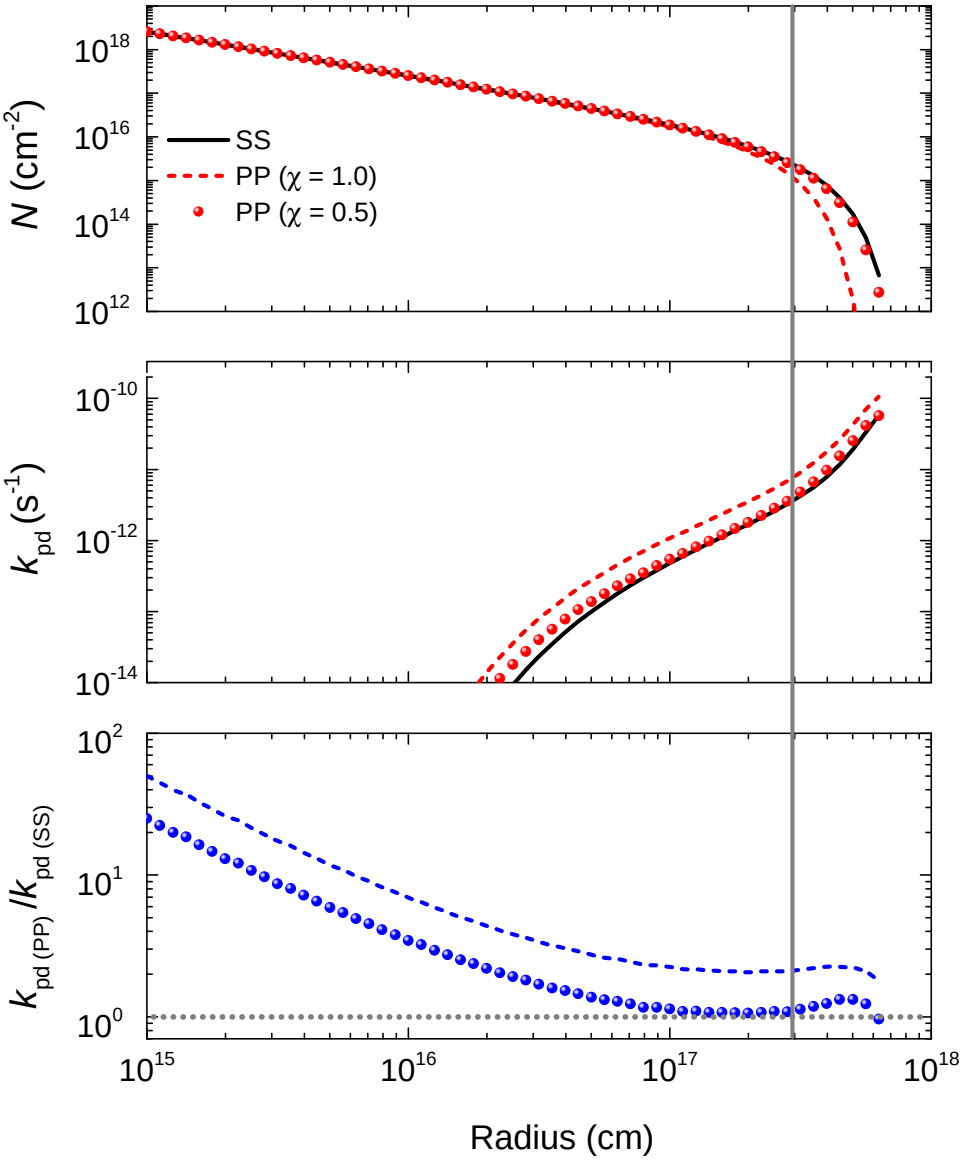

Figure 3.3 — Plots of the N_2 column densities (top), photodissociation rates (middle) and their ratios (bottom) when calculated using the plane-parallel (dashed lines: $\chi = 1.0$; spheres: $\chi = 0.5$) and spherically-symmetric (black solid lines) models as a function of radius. The dotted horizontal line indicates $k_{\rm pd}({\rm PP}) = k_{\rm pd}({\rm SS})$. Outside the solid vertical line N_2 photodissociation becomes considerable.

whereas when assuming $\chi = 1.0$, the PP rate is up to a factor of two higher at the outer edge. As a result, the PP model with $\chi = 1.0$ underestimates the N_2 column density at this location, but the $\chi = 0.5$ model results are very close to those of the SS model. The bottom panel of Fig. 3 shows that the PP and SS models start to deviate more in the inner envelope, where the PP model gives a much higher photodissociation rate. However, the absolute photodissociation rates are so small here that they are negligible in the chemistry. Overall, we conclude that for the CSE chemistry of IRC +10216, the PP model with a scaling factor of $\chi = 0.5$ provides excellent agreement with the full SS

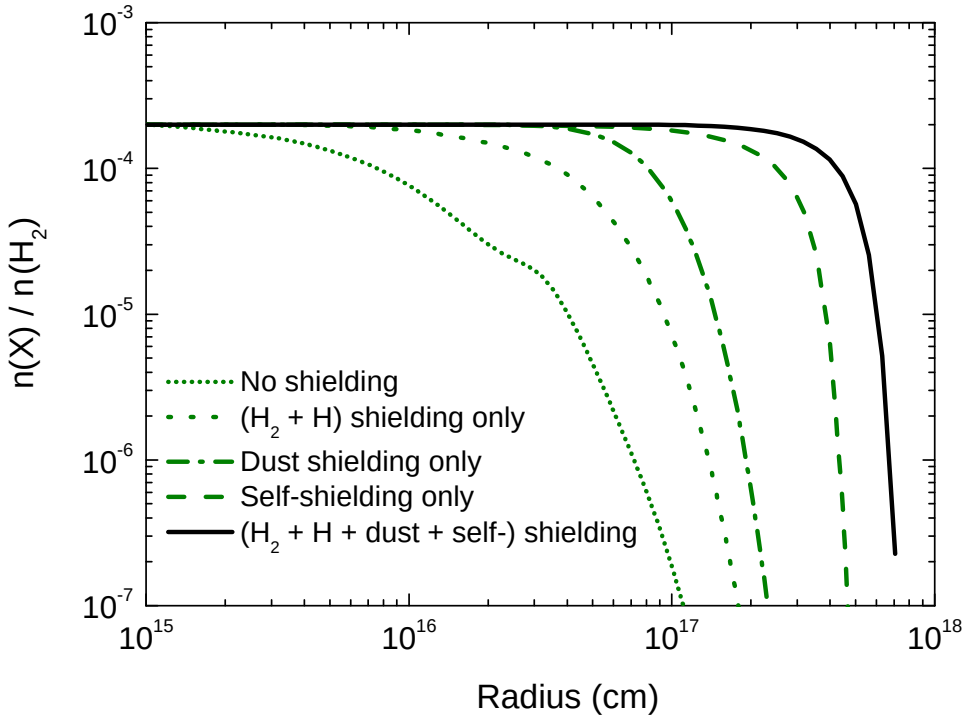

Figure 3.4 — Plot of the fractional abundance of N_2, relative to H_2, as a function of radius with different shielding effects. In all cases, photons are considered from all directions in space (in SS model).

model.

In the SS model the abundance of N_2 is higher than that in the PP model in the outer envelope. The distribution of CO in the SS and PP models is similar to that for N_2, also indicating a higher abundance of CO at the edge of the cloud for the SS case.

Including or excluding different shielding effects in the model is another crucial factor in the investigation of N_2 and CO photodissociation. Shielding effects, which act like a 'smoke screen', help molecules survive in photon dominated regions. N_2 and CO can be significantly shielded by both dust (wavelength independent) and molecules (wavelength dependent, line-by-line shielding). Fig. 3.4 presents the various shielding effects on N_2 photodissociation. Self-shielding is the most significant shielding effect, whereas (H_2 + H) shielding contributes the least. Shielding from dust largely depends on the properties of the dust (van Dishoeck et al. 2006). It is necessary to include all sources of shielding for N_2 because the combined effect has a strong influence on the abundance and distribution of N_2.

Figure 3.5 shows the fractional abundances of N_2 and N, calculated using various models. The location of the transition zone from N_2 to N is shifted outwards by a factor of 5 when molecular shielding is taken into account in the PP ($\chi = 1.0$) model. Further changes happen when we use the SS model and PP ($\chi = 0.5$) model.

The photodissociation of CO has an impact on both carbon and nitrogen chemistry. In particular, reactions with C^+ are important destruction mechanisms for quite a few N-bearing species, for example C_nN^- (n=1, 3, 5). As shown in Fig. 3.6, the conversion of CO to C and C^+ is affected when CO self-shielding is calculated using the updated

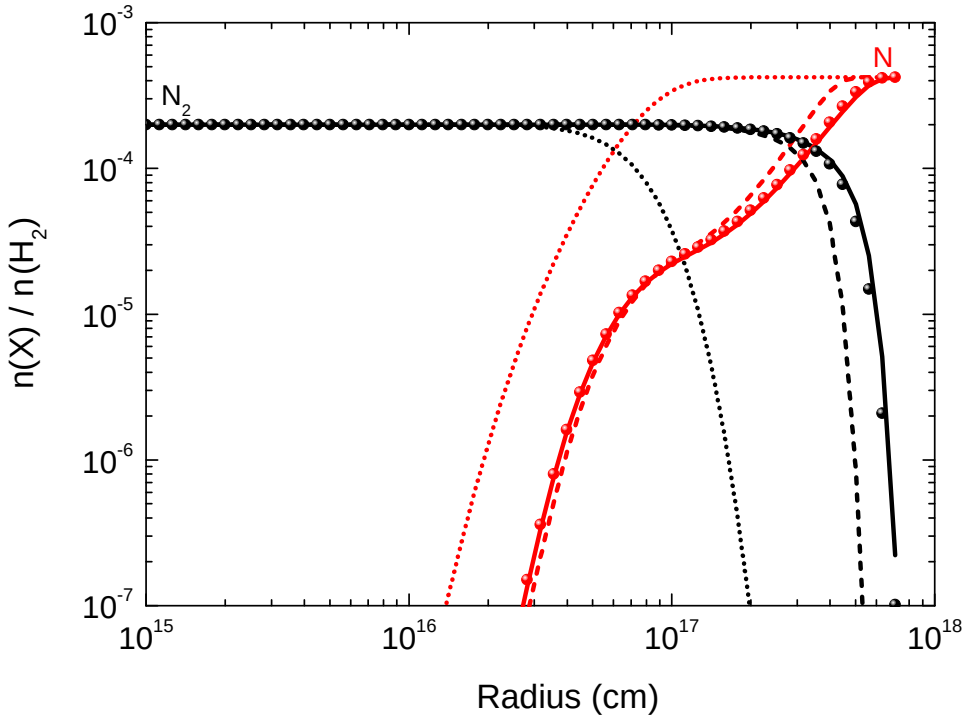

Figure 3.5 — Plot of the fractional abundances, relative to H_2, of N_2 and N as a function of radius. Dotted lines: McElroy et al. (2013) model, dust shielding only. Spheres, dashed and solid lines: PP model ($\chi = 0.5$), PP model ($\chi = 1.0$), and SS model, with full shielding (dust + self- + H + H_2).

shielding functions. The chemistry of other C-containing molecules is also affected by the photodissociation of CO, but are beyond the scope of this work. The SS model with full shielding predicts that CO is relatively abundant up to a radius of $\sim 6 \times 10^{17}$ cm, which is in better agreement with observations than the PP model (which is described further in Sect. 3.3.3.2).

3.3.2 Impacts of N_2 and CO photodissociation on the CSE chemistry

The photodissociation of N_2 and CO significantly affects the chemistry in the outer CSE. This influence has two observable aspects: one leads to changes in the radial distribution of the species' peak abundances. These distributions will become increasingly observable after exploiting the increased spatial resolution and sensitivity of new facilities such as ALMA. The other effect leads to changes in the peak abundances, which are directly reflected in total column densities. In the following subsections, we discuss fractional abundances of the most interesting (detectable or promisingly detectable) species which are sensitive to the photodissociation of N_2 and CO. Special attention is given to N-bearing species. Unless stated elsewhere, comparisons are made between the SS model including the updated N_2 and CO shielding and a recreation of the model of McElroy et al. (2013). Additional comparisons between observations and simulations from this study and McElroy et al. (2013) with regards to the 46 detected species in IRC +10216 are discussed in Sect. 3.3.3.

The dominant formation and destruction mechanisms of most species vary with physi-

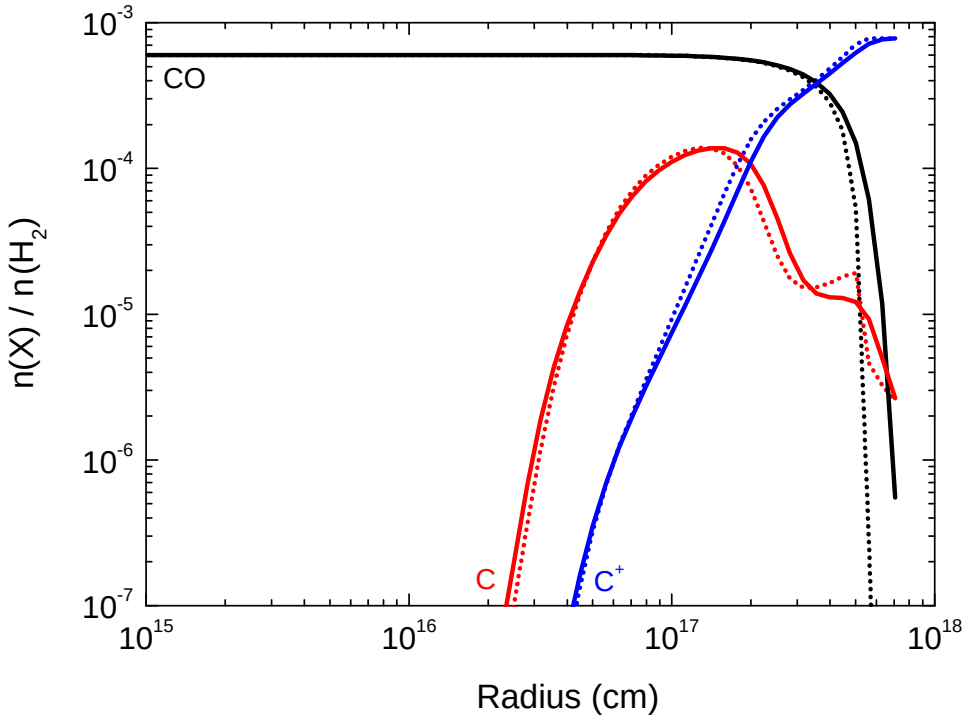

Figure 3.6 — Plot of the fractional abundances of CO, C, and C^+, relative to H_2, as a function of radius. Dotted lines: McElroy et al. (2013) model employing an earlier CO self-shielding function (Morris & Jura 1983) and photodissociation rates (van Dishoeck 1988). Solid lines: SS model, employing the newly calculated self-shielding function and photodissociation rate of CO (Visser et al. 2009).

cal conditions in the CSE. Here, we mainly focus on the chemistry of the outer CSE where photodissociation processes dominate.

3.3.2.1 CN^-, C_3N^- & C_5N^-

When N_2 photodissociation is treated in an appropriate manner, a higher abundance of N_2 is present in the outer CSE with a corresponding decrease in N. The most direct effects are on those N-bearing species whose formation processes require atomic N. C_nN^- (n=1, 3, 5) have already been observed in the CSE of IRC +10216 (Agúndez et al. 2010b; Thaddeus et al. 2008; Cernicharo et al. 2008). The following discussion of C_nN^- chemistry is based on the adopted reaction network from Walsh et al. (2009) which was incorporated into McElroy et al. (2013) and our model. Many of the adopted rate coefficients come from Eichelberger et al. (2007).

The chemistry of the molecular anions, CN^- and C_3N^-, in the CSE of IRC +10216 has been described in Kumar et al. (2013). As shown in Fig 3.7, C_nN^- (n=1, 3, 5) are very sensitive to N_2 photodissociation and are significantly decreased in the new treatment. This is because their formation processes are strongly affected by the abundance of atomic N in the outer CSE. As an example, at 1.0×10^{17} cm CN^- and C_3N^- are mainly formed through:

$$\mathrm{N} + \mathrm{C}_n^- \rightarrow \mathrm{CN}^- + \mathrm{C}_{n-1} \quad (n = 5, 6, 7, 8, 9, 10), \tag{3.9}$$

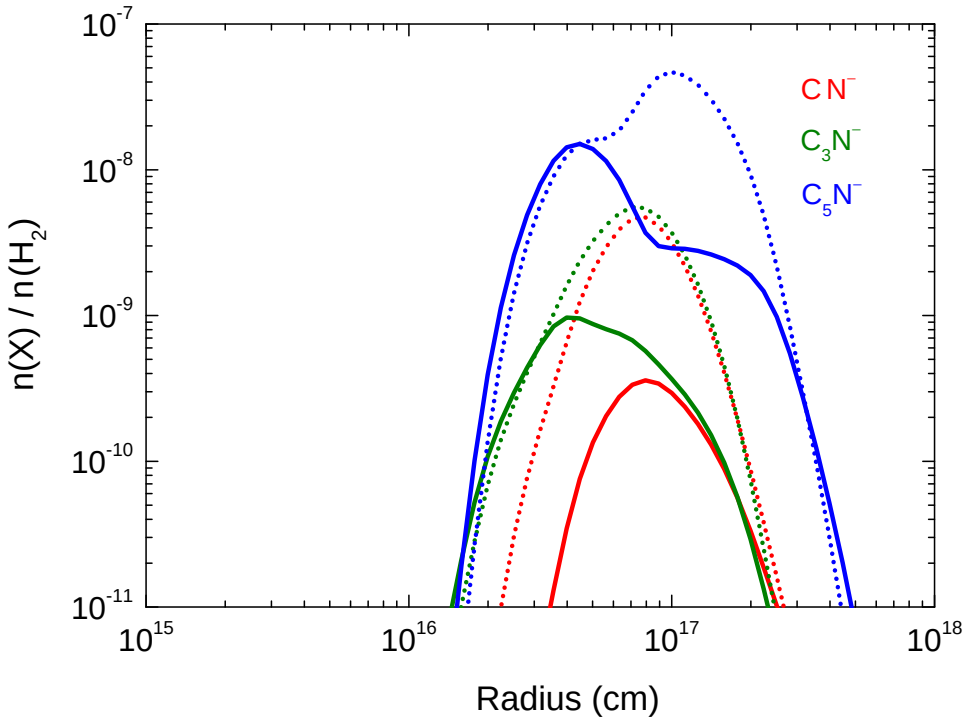

Figure 3.7 — Plot of the fractional abundances, relative to H_2, of C_nN^- (n=1, 3, 5) as a function of radius. Dotted lines: McElroy et al. (2013) model. Solid lines: SS model with updated shielding of N_2 and CO, details are described in Section 3.2.2.

$$N + C_n^- \rightarrow C_3N^- + C_{n-3} \quad (n = 6, 7, 8, 9, 10). \tag{3.10}$$

The abundances of these anions decrease with the decreasing abundance of N. As shown in Fig. 3.5, the fractional abundance of N drops from 4×10^{-4} (McElroy et al. (2013) model) to 3×10^{-5} (SS model) at 10^{17} cm, leading to ~ 1 order of magnitude drop in CN^- and C_3N^-. Interestingly, C_5N^- has a different formation route. It comes primarily from C_5N, via

$$C_5N + e^- \rightarrow C_5N^- + h\nu. \tag{3.11}$$

The radiative electron attachment of C_5N in Eq. (3.11) is very efficient compared with C_3N, which leads to the higher abundance of C_5N^- (see, e.g., Herbst & Osamura 2008).

3.3.2.2 CN, C_3N & C_5N

The chemistry of C_nN (n=1, 3, 5) are also sensitive to N_2 photodissociation, but not as sensitive as C_nN^- (n=1, 3, 5). This is because they are only partly affected by the available abundance of atomic N. Take CN as an example, it is mostly formed by the following reactions,

$$HCN + h\nu \rightarrow CN + H, \tag{3.12}$$
$$N + C_2 \rightarrow CN + C, \tag{3.13}$$
$$N + CH \rightarrow CN + H. \tag{3.14}$$

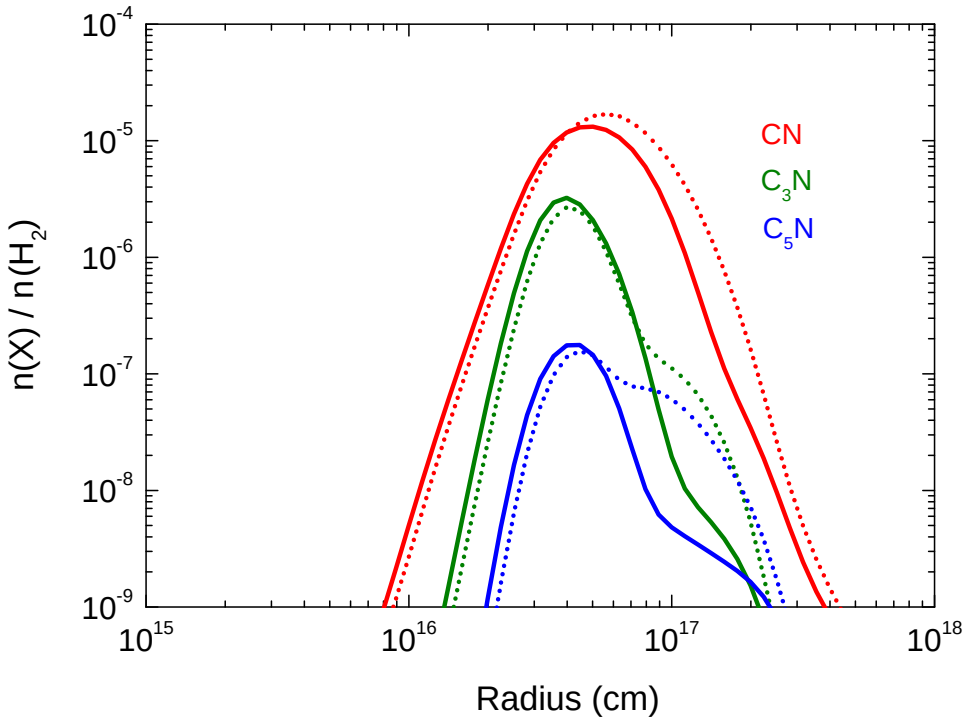

Figure 3.8 — Plot of the fractional abundances, relative to H_2, of C_nN (n=1, 3, 5) as functions of radii. Dotted and solid lines exhibit the results from the model of McElroy et al. (2013) and the SS model.

The photodissociation of HCN dominates CN formation inside a radius of $\sim 4{\times}10^{16}$ cm. Further out, the reactions involving atomic N play a role, although these reactions do not affect its peak abundance, see Fig. 3.8. The cases of C_3N and C_5N are similar to CN.

There is a shift in the peak abundances of CN, C_3N^- and C_5N^- from the outside of the envelope inwards towards the star. In the case of C_5N^-, this shift is from 10^{17} to 4×10^{16} cm. This difference is caused by the change in location of the N_2 to N transition zone when full shielding is included.

3.3.2.3 C_7N & C_9N

As shown in Fig. 3.9, the peak abundances of C_7N and C_9N are located at radii between 5×10^{16} and 1×10^{17} cm. Formation mechanisms for C_7N and C_9N are thought to be very similar to those of C_nN (n=1, 3, 5). They have a formation route via:

$$N + C_7^- \rightarrow C_7N + e^-, \tag{3.15}$$
$$N + C_9^- \rightarrow C_9N + e^-. \tag{3.16}$$

These larger C_nN molecules have not yet been identified in IRC +10216, but they are also sensitive to N_2 photodissociation and may be useful in indirect investigations of the chemistry and abundance of N_2. Their predicted peak abundances are around one order of magnitude lower than that of C_5N·

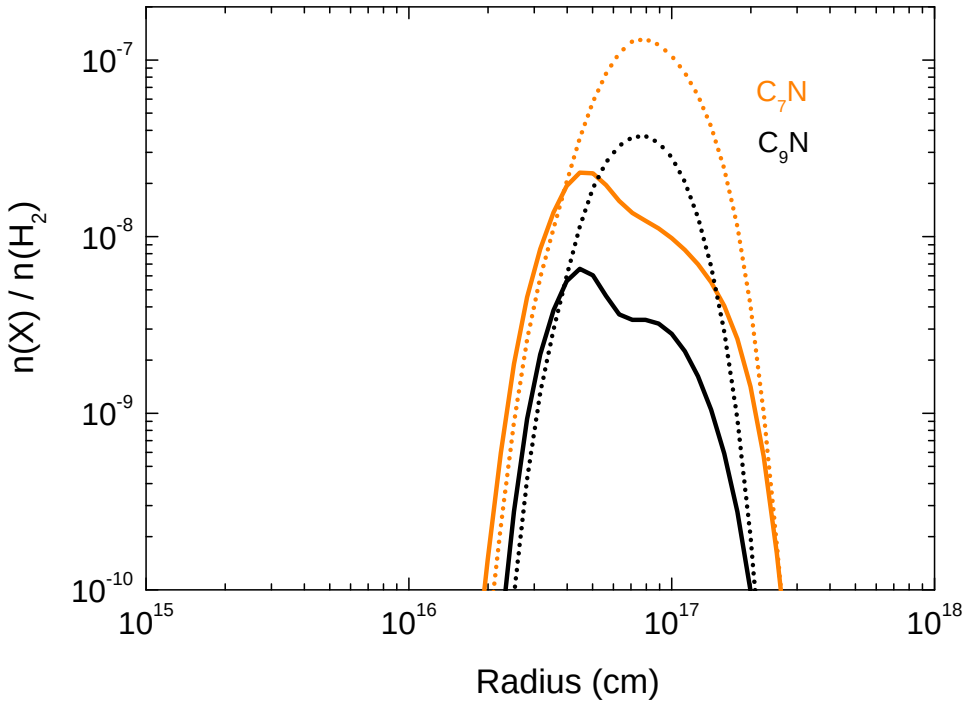

Figure 3.9 — Plot of the fractional abundances, relative to H_2, of C_7N and C_9N as a function of radius from the center of the star towards the outside of the envelope. Dotted and solid lines exhibit the results from the model of McElroy et al. (2013) and the SS model.

3.3.2.4 HC_nN (n = 3, 5, 7, 9)

The cyanopolyynes, HC_nN ($n = 3, 5, 7, 9$), are also influenced by N_2 photodissociation, especially in the outer shell where photodissociation processes are important, as shown in Fig. 3.10. The fractional abundances of HC_nN ($n = 3, 5, 7, 9$) are all affected when the full shielding of N_2 is considered. The most significantly affected species is HC_5N. The changes in their total column densities are rather small because the peak abundances, which contribute most to the column densities, are unchanged. However, the radial distribution of HC_5N may be spatially resolvable by sensitive interferometers.

The chemistry of large organic molecules is more complex than for simple species. At the photon-dominated radius $\sim 10^{17}$ cm, the main destruction process for the parent species, HCN, is photodissociation, which gives rise to its daughter molecule CN. Another important process for the destruction of HCN is by C^+, via

$$HCN + C^+ \rightarrow CNC^+ + H. \tag{3.17}$$

However, there are quite a few reformation reactions at this location. Amongst the most important are two reactions relevant to the present study,

$$N + CH_2 \rightarrow HCN + H, \tag{3.18}$$
$$H + CN^- \rightarrow HCN + e^-. \tag{3.19}$$

The decrease of HCN in the outer CSE, shown in Fig. 3.10, is largely due to the enhanced shielding of N_2, through the decreased abundance of N and, indirectly, CN^-.

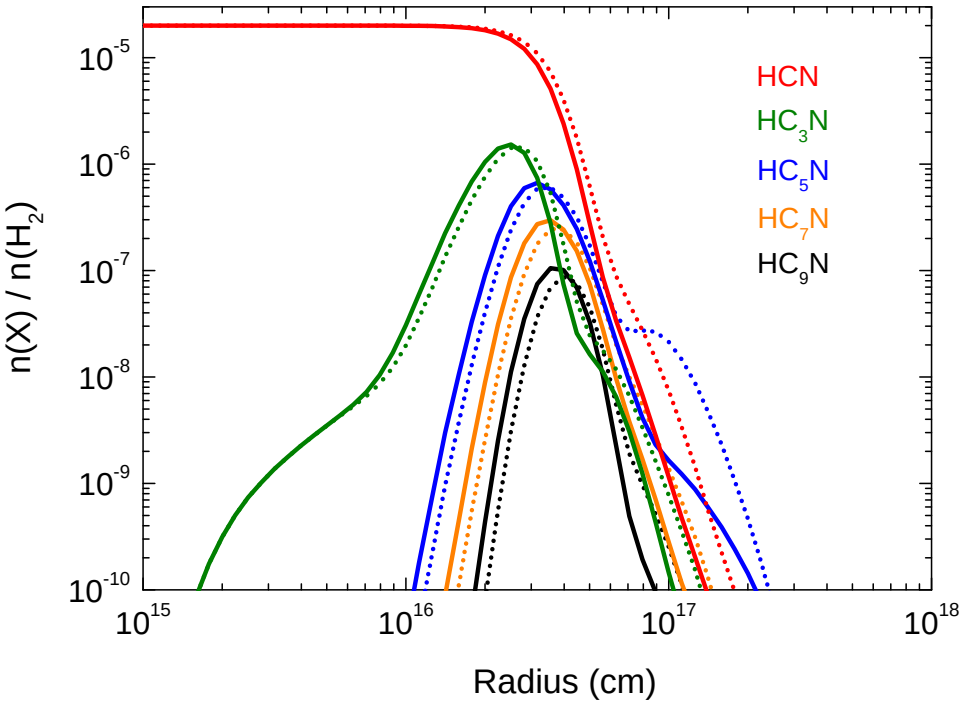

Figure 3.10 — Plot of the fractional abundances, relative to H_2, of HC_nN (n=1, 3, 5, 7, 9) as a function of radius from the center of the star towards the outside of the envelope. Dotted and solid lines exhibit the results from the model of McElroy et al. (2013) and the SS model.

In our calculations, HC_nN are synthesised by the reactions

$$HC_{n-1}H + CN \rightarrow HC_nN + H \quad (n = 3, 7, 9). \tag{3.20}$$

The changes in the radial distributions for HC_nN (n=3, 7, 9) are very similar to those of CN, see Fig. 3.8. HC_5N is an exception, and has the largest change among all HC_nN species in the photodissociation region. This is because the main formation process for HC_5N is via associative electron detachment,

$$H + C_5N^- \rightarrow HC_5N + e^-. \tag{3.21}$$

As discussed previously, the abundance and distribution of C_5N^- is strongly affected by the inclusion of N_2 shielding, thus, the abundance of HC_5N is also affected.

3.3.2.5 H_2CN & CH_2CN

The H_2CN and CH_2CN peak abundances are also significantly decreased when full N_2 shielding is included, as shown in Fig.3.11. Their main formation processes in the outer CSE are

$$N + CH_3 \rightarrow H_2CN + H \tag{3.22}$$

and

$$N + C_2H_3 \rightarrow CH_2CN + H. \tag{3.23}$$

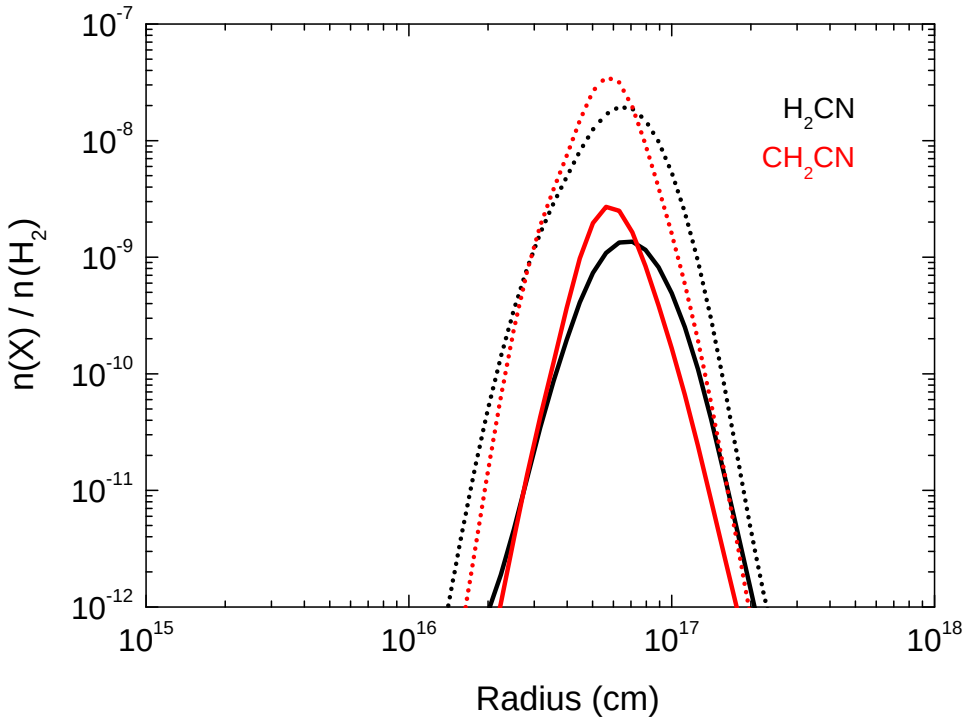

Figure 3.11 — Plot of the fractional abundances, relative to H_2, of H_2CN and CH_2CN as a function of radius from the center of the star towards the outside of the envelope. Dotted and solid lines exhibit the results from the model of McElroy et al. (2013) and the SS model.

There has already been a detection of CH_2CN in IRC +10216 (Agúndez et al. 2008b), whereas H_2CN has only been detected in dark clouds (Ohishi et al. 1994). Since the column density computed here is close to the value observed in dark clouds, this species could also be detectable in IRC +10216. Because the chemistry of the two species are relatively simple and largely depend on the availability of N, we may be able to use them to constrain the fractional abundance of N_2 in space by comparing observations with models.

3.3.2.6 PN

The chemistry of P-bearing and Si-bearing species in C-rich CSEs are not completely understood (McElroy et al. 2013). The most sensitive P-bearing and Si-bearing species to N_2 shielding are HNSi, SiN, and PN, see Fig. 3.12. Here we concentrate only on the chemistry of PN, which is mainly formed through the following route at a radius of 10^{17} cm:

$$\mathrm{N} + \mathrm{PH} \rightarrow \mathrm{PN} + \mathrm{H}. \tag{3.24}$$

This process is largely reliant on atomic nitrogen, which is significantly decreased at the PN peak radius when updated shielding is used.

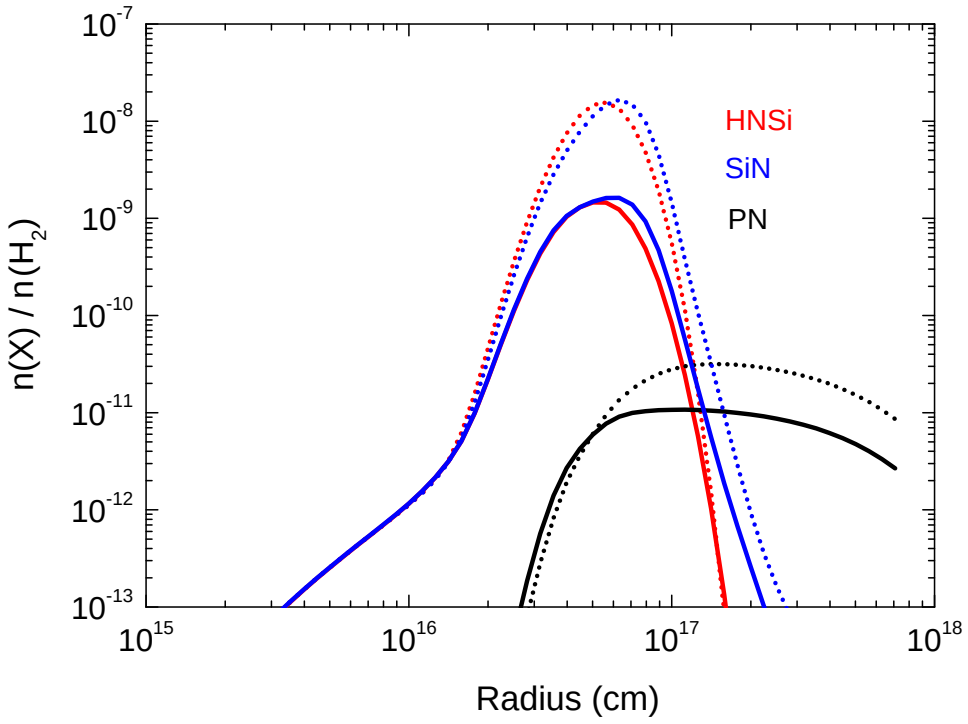

Figure 3.12 — Plot of the fractional abundances, relative to H_2, of PN, SiN and HNSi as a function of radius from the center of the star towards the outside of the envelope. Dotted and solid lines exhibit the results from the model of McElroy et al. (2013) and the SS model.

3.3.3 Comparison with observations

3.3.3.1 Column density

The radially-integrated column densities of most species are controlled by their peak abundances. After investigation, the abundances of quite a few of the 467 species in the network are affected when we use an appropriate method to calculated the photodissociation of N_2 and CO. A summary of the changes in column densities is an efficient way to extract the effects of these updates on the chemistry in the CSE. Here, we concentrate on those 46 species which have been observed in IRC +10216. The calculated and observed column densities are listed in Table 3.3. Of these, the calculated values for 14 species vary by more than 30%, and the values for 6 species vary by more than 80%, when compared with results from McElroy et al. (2013). The most affected N-bearing species with respect to the previous model are CN^- (-91%), SiN (-85%), and CH_2CN (-93%).

All of the species listed in Table 3.3 contain nitrogen and/or carbon and their formation and destruction may be influenced by N_2 and CO photodissociation. The important reactions for some of these species have been discussed in the previous subsections. The most significantly altered column densities include CN^- and C_3N^-, whose formation is sensitive to the available N, which is reduced by the increased shielding of N_2 in our new calculations. A factor-of-10 decrease for SiN and CH_2CN column densities can be similarly explained.

Some of these changes reduce the agreement of the CSE chemistry model with observed

column densities. There are many possible reasons for the discrepancies. First of all, some of the assumptions in the physical model of the CSE, unrelated to photodissociation (see Table 3.1), may be too simple. Further refinement of these assumptions may improve the agreement. For example, in this study, we ignored the presence of gas and dust shells in the expanding envelope. According to the study of Cordiner & Millar (2009), the inclusion of these shells gives a significant improvement in both modelled column densities and spatial distributions. A study of photodetachment as a destruction mechanism for the N-bearing anions, CN^- and C_3N^-, in the CSE of IRC +10216, concluded that the inclusion of shells with enhanced density, similar to the model of Cordiner & Millar (2009), increases the column densities of the anions by about 20% (Kumar et al. 2013).

One of the challenges in CSE simulations is the uncertainty in the abundance of parent species (see Table 3.2). In particular the modelled column densities of Si-bearing and P-bearing species in Table 3.3 are several orders of magnitude lower than that suggested by observations. Possibly, the currently modelled Si-bearing and P-bearing parent species should have a higher abundance or there exist other Si- and P-containing parent species. On the other hand, the uncertainties of some observations are considerable. Take SiC_2 as an example. The cited column density for this molecule in Table 3.3 is 2.0 $\times 10^{14}$ cm^{-2} (Thaddeus et al. 1984). However, according to a more recent study by Cernicharo et al. (2010) employing high quality Herschel/HIFI spectra an average column density of $\sim$ 6.4$\times 10^{15}$ cm^{-2} was found. Our computed value, 2.6×10^{15} cm^{-2}, is in better agreement with the latter observed value.

3.3.3.2 Radius of peak abundance

The radial location of peak molecular abundance is another observable parameter and is of equal importance to the column densities. Many daughter species have a clear radial peak in their modelled abundances which we may directly compare with spatially resolved observations. A selection of such observations have been reduced to their peak radii (without considering detailed excitation or radiative transfer) and compared with our model calculations, and are summarised in Table 3.3 and Fig. 3.13.

The model predicts that most peak radii fall within shells between 1×10^{16} ($4''$) and 2×10^{17} cm ($89''$) from the central star. Here, the distance between the Earth and IRC +10216 is assumed to be 150 pc, based on the study by De Beck et al. (2012). Different values for this parameter have been employed in other work which may affect intercomparison, e.g., Huggins et al. (1988) who assumed 200 pc, and Cordiner & Millar (2009) who employed 130 pc.

The outer radius of CO using the SS model is slightly larger, $\sim 7 \times 10^{17}$ cm ($\sim 310''$), than the previous value, see Fig. 3.6. Emission from CO in IRC +10216 has been extensively investigated. A good summary can be found in De Beck et al. (2012), who also obtained various physical parameters of the structure of IRC +10216. However, conclusions from these observations are not always the same. For instance, Huggins et al. (1988) detected CO emission out to $\sim 210''$ in the $J = 1 - 0$ line and $180''$ in the $J = 2 - 1$ line. Later, the $J = 1 - 0$ line was detected out to $190''$ (Fong et al. 2003, 2006). Recently, Cernicharo et al. (private communication) observed weak $J = 2 - 1$ emission out to a radius of $\sim 300''$, in excellent agreement with the present simulations.

Figure 3.13 compares the simulated and observed peak abundance radii for a few

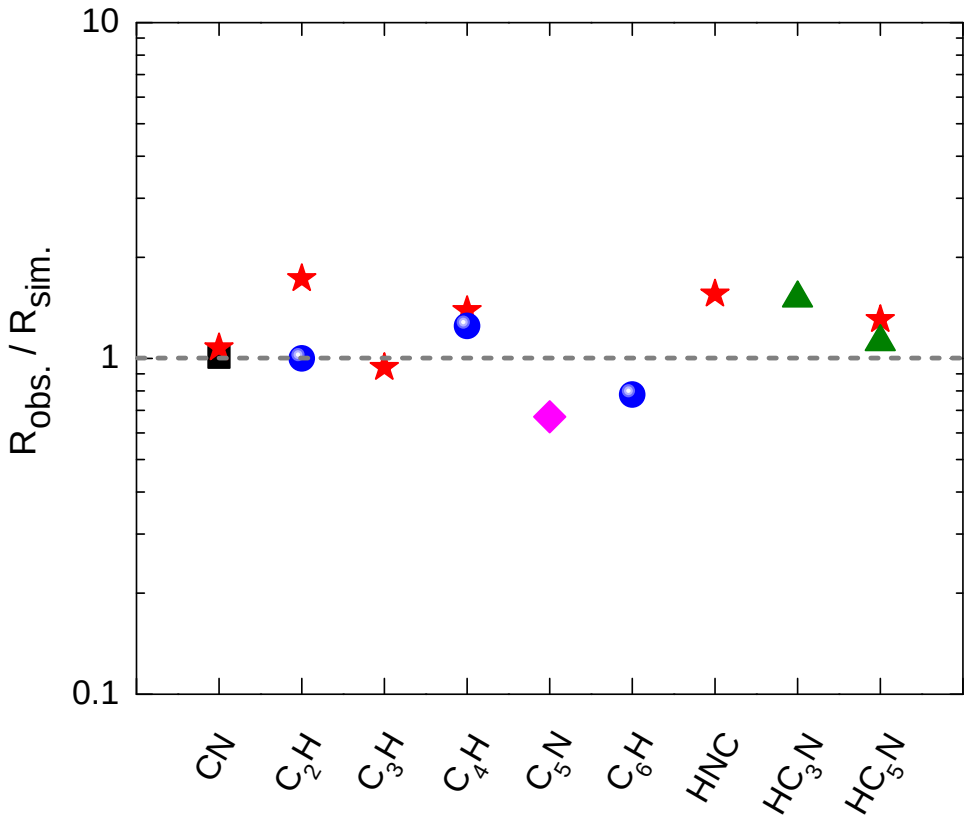

Figure 3.13 — Ratio of observed and simulated peak abundance radii ($R_{\rm obs.}$ and $R_{\rm sim.}$) for selected species. In all cases, $R_{\rm sim.}$ is obtained from our SS model. $R_{\rm obs.}$ is estimated from the interferometric maps of Lucas et al. (1995) (black squares), Guélin et al. (1998) (pink diamond), Guélin et al. (1999) (blue spheres), Dinh-V-Trung & Lim (2008) (green triangles), and Guélin (2011) (red stars). The dashed horizontal line indicates the position where $R_{\rm sim.} = R_{\rm obs.}$.

selected species for which interferometric maps are available. The observed peak radii, $R_{\rm obs}$, were deduced from direct measurement of the peak radius and averaged over those maps for which multiple rotational transitions were available. These observations were done with high angular resolution telescopes, such as the Plateau de Bure Interfrometer (PdBI) (Guélin et al. 1998, 1999; Guélin 2011) and the Very Large Array (VLA) (Dinh-V-Trung & Lim 2008). In our models, it is assumed that the peak emission occurs at the peak abundance position, i.e., no excitation or radiative transfer of the model lines is performed.

With these assumptions, it is seen in Fig. 3.13 that the overall agreement between our simulations and observations is within a factor of two. Interestingly, the simulations predict a peak abundance at 18″ for the parent species SiC_2 (see Table 3.3). This is very close to the value estimated from observations (Lucas et al. 1995; Guélin 2011), 16″. No other parent species exhibits a similar maximum.

None of the peak radii of observationally-mapped species were found to be significantly altered by the introduction of a more appropriate photodissociation treatment, even if their column densities were substantially changed. However, large differences were deduced for some unmapped carbon chain molecules and anions, specifically C_3N^-, C_5N^-,

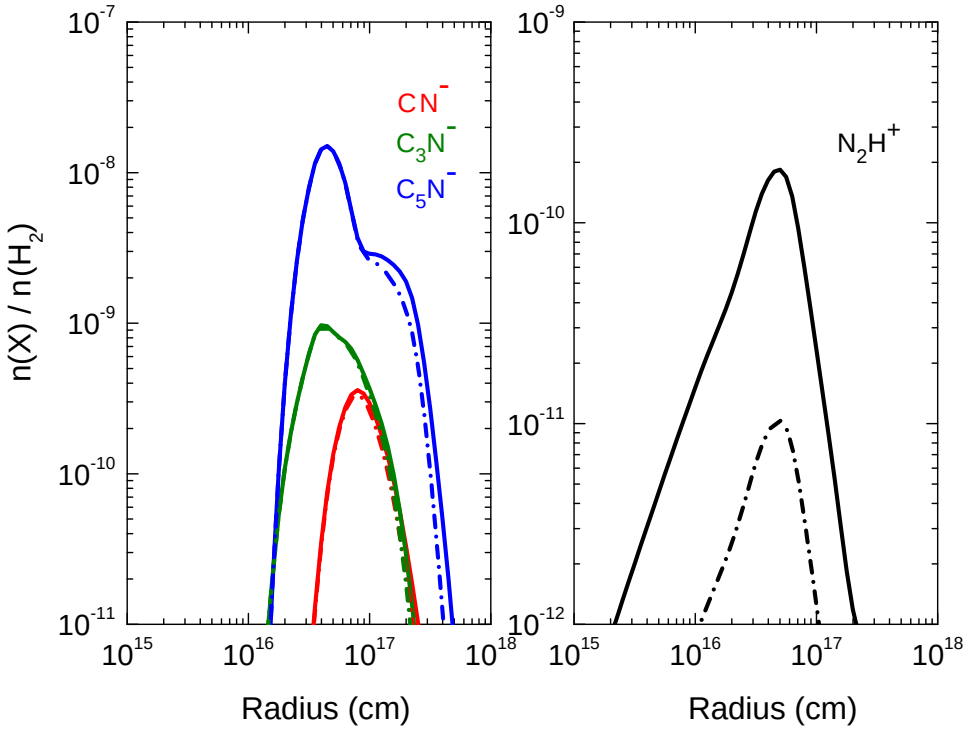

Figure 3.14 — Plot of the fractional abundances, relative to H_2, of C_nN^- (n = 1, 3, 5) (left panel) and N_2H^+ (right panel) as a function of radius. Solid lines: calculated using an initial N_2 abundance of 2×10^{-4} (relative to H_2). Dash-dotted lines: calculated using an initial N_2 abundance of 1×10^{-5}. In both cases, the SS model with updated shielding was employed.

C_5N, C_7N, and C_9N. The peak radii of these species all shift inwards after applying the new photodissociation shielding functions. For the case of C_5N^-, the peak radius retreats by a factor of 2.5, from 1.0×10^{17} (44″) to 4.5×10^{16} (20″) cm.

Our new model predicts that the CN^- peaks at a somewhat larger radius than its corresponding neutral CN, whereas the peaks of C_3N^- and C_5N^- match those of C_3N and C_5N, respectively, as shown in Table 3.3, Fig. 3.7, and Fig. 3.8. This conclusion differs from some previous models, e.g., Kumar et al. (2013) and references therein. Similar differences were found between the modelled peak radii of the neutral and anionic forms of C_nH (n=2, 4, 6) (Table 3.3). Interferometric maps of these species could serve as a test of the model predictions.

3.3.4 N_2 abundance in IRC +10216

There is some uncertainty in the initial abundance of N_2 (a parent species) in the CSE of IRC +10216. In previous models, its adopted abundance relative to H_2 lay between 1 $\times 10^{-5}$ and 2×10^{-4} (e.g., Nejad & Millar 1987; Millar et al. 2000; MacKay & Charnley 2001; Agúndez & Cernicharo 2006). In the present work, we employ the same abundance as that in the model of McElroy et al. (2013), 2×10^{-4}, which gives an overall good agreement between the modelled and observed N-bearing species' abundances in Table 3.3. However, the observational investigation of Milam et al. (2008) deduced an N_2 abundance of $\sim 1 \times 10^{-7}$. They used the observation of PN to infer an N_2 abundance by assuming

approximate equality of the abundance ratios, $PN/N_2 \simeq [P]/[N]$ and $[P]/[N] \simeq HCP/HCN \simeq 0.001$.

To test the sensitivity of daughter species to the initial N_2 abundance we recomputed their chemical abundances after lowering the parent N_2 abundance to 1×10^{-5}, a factor of 20 lower than in our fiducial models. The results for four species, CN^-, C_5N^-, C_5N^-, and N_2H^+ are shown Fig. 3.14.

N_2H^+ has not been observed in IRC +10216, but has been detected in other interstellar and circumstellar environments (e.g., Liu et al. 2013; Qi et al. 2013; Codella et al. 2013). This species is thought to be a good tracer for N_2, from which it forms directly via the reaction,

$$N_2 + H_3^+ \rightarrow N_2H^+ + H. \tag{3.25}$$

The utility of N_2H^+ as an N_2 tracer is supported by the calculated abundances plotted in Fig. 3.14, which are directly proportional to the assumed N_2 abundance. The predicted column density of N_2H^+ assuming initial N_2 abundances of 2×10^{-4} and 1×10^{-5} are 9.4 $\times$ 10^{10} and 5.3 $\times$ 10^9 cm^{-2}, respectively. The peak abundance of N_2H^+ is located at a radius of 5×10^{16} cm (22″). Future deeper observations of IRC+10216 with ALMA may determine the column density of N_2H^+ and allow for a new estimate of the N_2 abundance. Note that the abundances of neither N_2H^+ nor HCO^+, formed through a similar reaction between CO and H_3^+, are significantly affected by the new model treatment.

The abundances of C_nN^- anions are also not significantly affected by the altered parent N_2 abundance. These molecules are strongly dependent on the availability of atomic nitrogen (Sec. 3.3.2.1) which in the region of their peak abundance forms primarily from the photodissociation of HCN. Thus, HCN is the important N-bearing parent species affecting their column densities. Note that the main source of atomic N further out in the envelope is via the photodissociation of N_2.

3.4 Concluding remarks

In this work, the effect of self-shielding of N_2 and CO, and mutual-shielding by H_2, in the outer envelope of the C-rich AGB star, IRC +10216, was studied for the first time. This was performed using the latest available data for N_2 and CO photodissociation, and using an extended spherically-symmetric model for molecular self-shielding. The impact of these two improvements on the chemical evolution of the expanding envelope was investigated, with special attention paid to nitrogen chemistry and detectable species.

Key points from this study are:

1. N_2 and CO are more abundant at the edge of the CSE than predicted by previous models due to molecular shielding from photodissociation.
2. The photodissociation of N_2 and CO affects the chemistry of most species in the outer CSE. Following its improved treatment here, the transition zones of $N_2 \rightarrow N$ and $CO \rightarrow C^+ \rightarrow C$ shift towards the outer edge of the envelope. The abundances of some species formed from N are reduced in the outer CSE. This induces large changes in the predicted column densities (factor of 10) of some species (e.g., C_nN and C_nN^- carbon chains) and the radii of their peak abundances.

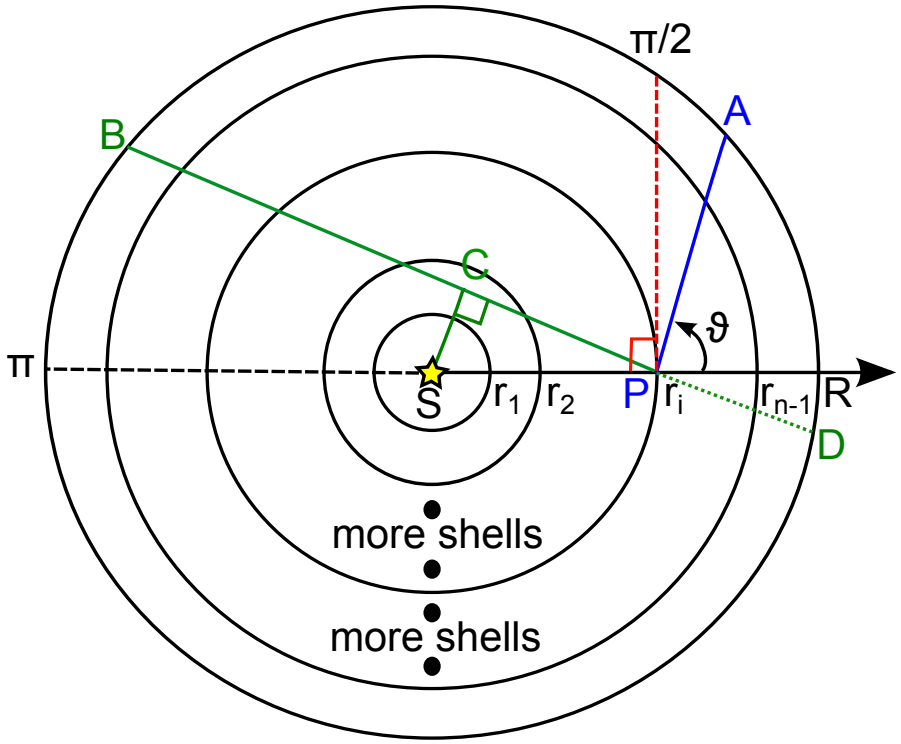

Figure 3.15 — Structure of the circumstellar envelope model of an AGB star.

3. Predictions are made for column densities and peak radii of molecules whose abundances are sensitive to N_2 and CO photodissociation and which could conceivably be detected. These may be verified by observations using high resolution and high sensitivity telescopes, especially ALMA and PdBI.
4. The abundances obtained from models which treat the full angularly-resolved spherically-symmetric radiation field incident on the outer CSE are very similar to those found in plane-parallel models in which the radiation is incident normally but with the intensity reduced by half. The proposed iterative method for implementing molecular shielding functions is most efficient when assuming that the molecule is fully shielded at the beginning of the calculation.

Other astrochemical models simulating the CSEs of AGB stars or other environments may show a similar sensitivity using a more realistic treatment of self-shielding and spherically-symmetric radiation as was found in this model of IRC +10216.

The photodissociation processes for N_2 and CO (both the unshielded rate as well as the depth dependence) are now very well understood, so any major discrepancies between observations and models are likely due to other assumptions in the model.

3.5 Appendix: Spherically-symmetric model

In this appendix we describe the SS model employed in this work for the computation of the angle-dependent column densities of species at each radius. The SS model is shown in Fig. 3.15. The star is located at point S and ejects dust and molecules to various shells

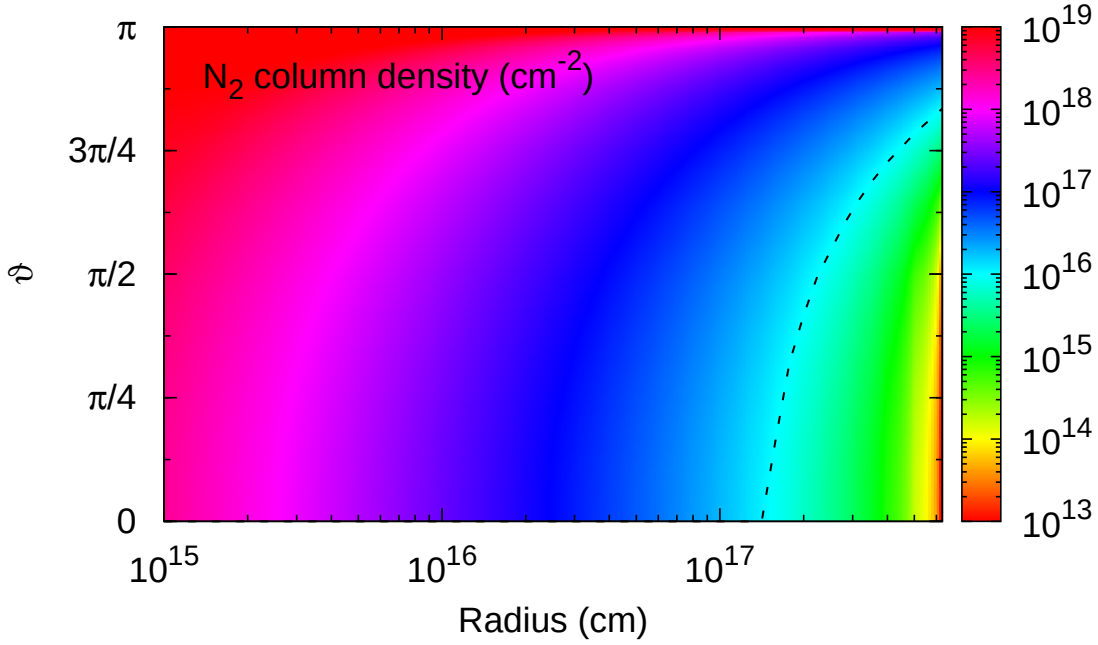

Figure 3.16 — Map of N_2 column density as a function of radius and the angle ϑ with respect to the normal direction, as described in Fig. 3.15. The dashed line shows the critical column density (1.0×10^{16} cm^{-2}). In practice, molecular N_2 is $\sim$ fully shielded when its column density is higher than this value.

with radii r_i (not equidistant). Since the star itself is too cool to generate photons that can induce photodissociation of molecules (in our case, IRC +10216, $\sim$ 2330 K), one only needs to consider photons from the interstellar radiation field. For a specific position P at radius r_i, suppose ϑ is the angle between the direction of the incoming ray and the radius vector from the central star. Generally, the column density, N, of a species is defined as

$$N \equiv \int_0^\infty n \, \mathrm{d}z \quad \mathrm{cm}^{-2}, \tag{3.26}$$

where n is the number density in units of cm^{-3} and z is the integral path length in units of cm. In the present study, the total column density, $N(r_i, \vartheta)$, of a species integrated along a ray from point P to infinity is given by two cases:

(1) $0 \leq \vartheta \leq \pi/2$, for example, $\overline{\mathrm{PA}}$, yielding

$$\begin{aligned} N_{\overline{\mathrm{PA}}}(r_i, \vartheta) = {} & \frac{1}{2}\left(\sqrt{r_{i+1}^2 - r_i^2 \sin^2\vartheta} - r_i \cos\vartheta\right)[n(i) + n(i+1)] \\ & + \frac{1}{2}\sum_{j=i+1}^{n-1}\left(\sqrt{r_{j+1}^2 - r_i^2 \sin^2\vartheta} - \sqrt{r_j^2 - r_i^2 \sin^2\vartheta}\right) \\ & [n(j) + n(j+1)] \quad \mathrm{cm}^{-2}, \end{aligned} \tag{3.27}$$

where $n(i)$ is the number density of the molecule at radius r_i.

(2) $\pi/2 < \vartheta \leq \pi$, for instance $\overline{\mathrm{BP}}$. Since we assume the model is spherically symmetric, one may simplify the calculations by finding a point C that satisfies $\overline{\mathrm{SC}} \perp \overline{\mathrm{BD}}$, then

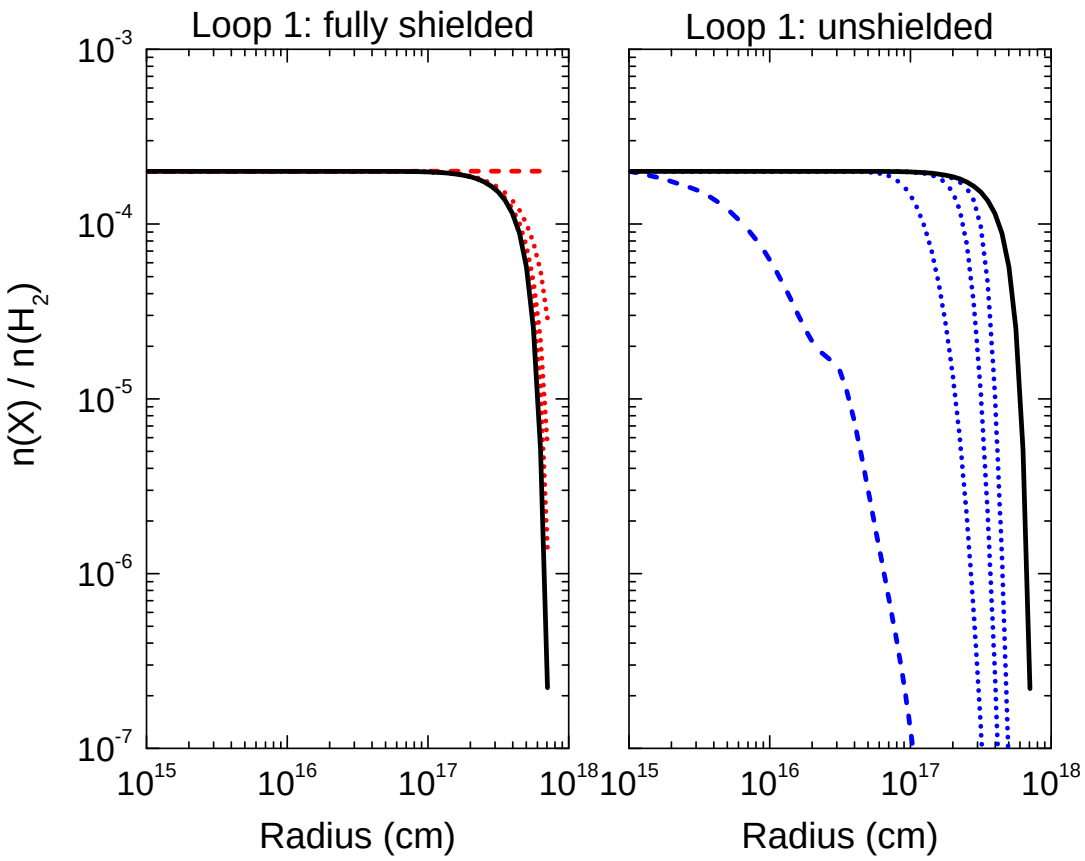

Figure 3.17 — Illustrations of the numerical method employed for implementing N_2 (and CO) shielding functions in this work. The plots show the fractional abundances of N_2 as functions of radii. It is seen that one can obtain the same converged results (solid lines in black) by assuming N_2 is either fully shielded (dashed line in red, left panel) or unshielded (dashed line in blue, right panel) at the first loop. The dotted lines show the intermediate abundances before reaching the final results.

get the column density along $\overline{\mathrm{BP}}$ with

$$N_{\overline{\mathrm{PB}}}(r_i, \vartheta) = 2N_{\overline{\mathrm{CB}}}(r_i, \pi/2) - N_{\overline{\mathrm{PD}}}(r_i, \pi - \vartheta) \quad \mathrm{cm}^{-2}. \tag{3.28}$$

Both $N_{\overline{\mathrm{CB}}}(r_i, \pi/2)$ and $N_{\overline{\mathrm{PD}}}(r_i, \pi - \vartheta)$ can be conveniently calculated by case (1). Then, it is necessary to interpolate an abundance between the radially-gridded values in our model for points near the star, such as C.

Figure 3.16 shows $N(r_i, \vartheta)$ for molecular N_2. According to our calculations, the major contribution of photons that induce photodissociation of N_2 come from the area within the dashed line ($N(r_i, \vartheta) < 1.0 \times 10^{-16}$ cm^{-2}), where $r_i > 1.6 \times 10^{17}$ cm and $\vartheta < 3\pi/4$. Deeper in the envelope, the fractional abundance of N_2 stays constant because it is fully shielded.

3.6 Appendix: Implementing the molecular shielding functions

In this Appendix we introduce the new procedure employed in the current work for the implementation of molecular shielding functions. Here we take N_2 as an example for the demonstration. The method has five steps.

1. Set up the initial condition. Suppose N_2 is fully shielded everywhere in the CSE, then we can set $k^{\rm initial}(r_i) \simeq 0$ for each radius, r_i, which means the corresponding shielding functions from dust and molecules are zero, i.e., $\Theta^{\rm initial}_{\rm dust}(r_i, \vartheta) = 0$, and $\Theta^{\rm initial}_{\rm mol}(r_i, \vartheta) = 0$. In all cases, we consider 201 incident rays as a function of ϑ between 0 and π, where $\vartheta = 0$ gives the normal direction.
2. Loop 1: compute the CSE chemistry for the first time, employing $k^{\rm initial}(r_i)$ prepared from Step 1. The calculated N_2 abundance generates column densities, $N(r_i, \vartheta)$, and corresponding dust and molecular shielding functions, $\Theta^{\rm loop1}_{\rm dust}(r_i, \vartheta)$, and $\Theta^{\rm loop1}_{\rm mol}(r_i, \vartheta)$, and new photodissociation rates $k^{\rm loop1}(r_i)$.
3. Loop 2: repeat the simulations of the CSE chemistry, but employing $k^{\rm loop1}(r_i)$ produced in Step 2 for each radius. Using the same method, generate another set of photodissociation rates, $k^{\rm loop2}(r_i)$.
4. Compare the fractional abundances of N_2 at each radius for Loop 1 and Loop 2, to see if they are the same. If no changes are found, go to Step 5, otherwise go to Step 3, continuing the calculations.
5. Stop the calculation. The outputs at this step are the final results.

The simulations can also approach convergence by assuming N_2 is unshielded in Step 1, namely $k^{\rm initial}(r_i) = k^0$ at each radius. In this case, the fractional abundance of N_2 will steeply decrease after starting the evolution of the chemical network, then approach the converged results quickly, as illustrated in Fig. 3.17. The same converged results can be obtained from the two possible assumptions in Step 1. In practice, the fractional abundances of both N_2 and CO (as well as all other species) reach their converged abundances after ~ 15 loops. In practice, starting the calculation assuming full shielding in Loop 1 is most efficient.

The iterative method proposed here may be used in other models, where output variables are also required as inputs.

Acknowledgements

The authors would like to thank the anonymous referee for his/her valuable comments and constructive suggestions. X. Li is delighted to thank TJM for his hospitality during a two-week visit to Queen's University Belfast (QUB) in 2013, and thank Dr. Markus Schmalzl and Prof. Xander Tielens for some stimulating discussions.

Astrochemistry in Leiden is supported by the Netherlands Research School for Astronomy (NOVA), by a Spinoza grant and grant 648.000.002 from the Netherlands Organisation for Scientific Research (NWO), and by the European Community's Seventh Framework Programme FP7/2007-2013 under grant agreements 291141 (CHEMPLAN) and 238258 (LASSIE). Astrophysics at QUB is supported by a grant from the STFC. C. W. acknowledges support from the NWO (program number 639.041.335).

Table 3.3 — Calculated and observed column densities, as well as peak abundance radii of species detected in the CSE of IRC +10216 [a].

No.	Species [b]	Observed[c] (cm^{-2})	Calculated[d] (This work) (cm^{-2})	Calculated [e] (RATE12 model) (cm^{-2})	Percentage change[f]	Radius of peak[g] abundance (cm & arcsecond, $''$)	Radius of peak[h] emission (cm & arcsecond, $''$)
1	CN	1.1(15)	3.5(15)	4.1(15)	-15	5.0(16) & 22	5.4(16) & 24
2	**C_3N**	**2-4(14)**	**6.7(14)**	**5.1(14)**	**31**	4.0(16) & 18	
3	C_5N	3-6(12)	3.6(13)	3.5(13)	3	4.5(16) & 20	3.0(16) & 13
4	**CN^-**	**5.0(12)**	**6.0(10)**	**7.0(11)**	**-91**	7.9(16) & 35	
5	**C_3N^-**	**2.0(12)**	**3.2(11)**	**1.0(12)**	**-68**	4.0(16) & 18	
6	**C_5N^-**	**3.0(12)**	**3.8(12)**	**7.7(12)**	**-51**	4.5(16) & 20	
7	HC_3N	1-2(15)	5.4(14)	4.8(14)	13	2.5(16) & 11	3.8(16) & 17
8	HC_5N	2-3(14)	1.7(14)	1.4(14)	21	3.2(16) & 14	
9	HC_7N	1.0(14)	6.0(13)	4.7(13)	28	3.5(16) & 16	
10	**HC_9N**	**3.0(13)**	**1.8(13)**	**1.3(13)**	**38**	3.5(16) & 16	4.3(16) & 19
11	**PN**	**1.0(13)**	**2.6(09)**	**5.4(09)**	**-52**	**1.1(16)** & **5**	
12	**SiN**	**4.0(13)**	**3.5(11)**	**2.4(12)**	**-85**	6.3(16) & 28	
13	SiNC	2.0(12)	8.7(08)	1.2(09)	-28	4.5(16) & 20	
14	CH_2NH	9.0(12)	2.8(11)	2.4(11)	17	2.8(16) & 12	
15	**CH_2CN**	**8.4(12)**	**3.0(11)**	**4.2(12)**	**-93**	5.6(16) & 25	
16	CH_2CHCN	5.0(12)	5.1(11)	5.3(11)	-4	5.6(16) & 25	
17	CH_3CN	6-30(12)	4.9(12)	5.6(12)	-13	4.0(16) & 18	
18	C	1.1(16)	1.9(16)	1.9(16)	0	1.4(17) & 62	
19	C_2	7.9(14)	5.2(15)	4.2(15)	24	5.0(16) & 22	
20	C_3	1.0(15)	2.0(14)	1.8(14)	11	3.5(16) & 16	
21	**C_5**	1.0(14)	2.0(14)	1.5(14)	**33**	7.1(16) & 32	
22	CP	1.0(14)	2.4(12)	2.2(12)	9	4.0(16) & 18	
23	**C_2P**	1.0(12)	1.1(09)	8.3(09)	**-87**	6.3(16) & 28	
24	**SiC**	6.0(13)	1.5(13)	1.0(13)	**50**	7.1(16) & 32	
25	SiC_2	2.0(14)	2.6(15)	2.6(15)	0	4.0(16) & 18	3.6(16) & 16
26	SiC_3	4.0(12)	1.7(12)	1.5(12)	13	4.5(16) & 20	
27	SiC_4	7.0(12)	9.6(10)	9.5(10)	1	5.6(16) & 25	
28	H_2CS	1.0(13)	4.7(11)	3.8(11)	24	5.6(16) & 25	
29	C_2S	9-15(13)	1.7(13)	1.4(13)	21	6.3(16) & 28	
30	C_3S	6-11(13)	1.6(13)	1.3(13)	23	4.0(16) & 18	
31	C_3O	1.0(12)	6.4(11)	6.0(11)	7	4.5(16) & 20	
32	H_2CO	5.0(12)	1.9(11)	1.6(11)	19	5.6(16) & 25	
33	HCO^+	3-4(12)	1.4(12)	1.3(12)	8	5.0(16) & 22	
34	C_2H	3-5(15)	1.1(16)	9.7(15)	13	3.5(16) & 16	3.4(16) & 15
35	C_3H	3-7(13)	1.5(14)	1.4(14)	7	3.5(16) & 16	3.3(16) & 15
36	*c*-C_3H_2	2.0(13)	6.1(13)	5.5(13)	11	3.5(16) & 16	
37	*l*-C_3H_2	3.0(12)	1.3(13)	1.1(13)	18	2.5(16) & 11	
38	CH_3CCH	1.6(13)	1.4(12)	1.3(12)	8	2.5(16) & 11	
39	C_4H	2-9(15)	7.2(14)	6.5(14)	11	2.8(16) & 12	3.4(16) & 15
40	C_5H	2-50(13)	4.5(13)	4.1(13)	10	3.5(16) & 16	
41	C_6H	7.0(13)	7.3(14)	5.7(14)	28	4.5(16) & 20	3.4(16) & 15
42	C_7H	1-2(12)	8.2(13)	7.3(13)	12	5.6(16) & 25	
43	**C_8H**	5.0(12)	1.6(14)	1.2(14)	**33**	4.0(16) & 18	
44	C_4H^-	7.0(11)	1.3(13)	1.3(13)	0	2.5(16) & 11	
45	**C_6H^-**	4.0(12)	9.8(13)	8.2(13)	20	**1.3(17)** & **58**	
46	C_8H^-	2.0(12)	3.2(12)	2.9(12)	10	4.0(16) & 18	

[a] a(b) = $a \times 10$ [b]. Boldface values indicate column densities showing big percentage changes (> 30%) between different models, in addition to the largest and smallest radii of peak abundances

[b] *c*-C_3H_2 and *l*-C_3H_2 represent cyclic- and linear- C_3H_2

[c] The compiled observational results were taken from Table 7 of McElroy et al. (2013).

[d] The most complete model (SS model with full shielding) in this work.

[e] Model similar to that of McElroy et al. (2013) with only a few modifications, e.g.,the photodissociation rates of CN^- and C_3N^- have been updated. These have only a small effect on the calculated column densities of species apart from CH_3CCH (old vs. new, 4.9 $\times 10^{11}$ vs. 1.4×10^{12} cm^{-2}) and CH_2CHCN (3.6×10^{10} vs. 5.3×10^{11} cm^{-2}).

[f] Comparison of computational results between the SS model and the model of McElroy et al. (2013), estimated by $100 \times (N_{\rm This} - N_{\rm RATE12}) \,/\, N_{\rm RATE12}$.

[g] The currently predicted radii of peak abundances for the species.

[h] Observed radii of peak emission for a few species, estimated from their interferometric maps. Observational references are given under Fig. 3.13, with priority given to the newer detections.

Chapter 4

New chemistry in O-rich AGB stars

Abstract.
Context. Thanks to the advent of *Herschel* and ALMA, new high-quality observations of molecules present in the circumstellar envelopes of AGB stars are being reported, which reveal large differences to existing chemical models. New molecular data and more comprehensive models of the chemistry in circumstellar envelopes are now available.
Aims. The aims are to determine and study the important formation and destruction pathways in the envelopes of O-rich AGB stars, and to provide more reliable predictions of abundances, column densities, and radial distributions for potentially-detectable species, with physical conditions applicable to the envelope surrounding IK Tau.
Methods. We use a large gas-phase chemical model of an AGB envelope including the effects of CO and N_2 self-shielding in a spherical geometry and a newly-compiled list of inner-CSE parent species derived from detailed modelling and observations. We trace the dominant chemistry in the expanding envelope and investigate the chemistry as a probe for the physics of the AGB phase by studying variations of abundances with mass loss rates and expansion velocities.
Results. We find a pattern of daughter molecules forming from the photodissociation products of parent species, with contributions from ion-neutral abstraction and dissociative recombination. The chemistry in the outer zones differs from that in traditional PDRs in that photoionization of daughter species plays a significant role. With the proper treatment of self-shielding, the N $\rightarrow N_2$ and $C^+ \rightarrow$ CO transitions are shifted outward by factors of 7 and 2 compared with earlier models, respectively. An upper limit on the abundance of CH_4 as a parent species of ($\lesssim 2.5 \times 10^{-6}$ with respect to H_2) is found for IK Tau, and several potentially-observable molecules with relatively simple chemical links to other parent species are determined. The assumed stellar mass-loss rate, in particular, has an impact on the calculated abundances of cations and the peak-abundance radius of both cations and neutrals: as the mass-loss rate increases, the peak abundance of cations generally decrease and the peak-abundance radius of all species moves outwards. The effects of varying the envelope expansion velocity and cosmic-ray ionisation rate are not as significant.

X. Li, T. J. Millar, A. N. Heays, C. Walsh, E. F. van Dishoeck, and I. Cherchneff
Submitted to *A&A* (2015).

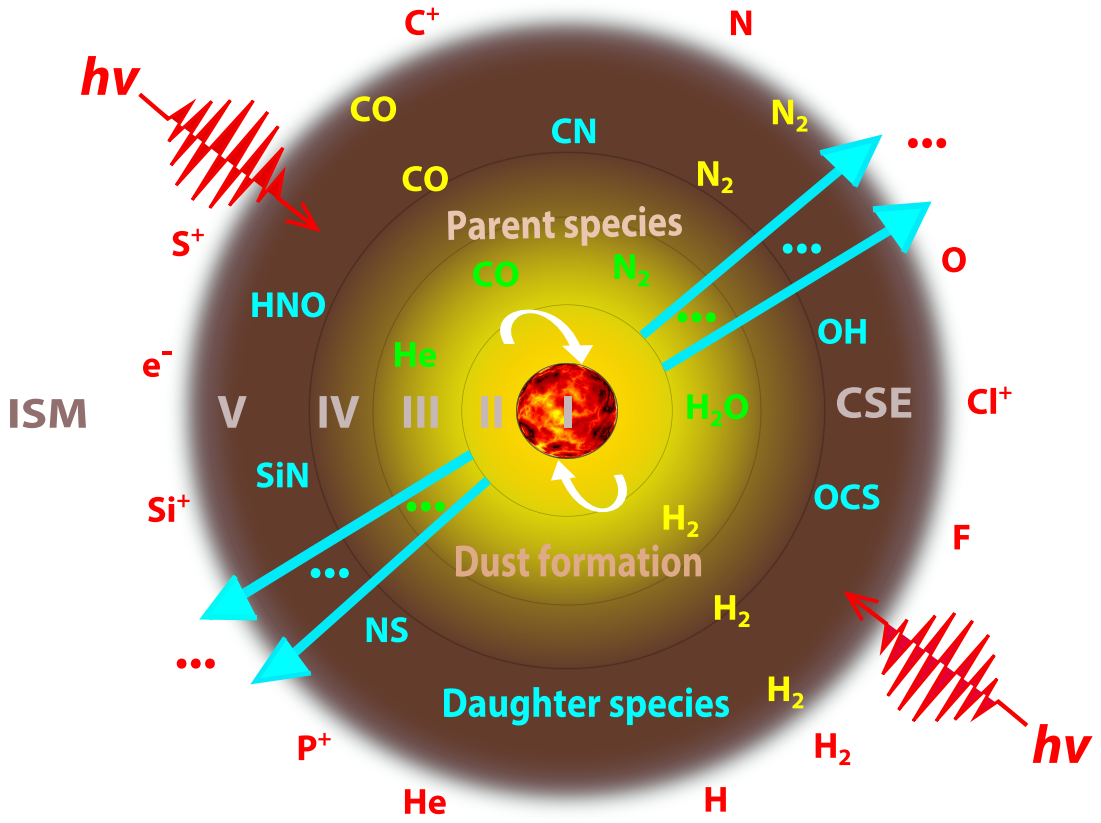

Figure 4.1 — Schematic structure of the CSE for an O-rich AGB star, which is divided into 6 regions for modelling purposes. (I): a degenerate C/O core and He/H burning shell, (II): a convective atmosphere, (III): a shocked inner wind where some parent species (mainly H_2O, CO, and SiO) are formed, (IV): an intermediate expanding envelope where gas-phase chemistry may play a role, (V): an outer CSE where daughter species are formed primarily by photodissociation, (VI): the interstellar medium (ISM). This study focusses on the outer CSE where chemistry is mainly driven by the photodissociation and photoionization of molecules.

4.1 Introduction

The asymptotic giant branch (AGB) phase occurs when stars from 0.8 to 8 $M_\odot$ are undergoing their last nuclear burning (Iben & Renzini 1983; Herwig 2005) and is a particularly interesting environment in which to study molecule formation and destruction. As shown in Fig. 4.1, the distribution and chemistry of species in the outer expanding circumstellar envelopes (CSEs), namely "daughter" species, are driven by hot (1000 – 2000 K) and shocked processes in the inner CSE where "parent" species are formed.

There are three types of AGB stars: C-rich (C/O $>$ 1), S-type (C/O $\approx$ 1), and O-rich (M-type, C/O $<$ 1). The largest variety of molecules is found in the CSE of C-rich stars, from simple CO to large polycyclic aromatic hydrocarbons (PAHs, e.g., Boersma et al. 2006; Cherchneff 2012). The best-investigated AGB star, both observationally and theoretically, is the nearest C-rich star, IRC +10216 (e.g., Millar et al. 2000; Cernicharo et al. 2000; Woods et al. 2003; Cordiner & Millar 2009; Decin et al. 2010; De Beck et al. 2012; Cherchneff 2012; McElroy et al. 2013; Li et al. 2014). To date, more than 44% of the

180 identified species in the interstellar medium (ISM) or CSEs[a] have been detected in this star, with some being first detections in astrophysical environments, e.g., the cyanide anion CN^- (Agúndez et al. 2010b), and FeCN (Zack et al. 2011). A relatively small, but increasing, number of investigations have been made into S-type AGB stars (e.g., Ramstedt et al. 2006, 2009, 2011; Schöier et al. 2011; Danilovich et al. 2014), in which the central stars are undergoing evolution from an O-rich to a C-rich phase. During this transition, mixed chemistry may occur, especially when the O-rich material is stored in a stable disk around the central star, and features of both C-rich and O-rich chemistry may appear (Willems & de Jong 1986; Szczerba et al. 2007). This interesting dual chemistry may continue to post-AGB stars, and even proto-planetary nebulae (pPNe, see Gielen et al. 2011,and references therein).

Significant progress in the investigation of O-rich circumstellar envelopes has been driven by new telescopes (Ziurys et al. 2007; Tenenbaum et al. 2010; Decin 2012), especially the Heterodyne Instrument for the Far-Infrared (HIFI) aboard the *Herschel Space Observatory* (Pilbratt et al. 2010), which provided velocity-resolved spectra at far-infrared wavelengths that are not accessible from the ground. Several small molecules have been identified in O-rich evolved stars, for instance, CO, H_2O, HCN, HNC, CN, OH, NO, SiS, and SiO, (e.g., Cho & Ukita 1998; Ziurys 2006; Schöier et al. 2007; Ziurys et al. 2009; Maercker et al. 2009; Decin et al. 2010a). In addition, some O-bearing inorganic species, e.g., AlO and AlOH, have been identified in the supergiant VY Canis Majoris (Tenenbaum & Ziurys 2010). Moreover, emission from PAHs and fullerenes C_{60} have also surprisingly been found in O-rich binary post-AGB sources (Gielen et al. 2011). All of these studies clearly show a rich inventory of molecules due to complex chemistry in the CSEs around O-rich central stars. The Atacama Large Millimeter/submillimeter Array (ALMA) is now starting to provide very sensitive, spatially resolved images of AGB envelopes as evidenced by the resolved shells of the AGB star R Sculptoris by Maercker et al. (2012). It is therefore timely to revisit the chemistry in these sources with an updated chemistry network.

In this work, we mainly focus on the well-observed O-rich AGB star, IK Tau. This source has a large mass-loss rate of $\sim 4.5 \times 10^{-6}$ $M_\odot$ yr^{-1} (De Beck et al. 2010) in a wind that expands at a terminal velocity of 24 km s^{-1} (Justtanont et al. 2012). Note that these values are model dependent and may be different from those deduced from other observations (e.g., Maercker et al. 2008; Decin et al. 2010a). A few 'parent' species (i.e., those formed close to the stellar photosphere) have been detected in the inner CSE of IK Tau in recent years, for instance, CO, HCN, CS, SiS, SiO, SO, and SO_2 (Decin et al. 2010a; Kim et al. 2010), H_2O (Decin et al. 2010b), NH_3 (Menten et al. 2010), PN and PO (De Beck et al. 2013). Schöier et al. (2013) conducted a survey of HCN in a sample of 69 stars which included all three types of AGB stars, including IK Tau, and concluded that the HCN abundances in C-rich AGB stars are, on average, around two orders of magnitude higher than those in O-rich stars. Fractional abundances of only two daughter species have been deduced from observations of IK Tau, CN (Decin et al. 2010a; Kim et al. 2010) and HCO^+ (Pulliam et al. 2011). OH emission was identified but not quantified (Polehampton et al. 2010). In addition, thermal CO and SiO polarization has

[a] `http://www.astro.uni-koeln.de/cdms/molecules/`

been mapped for IK Tau to study the orientation of its magnetic field (Vlemmings et al. 2012).

Theoretically, Willacy & Millar (1997) built a model specifically for O-rich CSEs and discussed the chemistry of daughter species in four sources: R Dor, TX Cam, OH231.8 +4.2, and IK Tau. At that time, only limited observational data and a restricted chemical network were available, therefore, some assumptions made in that work have since been discounted, e.g., CH_4 was assumed to be a parent species but the observations by Marvel (2005) provided no evidence for CH_4 based on sensitive searches for the chemically related CH_3OH and C_2H molecules. Agúndez et al. (2010a) employed an improved model to investigate the chemistry in both O-rich and C-rich AGB stars, and suggested that the model predictions could be altered by taking into account a clumpy structure for the CSE, even with a simple approach. An improved list of parent species from observations was employed, but some parent species, e.g., NH_3 and HCN, had not yet been observed at that time, and therefore were not included as parents. The assumed abundances of parent species is very important in the simulation of outer CSE chemistry, because these species trigger and drive the chemistry of daughter species. Previously, local thermodynamical equilibrium (LTE) predictions were used to determine the parent species. However, predictions from shock-induced non-LTE calculations (Duari et al. 1999; Cherchneff 2006) significantly differ from these, e.g., Cherchneff (2006) concluded that four species, CO, SiO, HCN, and CS, can exist in both C-rich and O-rich stars. The conclusion was later confirmed through observations (Decin et al. 2008).

In previous work we developed a model that, for the first time, accurately treated the photodissociation of two significant parent species, CO and N_2, in the CSE of a C-rich star, IRC +10216 (Li et al. 2014). Here, we adapt this model to study the chemistry of O-rich AGB stars. The recent progress of both observations and models makes a detailed and more reliable simulation possible. The chemistry of a large number of potentially observable species, including C-, N-, O-, Si-, S-, P-, Cl-, and F-bearing species, are discussed.

This chapter is organised as follows: the CSE model and improvements in this study are described in Sect. 4.2, followed by the results and discussion in Sect. 4.3, and conclusions, in Sect. 4.4. A general investigation of the effects of varying the mass-loss rate and expansion velocity on the distributions of species is included in the Appendix.

4.2 Improvements in our models

4.2.1 Improvements in the model

The CSE model assumes that the gas expands in a smoothly expanding envelope with a constant mass-loss rate and velocity. The main assumptions of the model and envelope parameters of the O-rich AGB star, IK Tau, are listed in Table 4.1. More details about the CSE model can be found in McElroy et al. (2013), Millar et al. (2000), and Cordiner & Millar (2009). The kinetic temperature of the gas, T, number density of molecular hydrogen, $n(H_2)$, and visual extinction, A_V, are shown in Fig. 4.2. The density follows a r^{-2} behaviour dictated by conservation of mass and the temperature structure

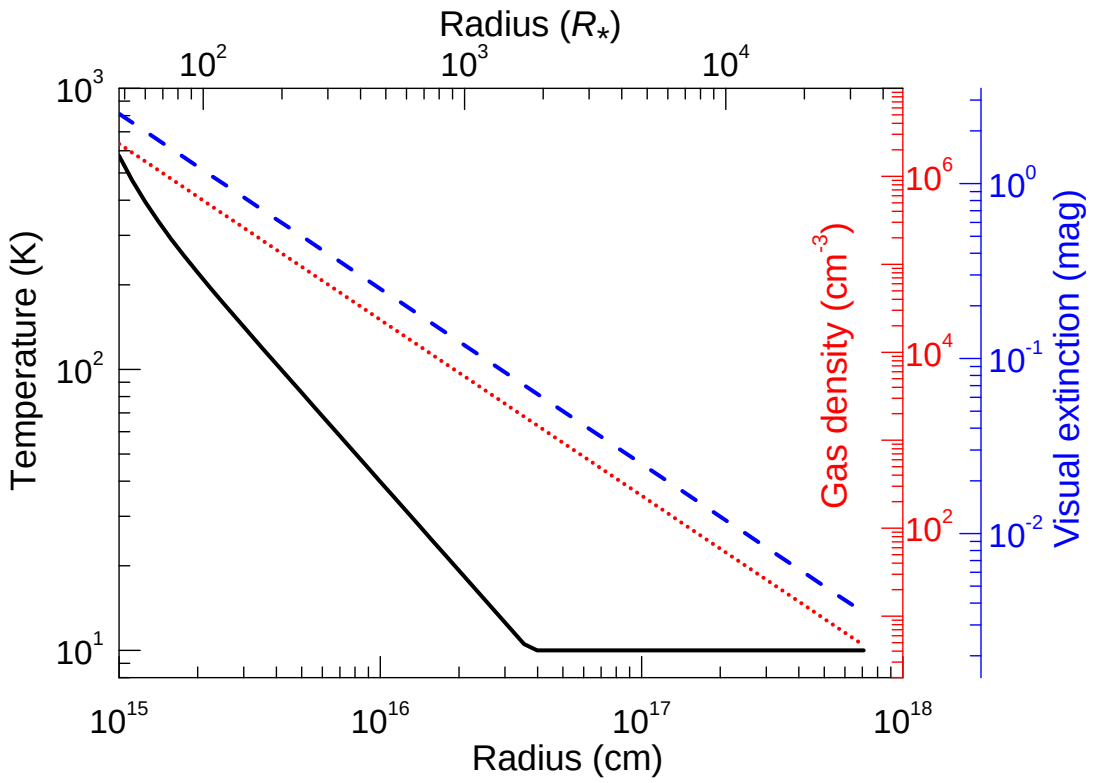

Figure 4.2 — Gas density, visual extinction, and gas temperature as a function of radius for the CSE of IK Tau from the center of the star towards the outside of the envelope. The radius is given in units of cm and stellar radii, R_*.

Table 4.1 — Envelope parameters and assumptions for IK Tau in our fiducial model.

1.	Shape	Spherical
2.	Mass-loss rate	4.5(-6) $M_\odot$ yr^{-1} (De Beck et al. 2010)
3.	Envelope expansion velocity	24 km s^{-1} (Justtanont et al. 2012)
4.	Stellar radius, R_*	2.1×10^{13} cm (Duari et al. 1999)
5.	Inner radius of CSE	10^{15} cm
6.	External radiation field	Draine (1978) field, isotropic incidence
7.	Grain surface reactions	Ignored
8.	Gas density distribution	Falls as r^{-2}, where r is the radius
9.	Chemical evolution	Kinetic equations solved as a function of radius
10.	H_2	Fully self-shielded, no photodissociation
11.	Parent species	See Table 4.2
12.	T, A_V, and gas density	See Fig. 4.2
13.	Cosmic-ray ionisation rate scaling factor	1

is calculated according to the following relation enforcing a 10 K lower limit

$$T(r) = \max\left(100\,(r/r_i)^{-0.79}, 10\right), \tag{4.1}$$

where r_i is the inner radius of our model. Extinction of the incident radiation is derived assuming purely absorbing grains and using standard values for the interstellar gas-to-dust ratio and extinction curve (Bohlin et al. 1978; Savage & Mathis 1979).

The chemistry of daughter species in the outer CSE is dominated by photodissociation. FUV photons from all directions of the interstellar medium are considered to contribute to the photodissociation rate of each species. IK Tau is of spectral type M6 with an effective temperature ≈ 2100 K (see, e.g, Duari et al. 1999); hence, the UV flux arising from the star itself is negligible. The model is assumed to be fully spherically-symmetric (SS model, Li et al. 2014) and accurately calculates the shielding effects of molecules in an isotropic interstellar radiation field.

The fifth release of the UMIST Database for Astrochemistry (UDfA, McElroy et al. 2013), hereafter RATE12, which contains 6173 gas-phase reactions involving 467 species, is further updated with a few new rate coefficients for the most significant nitrogen reactions (Wakelam et al. 2013), and adopted in all of the calculations. Very minor differences (within 2%) of the predicted peak abundances of the species are found when using these new rate coefficients, compared with those using RATE12.

The treatment of N_2 and CO photodissociation is the same as that described in our previous work (Li et al. 2014). Accurate photodissociation rates and shielding functions of N_2 (Li et al. 2013; Heays et al. 2014) are used. These data come from a concerted laboratory (e.g., Ajello et al. 1989; Helm et al. 1993; Sprengers et al. 2004; Stark et al. 2008; Lewis et al. 2008b; Heays et al. 2011) and theoretical (e.g., Spelsberg & Meyer 2001; Lewis et al. 2005b; Lewis et al. 2008c; Ndome et al. 2008) effort over the last two decades. The CO photodissociation calculation uses the new rate and self-shielding functions from Visser et al. (2009). In the CSE model from (McElroy et al. 2013), the photodissociation rates of N_2 and CO were adopted from van Dishoeck (1988), with self-shielding of CO treated only approximately (Morris & Jura 1983).

4.2.2 A new list of parent species

The identification and abundance of parent species at inner radii is the first key question to consider when modelling CSE chemistry. Typically three methods are used to constrain the parent species: TE predictions, shock-induced non-LTE predictions, and observations. The main benefit of theoretical predictions (TE and non-LTE) lies in that such models can provide a detailed list of all parent species. However, the disadvantage is that models are never as accurate as reality. Even assuming that the fundamental basis for the formation of these molecules is correct, the uncertainties in the physical processes in the inner CSE, chemical networks, and the initial abundances may still be significant. On the other hand, observationally, although high-quality data from powerful telescopes (e.g., *Herschel*, APEX, ALMA, amongst others) provide direct constraints, some species are non-detectable. For example, N_2, which is predicted to be the major elemental N reservoir in the inner layers. N_2 is symmetric and thus possesses no electric-dipole-allowed pure rotational spectrum. In addition, the identification of many species is not straightforward, due to the lack of detailed molecular data. Moreover, deduced results from spatially unresolved spectra are sometimes very model-dependent, which means considerable uncertainties also possibly exist.

Thanks to the recent progress in observations of O-rich AGB stars (e.g., Decin et al. 2010; Decin et al. 2010a,b; Kim et al. 2010; Menten et al. 2010; De Beck et al. 2013) and shock-induced non-LTE simulations (e.g., Cherchneff 2006), we are now able to employ an improved list of parent species (see Table 4.2) in this study. Wherever available, we employ

Table 4.2 — Initial fractional abundances, f_0(X) [a], of parent species, relative to H_2, for the O-rich AGB star, IK Tau.

No.	Species	f_0(X)	Comment
1	He	1.7(–1)	Solar abundance[b]
2	CO	2.0(–4)	Observation[c]
3	H_2O	6.6(–5)	Observation[d]
4	N_2	1.5(–4)	Shock-induced non-LTE abundance[e]
5	NH_3	2.0(–6)	Observation[f]
6	HCN	4.4(–7)	Observation[c]
7	CO_2	4.4(–9)	Shock-induced non-LTE abundance[e]
8	CS	8.0(–8)	Observation[c]
9	SiS	1.1(–5)	Observation[c]
10	SiO	1.6(–5)	Observation[d]
11	SO	2.0(–6)	Observation[d]
12	SO_2	2.0(–6)	Observation[c]
13	H_2S	1.0(–8)	Shock-induced non-LTE abundance[e]
14	HS	2.3(–8)	Shock-induced non-LTE abundance[g]
15	PN	3.0(–7)	Observation[h]
16	PO	9.0(–8)	Observation[h]
17	HCl	3.7(–7)	Shock-induced non-LTE abundance[e]
18	HF	7.3(–7)	TE prediction, 2[i]

[a]For species X, $f_0(X) = n(X)/n(H_2)$.
[b]Asplund et al. (2009).
[c]See Table 6 of Decin et al. (2010a).
[d]Decin et al. (2010b).
[e]Gobrecht et al. (2015).
[f]Menten et al. (2010).
[g]Gobrecht et al. (2014).
[h]De Beck et al. (2013).
[i]TE prediction, assuming elemental F has the solar abundance.

the abundance of parent species from the latest high-quality observations, otherwise those from shock-induced non-LTE abundances are adopted. Predictions from TE will only be used when no data are available from non-LTE or observational investigations. The effect of uncertainties in the abundances assumed for parent species is discussed in Sect. 4.3.12. Note that we do not simulate the chemistry in the intermediate envelope ($\lesssim$ 100 R_*) within which gas-phase chemistry may alter the abundances of parent species.

4.3 Results

4.3.1 General chemistry

Photochemistry induced by external UV photons dominates the chemistry in the expanding envelope of an AGB star. Generally, the formation and destruction processes of daughter species are controlled by the conversion XY $\rightarrow$ X $\rightarrow$ X^+, as shown in Fig. 4.3. A major finding in this work is that photoionization of molecules is also significant

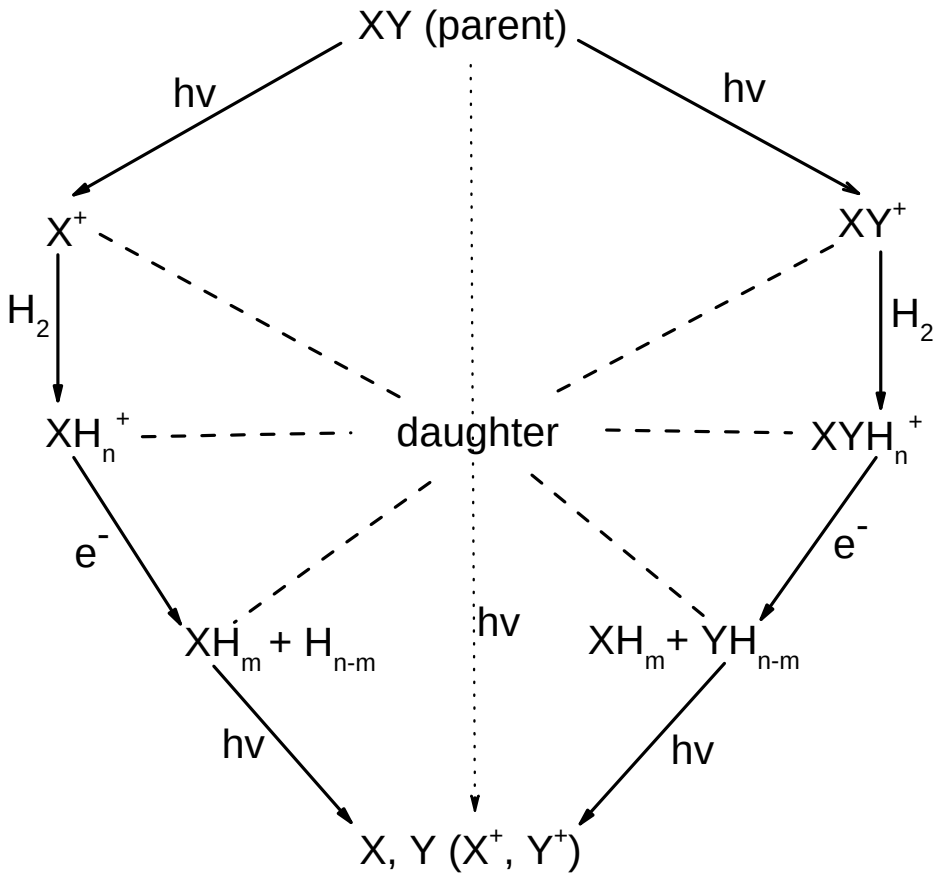

Figure 4.3 — Sketch of general pathways for parent species giving rise to daughter species in the outer CSE of an O-rich AGB star.

in the outer layers: $XY \rightarrow XY^+$. In this sense, the CSE chemistry of O-rich AGB stars differs from that found in standard photon-dominated region (PDR) models in which the ion-molecule chemistry of O-bearing species is driven by charge exchange reactions with abundant cations (see, e.g., Sternberg & Dalgarno 1995; Jansen et al. 1995a,b).

The synthesis continues with X^+ (and XY^+) abstracting H from H_2 by ion-molecule reactions forming molecular hydride cations, which is frequently followed by dissociative recombination that leads to neutral molecular hydrides, and ends up in the formation of atoms or cations at the edge of the CSE. The model predicts that negative ions are not abundant in O-rich AGB stars.

4.3.2 Impact of new N_2 and CO photodissociation rates

A proper treatment of the shielding of both N_2 and CO photodissociation has a significant impact on the chemistry in the outer CSE of AGB stars. Amongst the various shielding effects, self-shielding is the key factor in reducing the photodissociation rate of N_2 and CO (Li et al. 2014). As shown in Fig. 4.4, self-shielding of CO and N_2 becomes considerable at a large radius, around 2×10^{17} cm, where photodissociation from the external interstellar field is important. To accurately investigate the chemistry at smaller radii, we have considered full shielding (from dust, molecular H_2, atomic H, and

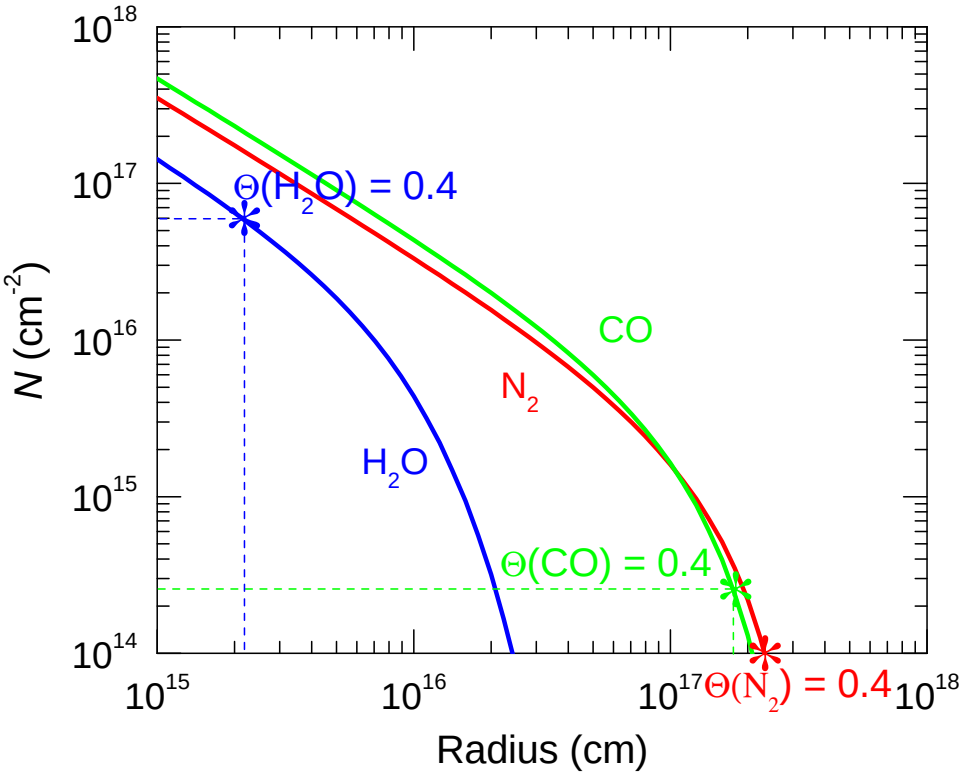

Figure 4.4 — Plot of the column densities of H_2O, CO and N_2 as a function of radius. The asterisks indicate a value of the column density that corresponds to a self-shielding factor of 0.4 for these molecules. Shielding effects become considerable when the column densities are higher than those indicated.

the molecule itself) of both N_2 and CO in all of our calculations.

Fig. 4.5 shows that the location of the transition zone from $N_2 \rightarrow$ N is shifted outwards by a factor of 7 when accurately considering shielding effects of N_2 with the SS model, whereas the location for the conversion from CO $\rightarrow C^+$ moves outwards by a factor of 2 when using updated shielding functions. These changes result in an important difference in the distributions of some daughter species whose chemistry is directly related to these species, e.g., NO and N_2H^+, as illustrated in Fig. 4.6. Other species, for instance HCN and CN, are less affected.

Another highly-abundant species, H_2O, is found to be significantly self-shielded in high abundance regions such as the planet-forming zones of circumstellar disks (Bethell & Bergin 2009). In the case of O-rich AGB stars, the self-shielding of H_2O is only considerable at radii less than 2×10^{15} cm, where the photodissociation of H_2O has not yet started to dominate its chemistry. This implies that the abundance of H_2O is too low to be self-shielded at larger radii where photodissociation becomes significant, and it is not necessary to consider self-shielding of H_2O in the CSE of AGB stars.

4.3.3 O-bearing species

The chemistry of daughter species with column densities higher than 10^{11} cm^{-2} are now discussed in different subsections based on their chemical families. To avoid repetition,

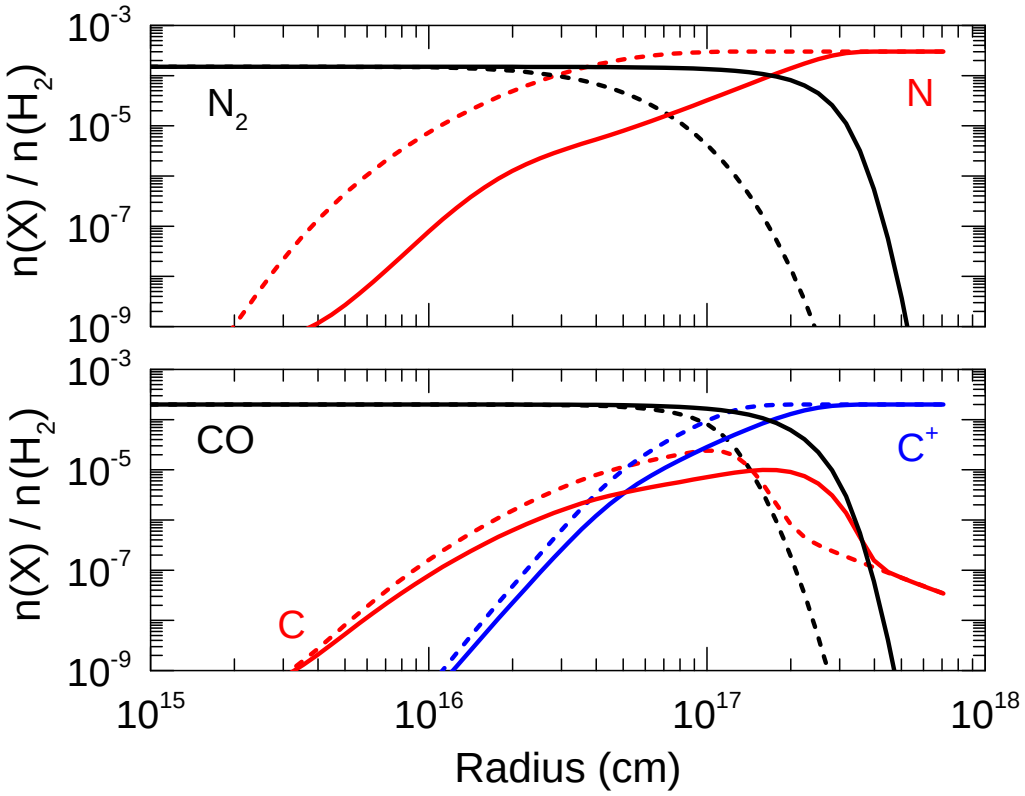

Figure 4.5 — Plot of the fractional abundances, relative to H_2, of N_2 and N (top panel), and , C^+, C, and CO (bottom panel), as a function of radius. Solid lines: from the SS model (Li et al. 2014), full shielding (dust + self- + H_2 + H) are considered using an updated N_2 photodissociation rate and self-shielding function (Li et al. 2013). Dashed lines: calculated from a model similar to that of McElroy et al. (2013) but adopting assumptions specifically for IK Tau. In this model only dust shielding is considered when calculating N_2 photodissociation, and CO self-shielding is treated only approximately.

species that can be included in multiple subsections are only discussed once. For instance, the molecule CNO, which could be discussed in the subsections of C-, O-, or N- bearing species, is only discussed in the section for N-bearing species.

The dominant chemistry for many species depends on radius, due to the large gradient in the physical conditions (i.e., visual extinction, temperatures, and gas density) in the CSEs of AGB stars. Thus, the dominating formation and destruction routes might be different in other O-rich AGB stars. In addition, different assumed abundances of parent species may lead to quite different reaction paths for the daughter species.

The most abundant O-bearing daughter species triggered by the chemistry of H_2O are OH, O_2, and H_3O^+, whose radii of peak abundances are found in the region of $(1-4)\times 10^{16}$ cm, as shown in panel (a) of Fig. 4.7. The chemistry of OH and O_2 is relatively simple, with both formed mainly via the two reactions,

$$H_2O + h\nu \rightarrow OH + H, \tag{4.2}$$
$$OH + O \rightarrow O_2 + H. \tag{4.3}$$

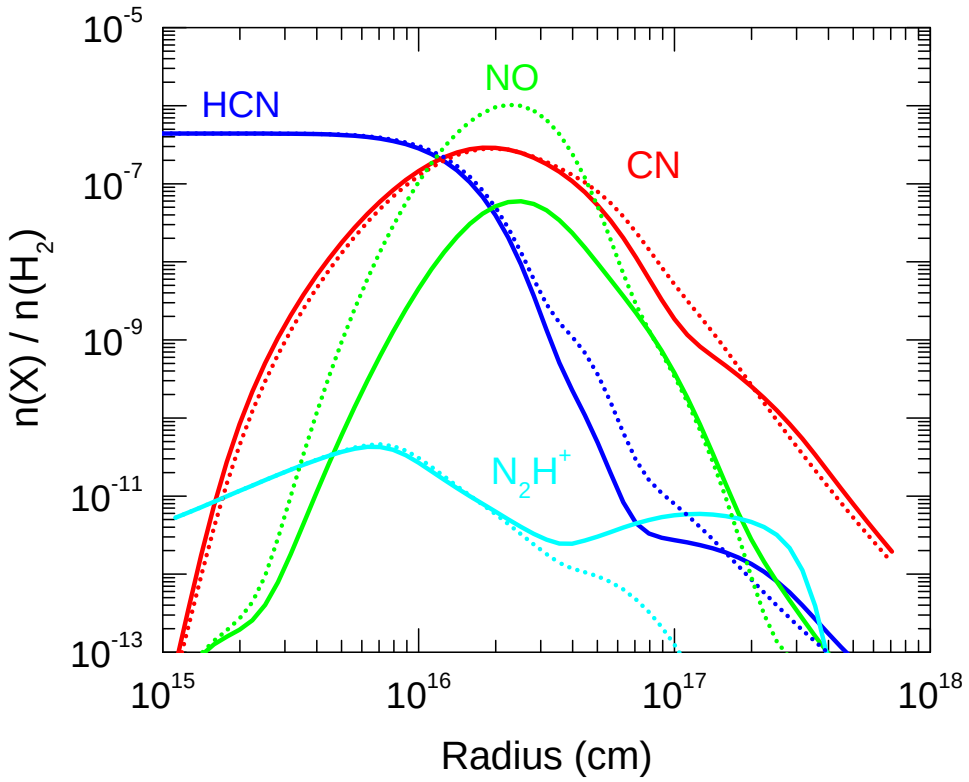

Figure 4.6 — Plot of the fractional abundances of HCN, CN, N_2H^+ and NO, relative to H_2, as a function of radius. Solid and dashed lines exhibit the results calculated from the SS model (Li et al. 2014) and that based on the updated model of McElroy et al. (2013), respectively.

H_3O^+ is mainly formed through

$$H_2O^+ + H_2 \rightarrow H_3O^+ + H, \tag{4.4}$$

where H_2O^+ comes from various routes with the relative importance depending on radius, for instance,

$$H_3^+ + O \rightarrow H_2O^+ + H, \tag{4.5}$$
$$OH^+ + H_2 \rightarrow H_2O^+ + H, \tag{4.6}$$
$$H_2O + h\nu \rightarrow H_2O^+ + e^-. \tag{4.7}$$

In the inner CSE, e.g., $\lesssim 2 \times 10^{15}$ cm, OH^+ is mainly generated by

$$He^+ + H_2O \rightarrow OH^+ + H + He, \tag{4.8}$$

where He^+ is generated by cosmic-ray ionisation. Direct OH photoionization becomes important for radii within 10^{17} cm, whilst $H_3^+ + O$ produces OH^+ at larger radii. As noted above, this is different from traditional diffuse/PDR chemistry (e.g., Gerin et al. 2010) because of the high abundance of OH here. H_3^+ is formed by the reaction between H_2 and H_2^+, where H_2^+ comes from the cosmic-ray ionization of H_2.

The destruction of most O-bearing species is dominated by photodissociation. In addition to H_2O, photodissociation of other O-bearing species, e.g., SiO, SO, CO_2, and

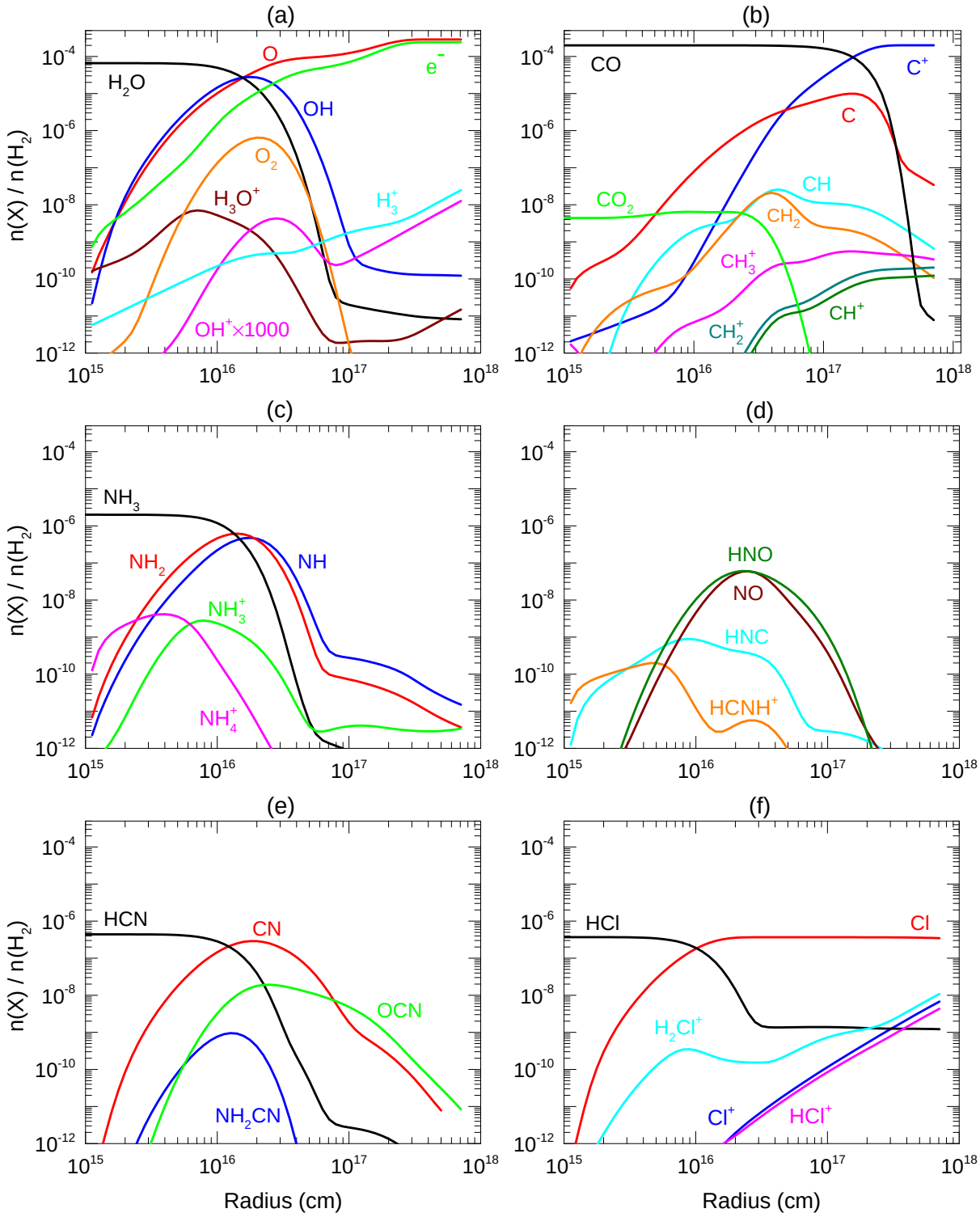

Figure 4.7 — Plot of the fractional abundances, relative to H_2, of the most abundant species in the outer CSE of the O-rich AGB star, IK Tau.

PO, amongst others, can liberate atomic oxygen at the outer edge of the CSE. CO is the key contributor at radii greater than 10^{17} cm, where A_v is less than 0.3 mag. The

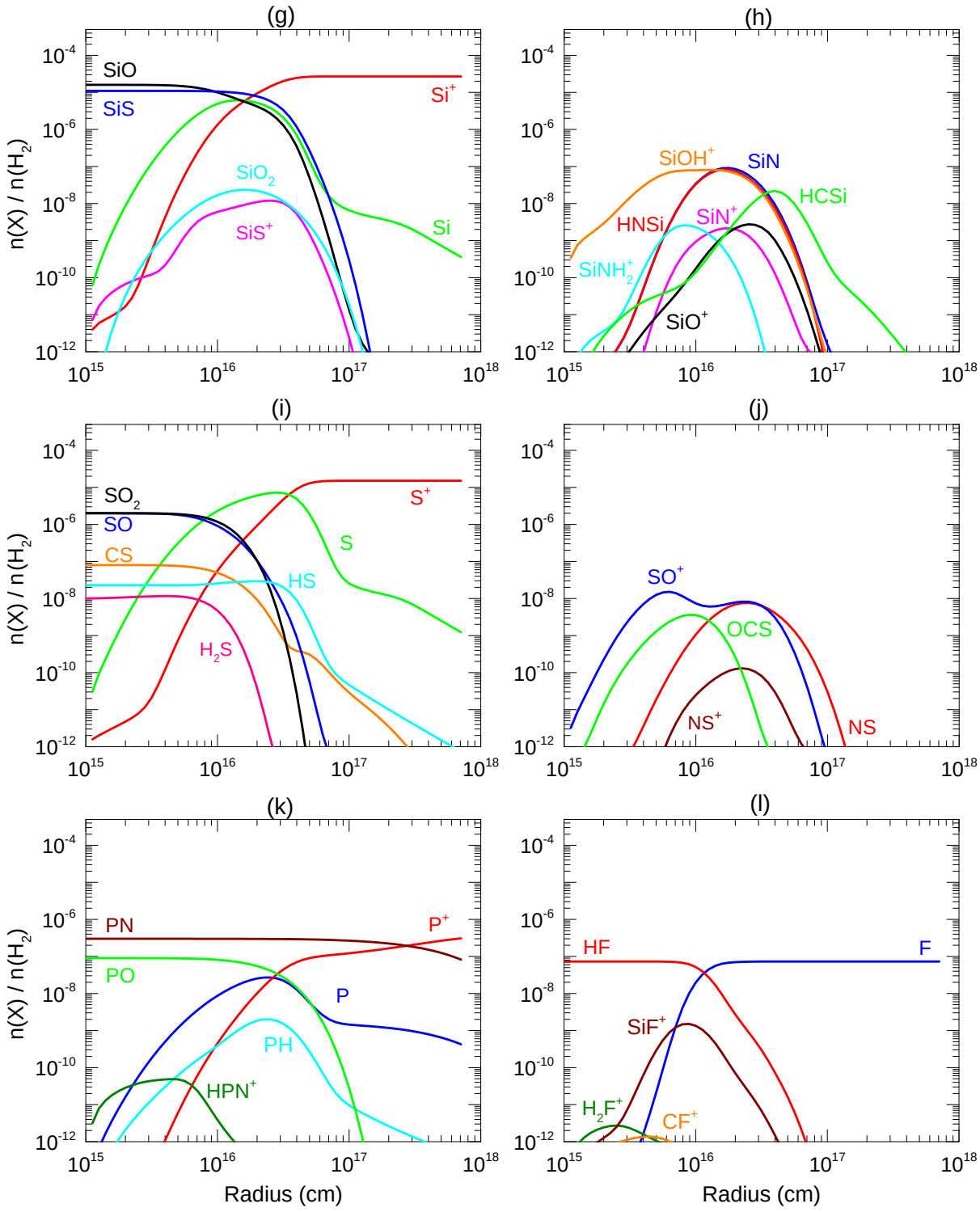

Figure 4.7 — Continued.

chemistry of CO is discussed in the following subsection. The O-bearing cations are predominantly destroyed by dissociative recombination with electrons, e.g., H_3O^+ can be

destroyed by the reaction,

$$H_3O^+ + e^- \rightarrow \text{products}. \tag{4.9}$$

The fraction of electrons is a key factor in the ion-molecule chemistry (see panel (a) of Fig. 4.7). Initially, at inner radii, e.g., $\lesssim 2 \times 10^{15}$ cm, electrons mainly arise from the cosmic-ray ionization of H_2,

$$H_2 + \text{crp} \rightarrow {H_2}^+ + e^-, \tag{4.10}$$

where crp depicts cosmic-ray particles. As the radius increases to the region where the photodissociation of H_2O becomes important, for instance, at 10^{16} cm, electrons are produced by Eq. (4.7). Further out in the CSE, e.g., 3×10^{16} cm, contributions are mainly from three channels,

$$C + h\nu \rightarrow C^+ + e^-, \tag{4.11}$$

$$S + h\nu \rightarrow S^+ + e^-, \tag{4.12}$$

$$Si + h\nu \rightarrow Si^+ + e^-. \tag{4.13}$$

At the edge of the CSE, with radius greater than 10^{17} cm, the electron density is controlled by the most abundant element, C. Further in, the electron fraction as a function of radius is significantly affected by the assumption of key parent species, especially H_2O, CO, SiS, and SiO.

4.3.4 C-bearing species

Carbon is mostly in the form of CO before it is converted into C^+ at the edge of the envelope (panel (b) of Fig. 4.7). The CO $\rightarrow$ C $\rightarrow$ C^+ conversion controls the carbon chemistry. The non-self-shielding parent species, CO_2, is less abundant and photodissociates from a radius of 3×10^{16} cm outwards. Four carbon compounds, CH, CH_2, ${CH_3}^+$, and ${CH_2}^+$ are found to be quite abundant, and are distributed at radii greater than 3×10^{16} cm, where the temperature is less than 50 K (in our model, $\sim$ 10 K, see Fig. 4.2). Therefore, their emission would only be detectable from low rotational energy levels.

The formation of CH_2 varies with radius. For instance, at 3×10^{16} cm, it is mainly formed by

$${SiCH_2}^+ + e^- \rightarrow Si + CH_2, \tag{4.14}$$

The chemistry of ${SiCH_2}^+$ is discussed in Sect. 4.3.6. At 10^{17} cm, CH_2 is mainly produced by

$${CH_3}^+ + e^- \rightarrow CH_2 + H. \tag{4.15}$$

In both cases, CH is formed through

$${CH_3}^+ + e^- \rightarrow CH + H_2, \tag{4.16}$$

whereas ${CH_3}^+$ arises from the following process at all radii,

$${CH_2}^+ + H_2 \rightarrow {CH_3}^+ + H. \tag{4.17}$$

CH_2^+ is generated through multiple channels, by

$$C^+ + H_2 \rightarrow CH_2^+ + h\nu, \tag{4.18}$$
$$CH^+ + H_2 \rightarrow CH_2^+ + H, \tag{4.19}$$

and

$$CH_2 + h\nu \rightarrow CH_2^+ + e^-. \tag{4.20}$$

In the above reactions, the majority of CH^+ is produced via the photoionization of CH, and is destroyed by Eq. (4.19) at all radii. The destruction of the neutral carbon hydrides, CH and CH_2, is dominated by photodissociation whereas that of most cations, e.g., CH_3^+, is via dissociative recombination. Interestingly, the destruction of CH_2^+ is dominated by Eq. (4.17), rather than electrons. The chemistry of four other C-bearing species, namely C_2, C_2H, CH_3OH, and HCO^+, are discussed in Sect. 4.3.12.

4.3.5 N-bearing species

The chemistry of the parent species ammonia, NH_3, controls the distribution of most N-bearing species, amongst which eight are found above the 10^{-11} abundance threshold (panel (c) of Fig. 4.7). These species are mainly located at radii between 5×10^{15} and 5×10^{16} cm from the star. The most abundant daughter species generated by NH_3 are NH_2 and NH, which have peak fractional abundances around 10^{-6}. In analogy with the corresponding oxygen and carbon species, NH_2 is produced by the photodissociation of NH_3 at radii less than its peak radius, 2.2×10^{16} cm, whereas dissociative recombination of NH_3^+ with e^- dominates at greater radii. NH is the product of the photodissociation of NH_3 and NH_2 throughout the entire CSE, but with a significant contribution from the reaction between NH_3^+ and e^- when the radius is greater than 1×10^{17} cm.

The relatively abundant cation, NH_3^+, is mainly formed through the photoionization of NH_3 for radii inside its peak abundance, and by the reaction between NH_2^+ and H_2 at greater radii. NH_2^+ comes from the photoionization of NH_2 and reactions between NH^+ and H_2. The chemistry of NH_4^+ is less complex, and forms mainly via the reaction between NH_3^+ and H_2. Only at very inner radii, e.g., 2×10^{15} cm, is it formed by the reaction of NH_3 and H_3O^+.

The chemistry of NH_3 also gives rise to other N-bearing species, such as HNO, NO, HNC and $HCNH^+$ (panel (d) of Fig. 4.7) at radii between $10^{16} - 10^{17}$ cm. First, the breaking down of NH_3 generates NH_2, which reacts with atomic O and produces HNO. Then, HNO is photodissociated to NO. The formation channels of NO vary with radius, e.g., a non-negligible amount of NO is formed from the reaction between N and OH in the inner regions $\leq 2 \times 10^{15}$ cm, and by OCN + O at radii greater than 5×10^{17} cm.

Throughout the CSE, HNC is mainly produced via $HCNH^+$, in the following two reactions

$$HCNH^+ + NH_3 \rightarrow HNC + NH_4^+, \tag{4.21}$$

and

$$HCNH^+ + e^- \rightarrow HNC + H. \tag{4.22}$$

The formation of $HCNH^+$ is complex. At radii less than 10^{16} cm, it is mainly formed via the reaction between H_3O^+ and HCN. However, at larger radii, it is entirely formed via

$$HCN^+ + H_2 \rightarrow HCNH^+ + H, \tag{4.23}$$

where HCN^+ is the product of reactions between $C^+ + NH_2$, and $CN^+ + H_2$. CN^+ comes from the reaction between C^+ and NH. Therefore, HCN contributes most to the formation of HNC in the inner regions whereas NH_3 plays the most important role in the outer regions.

Another important N-bearing parent species, HCN, controls the chemistry of CN, OCN, and NH_2CN (panel (e) of Fig. 4.7). In our model, HCN starts to photodissociate at a radius of 10^{16} cm, breaking down into its daughter species, CN. Note that there are other routes leading to the formation of CN at its peak radius, i.e., the photodissociation of HNC, and the reaction between OCN and H. Its destruction at large radii is simply dominated by photodissociation.

The species OCN is mainly formed via

$$OH + CN \rightarrow OCN + H \tag{4.24}$$

at radii less than 8×10^{16} cm, whereas dissociative recombination dominates its formation at greater radii, via

$$HNCO^+ + e^- \rightarrow OCN + H \tag{4.25}$$

and

$$HOCN^+ + e^- \rightarrow OCN + H \tag{4.26}$$

with assumed-equal reaction rate constants, $1.5 \times 10^{-7}\,cm^3\,s^{-1}$. However, $HNCO^+$ and $HOCN^+$ are totally formed by the reaction between OCN and $H_3{}^+$ (with a reaction rate constant of $1.6 \times 10^{-8}\,cm^3\,s^{-1}$) and so comprise a cyclic formation pathway and not the dominant route to OCN bond formation. The rates for the above reactions are adopted from Quan et al. (2010), where more detailed discussions about these species can be found.

The chemistry of NH_2CN is dependent on both NH_3 and HCN. This species is simply formed by the following reaction,

$$NH_3 + CN \rightarrow NH_2CN + H. \tag{4.27}$$

and destroyed by photodissociation,

$$NH_2CN + h\nu \rightarrow NH_2 + CN. \tag{4.28}$$

4.3.6 Si-bearing species

The photodissociation/photoionization processes of parent species, SiO/SiS $\rightarrow$ Si $\rightarrow$ Si^+, control the silicon chemistry and gives rise to other Si-bearing species (panels (g) and (h) of Fig. 4.7). Similar to N-bearing species, most silicon compounds have peak abundances for radii between 10^{16} and 10^{17} cm. In total, seven high-abundance daughter molecules are found: SiS^+, SiO_2, $SiOH^+$, SiN, HNSi, SiN^+ and $SiNH_2{}^+$.

In the inner layers, at radii smaller than 2×10^{16} cm, the abundance of Si is higher than Si^+ and its formation is dominated by the photodissociation of SiO. As the distance from the star increases, Si is photoionized to form Si^+, and therefore contributes to the electron density. SiS^+ comes from SiS, via charge exchange

$$SiS + S^+ \rightarrow SiS^+ + S, \tag{4.29}$$

around its peak radius, and by the reaction between C^+ and SiS in other regions. Its destruction is dominated by

$$SiS^+ + e^- \rightarrow Si + S. \tag{4.30}$$

The presence of OH at a high abundance ($\sim 10^{-5}$) generates a significant abundance of $SiOH^+$ in an O-rich CSE,

$$Si^+ + OH \rightarrow SiO^+ + H, \tag{4.31}$$
$$SiO^+ + H_2 \rightarrow SiOH^+, \tag{4.32}$$

which is destroyed by dissociative recombination in the outer layers,

$$SiOH^+ + e^- \rightarrow Si + OH, \tag{4.33}$$
$$SiOH^+ + e^- \rightarrow SiO + H. \tag{4.34}$$

Reactions (4.31) and (4.32) dominate the formation and destruction of SiO^+. Similarly, the parent species NH_3 generates NH, then increases the abundance of SiN^+, which is formed and destroyed via the following processes at all radii

$$NH + Si^+ \rightarrow SiN^+ + H, \tag{4.35}$$
$$SiN^+ + e^- \rightarrow Si + N. \tag{4.36}$$

$SiNH_2{}^+$ is formed and destroyed in a very similar way, via

$$NH_3 + Si^+ \rightarrow SiNH_2{}^+ + H, \tag{4.37}$$
$$SiNH_2{}^+ + e^- \rightarrow SiN + H_2, \tag{4.38}$$
$$SiNH_2{}^+ + e^- \rightarrow HNSi + H. \tag{4.39}$$

The chemistry of SiO_2 is triggered by SiO, via the following reaction throughout the envelope,

$$SiO + OH \rightarrow SiO_2 + H. \tag{4.40}$$

SiN is mainly generated by Eq. (4.38) within 10^{16} cm, but from the photodissociation of HNSi at greater radii. At all radii, HNSi is produced by Eq. (4.39). The destruction of all of these neutral silicon compounds is dominated by photodissociation, although their actual rates are quite uncertain and are experimentally difficult to measure.

The species HCSi peaks at a relatively larger radius, 4×10^{16} cm, arising from SiS, through

$$\mathrm{SiS} + \mathrm{C}^+ \rightarrow \mathrm{SiC}^+ + \mathrm{S}, \tag{4.41}$$
$$\mathrm{SiC}^+ + \mathrm{H_2} \rightarrow \mathrm{HCSi}^+ + \mathrm{H}, \tag{4.42}$$
$$\mathrm{HCSi}^+ + \mathrm{H_2} \rightarrow \mathrm{SiCH_2}^+ + \mathrm{H}, \tag{4.43}$$

and

$$\mathrm{SiCH_2}^+ + \mathrm{e}^- \rightarrow \mathrm{HCSi} + \mathrm{H}, \tag{4.44}$$

and is dissociated by UV photons.

4.3.7 S-bearing species

The conversion from the parents $\mathrm{SO_2/SO/SiS} \rightarrow \mathrm{S} \rightarrow \mathrm{S}^+$ in the CSE is the key to the sulphur chemistry (panels (i) and (j) of Fig. 4.7). The increase in atomic S is caused by the photodissociation of SO and $\mathrm{SO_2}$ (first releasing SO then S) at radii less than 10^{16} cm, with a contribution from the breaking down of SiS at larger radii, $\geq 3 \times 10^{16}$ cm. Beyond this point, S is converted into S^+ by photoionization. The less abundant parent species, $\mathrm{H_2S}$ and HS, play a less important role in the chemical network.

In total, we find four abundant daughter species. At all radii, OCS is formed via

$$\mathrm{CS} + \mathrm{OH} \rightarrow \mathrm{OCS} + \mathrm{H}, \tag{4.45}$$

and NS is formed via

$$\mathrm{NH} + \mathrm{S} \rightarrow \mathrm{NS} + \mathrm{H}. \tag{4.46}$$

Similar to other neutral species, the destruction of OCS and NS is dominated by photodissociation. NS^+ has a relatively low abundance, coming from NH reacting with S^+. Like most cations, it is destroyed by dissociative recombination. SO^+ is produced by the following two reactions,

$$\mathrm{SO} + \mathrm{h}\nu \rightarrow \mathrm{SO}^+ + \mathrm{e}^-, \tag{4.47}$$
$$\mathrm{OH} + \mathrm{S}^+ \rightarrow \mathrm{SO}^+ + \mathrm{H}, \tag{4.48}$$

and, again, is destroyed by dissociative recombination.

4.3.8 P-bearing species

PN and PO are the two phosphorus-bearing parent species in our model. The conversion process $\mathrm{PN/PO} \rightarrow \mathrm{P} \rightarrow \mathrm{P}^+$, which is dominated by the photodissociation and photoionization, controls the the phosphorus chemistry (panel (h) in Fig. 4.7). Our model produces a significant and likely unrealistic abundance of PN at very large radii where all other molecular species have been destroyed by the interstellar radiation field. This is due to the neglect of PN photoionisation in the Rate12 reaction network despite the low ionisation threshold of this molecule (Wu & Fehlner 1975) and a photoabsorption cross section that is likely to be comparable to that of electronically-similar CO and $\mathrm{N_2}$.

Two species, HPN^+ and PN, are found to be abundant. HPN^+ is mainly formed via

$$H_3O^+ + PN \rightarrow HPN^+ + H_2O, \tag{4.49}$$

and destroyed by three channels assumed to have equal branching ratios,

$$HPN^+ + e^- \rightarrow PH + N, \tag{4.50}$$
$$HPN^+ + e^- \rightarrow P + NH, \tag{4.51}$$
$$HPN^+ + e^- \rightarrow PN + H. \tag{4.52}$$

PH arises from Eq. (4.50) at radii smaller than 1×10^{16} cm. Contribution from the routes

$$H_2O + P^+ \rightarrow HPO^+ + H, \tag{4.53}$$
$$HPO^+ + e^- \rightarrow PH + O, \tag{4.54}$$

becomes most important as the radius increases. Its destruction is dominated by photodissociation.

4.3.9 Cl-bearing species

The chemistry of Cl-bearing species is initiated by the photodissociation of the parent species, HCl (panel (f) of Fig. 4.7). The most abundant Cl-bearing daughter molecule in this model is H_2Cl^+. The breakdown of HCl leads to two species,

$$HCl + h\nu \rightarrow Cl + H, \tag{4.55}$$
$$HCl + h\nu \rightarrow HCl^+ + e^-, \tag{4.56}$$

At all radii, ∼90% of HCl goes to Eq. (4.55) whereas ∼10% goes to Eq. (4.56). H_2Cl^+ is formed via

$$HCl^+ + H_2 \rightarrow H_2Cl^+ + H. \tag{4.57}$$

and destroyed by

$$H_2Cl^+ + e^- \rightarrow Cl + H_2. \tag{4.58}$$

The cation, Cl^+, arises from the photoionization of Cl. It is worth mentioning that H_2Cl^+, HCl^+, and H_2O^+ have been detected by the *H*erschel space observatory in the diffuse interstellar medium (e.g. Gerin et al. 2010; Lis et al. 2010; De Luca et al. 2012; Neufeld et al. 2012; Gerin et al. 2013). Another Cl-bearing species, NaCl, has been found in IK Tau with an abundance of 4×10^{-9} (Milam et al. 2007). Unfortunately we don't have the chemistry of Na-bearing species in our network, thereby an extension of the chemical network would be useful for a further understanding of the chlorine chemistry. Our model shows that the abundance of CCl^+ is negligible and is not shown in the plot.

4.3.10 F-bearing species

This is the first time that F-chemistry is included in a CSE model of an O-rich AGB star. The photodissociation of the parent species, HF, liberates atomic F and gives rise to other F-bearing species (panel (l) of Fig. 4.7). Three daughter species, SiF^+, CF^+, and H_2F^+ are found to be most abundant. In particular, SiF^+ has not been detected in the ISM due to the the depleted elemental abundance of silicon. However, we predict that it may be detectable in IK Tau at a radius of $(2-4)\times10^{16}$ cm. At all radii, SiF^+ and CF^+ are formed by the reactions,

$$HF + Si^+ \rightarrow SiF^+ + H, \tag{4.59}$$
$$HF + C^+ \rightarrow CF^+ + H, \tag{4.60}$$

and are destroyed by

$$SiF^+ + e^- \rightarrow Si + F, \tag{4.61}$$
$$CF^+ + e^- \rightarrow C + F. \tag{4.62}$$

H_2F^+ is formed via two routes,

$$HF + {H_3}^+ \rightarrow H_2F^+ + H_2, \tag{4.63}$$
$$HF^+ + H_2 \rightarrow H_2F^+ + H, \tag{4.64}$$

where HF^+ arises from

$$He^+ + HF \rightarrow F^+ + He + H, \tag{4.65}$$

and

$$F^+ + H_2 \rightarrow HF^+ + H. \tag{4.66}$$

The destruction of H_2F^+ is dominated by

$$H_2F^+ + e^- \rightarrow F + H_2, \tag{4.67}$$

and

$$H_2F^+ + e^- \rightarrow HF + H. \tag{4.68}$$

4.3.11 Comparison with observations

The calculated fractional abundances, peak radii, and total column densities of the top 36 daughter species in IK Tau are presented in Table 4.3. Observational information is only available for CN and HCO^+. For CN, the calculated peak abundance, total column density, and peak radius are in good agreement with the observations from Kim et al. (2010) and Decin et al. (2010a). For HCO^+, the calculated peak radius is in excellent agreement with the observations of Pulliam et al. (2011), but the fractional abundance and total column density are orders-of-magnitude lower than the observations. This will be discussed in the following section. The calculated total column densities of a few parent

Table 4.3 — Calculated total column densities, peak abundances (relative to H_2), and peak radii of the daughter molecules in the CSE of the O-rich AGB star, IK Tau.

No.	Species	$N_{\rm total}$ ($\rm cm^{-2}$)	Peak abundance	Peak radius (cm)
1	OH	5.4(15)	2.8(–5)	1.8(16)
2	C	4.0(14)	9.9(–6)	1.6(17)
3	NH_2	1.4(14)	6.2(–7)	1.4(16)
4	NH	8.2(13)	4.8(–7)	1.8(16)
5	O_2	7.8(13)	6.5(–7)	2.0(16)
6	CN	5.8(13)	2.9(–7)[a]	1.8(16)
7	$SiOH^+$	4.0(13)	8.1(–8)	1.3(16)
8	SiN	1.3(13)	9.1(–8)	1.8(16)
9	HNSi	1.2(13)	8.2(–8)	1.6(16)
10	HNO	7.9(12)	6.1(–8)	2.2(16)
11	SO^+	6.6(12)	1.5(–8)	6.3(15)
12	NO	5.9(12)	6.0(–8)	2.5(16)
13	SiO_2	5.9(12)	2.4(–8)	1.6(16)
14	NH_4^+	3.7(12)	4.1(–9)	4.0(15)
15	SiC	3.3(12)	6.7(–8)	4.5(16)
16	H_3O^+	3.0(12)	7.1(–9)	7.1(15)
17	OCN	2.7(12)	1.9(–8)	2.5(16)
18	SiS^+	2.4(12)	1.2(–8)	2.5(16)
19	CH	2.0(12)	2.6(–8)	4.5(16)
20	CH_2	1.2(12)	2.1(–8)	4.0(16)
21	HCSi	1.1(12)	2.2(–8)	4.0(16)
22	OCS	1.1(12)	3.6(–9)	8.9(15)
23	NS	9.1(11)	7.6(–9)	2.5(16)
24	NH_3^+	8.9(11)	2.8(–9)	7.9(15)
25	$SiNH_2^+$	6.5(11)	2.6(–9)	7.9(15)
26	HNC	3.9(11)	8.9(–10)	8.9(15)
27	SiF^+	3.3(11)	1.5(–9)	8.9(15)
28	SiN^+	3.2(11)	2.2(–9)	1.8(16)
29	PH	2.7(11)	2.0(–9)	2.5(16)
30	H_3^+	2.5(11)	2.5(–8)	7.1(17)
31	SiO^+	2.5(11)	2.7(–9)	2.5(16)
32	C_2	2.3(11)	7.6(–9)	6.3(16)
33	NH_2CN	1.9(11)	9.5(–10)	1.3(16)
34	$HCNH^+$	1.8(11)	2.0(–10)	5.0(15)
35	H_2Cl^+	1.7(11)	1.1(–8)	7.1(17)
36	HCO^+	1.6(11)[b]	4.0(–10)[c]	2.5(16)[c]

[a]Observationally, Decin et al. (2010a) obtained 2(-10) − 6(-8), whereas Kim et al. (2010) deduced two values, 5.1(-8) or 1.6(-7), corresponding to two cases where two different radii of CN were assumed in their models.

[b]Observationally, Edwards et al. deduced 1.0(13) $\rm cm^{-2}$ (Priv. Comm.)

[c]Observationally, Pulliam et al. (2011) obtained a peak abundance of 4.4(-8) at radius 3.9(16) cm.

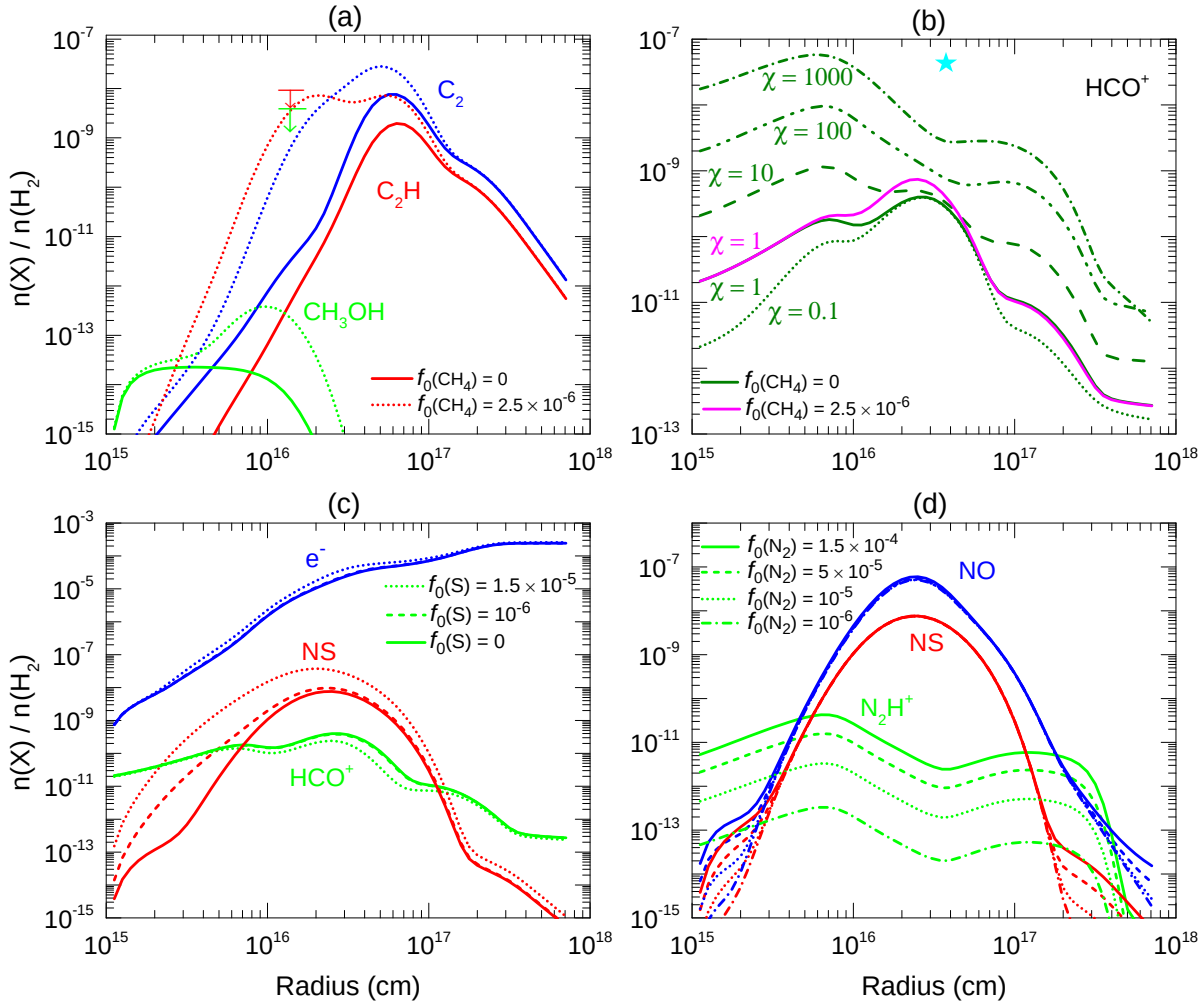

Figure 4.8 — Plot of the fractional abundances of some daughter species as a function of radius, calculated using different initial fractions of CH_4 (panels a and b), atomic S (panel c), and N_2 (panel d), in addition to various cosmic-ray rates. In panel (a): the arrows depict the upper limits of C_2H (red) and CH_3OH (green) deduced in the observational work of Marvel (2005), where the peak radii of these species was assumed to be 1.5×10^{16} cm. In panel (b): χ is the scaling factor of the cosmic-ray ionisation rate and the star indicates the observational result from Pulliam et al. (2011).

species, such as HCN, CS, SiS, SiO, SO, and SO_2, are also compared to the observational results (Kim et al. 2010). Agreements are within a factor of 10 demonstrating that the parent species' abundances are not altered significantly by gas-phase chemistry *en route* through the inner region of the outer envelope. However, note that we have neglected gas-phase chemical processing through the intermediate envelope which may also affect the parent species' abundances. A thorough comparison with observations requires calculations of the excitation and radiative transfer to compute line intensities rather than column densities, which is beyond the scope of the present work.

4.3.12 Sensitivities to the initial abundances

The assumed abundance of parent species is of particular importance for the predicted distribution and abundance of daughter species. The identification and abundance of most of these species at inner radii can be well constrained by both observations and theoretical models. However, the initial abundances of some parent species, e.g., N_2, remain unclear. In addition, there is some discussion in the literature concerning the presence of additional species, e.g., atomic S and CH_4, in the inner envelope with non-negligible abundances (see, e.g., Willacy & Millar 1997; Cherchneff 2006). A possible solution for inferring the presence and abundance of these species is via a few relevant daughter species.

Methane (CH_4) is not assumed to be a parent species in the current study, based on the conclusions from the observational work of Marvel (2005), where the upper limits on abundances for C_2H and CH_3OH (methanol) were deduced to be 9.7×10^{-9} and 4.5×10^{-9}, respectively. Gobrecht et al. (2014) also find that CH_4 is not formed efficiently via gas-phase chemistry in the inner wind ($r \lesssim 10R_*$) in their model of IK Tau. Our model results are in general agreement with these conclusions. In the earlier photochemical model of Willacy & Millar (1997), CH_4 was assumed to be a parent molecule with a large fractional abundance, 3.0×10^{-5}, to explain the chemistry of a few carbon species, especially the unexpected presence of HCN in O-rich envelopes. At that time HCN was thought to be a daughter species and formed via reactions between atomic N, CH_2 and CH_3, which are photoproducts of N_2 and CH_4. The presence of CH_4 as a parent also significantly increases the fractions of both C_2H and CH_3OH, by which one can constrain the upper limits for methane.

We find that the maximum abundance of CH_4 in the O-rich AGB star, IK Tau, is 2.5×10^{-6}, in order to be consistent with the observed upper limit for the C_2H abundance, see panel (a) of Fig. 4.8. Regardless of including or excluding CH_4 as a parent molecule in the model, the predicted CH_3OH is at least 5 orders of magnitude lower than its observational upper limit, peaking at radii between $10^{15} - 10^{16}$ cm. One of the most important channels for CH_3OH formation is via

$$CH_3^+ + H_2O \rightarrow CH_3OH_2^+ + h\nu, \tag{4.69}$$
$$CH_3OH_2^+ + e^- \rightarrow CH_3OH + H, \tag{4.70}$$

where the chemistry of CH_3^+ is discussed in Sect. 4.3.4. Note that in dense interstellar clouds, CH_3OH is mainly formed on grain surfaces (Watanabe & Kouchi 2002; Garrod & Herbst 2006; Geppert et al. 2006; Fuchs et al. 2009) which is neglected here, however, the physical conditions in the CSE are not amenable to ice formation. Typically, ices exist in regions where $A_v > 1$ which corresponds to the high temperature region (> 600 K) in our model of IK Tau, see Fig. 4.2. Nevertheless, our results for gas-phase methanol are well within the observed upper limit from Marvel (2005).

At the radii where C_2 possesses its peak abundance, it mainly arises from

$$C^+ + SiC \rightarrow Si^+ + C_2. \tag{4.71}$$

C_2H can be formed via multiple channels, amongst which the following routes contribute

most,

$$\mathrm{C_2} + \mathrm{h}\nu \rightarrow \mathrm{C_2}^+ + \mathrm{e}^-, \tag{4.72}$$
$$\mathrm{C_2}^+ + \mathrm{H_2} \rightarrow \mathrm{C_2H}^+ + \mathrm{H}, \tag{4.73}$$
$$\mathrm{C_2H}^+ + \mathrm{H_2} \rightarrow \mathrm{C_2H_2}^+ + \mathrm{H}, \tag{4.74}$$
$$\mathrm{C_2H_2}^+ + \mathrm{e}^- \rightarrow \mathrm{C_2H} + \mathrm{H}. \tag{4.75}$$

HCO^+ has been detected in IK Tau, with an abundance of 4.4×10^{-8} at a radius of 3.9×10^{16} cm (Pulliam et al. 2011). The current model gives a peak radius that is in excellent agreement with this observation, but produces a lower abundance of HCO^+. This is the case even where the cosmic-ray ionisation rate of $\mathrm{H_2}$ is increased with respect to its standard value in our models of $1.2 \times 10^{17}\,\mathrm{s}^{-1}$ by a scaling factor, χ, up to a value of $\times 1000$. The inclusion of the maximum amount of $\mathrm{CH_4}$ consistent with observations, 2.5×10^{-6}, only increases HCO^+ by a minor amount, see panel (b) of Fig. 4.8. Another model assuming a higher abundance for the initial CO only slightly enhances the peak abundance of HCO^+. At the radius of its peak abundance, i.e., 3×10^{16} cm, HCO^+ is mainly formed from C^+ with CO^+ and HOC^+ as intermediates via the reactions

$$\mathrm{C}^+ + \mathrm{OH} \rightarrow \mathrm{CO}^+ + \mathrm{H}, \tag{4.76}$$
$$\mathrm{CO}^+ + \mathrm{H_2} \rightarrow \mathrm{HOC}^+ + \mathrm{H}, \tag{4.77}$$
$$\mathrm{CO}^+ + \mathrm{H_2} \rightarrow \mathrm{HCO}^+ + \mathrm{H}, \tag{4.78}$$
$$\mathrm{C}^+ + \mathrm{H_2O} \rightarrow \mathrm{HOC}^+ + \mathrm{H}, \tag{4.79}$$
$$\tag{4.80}$$

and

$$\mathrm{HOC}^+ + \mathrm{H_2} \rightarrow \mathrm{HCO}^+ + \mathrm{H_2}. \tag{4.81}$$

Only a minor amount (10%) of HCO^+ is formed by the reaction between C^+ and $\mathrm{H_2O}$. If the abundance of parent species in our model photodissociating to form C^+ is increased then a minor enhancement of HCO^+ results. The destruction of HCO^+ at its peak location is controlled only by the reaction

$$\mathrm{HCO}^+ + \mathrm{e}^- \rightarrow \mathrm{CO} + \mathrm{H}. \tag{4.82}$$

The peak abundance of HCO^+ may also be enhanced by the inclusion of the neutral analogue, HCO, as a parent species. A potential route to HCO in the inner CSE is via the reaction between H and CO with a third body (see, e.g., Baulch et al. 2005). The backwards reaction has a large energy barrier ($\approx$ 8000 K Baulch et al. 2005); hence, potentially leading to appreciable abundances of HCO. The inclusion of HCO formation and destruction in models of the inner CSE of O-rich AGB stars are worth investigating in the future.

The electron abundance, which has been discussed in Sect. 4.3.3, is the most significant factor in destroying many cations. The C-, S-, and Si-bearing parent species contribute most to the formation of electrons, depending on the radius. However, the abundances of

C and Si related species are strongly constrained as discussed in Sect. 4.2.2 and here we only explore the effect of the uncertainty introduced by the unknown amount of atomic S amongst the parent species.

In our fiducial model we exclude atomic S as a parent species. However, the shock-induced non-LTE simulation of Cherchneff (2006) suggested that most elemental S is in atomic form for O-rich AGB stars, which was further confirmed in the latest simulations specifically focussing on IK Tau (Cherchneff, Priv. Comm.). Since the solar abundance of elemental S relative to H_2 is 2.6×10^{-5} (Asplund et al. 2009), and we have 1.1×10^{-5} in SiS in our model (see Table 4.2), we assume the maximum amount of S in the inner CSE to be 1.5×10^{-5}. As can be seen in panel (c) of Fig. 4.8, the uncertainty of including or excluding atomic S has a minor effect on the total abundance of electrons, and therefore on HCO^+. Interestingly, NS is found to be sensitive to the initial abundance of atomic S, and may be useful as a diagnostic measurement. More interestingly, as can be seen in panel (d) of Fig. 4.8, both NS and NO are hardly affected by the initial N_2 abundance. It is hard to detect N_2 directly, but it can be indirectly constrained by the abundance of N_2H^+, which is mainly formed via the reaction

$$N_2 + H_3{}^+ \rightarrow N_2H^+ + H_2. \tag{4.83}$$

At larger radii, e.g., 10^{17} cm, its formation is dominated by

$$N_2 + He^+ \rightarrow N_2{}^+ + He, \tag{4.84}$$

$$N_2{}^+ + H_2 \rightarrow N_2H^+ + H, \tag{4.85}$$

where the He^+ is generated by cosmic-ray ionization. In all situations, the abundance of N_2H^+ is directly related to the initial abundance of N_2, but this species has not yet been detected in the CSEs of AGB stars.

4.4 Concluding remarks

We simulated the chemistry in O-rich circumstellar envelopes of AGB stars. We have calculated radial abundances suitable for guiding future observational studies and identified the most abundant species. Our model includes the latest gas-phase reaction network and photodissociation processes, including a spectroscopically realistic treatment of N_2 and CO self-shielding. The H_2O column is found to be too low to self shield. With the proper self-shielding factors, the $N \rightarrow N_2$ and $C^+ \rightarrow CO$ transitions are shifted outward by factors of 7 and 2, respectively, in the fiducial model representing IK Tau. We also adopt a selection of precursor parent species based on observations and the latest non-LTE model of the interior CSE of IK Tau.

There are few quantitative observational constraints on the molecular abundances in IK Tau but based on our experience with the C-rich CSE surrounding IRC +10216 (Li et al. 2014) we expect order-of-magnitude accuracy for our predictions of C-, N-, O-, and Si-bearing molecules. The reaction networks for less-abundant elements (S, P, Cl, and F) are not as well known but significant abundances of their host molecules are predicted by our model. Many molecules have peak abundance between 10^{16} to 10^{17} cm from the star where the ionisation and dissociation of parent species provides a source

of radicals but where molecules are still somewhat shielded from interstellar radiation. Key steps in the intervening chemistry are hydrogen abstraction of radical ions with H_2 and the production of neutral fragments by dissociative recombination and the ultimate destruction of all molecules by the ISRF.

We find chemical links between potentially-observable daughter molecules and the abundances of parent species in the inner CSE. Observationally-derived upper limits for the amount of C_2H and CH in IK Tau provide a low constraint on the relative abundance of the potential parent CH_4, $< 2.5 \times 10^{-6}$. We also find that observations of NS and N_2H^+ could provide indirect constraints on the parent abundances of atomic S and N_2.

Our modelled molecular abundances are also sensitive to the assumed physical parameters of the CSE. We find that the stellar mass-loss rate, which is usually not straightforward to obtain from observations, has a large impact on the calculated abundances. On the other hand, variations in the envelope expansion velocity and cosmic-ray ionisation rate are not as significant (see the Appendix).

Many of the predictions of our models (both overall abundances and peak abundance radii) can be tested directly by spatially resolved observations with ALMA in the near future.

Acknowledgements

X. Li thanks TJM for his hospitality during a two-week visit to Queen's University Belfast (QUB) in 2014, and thanks Profs. Xander Tielens and Leen Decin for some stimulating discussion. X. Li also would like to thank Drs. Jessica Edwards and Robin Pulliam for the discussion on HCO^+ in IK Tau.

Astrochemistry in Leiden is supported by the Netherlands Research School for Astronomy (NOVA), by a Spinoza grant and grant 648.000.002 from the Netherlands Organisation for Scientific Research (NWO), and by the European Community's Seventh Framework Programme FP7/2007-2013 under grant agreements 291141 (CHEMPLAN) and 238258 (LASSIE). Astrophysics at QUB is supported by a grant from the STFC. C. W. acknowledges support from NWO (program number 639.041.335).

4.5 Appendix: An extended investigation of the CSE species

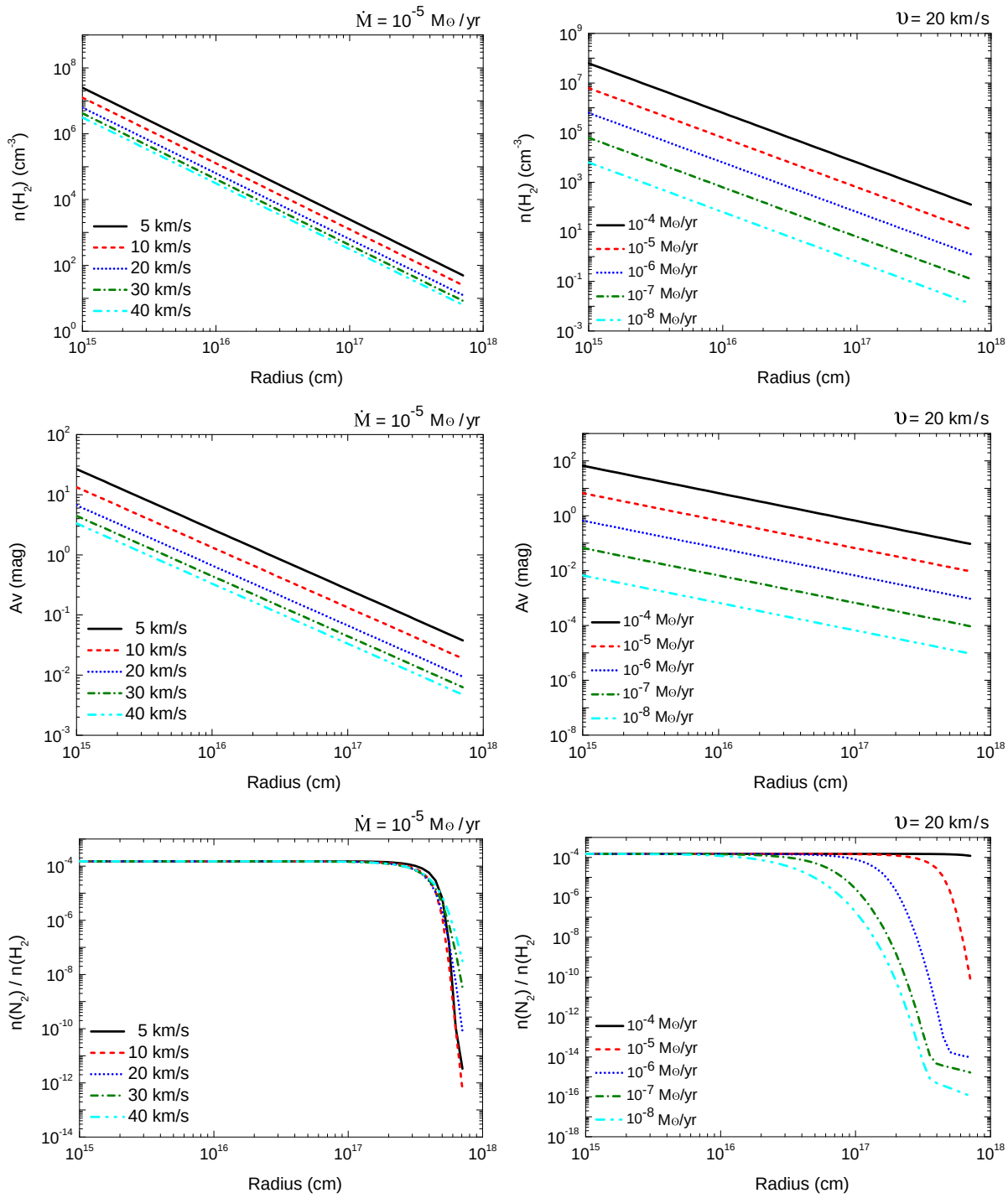

Figure 4.1 — Effects of envelope expansion velocity and mass-loss rate on gas density, visual extinction, and distributions of species in the outer layers of O-rich AGB stars, part A.

The chemical evolution of molecular species in an expanding CSE naturally depends on the physical structure of the AGB star and its envelope. In particular, the mass-loss

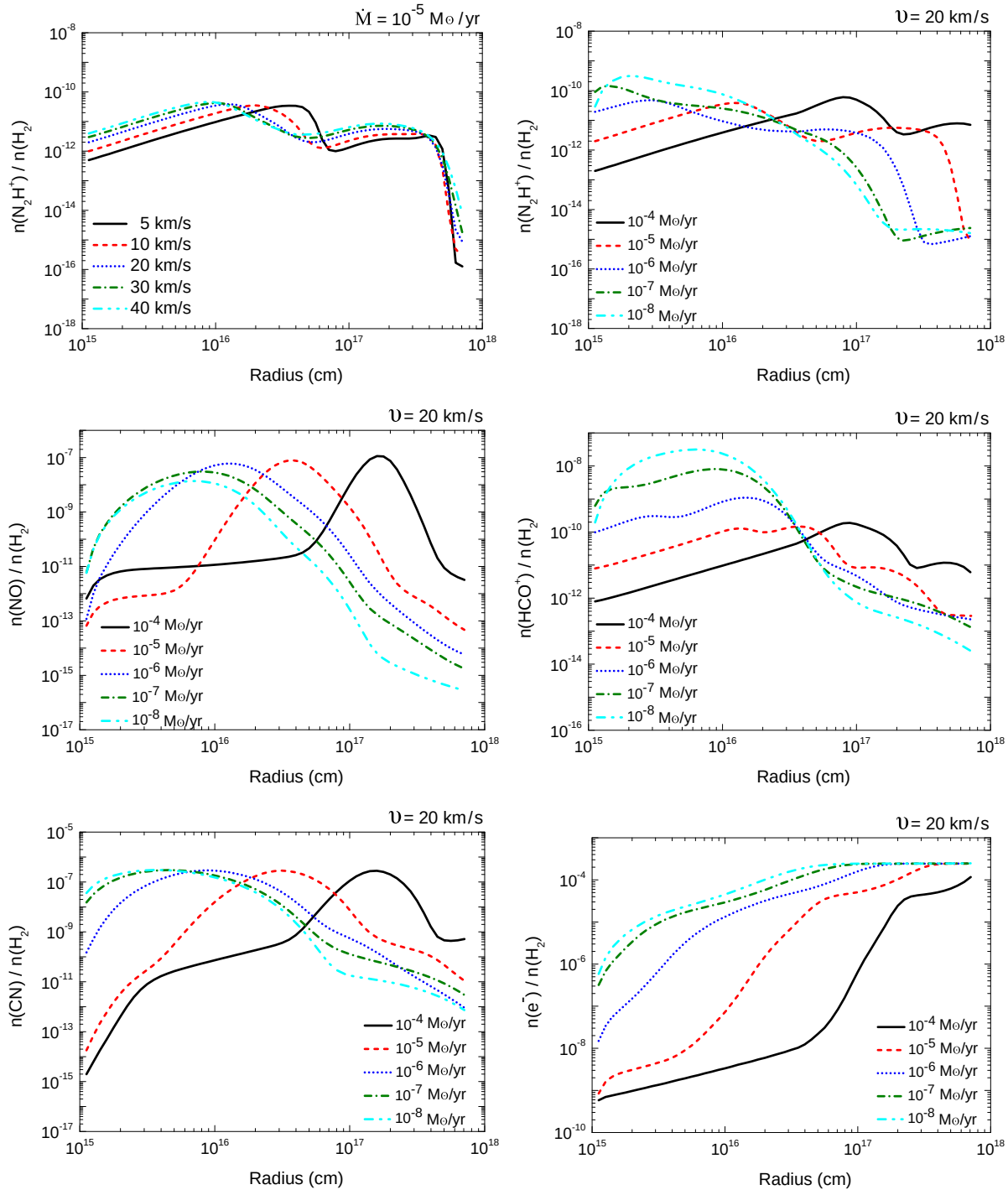

Figure 4.1 — Continued, part B.

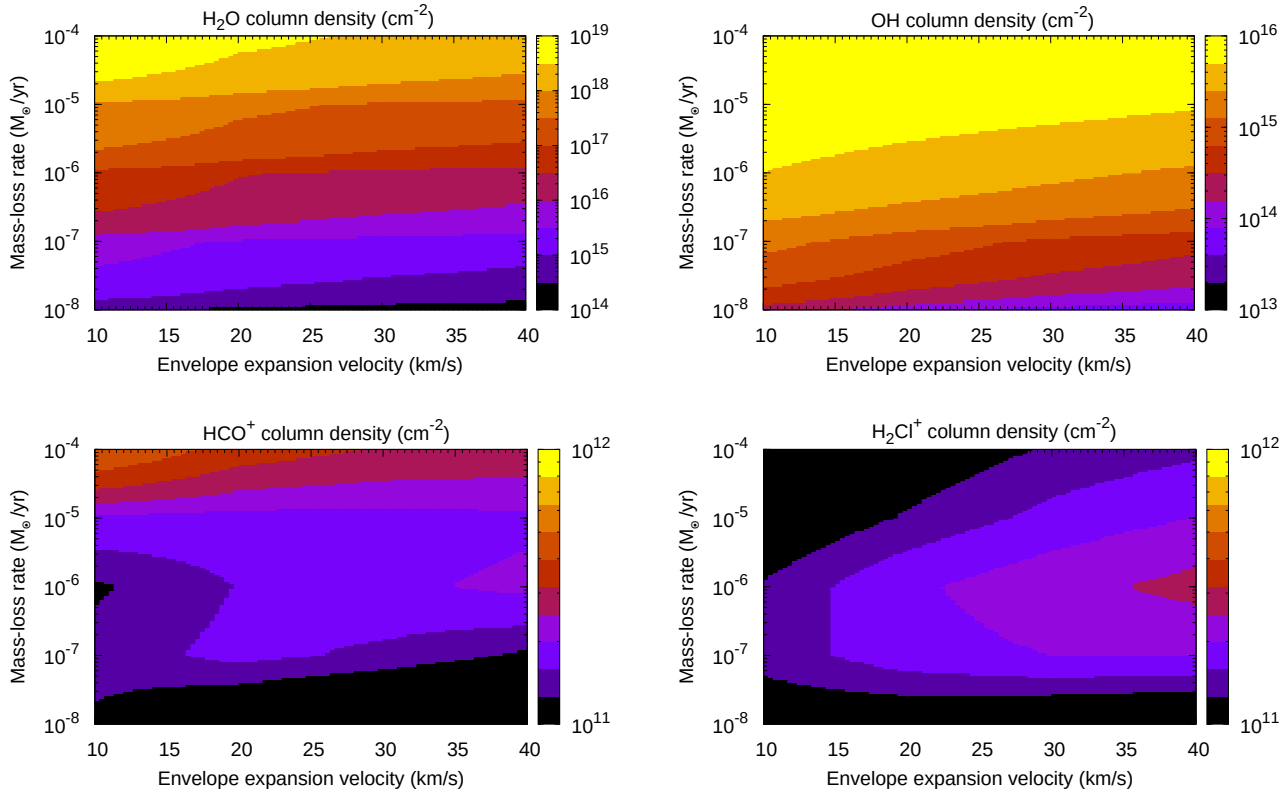

Figure 4.2 — Total column densities for a sample of species in the CSE of O-rich AGB stars, as a function of mass-loss rate and envelope expansion velocity.

rate plays an important role in the distribution of the molecules in the outer envelope, but large uncertainties always exist in its measurement. Starting from our physico-chemical model of IK Tau, we explore here the chemistry of a few interesting species over a range of typical mass-loss rates and gas expansion velocities, $10^{-8} - 10^{-4}$ $M_\odot$ yr^{-1} (Kwon & Suh 2012) and $5 - 40$ km s^{-1}, respectively. The predicted trends are relevant to O-rich AGB stars in general.

The effect of altering the mass-loss rate of an AGB star on gas density, visual extinction, and the abundance of molecular species (both parent and daughter) is studied assuming a fixed envelope expansion velocity, 20 km s^{-1}, whereas the dependence on expansion velocity is studied by assuming a fixed mass-loss rate of 10^{-5} $M_\odot$ yr^{-1}. Fig. 4.5.1 shows that stars possessing a large mass-loss rate can drive the gas to greater distances, whereas the peak abundances of most neutral species, e.g., CN, NO, are less affected. This implies that peak radii of daughter species retrieved from observations may give information about the mass-loss rate. In contrast, the peak abundances of cations, e.g., N_2H^+ and HCO^+, are decreased and the peak radius moves outwards with increasing mass-loss rate. Note that the decrease in peak abundance is more apparent for HCO^+ than N_2H^+ and for the highest mass-loss rate, 10^{-4} $M_\odot$ yr^{-1}, the peak abundance for the latter begins to increase as the peak is pushed outwards. This effect on cations is due to the physical structure of the CSE and not to their enhanced chemical destruction. This is, their destruction is dominated by dissociative recombination with electrons and the

electron density decreases significantly with increasing mass loss.

Total column densities of four molecular species are shown in Fig. 4.5.2 as functions of mass-loss rate and gas expansion velocity. This figure, together with the upper left panel of Fig. A.1, shows that the dependence of the chemistry on the expansion velocity is negligible within usual observational uncertainties. Trends for all parent species are similar to those plotted for H_2O, whose column density increases with increasing mass-loss rate. However, the modelled column density trends for daughter species are quite variable, e.g., the behaviour of OH is similar to that of its parent species H_2O, whereas H_2Cl^+ exhibits a quite different trend. According to this study, the upper-limit of the HCO^+ column density in O-rich envelope is 5×10^{11} cm^{-2}.

Chapter 5

State-selective and thermal rates for $H + OH(v, j) \longrightarrow O + H_2$

Abstract.
The dynamics of the reaction H + OH → O (^{3}P) + H_2 have been studied in a series of quasi-classical trajectory (QCT) calculations and transition state theory (TST) methods using high quality $^3A'$ and $^3A''$ potential energy surfaces (PESs). Accurate OH(v, j) state resolved cross sections and rate constants on both potential energy surfaces are presented and fitted for OH at ($v = 0,\ j = 0 - 16$) and ($v = 1,\ j = 0 - 6$). The cross sections were calculated for different collisional energies (E_c), ranging from the threshold energy at each specific rovibrational state up to 1.0 eV with step sizes of 0.1 eV or less. They increase steeply with collision energy when the barrier to reaction can be overcome, after which the cross sections stay nearly constant with energy. State resolved rate constants in the temperature range 200 – 2500 K are presented based on the cross sections. Total thermal rate constants were calculated by summing the rates for reaction on the $^3A'$ and $^3A''$ potential energy surfaces weighted by 1/3 and taking into account the thermal populations of the rovibrational states of the OH molecules. The current calculated thermal rate constants generally agree well with previous indirectly obtained rate constants by Tsang *et al.* (1986). It is shown that the improved canonical variational transition (CVT) treatments with the approximation of zero-curvature tunneling (ZCT) or small-curvature tunneling (SCT) produce results more in accord with the QCT results than the TST and CVT methods. The reactions are governed by the direct reaction mechanism. The rate constants for OH in excited vibrational and rotational states are orders of magnitude larger than the thermal rate constants, which needs to be taken into account in astrochemical models.

X. Li, C. Arasa, M. C. van Hemert, and E. F. van Dishoeck
J. Phys. Chem. A, **117** , 12889 (2013)

5.1 Introduction

The O (^{3}P) + H_2 system has attracted interest for more than half a century (Garton et al. 2003). In addition to its fundamental significance in chemical dynamics, it is also known to be a participant in combustion processes (Baulch et al. 1992) and plays an important role in warm interstellar gas such as shocks, clouds exposed to intense UV radiation and the inner regions of protoplanetary disks (Graff & Dalgarno 1987; Sternberg & Dalgarno 1995; Agúndez et al. 2008a). Extensive theoretical (Zhai et al. 2012; Han & Zheng 2011; Liu & Shi 2010; Li & Han 2009; Pettey & Wyatt 2008; Weck et al. 2006; Wang et al. 2006; Garashchuk et al. 2006; Atahan et al. 2006; Chu et al. 2005; Braunstein et al. 2004; Brandão et al. 2004; Balakrishnan 2004; Maiti & Schatz 2003; Balakrishnan 2003; Rogers et al. 2000a; Hoffmann & Schatz 2000; Varandas et al. 1997; Chatfield et al. 1993; Joseph et al. 1988; Robie et al. 1987; Schatz 1985; Bowman et al. 1984; Schatz et al. 1981; Walch et al. 1980; Howard et al. 1979; Light 1978) and experimental (Garton et al. 2006), investigations have been carried out to elucidate the dynamics of the O (^{3}P) + H_2 reaction, which has a classical energy barrier of about 0.57 eV (Rogers et al. 2000a) and at low temperatures occurs mainly through tunneling (Robie et al. 1987). Thanks to long-term efforts of constructing and improving the potential energy surfaces (Zhai et al. 2012; Atahan et al. 2006; Brandão et al. 2004; Rogers et al. 2000a; Joseph et al. 1988; Howard et al. 1979), classical and quantum mechanical calculations have been carried out to provide fruitful information on many aspects of this system, such as the kinetics (Westenberg & Haas 1967; Baulch et al. 1994), isotope effects (Sultanov & Balakrishnan 2004), state selective dynamics (Light 1978; Johnson & Winter 1977; Reynard & Donaldson 2001), intersystem crossing (Chu et al. 2005; Robie et al. 1987), nonadiabatic effects (Han & Zheng 2011; Li & Han 2009; Garashchuk et al. 2006), and stereodynamics (Liu & Shi 2010; Wei et al. 2010). Among these PESs, the high quality generalized London-Eyring-Polanyi-Sato (LEPS) double-polynomial (GLDP) surfaces ($^3A'$ and $^3A''$) reported by Rogers et al. (2000a) are widely adopted in scattering simulations and can yield chemically accurate results which are in good agreement with experiments (Garton et al. 2003; Weck et al. 2006; Garton et al. 2006). For example, the reaction cross sections measured by crossed molecular beam experiments are well reproduced by quantum wave packet calculations based on this PES (Garton et al. 2003). Another combined experimental and theoretical investigation on the isotopic substituted reaction O (^{3}P) + D_2 also found good qualitative agreement between the measured dynamic results and the single-surface quasi-classical trajectory calculations (Garton et al. 2003, 2006). These studies also showed that intersystem crossing with the excited singlet states have at most a very minor effect on the reaction probabilities. In fact, according to the exact quantum study of spin-orbit-induced intersystem crossing by Chu *et al.* (Chu et al. 2005, 2006), the effects of spin-orbit coupling on the total reaction cross sections are insignificant if the fine-structure resolved cross sections in the O ($^3P_{2,1,0}$) + H_2 reaction are treated statistically. The quantum scattering calculations performed by Balakrishnan *et al.* (Garashchuk et al. 2006; Balakrishnan 2004, 2003) mainly reported thermal rate coefficients, and found the reaction probability of the $^3A'$ PES to be slightly smaller than that of the $^3A''$ PES in the energy range of 0.5 – 1.2 eV. Brandão et al. (2004) extended the $^3A''$ PES from Rogers et al. (2000a). with van der Waals interactions and used it to study the influence

of the long-range potential on the reaction rates, especially at (ultra) cold temperatures, where tunneling and resonances are significant.

There are far fewer studies of the reverse reaction. The most detailed calculations have focused on the cross sections, thermal rate constants and rate coefficients of the isotope exchange reaction D + OH → OD + H, which plays an important role in interstellar clouds (Atahan et al. 2005; Howard & Smith 1982; Dunne & Murrell 1983; Margitan et al. 1975). However, few studies have been done for the more basic process

$$\mathrm{H}(^2\mathrm{S}) + \mathrm{OH}(^2\Pi)(v,\ j) \underset{k_{-1}}{\overset{k_1}{\rightleftharpoons}} \mathrm{O}(^3\mathrm{P}) + \mathrm{H}_2(^1\Sigma_g^+) \tag{5.1}$$

This is partly because obtaining a beam of OH is experimentally challenging (Radenovic et al. 2003). The rate constant for k_1 in Eq. 5.1 offered in the National Institute of Standards and Technology (NIST) Chemical Kinetics Database (Fernandez-Ramos et al. 2013), which is often employed in astrochemical models but dates from 1986, was derived from the rate constant of the reverse reaction,

$$k_1 = K \,/\, k_{-1} \tag{5.2}$$

where K is the kinetic reactive rate constant. The k_{-1} was suggested according to a combined experimental and TST investigations where the transition state theory (TST) calculations were based on an older PES (Cohen & Westberg 1983). Since the uncertainty of k_1 arises from the uncertainties in both K and k_{-1}, determination of more reliable rate constants for this reaction using a more accurate PES are warranted. Moreover, there is a growing need in astrochemical models for state-specific rate constants in addition to thermal rates (Tappe et al. 2008; Mandell et al. 2012; Salyk et al. 2008; Pontoppidan et al. 2010). Specifically, non-thermal excitation of OH in high rotational and/or vibrational states has been observed in shocks (Tappe et al. 2008) and in the inner regions of protoplanetary disks (Mandell et al. 2012; Salyk et al. 2008; Pontoppidan et al. 2010), which may drive the H + OH reaction. In these regions, gas temperatures are up to 2000 K.

In this chapter, we have carried out the first QCT, TST, and variational transition state theory (VTST) calculations for the title reactions on the $^3A'$ and $^3A''$ GLDP PESs (Rogers et al. 2000a) of OH(v, j) resolved rate constants and thermal rate constants are reported. Other than using the approximate ZCT and SCT methods, tunneling is ignored in the chapter due to the classical nature of the QCT approach. The chapter is organized as follows: in Section 2 we briefly review the theoretical methodologies. In Section 3, results and discussion are presented. Finally, Section 4 closes with the conclusions.

5.2 Chemical models

5.2.1 Potential Energy surface

Scattering calculations were performed on the $^3A'$ and $^3A''$ potential energy surfaces of Rogers et al. (2000a), which are the most accurate published surfaces to date for this reaction. These surfaces, generated from 951 geometries and with high-accuracy for a subset of 112 of these geometries, were based on complete-active-space self-consistent-field (CASSCF) computations using correlation-consistent basis sets. Two different fitting methods, the rotating Morse spline (RMOS) method and the GLDP method, were

employed and compared to each other and also to a previous empirical LEPS surface. Overall, the GLDP fit and RMOS fit to the *ab initio* data are very similar, but the GLDP fit has a higher fitting accuracy and should yield accurate reactive scattering calculations. The GLDP PESs employed in our work consist of two terms:

$$V_{\mathrm{GLDP}} = V_{\mathrm{GLEPS}} + V_{\mathrm{DPOLY}} \tag{5.3}$$

V_{GLEPS} is a Generalized LEPS term and V_{DPOLY} a sum of two high-order polynomials (as functions of the three interatomic distances) multiplied by switching functions. In V_{GLEPS}, a cubic spline fit of near-asymptotic *ab initio* data for each of the three isolated diatomic molecules is used instead of the Morse function of the usual LEPS function. Further details can be found in the original reference (Rogers et al. 2000a).

A typical A + BC reaction can lead to four possible scattering channels: A + BC, AB + C, AC + B, and A + B + C. We have focused on the H + OH → O + H_2 abstraction reaction both on the $^3A'$ and on the $^3A''$ PESs. The two potential energy surfaces have similar characteristics and are degenerate for collinear configurations. Both of them are dominated by a barrier and have a broad van der Waals well along the entrance valley. The barrier heights on the $^3A'$ and $^3A''$ PESs are 0.476 and 0.468 eV, and the depths of the wells are 0.009 and 0.004 eV, respectively. The differences in barrier heights and van der Waals depths in the two PESs are smaller than the root-mean-square (rms) error (±0.0129 eV) induced by the fitting procedure and are in any case not relevant for the temperature range considered here. However, these small differences may be responsible for slightly different reaction thresholds, and also play a role in quantum mechanical studies at low collision energies and stereodynamics studies.

The corresponding energy-level diagram for different rovibrational states $(v,\ j)$ of the OH molecule is shown in Figure 5.1. The rovibrational energy levels $E_{v,j}$ were calculated from the PESs using the QCT code and are presented both with and without the zero-point energies. In practice, the zero-point energy of OH molecule needs to be taken into account for the reactive channel. In our case, j is the purely rotational angular momentum of the OH molecule (often denoted as N in the spectroscopic literature) since in our work electronic orbital and spin angular momenta are discarded. Each OH rotational level j modeled here, is in reality split into two different spin states, $^2\Pi_{1/2}$ and $^2\Pi_{3/2}$, which have an energy difference of only 0.017 eV (Maillard et al. 1976). This difference is ignored in our calculations.

5.2.2 Quasi-classical trajectory calculations

In this work, we have used the Venus96 QCT code developed by Hase et al. (1996) to compute cross sections as functions of energy, from which state-resolved rate constants as well as the thermal rate constants are subsequently calculated. In all cases, the initial parameters are as follows. An initial distance of 6.4 Å is adopted between the attacking H atom and the center of mass of the target OH molecule. Batches of 2×10^4 trajectories have been carried out for each collision energy of the incident hydrogen atom. The integration step size is chosen to be 0.1 fs, which is small enough to ensure the conservation of the total energy and the total angular momentum. To calculate thermal rate constants, for both $^3A'$ and $^3A''$ PESs, the initial rovibrational conditions of the OH molecule were

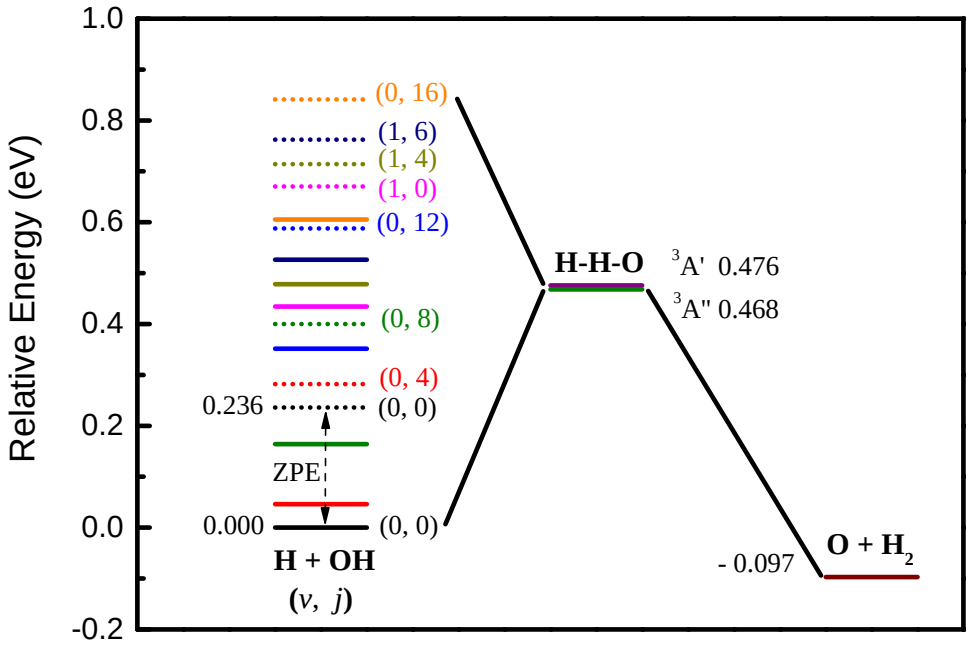

Figure 5.1 — Schematic energy-level diagram for the abstraction reactions H+OH($v,\ j$) $\rightarrow O(^3\mathrm{P}) + \mathrm{H}_2$ at various rovibrational ($v,\ j$) states of OH, in solid lines. Dotted lines: corrected energy levels which include the zero-point vibrational energy (ZPE). For the H + OH channel, this ZPE is taken into account in the QCT calculations.

chosen to include the range of states ($v = 0,\ j = 0 - 16$) and ($v = 1,\ j = 0 - 6$). To evaluate the cross sections, the collision energies (E_c) were set up on a finely spaced grid: on the $^3A'$ PES, for $v = 0$ at $j = 0$ up to 16, E_c were chosen as follows: from 0.2 to 0.32 with a step size of 0.02 eV; 0.35 eV, and from 0.4 to 1.0 eV with a step size of 0.1 eV. For $v = 1$ at $j = 0$ up to 6, E_c were chosen at 0.06, 0.08, 0.10, 0.12, 0.15, 0.2, 0.25, and from 0.3 to 1.0 eV with a step size of 0.1 eV. For the $^3A''$ state, the selected E_c are the same as those on $^3A'$ state except those at $v = 0$ and $j = 7$ up to 16, which employed the same energy values as for $v = 1$, $j = 0$ up to 6 on the $^3A'$ PES.

During the QCT simulations, the impact parameter b is sampled from $0 \leq b \leq b_{\max}$ by $b = b_{\max}\xi_0^{1/2}$, where ξ_0 is a pseudorandom number, and the maximum impact parameter, b_{max}, is the value of b for which the reactive probability drops to zero when $b \geq b_{\max}$. In our work, b_{max} is optimized by trial calculations with a range of b_{max} values at fixed initial condition of the reactants, until the reactive probability of the observed channel is zero while $b = b_{max}$. The criterion is that at most one reactive trajectory occurs among a large sum of total trajectories (for example, 10^4), thus the reaction probability is approximately zero. Generally, 3 – 6 trials are necessary to optimize b_{max} at a fixed E_c. In the present calculations, b_{max} has been determined by running batches of 10^4 trajectories. Overall, the value of b_{max} increases with increasing rovibrational state of the OH reactant at each fixed E_c leading to a corresponding enhancement of the cross section as well as the relevant rate constant. According to our experience, a slightly higher b_{max} does not affect the cross sections much, whereas a too small value will result in significant errors.

The integral cross section, $\sigma(v, j)$, and the associated uncertainties $\Delta\sigma(v,\ j)$ at a

certain rovibrational level $(v,\ j)$ can be determined from (Karplus et al. 1965)

$$\sigma(v,j) = \pi b_{\max}^2 \frac{N_r(v,j)}{N(v,j)},$$
$$\Delta\sigma(v,j) = \sqrt{\frac{N(v,j) - N_r(v,j)}{N(v,j)N_r(v,j)}}\sigma(v,j) \tag{5.4}$$

where N and Nr denote the total number of sampled and reactive trajectories, respectively. Eq. 5.4 is only valid when the $\xi_0^{1/2}$ sampling method is used. Since we have employed a large number of trajectories, the standard error is $\pm 20\%$ for collisional energies near threshold and less than $\pm 6\%$ when the collisional energy is more than 0.4 eV.

Subsequently, the specific rate constant at a temperature T for an initial rovibrational $(v,\ j)$ state of the OH molecule is calculated from the integral cross sections by averaging over a Maxwell distribution of energies through

$$k(T;v,j) = \sqrt{\frac{8k_{\rm B}T}{\pi\mu_R}}(k_{\rm B}T)^{-2}\int_0^{1.0} E_c\sigma(v,j)\exp\left(\frac{-E_c}{k_{\rm B}T}\right)dE_c \tag{5.5}$$

where $k_{\rm B}$ is the Boltzmann constant, μ_R the reduced mass of the reactants, and E_c the collision energy.

The thermal rate constant for an initial vibrational state can be written as

$$k(T) = \sum_{v=0}\sum_{j=0} p_{vj}(T)k(T;v,j) \tag{5.6}$$

where $p_{vj}(T)$ are the fractional population of the OH molecule for a thermal distribution at temperature T, calculated by

$$p_{vj}(T) = (2j+1)\exp\left(-E_{v,j}/k_{\rm B}T\right)/Q_{v,j}(T) \tag{5.7}$$

with

$$Q_j(T) = \sum_{v}^{\infty}\sum_{j=0}^{\infty}(2j+1)\exp\left(-E_{v,j}/k_{\rm B}T\right) \tag{5.8}$$

The fractional populations of the OH molecule as functions of j at various temperatures are shown in Figure 5.2. This figure demonstrates that j levels up to 16 in $v = 0$ indeed need to be included at higher temperatures. In the calculations, the sum of Eq. 5.6 is truncated at $j =$ 16 for $v = 0$ and $j = 6$ for $v = 1$ for both PESs. The rate constants have been calculated by summing the rates on each of the potential energy surfaces ($^3A'$ and $^3A''$) weighted by 1/3 (Schatz 1985; Bowman et al. 1984; Balakrishnan 2003; Walch et al. 1980). This is because the overall reaction leads to 3 triplet potential energy surfaces, 2 having A'' symmetry, and 1 A'. One of the A'' symmetry PESs does not contribute to the reaction since it has a higher energy barrier (Wang et al. 2006). Finally, to make these data available to astronomers in a convenient form, the specific rate constants for individual OH$(v,\ j)$ states were fitted to the Arrhenius form, $k(T) = \alpha \times (T/300)^{\beta} \times e^{(-\gamma/T)}$, where T is the gas temperature, α is known as the pre-exponential factor, β dictates the temperature dependence of the rate coefficient and γ is the activation energy of the reaction in units of K.

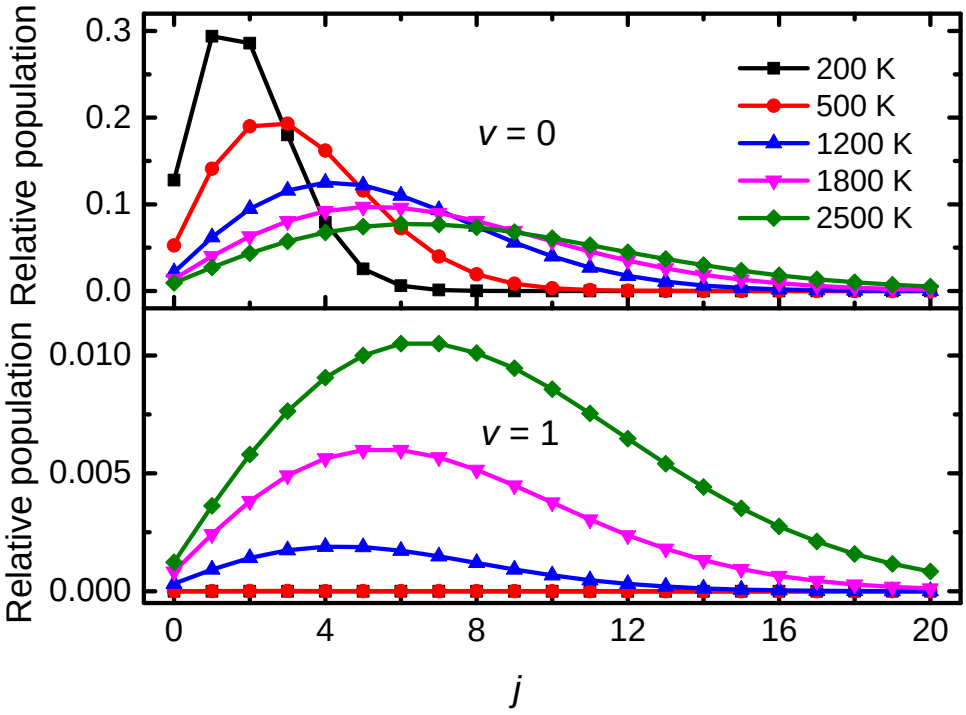

Figure 5.2 — Relative populations of OH $(v,\ j)$ molecules as a function of j for thermal excitation at various temperatures, for $v = 0$ and 1.

5.2.3 Transition state theory

Transition state theory is a useful tool for calculating approximate rate constants for reactions occurring in the gas phase and in the condensed phases based on the barrier height, the density of states at the transition state Q, and on the (products of the) partition functions of the reactants F. The rate constant calculations can be improved by the variational transition state theory (VTST), where a dividing surface is defined so that all reactive trajectories must pass through it. The dividing surface is defined along the reaction coordinate s, which is the distance along the minimum energy path (MEP), with $s = 0$ at the saddle point, negative on the reactant side, and positive on the product side. The rate constants according to the generalized transition state theory (GTST) as a function of temperature T and s (Ju et al. 2009; Truhlar & Garrett 1984) is given by

$$k^{\mathrm{GTST}}(T,s) = \frac{\alpha}{\beta h}\frac{Q^{\mathrm{GTST}}(T,s)}{\Phi^{\mathrm{R}}(T)}e^{-\beta V_{\mathrm{MEP}}(s)} \tag{5.9}$$

where α is the number of symmetry equivalent reaction paths, $\beta = \frac{1}{k_{\mathrm{B}}T}$, and h is Planck's constant. $Q^{\mathrm{GTST}}(T,\ s)$ and $\Phi^{\mathrm{R}}(T)$ are the density of states at the generalized transition state at point s and the partition function of the reactants, respectively. $V_{\mathrm{MEP}}(s)$ is the potential energy at point s along the minimum energy path. The VTST rate constant k^{VTST} is the minimum value of the GTST rate constant (Eq. 5.9) at a given T:

$$k^{\mathrm{VTST}}(T) = \min_s k^{\mathrm{GTST}}(T,s) = k^{\mathrm{GTST}}(T, s^{\mathrm{CVT}}(T)) \tag{5.10}$$

Table 5.1 — Parameters of the fitting formula $\sigma = P_1 \times (1 - (P_2/E_c)^2)^3 \times E_c^{P_3}$ for the cross sections σ (Å^2) as a function of collision energy E_c for various OH($v,\ j$) states on the $^3A'$ and $^3A''$ potential energy surfaces.

	$^3A'$			$^3A''$		
$(v,\ j)$	P_1	P_2	P_3	P_1	P_2	P_3
(0, 0)	0.328	0.215	0.226	0.456	0.235	0.730
(0, 1)	0.358	0.217	0.420	0.446	0.237	0.625
(0, 2)	0.355	0.218	0.610	0.441	0.234	0.637
(0, 3)	0.359	0.225	0.572	0.431	0.234	0.636
(0, 4)	0.380	0.235	0.602	0.437	0.232	0.516
(0, 5)	0.402	0.238	0.638	0.460	0.224	0.631
(0, 6)	0.407	0.236	0.724	0.455	0.212	0.620
(0, 7)	0.426	0.220	0.890	0.463	0.135	1.181
(0, 8)	0.414	0.217	0.676	0.476	0.132	1.010
(0, 9)	0.440	0.203	0.745	0.525	0.129	0.971
(0, 10)	0.482	0.206	0.620	0.592	0.129	0.876
(0, 11)	0.513	0.201	0.590	0.633	0.125	0.772
(0, 12)	0.555	0.196	0.573	0.715	0.123	0.697
(0, 13)	0.613	0.182	0.701	0.715	0.123	0.697
(0, 14)	0.661	0.180	0.630	0.840	0.116	0.473
(0, 15)	0.719	0.183	0.532	0.898	0.108	0.377
(0, 16)	0.747	0.181	0.407	0.959	0.094	0.391
(1, 0)	0.794	0.018	0.172	1.101	0.025	0.317
(1, 1)	0.841	0.034	0.212	1.124	0.026	0.429
(1, 2)	0.859	0.052	0.257	1.042	0.058	0.239
(1, 3)	0.845	0.071	0.211	1.017	0.061	0.254
(1, 4)	0.894	0.074	0.333	1.056	0.062	0.329
(1, 5)	0.960	0.076	0.469	1.077	0.062	0.355
(1, 6)	0.988	0.076	0.547	1.106	0.061	0.341

where $s^{\mathrm{CVT}}(T)$ is the location of the Canonical Variational Transition (CVT) state at a given temperature T. Quantum effects may be important for light systems and at lower temperatures, especially for tunneling along the reaction-coordinate motion. In order to include these effects, the $k^{\mathrm{VTST}}\ (T)$ is multiplied by a transmission coefficient, usually by the approximation of Zero Curvature Tunneling (ZCT) or Small Curvature Tunneling (SCT), see Ju et al. (2009). Here, TST, CVT, CVT/ZCT and CVT/SCT have been employed to calculate the rate constants on the $^3A'$ and $^3A''$ surfaces for the $(v = 0,\ j = 0)$ state of the reactant molecule, yielding the corresponding rate constants in the temperature range of 200 – 2500 K. In all transition state calculations the polyrate program (Fernandez-Ramos et al. 2007) was used.

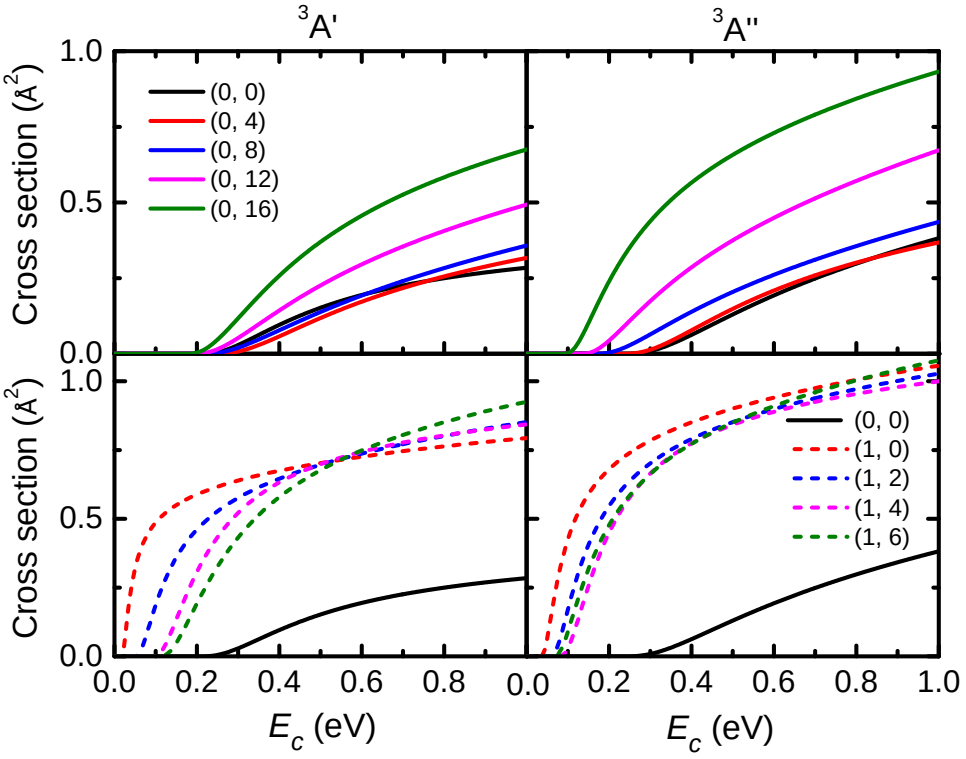

Figure 5.3 — Integral cross sections as functions of collision energy for the title reaction at different rovibrational levels $(v,\ j)$ of OH for the two PESs $^3A'$ and $^3A''$.

5.3 Results and Discussion

5.3.1 Integral cross sections

Cross sections starting from various initial excitation states, $(v,\ j)$, of the OH molecule have been computed to obtain the thermal rate constant for the title reaction. For $^3A'$ and $^3A''$ PESs, integral cross sections for $(v = 0,\ j = 0 - 16)$ and $(v = 1,\ j = 0 - 6)$ have been calculated. All of these cross sections are fitted to the formula $\sigma = P_1 \times (1 - (P_2/E_c)^2)^3 \times E_c^{P_3}$ and listed in Table 5.1, here P_2 gives the threshold energy of the corresponding reaction.

In Figure 5.3, the integral cross sections as functions of collision energies E_c (the excitation functions) are displayed for selected $(v,\ j)$ states. The two PESs show a similar behavior which is not surprising since they are very comparable, see section 2.1. For both PESs, the cross sections increase with increasing E_c, which is common for barrier-dominated reactions. Basically, the rovibrational excitation of the OH molecule increases the cross sections for $(v = 0,\ j)$ states. For states with $(v = 1)$, the reagent rotational excitation does not always help the reaction. In particular, the cross sections at lower collision energies (< 0.5 eV) decrease with increasing rotational excitation of OH molecule. This is probably because the increasing rotational quantum number j induces a barrier in the entrance valley of the potential energy surfaces, which will be especially relevant at low collision energies. Note that the errors in our QCT results near the threshold energy are large due to the very low reaction probabilities. In addition, the QCT method does

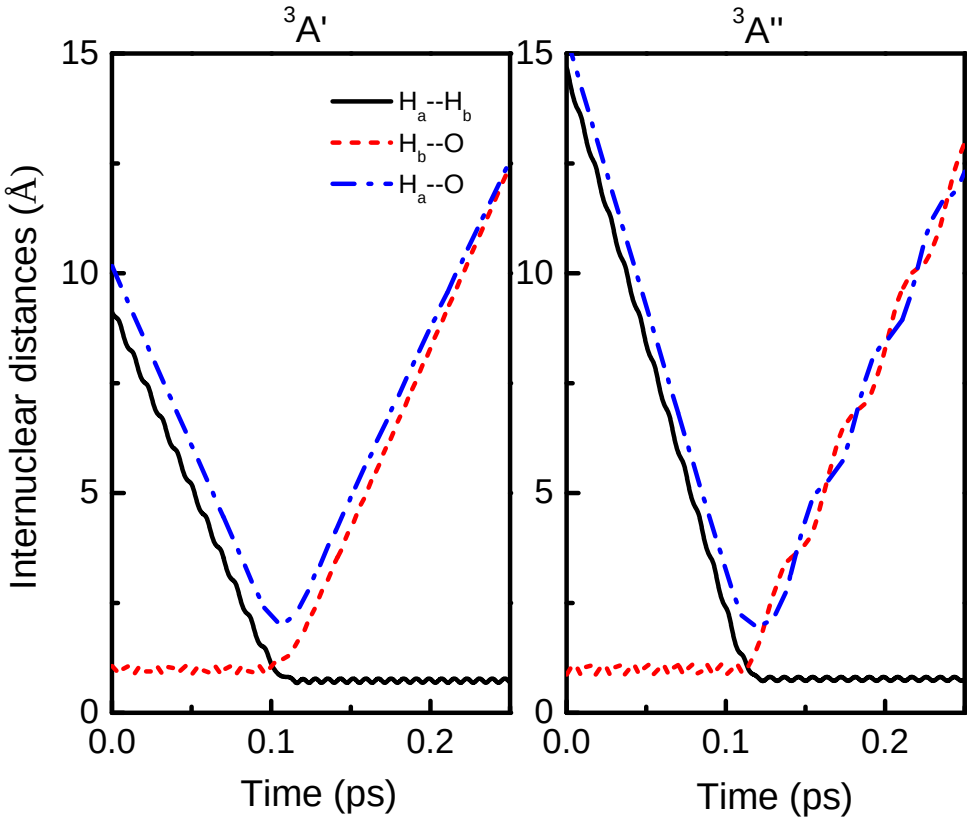

Figure 5.4 — Typical reactive trajectories for the abstraction reaction $H_a + H_bO \longrightarrow O + H_aH_b$ on the $^3A'$ and $^3A''$ PESs, namely internuclear distances of H_aH_b, H_bO and H_aO as functions of propagation time.

not include tunneling which could be important near threshold.

It is seen that the cross sections for different $(v,\ j)$ states are larger for the $^3A''$ PES than for the $^3A'$ surface, indicating that the $^3A''$ surface plays a more important role in the rate constants. The same conclusion was found previously in quantum mechanical investigations of the reverse reaction, O + H_2 in the energy range 0.5 – 1.2 eV (Balakrishnan 2003).

We "observed" a large number of trajectories over the two PESs in every rovibrational state and found that all reactions are dominated by the direct reaction mechanism, that is, the attacking atom H_a collides with the OH_b molecule and forms an H_2 that leaves immediately, indicating that the broad van der Waals well is too shallow to "trap" any atom, even near the threshold collision energy. Some typical trajectories are shown in Figure 5.4.

5.3.2 Rate constants

The specific reaction rates for various $OH(v,\ j)$ states as well as thermal rate constants were derived from the fitted cross sections, and then fitted to the Arrhenius form. By fitting the data separately to two temperature ranges (200 – 1000 K and 1000 – 2500 K) on a logarithmic scale, the fitting errors were significantly reduced compared to the fitting

Table 5.2 — Thermal rate constants fitted to $k(T) = \alpha \times (T/300)^{\beta} \times e^{(-\gamma/T)}$ (cm^3 molecule^{-1} s^{-1}).

	200 – 1000 K			1000 – 2500 K		
$(v,\ j)$	α	β	γ	α	β	γ
(0, 0)	2.32×10^{-16}	1.448	2597	1.60×10^{-11}	0.031	3992
(0, 1)	1.05×10^{-16}	1.557	2621	1.93×10^{-11}	0.012	4114
(0, 2)	1.25×10^{-16}	1.527	2656	1.60×10^{-11}	0.030	4124
(0, 3)	2.42×10^{-16}	1.440	2762	1.83×10^{-11}	0.013	4182
(0, 4)	4.37×10^{-16}	1.374	2881	2.00×10^{-11}	0.010	4227
(0, 5)	1.12×10^{-16}	1.553	2723	2.09×10^{-11}	0.008	4230
(0, 6)	8.32×10^{-17}	1.584	2544	1.35×10^{-11}	0.059	4043
(0, 7)	3.76×10^{-17}	1.669	2105	4.04×10^{-12}	0.200	3582
(0, 8)	8.20×10^{-17}	1.579	2047	5.03×10^{-12}	0.179	3439
(0, 9)	6.30×10^{-17}	1.614	1814	3.01×10^{-12}	0.247	3186
(0, 10)	1.67×10^{-16}	1.514	1914	5.34×10^{-12}	0.197	3225
(0, 11)	1.44×10^{-16}	1.535	1679	3.70×10^{-12}	0.248	2973
(0, 12)	2.45×10^{-16}	1.481	1626	3.96×10^{-12}	0.253	2866
(0, 13)	3.31×10^{-16}	1.447	1647	3.87×10^{-12}	0.260	2845
(0, 14)	9.26×10^{-16}	1.330	1431	3.61×10^{-12}	0.285	2509
(0, 15)	1.93×10^{-15}	1.245	1328	3.67×10^{-12}	0.294	2333
(0, 16)	2.16×10^{-15}	1.233	1148	3.01×10^{-12}	0.324	2127
(1, 0)	1.49×10^{-13}	0.722	307	3.90×10^{-12}	0.312	751
(1, 1)	1.69×10^{-13}	0.711	531	4.82×10^{-12}	0.290	991
(1, 2)	1.44×10^{-13}	0.735	750	6.21×10^{-12}	0.262	1261
(1, 3)	1.55×10^{-13}	0.735	979	1.14×10^{-11}	0.192	1543
(1, 4)	8.03×10^{-14}	0.828	1123	1.43×10^{-11}	0.170	1782
(1, 5)	2.59×10^{-14}	0.973	1064	1.07×10^{-11}	0.207	1816
(1, 6)	1.02×10^{-14}	1.085	883	6.33×10^{-12}	0.268	1693
Thermal	3.53×10^{-18}	2.078	2518	2.78×10^{-11}	0.059	4496

throughout the overall temperature range. The fitted parameters are listed in Table 5.2.

Selected rate constants for various OH($v,\ j$) states as a function of inverse temperature are shown in Figure 5.5. As expected, the rate constants increase with increasing temperature and follow an Arrhenius trend. For both PESs, the vibrational excitation of OH evidently accelerates the reaction. The rotational excitation of OH accelerates the reaction for ($v = 0,\ j$) states except for $j = 0$ on the $^3A'$ PES. For ($v = 1,\ j$) states, similar to the conclusions from the corresponding cross sections, rotational excitation reduces the rate constants due to the induced effective barriers at lower temperatures.

Figure 5.6 compares the calculated rate constants for the ($v = 0,\ j = 0$) level summed over both PESs by the different QCT, TST, CVT, CVT/ZCT, and CVT/SCT methods in the temperature range of 200 – 2500 K. The calculated TST and CVT rate constants are smaller than the QCT results in the temperature range below 500 K, whereas the improved CVT treatments, namely zero-curvature tunneling (ZCT) and small-curvature tunneling (SCT) methods, which attempt to take into account tunneling effects, indeed produce more accurate rate constants for the title reaction. The outcome of the transition state calculations is rather surprising. At low temperatures the TST rate is four orders of magnitude smaller than the QCT rate, but both rates are, due to the ~ 0.5 eV barrier,

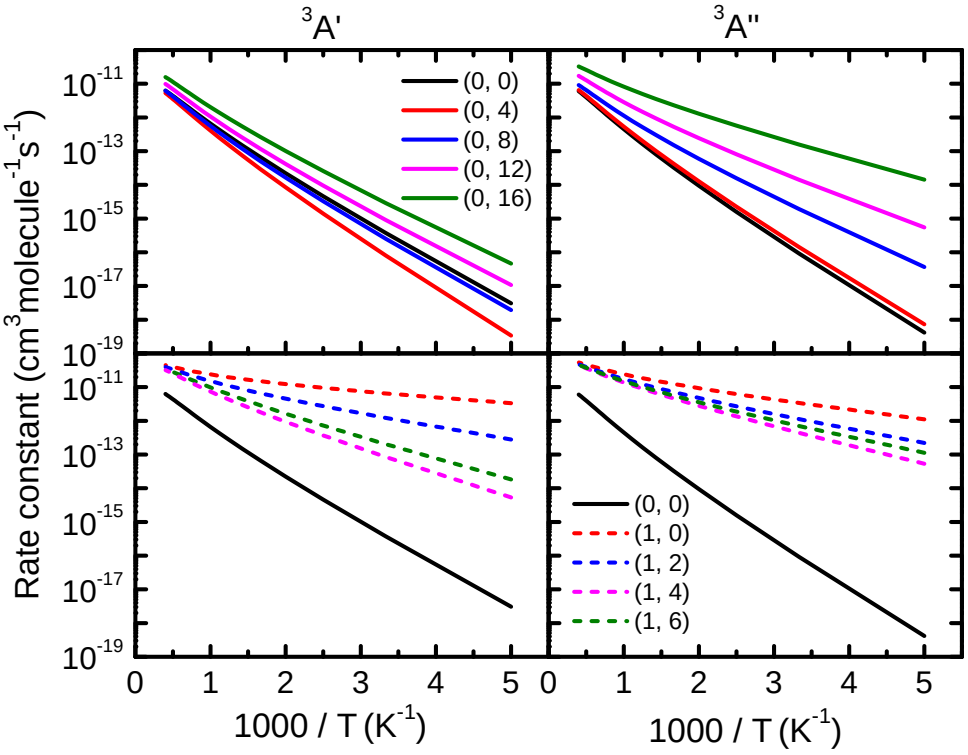

Figure 5.5 — State-resolved rate constants as functions of inverse temperature for individual OH(v, j) levels.

very low anyway. Both methods could at these low temperatures suffer from neglect of tunneling. The standard CVT method produces the same rates as pure TST at the low temperatures, but adding corrections for tunneling according to the SCT formalism makes the CVT/SCT rates agree with the QCT rates. This agreement between the QCT and CVT/SCT results at low temperatures must be largely fortuitous since QCT does not take tunneling into account. The question of the importance of tunneling can only be addressed properly by a full quantum mechanical (QM) calculation of the OH + H reaction rates on the triplet potential energy surfaces. Such calculations have not yet been performed and thus one can only speculate on the basis of results for other atom-diatom exchange reactions with a barrier for which full QM calculations have been performed. In the text book example of such a reaction, the H + D_2 hydrogen/deuterium exchange reaction, as discussed, e.g., in Ju et al. (2009), there is near perfect agreement (within 5% on average) between full QM and QCT rates even at temperatures as low as 200 K, suggesting that for the H + D_2 case tunneling is less important. In that study, also a CVT variant which includes tunneling corrections, named MCPVAG, was found to produce the same rates as were obtained with QCT and QM, while the native TST and CVT gave nearly identical but much lower rates. We therefore conclude that good agreement between QCT and CVT/SCT rates can be reached as found in both our studies and that in Ju et al. (2009), but for reasons that are not yet understood.

Figure 5.7 shows a blow-up of the QCT results in the 200-1000 K range on a linear scale. This figure also includes the previous studies by Tsang & Hampson (1986) whose

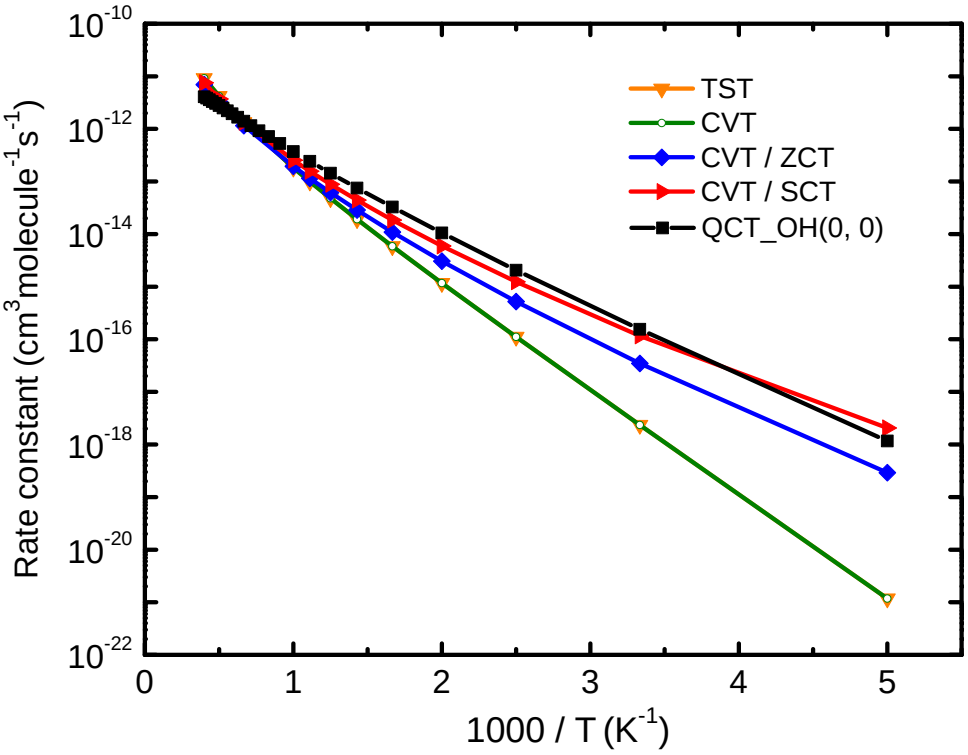

Figure 5.6 — Plot of rate constants for the title reaction with OH in the ($v = 0,\ j = 0$) state, as functions of inverse temperature in the range of 200 – 2500 K, which were calculated from QCT and various TST methods. Both the x- and y-axis are in base 10 logarithmic scales. Rate constants at each electronic state were calculated by considering the results from two PESs, i.e., $({}^3A' + {}^3A'')/3$.

rate constants were derived from the reverse O + H_2 reaction (over the 298 – 2500 K range) that obtained by Walch et al. (1980). The 1986 Tsang *et al.* results are in good agreement with the present thermal QCT results, which were calculated using a more accurate benchmark PESs, with differences typically 50%.

Another interesting phenomenon in Figure 5.7 is that the values of the thermal rate constants are higher than those at ($v = 0,\ j = 0$) state when $T > 600$ K, but lower when $T \sim 200$ K. This is because at higher temperatures, the higher rotational excitation states, ($v = 0,\ j = 3 - 10$), contribute more to the thermal rate constants, as seen in Figure 5.2. The values of the cross sections at those higher j states are significantly higher, especially at higher energies, see Figure 5.3. Therefore, the thermal rates are also higher.

The importance of the state-selective rate constants computed here for astrochemical applications is demonstrated with two examples. In interstellar shocks with kinetic temperatures $T_{\rm kin}$ of 500 – 2000 K, the OH molecules lose their internal energy more rapidly than their translational energy, so the rotational temperature $T_{\rm rot}$ characterizing the OH excitation is much lower than $T_{\rm kin}$. In this case, the state-specific rate constants for $j = 0$ will be lower than the thermal rate constants at high temperatures. The difference is 30% at 1000 K, increasing to 67% at 2000 K. A reverse situation is provided by the warm (few hundred K) surface layers of protoplanetary disks where OH may be produced by Lyman α photodissociation of H_2O in either vibrationally excited and/or highly excited

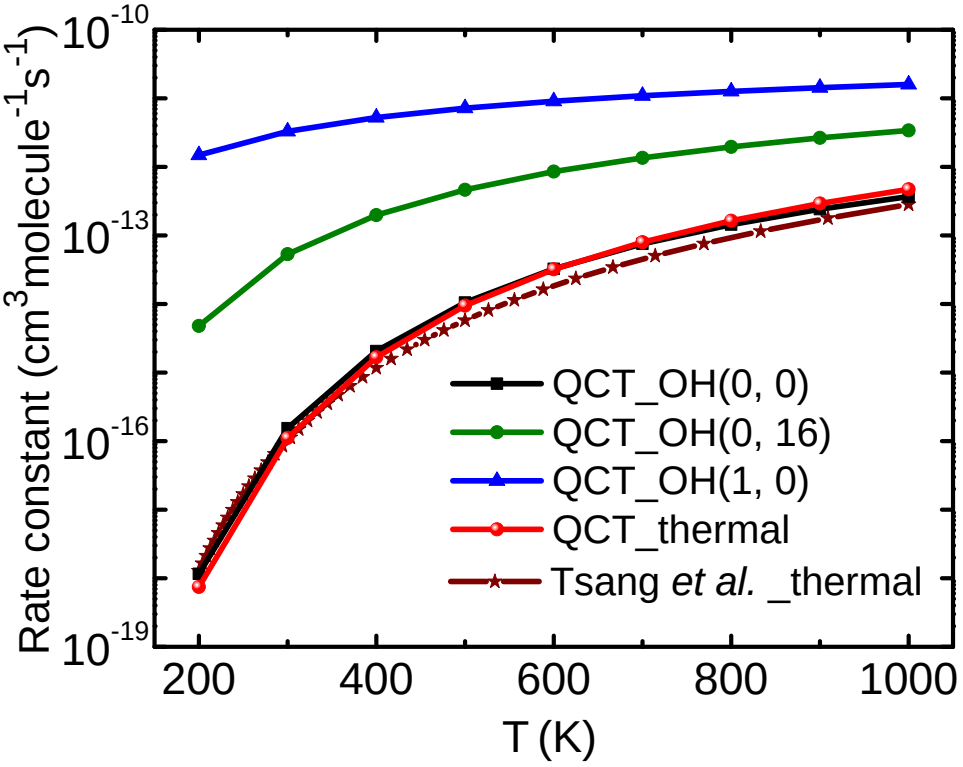

Figure 5.7 — Comparison of the presently calculated thermal rate constants with that of Cohen & Westberg (1983). The figure also illustrates the rotational and vibrational excitation effects on the rate constants. In the plot, x-axis is on a linear scale but the y-axis is on base 10 logarithmic scales. Rate constants for each electronic state were calculated by considering the results from two PESs, i.e., $(^3A' + {}^3A'')/3$.

rotational levels with values observed up to $j = 35$ (Mandell et al. 2012; Salyk et al. 2008; Pontoppidan et al. 2010). In this case the appropriate rate constants for the OH $(0, j)$ + H reaction are orders of magnitude larger than the thermal ones, as shown in Figure 5.7.

5.4 Concluding remarks

Using accurate *ab initio* PESs, integral cross sections and state-resolved rate constants were calculated for various OH$(v,\ j)$ states for the reaction OH + H $\rightarrow$ O + H_2 and presented in fitted form for temperatures $>$ 200 K. Moreover, thermal rate constants are reported. The reactions occurring on the $^3A'$ and $^3A''$ PESs are dominated by the direct reaction mechanism, belonging to the abstraction type. The $^3A''$ PES plays a more important role in the rate constants at lower temperatures whereas the $^3A'$ surface contributes at higher temperatures. Both the rotational and vibrational excitation of the OH molecules will enhance the reaction rates at higher collision energies, but the vibrational excitation has a larger impact than the rotational excitation. In particular, an effective barrier may be induced by the rotational excitation at lower collision energies ($<$ 0.6 eV).

The rate constants presented here should be more accurate than previous values used

in astrochemical models of warm interstellar gas. The state-selective values are found to make orders of magnitude differences compared with thermal ones.

Acknowledgments

X. Li thanks Prof. Keli Han for his continuous encouragement and inspiring advices and Dr. Alan Heays for valuable discussions. The authors thank Drs. Erik Deul and Mark Somers for their assistance. This work is supported by the Dutch astrochemistry network (DAN) from the Netherlands Organization for Scientific Research (NWO) under grant 648.000.002. Astrochemistry in Leiden is also supported by the Netherlands Research School for Astronomy (NOVA), by a NWO Spinoza grant, and by the European Community's Seventh Framework Program FP7/2007-2013 under grant agreement 238258 (LASSIE).

Nederlandse samenvatting

S.1 Het moleculaire heelal

Het heelal is *enorm*, maar veel van de hemellichamen die we 's nachts zien – planeten, sterren, sterrenstelsels – hebben hun oorsprong in microscopische processen tussen atomen en moleculen. Deze deeltjes zenden ook veel lijnen uit die kunnen worden gedetecteerd door gevoelige telescopen: daarom onderzoeken astronomen tegenwoordig het heelal door studie van *kleine* dingen − op de schaal van moleculen en hun interacties. Dit vereist kennis van zowel *sterrenkunde* als *chemische fysica*, daarbij bijdragend aan de vooruitgang van de *astrochemie* die, in principe, onze vragen over het heelal kan beantwoorden op het niveau van *kwantummechanica* − Wat fascinerend! De oorsprong van het heelal is mogelijk kwantummechanisch: we wonen in een 'moleculair heelal(Tielens 2013).

Tot op de dag van vandaag zijn bijna 180 verschillende moleculen (zonder isotopologen mee te tellen) geïdentificeerd in de ruimte met behulp van hun 'vingerafdrukken': de rotationele, vibrationele en electronische spectra [a]. Deze lijst bevat kleine moleculen zoals CO en H_2O, en grote moleculen zoals polycyclisch aromatische koolwaterstoffen (PAKs) en fullerenen, bijvoorbeeld C_{60}^+,C_{60} en C_{70}. Het is bekend dat moleculen abundant en wijd verspreid zijn in alle fases van het neutrale interstellaire medium, van diffuse wolken tot dichte ster- en planeetvormingsgebieden, en van de omhulsels van stervende sterren tot de centrale gebieden van sterrenstelsels. De rijke chemie van deze deeltjes opent mogelijkheden voor onderzoek naar de ontstaansgeschiedenis en evolutie van sterren, sterclusters, sterrenstelsels en interstellaire materie, zowel chemisch als fysisch. Dit komt doordat de excitatie en abondantie van moleculen worden bepaald door botsingen, die op hun beurt afhangen van gas dichtheid en temperatuur, en van het stralingsveld in hun omgeving (van Dishoeck 2014). Dit betekent dat moleculen kunnen worden gebruikt als 'leurstof´'an specifieke processen of omstandigheden.

Complexe, prebiotische interstellaire moleculen vertegenwoordigen mogelijk de eerste stappen richting leven elders in het heelal. De mens is niet alleen in het heelal − in elk geval niet vanuit het perspectief van zijn samenstelling: er is geen groot verschil tussen de moleculen waaruit wij bestaan en die gevonden worden in de moleculaire wolken, planeten, sterren, nevels en vele andere hemellichamen. Astrochemie kan dus helpen om de oorsprong en evolutie van onze eigen planeet en ons zonnestelsel en uiteindelijk 'nszelf´'eter te begrijpen. Met name door dit laatste aspect is dde onderzoeksinteresse in dit gebied de afgelopen jaren verder toegenomen.

S.2 De gouden tijd van de astrochemie

Astrochemie, ook bekend als moleculaire astrofysica, is de studie van de rijke en diverse chemie die voorkomt in het hele heelal (Herbst & Yates 2013). Meer specifiek is

[a] `http://www.astro.uni-koeln.de/cdms/molecules/`

dit de studie van de 'vorming, vernietiging en excitatie van moleculen in astronomische omgevingen en hun invloed op de structuur, dynamica en evolutie van astronomische objecten'(Dalgarno 2008). Met dank aan de snelle vooruitgang in wetenschap en technologie leven we nu in een gouden tijd voor de studie van de astrochemie.

Observationeel gezien is zeer veel vooruitgang geboekt door nieuwe telescopen. Er zijn bijvoorbeeld onlangs snelheid-opgeloste spectra beschikbaar gekomen op ver infrarode golflengtes die niet toegankelijk zijn van de grond. Dit geldt met name voor H_2O, waargenomen met behulp van het 'Heterodyne Instrument for the Far-Infrared' (HIFI) aan boord van de *Herschel Space Observatory* (Pilbratt et al. 2010; de Graauw et al. 2010). Men verwacht dat de Atacama Large Millimeter/submillimeter Array (ALMA) gaat leiden tot een nieuw decennium van astrochemie door een enorme toename van gevoeligheid en spatiële resolutie in vergelijking met eerdere faciliteiten. Samen met andere ruimtemissies zoals de James Webb Space Telescope (JWST), en verder in de toekomst, 30–40 m klasse optische-infrarode telescopen zoals de European Extremely Large Telescope (E-ELT) en de Thirty Meter Telescope (TMT), zullen deze instrumenten het mogelijk maken om astrochemie direct waar te nemen op de relevante fysische schaal, zowel spatieel als spectraal. Er bestaat geen enkele twijfel dat de vooruitgang onze verbeelding zal overtreffen, met als voorbeeld de recente Rosetta missie.

Rosetta vormt een mijlpaal in de sterrenkunde die geschiedenis heeft gemaakt door als eerste ruimteschip op een komeet te landen. Rosetta is een robot-ruimtesonde, gebouwd en gelanceerd door de European Space Agency, die momenteel bezig is met een gedetailleerde studie van komeet 67P/Churyumov-Gerasimenko, waarbij de instrumenten aan boord van de satelliet beelden en data verzamelen die informatie geven over de samenstelling van de komeet, inclusief de aanwezigheid van complexe organische moleculen. Zelfs sterrenkundige experts waren pas overtuigd van het succes van Rosetta toen ze de video en beelden van de satelliet en haar lander Philae 'life' zagen. Rosetta geeft een uniek beeld van het meest primitieve materiaal in ons eigen zonnestelsel, en dus van haar oorsprong.

Nauwkeurige reactie-coëfficiënten van belangrijke chemische processen zijn noodzakelijk voor astronomen vanuit chemisch-fysisch perspectief. Deze kunnen zowel experimenteel gemeten en/of theoretisch berekend zijn. Computationele methodes maken gebruik van (quasi-)klassieke en kwantummechanische methoden (of gemengde methoden), gebaseerd op zeer nauwkeurige *ab initio* potentiële energie oppervlakken. Deze methodes hebben enorm geprofiteerd van zowel de toenemende processorkracht en beschikbaarheid van krachtige (super) computers, als van nieuwe numerieke methodes.

Verscheidene chemische databases zijn nu online beschikbaar, met het doel om verschillende types astrochemische modellen te ondersteunen, en het is belangrijk dat ze up-to-date gehouden worden. Bijvoorbeeld de vijfde uitgave van de UMIST Database for Astrochemistry (UDfA, McElroy et al. 2013), hierna Rate12, bevat nu 6173 gasfase reacties van 467 soorten moleculen. Dit soort databases zijn nodig voor het simuleren van de chemie in verschillende fysische omgevingen, zoals donkere wolken, protoplanetaire schijven en circumstellaire omhullende gaswolken.

Moderne chemische fysica en astrochemie ondersteunen en inspireren elkaars vooruitgang, wat leidt tot een mooie en veelbelovende toekomst voor beide vakgebieden.

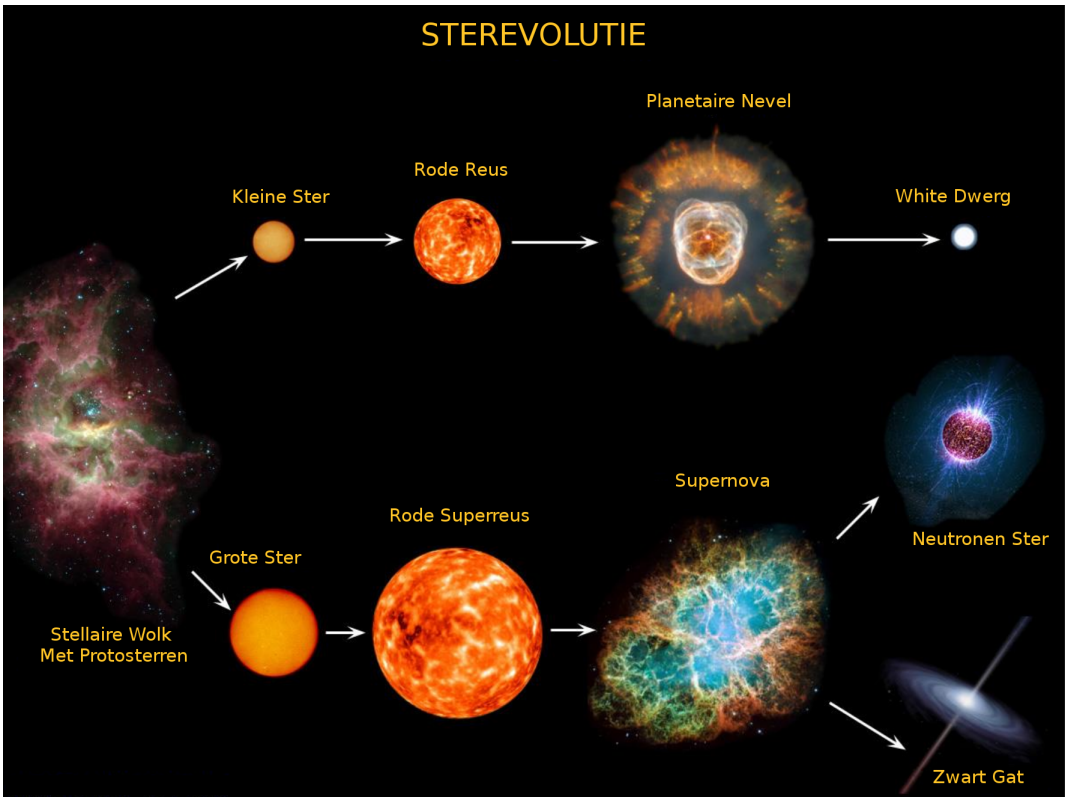

Figuur S.1 — De evolutie van een ster, gebaseerd op haar massa. Een lage massa ster eindigt als een witte dwerg, een massieve ster evolueert tot een neutronenster of een zwart gat. Figuur van E. Moravveji.

S.3 De vorming, evolutie en het afsterven van sterren

Het is bekend dat sterren worden gevormd in koude en dichte moleculaire wolken. Om een normale ster te vormen moeten deze wolken instorten, wat kan worden geïnduceerd door externe krachten ofwel door hun eigen zwaartekracht. Als de wolk zich bijvoorbeeld dichtbij een grote supernova bevindt kan de externe druk leiden tot haar instorting. Ook kunnen twee dichte moleculaire wolken met elkaar botsen door zwaartekracht. Meerdere sterren kunnen onmiddellijk worden geboren na de botsing van twee sterrenstelsels.

Fig. S.1 laat een algemeen beeld van de evolutie van een ster zien. Zodra deze gevormd is hangt haar toekomst af van de initiële massa. Lage massa (kleine) sterren, met name die met een massa van minder dan 8 M_{Zon}, passeren de rode reus en planetaire nevel fases voor ze eindigen als een witte dwerg. Massieve (grote) sterren gaan door de rode superreus fase en eindigen als supernova, waarbij ze een neutronenster of zwart gat produceren. Er zijn veel vragen rond deze scenario's, met name over het evolutionaire traject van de massieve ster, die plaatsvindt in een geclusterde omgeving. De discussie van dit proefschrift is gecentreerd rond de chemie van moleculen gedurende de geboorte en het overlijden van lage massa sterren, die beter begrepen zijn.

De vorming van een lage massa ster kan worden verdeeld in verscheidene evolutionaire fases. Het proces van de instorting van een donkere kern tot protoster tot pre-hoofdreeksster met een schijf waarin planeten vormen duurt enkele miljoenen jaren. Uiteindelijk verdwijnt ook deze schijf en er blijft een jonge ster met een kleine hoeveelheid

Figuur S.2 — De levenscyclus van moleculen in het heelal. Figuur door M. Persson, afkomstig van van Dishoeck (2014).

gruis in de schijf over. Ons zonnestelsel is door deze fases heen gegaan en nu, ongeveer 4.6 miljard jaar later, draagt ze nog steeds de sporen van deze vormingsprocessen. De gravitationele instorting van de wolk maakt warmte vrij waardoor de temperatuur van de protoster toeneemt en deuterium kernfusie induceert. Dit wordt gevolgd door waterstof kernfusie die zorgt dat de ster op de hoofdreeks blijft voor een lange stabiele periode. Lage massa sterren eindigen als een witte dwerg nadat het materiaal voor kernfusie uitgeput raakt. Een van de belangrijkste fases gedurende de late etappes van de evolutie is de asymptotische reuzentak (AGB). AGB sterren zijn in het bijzonder interessant omdat ze materiaal hun omgeving in schieten, waarbij een warm en dicht circumstellair omhulsel wordt gevormd. Dit proces leidt tot de vorming van nieuwe moleculen en de kernen van stofdeeltjes, en daarmee wordt gas en stof tot het ISM gerecycled voor de volgende cyclus van stervorming (Fig. S.2).

S.4 Inhoud van dit proefschrift en vooruitzicht

Dit proefschrift onderzoekt de chemie van interstellaire en circumstellaire moleculen gedurende de vorming en het afsterven van sterren. De onderwerpen van de vier hoofd-

stukken en de hoofdvragen waarop deze gericht zijn worden hieronder geschetst. Vanuit het perspectief van chemische fysica is het belangrijkste resultaat van dit proefschrift dat de snelheden voor twee essentiële reacties voor de eerste keer nauwkeurig bepaald zijn: N_2 fotolyse en reactiesnelheden van OH met H (zowel toestand-naar-toestand en thermisch).

In Hoofdstuk 2 wordt de fotodissociatie snelheid van interstellair N_2 bepaald. Stikstof is één van de meest abondante elementen in het heelal, en de verdeling van stikstof tussen N and N_2 bepaalt de vorming van meer complexe prebiotische stikstofhoudende moleculen. Fotodissociatie (of fotolyse) is de primaire vernietigingsroute van N_2 in elke omgeving waar UV-fotonen aanwezig zijn. Nieuwe fotolyse-snelheden en afschermingsfuncties voor N_2 zijn berekend op basis van een zeer nauwkeurig spectroscopisch model van het molecuul. Vervolgens zijn de N $\rightarrow$ N_2 overgangen in fotodissociatie gebieden PDRs) en andere astrofysische omgevingen gemodelleerd, en er wordt een vraagteken gesteld bij de enige, marginale detectie van N_2 in het absorptiespectrum van een diffuse wolk.

In Hoofdstuk 3 worden de nieuw afgeleide N_2 fotolyse-snelheden van Hoofdstuk 2 toegepast op de chemie in het circumstellaire omhulsel van een koolstof-rijke AGB ster, IRC +10216. Deze bron is de dichtstbijzijnde reuzetak-ster en het helderste object in het ver infrarode golflengtegebied, en één van de meest molecuulrijke bronnen aan de hemel. Volgens een gevoeligheidsanalyse van het gehele chemische netwerk is het $N_2 + h\nu \rightarrow N + N$ proces één van de meest significante reacties in de buitenste schil, maar de onzekerheid in dit proces was groot en het werd tot nu toe nooit correct geïmplementeerd. Naast de recent gerapporteerde fotolyse-snelheden en afschermingsfuncties van N_2 en CO in onze modellen, is ook een nieuw volledig 3D sferisch model van een isotroop interstellair stralingsveld gebruikt. De resultaten tonen aan dat met het RATE12 gasfase netwerk zonder de verbeterde fotolyse beschrijving de abondanties van veel N- en C-houdende moleculen heel anders zijn. De nieuwe resultaten worden vergeleken met observationele data en kloppen veel beter.

In Hoofdstuk 4 wordt de chemie van een zuurstof-rijke AGB ster bestudeerd met behulp van een benadering die vergelijkbaar is met Hoofdstuk 3, met onze nieuwe fotolyse beschrijving van N_2 en CO. De gemodelleerde schil is in dit geval dat rond de AGB star IK Tau, waarvoor veel data beschikbaar zijn. Ons verbeterde model van de circumstellaire chemie van Hoofdstuk 3 is gecombineerd met een nieuwe bepaling van de kritische 'moeder-moleculen', bijvoorbeeld de producten van de hoge temperatuur en schokchemie in de binnenste schil die de buitenste schil voeden. De belangrijke vorming en vernietigingsroutes van moleculen in IK Tau zijn geïdentificeerd, en we vinden hogere abundanties van O-houdende moleculen in vergelijking met Hoofdstuk 3, zoals H_2O, OH en NO. De aanwezigheid van verscheidene moleculen die gevormd zijn in de buitenste schillen kan worden gerelateerd aan de abondanties van moeder-moleculen, en kan dus limieten stellen aan hun abondanties door vergelijking met waarnemingen van IK Tau.

In Hoofdstuk 5 zijn toestandafhankelijke snelheidscoëfficiënten voor de experimenteel lastige reactie ($H + OH \longrightarrow O + H_2$) berekend. Het omgekeerde O (^{3}P) + H_2 systeem heeft meer dan een halve eeuw in de aandacht gestaan omdat het een belangrijk proces is bij verbranding en een significante rol speelt in warm interstellair gas zoals schokken, wolken die blootgesteld zijn aan UV-straling en de binnenste regionen van protoplanetaire schijven. Ondanks uitgebreid theoretisch en experimenteel onderzoek op O (^{3}P)

+ H_2, zijn er weinig studies gedaan naar de voorwaartse reactie, H + OH $(v, j) \rightarrow$ O + H_2. Nauwkeurige toestandspecifieke snelheidsconstantes van deze reactie, die nodig zijn in astrochemische modellen van dissociatieve schokken en schijven, ontbreken. In dit hoofdstuk worden zeer nauwkeurige *ab initio* potentiële energie oppervlakken gebruikt om quasi-klassieke trajectberekeningen en overgangs-toestand theorie uit te voeren. De berekende toestand-naar-toestand werkzame doorsnedes over een reeks van botsingsenergiën en interne rovibrationele excitatietoestanden worden vervolgens gebruikt om toestand-naar-toestand en thermische snelheidsconstantes te bepalen, inclusief hun temperatuurafhankelijkheden.

De hoofdresultaten van dit proefschrift zijn:

- Hoofdstuk 2. De nieuwe interstellaire N_2 fotolyse snelheid is bepaald met een onzekerheid van slechts 10%, een ordegrootte beter dan de vorige onzekerheid. Zelfafscherming en afscherming door H_2 en stof zijn effectiever dan afscherming door H en CO. De overgang van N $\rightarrow$ N_2 gebeurt bij vrijwel dezelfde diepte in een wolk als dat van $C^+ \rightarrow$ C $\rightarrow$ CO.
- Hoofdstuk 3. N_2 en CO zijn meer abondant aan de rand van een circumstellair omhulsel dan voorspeld bij vorige modellen dankzij een juiste behandeling van hun fotolyse processen. De nieuwe beschrijving induceert grote veranderingen in de voorspelde kolomdichtheden (factor 10) en piekstralen van sommige type moleculen (b.v., C_nN en C_nN^- koolstofketens) in het model van de koolstofrijke AGB-ster IRC +10216. De nieuwe modellen kunnen direct worden getest met toekomstige ALMA observaties.
- Hoofdstuk 4. De meest abondante dochter-moleculen die geschikt zijn voor toekomstige waarnemingen in de AGB-ster IK Tau zijn geïdentificeerd, gekwantificeerd en geanalyseerd, inclusief alle C-, N-, O-, Si-, S-, P-, Cl- en F-houdende moleculen. De belangrijke moleculaire processen in zuurstofrijke AGB omhulsels zijn fotoionisatie/fotolyse, ion-molecuul reacties en dissociatieve recombinatie. De bovenlimiet op het mogelijke moeder-molecuul CH_4 is $< 2.5 \times 10^{-6}$, gebaseerd op de waargenomen bovenlimieten van de twee dochter-moleculen, C_2H en CH_3OH. Toekomstige waarnemingen van NS en N_2H^+ kunnen worden gebruikt om de abondanties van moederdeeltjes S en N_2 te bepalen. Tenslotte heeft de snelheid waarmee de AGB ster massa verliest een grote invloed op de berekende abondanties, welke normaal gesproken moeilijk direct te bepalen is met waarnemingen.
- Hoofdstuk 5. Reactieconstantes voor OH in geëxciteerde vibrationele en rotationele toestanden met H zijn ordegroottes sneller dan de thermische reactieconstantes. Dit moet worden meegenomen in toekomstige astrochemische modellen. Een effectieve barrière kan worden geïnduceerd door de rotationele excitatie bij lagere botsingsenergiën (< 0.6 eV).

De toekomst van astrochemie ziet er goed uit. Dit blijkt uit de snelle vooruitgang in observationele technieken en theoretische en laboratorium fysica en chemie, en hun combinatie in geavanceerde modellen van astronomische objecten. Dit proefschrift tracht een reeks van deze astrochemische aspecten te beslaan. Meer waarnemingen zullen op zich nog meer vragen oproepen, en met verbeterde modellen zullen sommige vragen worden beantwoord. Maar het begrip van deze waarnemingen zal ongetwijfeld verdere inspanningen vragen van chemici om nauwkeurige snelheidscoëfficiënten te bepalen.

Men moet ook verder in de toekomst kijken. Neem opnieuw de Rosetta missie als voorbeeld. Deze missie, meer dan 30 jaar geleden gepland, heeft niet alleen geholpen in het beantwoorden van vele interessante astrochemische vragen maar heeft ook bewezen dat (vrijwel) alles is mogelijk in de toekomst zolang men een langetermijn visie heeft. Dit geldt met name voor de astrochemie.

中文结论

C.1 分子的宇宙

宇宙广袤无垠, 但很多我们在夜空中看到的物体——行星、恒星和星系——实际上源自于原子和分子之间的微观化学反应过程。原子与分子辐射的各种光谱谱线，可以通过灵敏的望远镜探测到。所以，天文学家能够"以小窥大"——通过研究分子来研究宇宙——从分子的尺度以及其相互作用的层面上。这需要天文学和化学物理（或者物理化学）两方面的知识。这种研究，刺激了近年来天体化学的迅速发展。从理论上讲，天体化学这门学科，可以从量子力学的高度上回答我们对宇宙的各种问题——这是多么让人振奋啊！宇宙的本质很可能是量子的！从这个角度来说，我们处在一个"分子的宇宙"中 (Tielens 2013)。

迄今为止，宇宙空间中已有近 180 个不同的分子（不包括同位素）被探测并识别。这主要是通过它们的的转动、振动以及电子光谱实现的[b]。其中包括小分子，如 CO 和 H_2O 分子, 以及大分子，如多环芳香烃 (PAHs), 以及富勒烯，例如 C_{60}^+、C_{60} 和 C_{70}。现在已经知道，分子普遍存在于中性星际介质的所有阶段，从弥漫云到致密分子云再到致密恒星——最后到行星形成的区域，从处于死亡阶段的恒星的包层到星系的中心区域。而且，分子在这些地方的丰度还比较高。这些分子以及它们的化学属性为我们探索恒星、星团、星系、以及星际物过去和未来，打开了一扇窗口，既包含其物理属性，亦包含其化学属性。这是因为，分子的激发和丰度取决于它们之间的碰撞，而碰撞又对气体的密度和温度以及其周围环境的辐射场非常敏感 (van Dishoeck 2014)。因此，分子是宇宙中星体或者其它物理环境的"染料"(或者说"失踪器")。

宇宙中其它地方很可能存在着生命。那些生命诞生的第一个步骤，很可能是一些被称作"生命起源以前的星际分子"的诞生过程。其后，这些分子之间的相互作用形成更为复杂的结构。我们人类在这个宇宙中并不孤独——至少从我们的构成来看是这样的。因为，从目前的研究成果来看，组成我们的所有分子，和组成宇宙中分子云、行星、恒星、星云，以及其它很多不同状态物体的分子，是没有什么太大的区别的。这意味着，天体化学的研究，不但能够帮助我们更好的理解我们所居住的行星以及太阳系的起源以及演化，最终肯定也能帮助我们更好的理解"生命"的起源以及未来，其中当然包括我们"人类"自己的过去和将来。因此，近年来，天体化学引起了越来越多的学者的研究兴趣，并得以迅速发展。

C.2 天体化学的黄金时代

天体化学，也被称作分子天体物理学，是研究发生在整个宇宙中的丰富多样的化学的一门学科 (Herbst & Yates 2013)。具体来讲，它是研究"分子在天文环境中的形成、解离、激发以及其对天文学研究对象的结构、动力学、以及演化的影响的一门学科"(Dalgarno 2008)。得益于迅速发展的科学技术，如今，我们生活在研究天体化学的黄金时代。

[b] http://www.astro.uni-koeln.de/cdms/molecules/

新的望远镜的应用推动了天文观测领域的显著进步。例如，许多分子在远红外波段的速度可分辨光谱用地球上的望远镜是观测不到的。如今，天文学家却已经获得了这样的数据，尤其是 H_2O 分子的光谱——借助于太空中的远红外望远镜，即赫歇尔空间天文台（Herschel Space Observatory），详见 Pilbratt et al. (2010); de Graauw et al. (2010)。

天体化学在未来十年内的发展必将突飞猛进，尤其是因为得益于地球上目前为止最强大的望远镜——阿塔卡玛大型毫米波天线阵（Atacama Large Millimeter/submillimeter Array，缩写为 ALMA，简称阿尔马）良好运行。与以前的望远镜相比，ALMA 在灵敏度和空间分辨率方面都有了巨大的提高。另外，其它太空望远镜，例如，詹姆斯·韦伯空间望远镜（James Webb Space Telescope，缩写为 JWST），以及未来的 30—40 米类的欧洲极大望远镜（European Extremely Large Telescope，简写 E-ELT），使得天文学家对所观测的天体对象的直接成像成为现实，可以从光谱和空间两方面来加以研究。毫无疑问，天体化学领域的某些进展将超过我们目前的想象。已经发生的例子，就是罗塞塔号计划（Rosetta mission）。

罗塞塔号取得的巨大成功是天文学领域的一个重大里程碑，已经被载入史册。简言之，罗塞塔号是欧洲空间局组织的机器人空间探测器计划，它将一颗人类制造的卫星成功发射到了彗星表面，使得那颗卫星和彗星一起在宇宙中漫游，并将该彗星的组成、结构等各种数据和图像源源不断的发射回地球，供天文学家研究。这些数据包括组成彗星的各种小分子和复杂的有机分子。那颗卫星的名字叫做 67P/楚留莫夫 - 格拉希门克（67P/Churyumov–Gerasimenko）。这在人类探索宇宙的道路上是一大壮举。即使是资深天文学家，只有在看到了这颗卫星和它所携带的登陆机器人（名称为 Philae）发送回地球上的清晰的视频和图片资料的时候，才相信了这个事实。罗塞塔号反馈给我们的是非常珍贵的资料——关于我们所生活的太阳系起源的信息，这是因为彗星是太阳系中最古老的存在之一。

从化学物理（或者物理化学）的角度来讲，天文学家需要很多化学反应的精确的反应速率。大部分这样的数据已经从实验中得到了测量，并且/或者从理论方面计算得到。计算方面，比较典型的方法有基于精确从头算 *ab initio* 势能面的准经典轨线计算方法和量子力学方法（或者两者混合的计算）。它们都极大受益于计算能力不断提高的强大的（超级）计算机，以及新的算法。

旨在支持不同类型天体化学模拟的化学网络数据库已经建成并被广泛使用。这种数据库需要不断的维护和更新。目前为止，使用最广泛的数据库是 UMIST (UDfA, McElroy et al. 2013)，也被称作 Rate12。这个数据库已经有近 30 年的历史，有不同的版本，每个版本包含的化学反应的数目和分子不太一样。目前为止，已经升级到第五版，包含 6173 种化学反应和 467 个分子。这些数据库在模拟不同天体的物理或者化学性质的时候非常有用，比如暗云、原行星盘系统、恒星包层等。

现代化学物理（或物理化学）和天体化学实际上彼此支持，彼此促进，使得这两个领域的前途都非常光明。

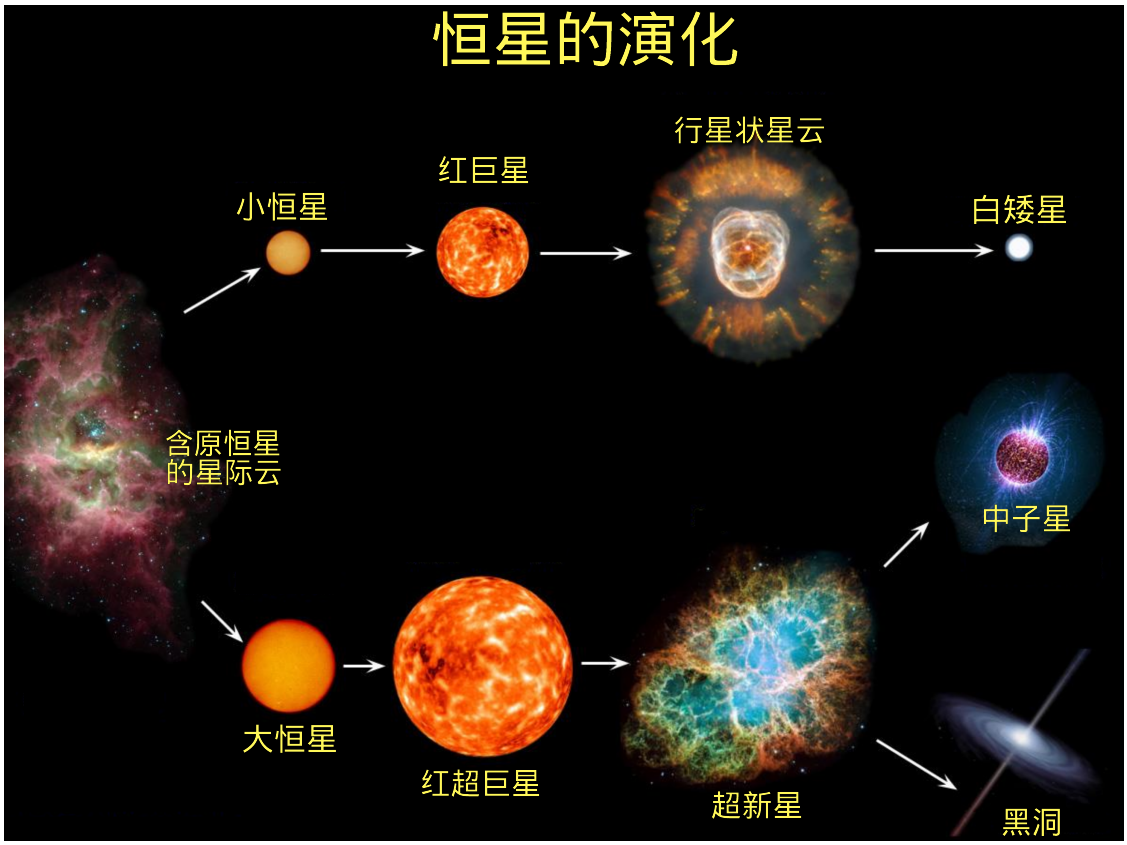

图 **C.1** — 恒星的演化过程，很大程度上取决于其质量的大小。质量小的恒星最终可能会演化为一颗白矮星，而质量大的恒星可能会演化为一颗中子星或者黑洞。该图是从 E. Moravveji 博士提供的原图的基础上翻译而成。

C.3 恒星的形成、演化和命运

我们知道，恒星诞生于致密分子云。但是，为了形成一颗普通的恒星，分子云必须坍塌。这可以由外力或由它们自身的引力作用来诱导完成。举例来说，如果分子云足够接近一个巨大的超新星，其外部压力可能会导致分子云坍塌。两个致密分子云也可以因为万有引力的原因相互碰撞。还有，两个星系如果碰撞，瞬间就可能导致很多恒星的产生。

图 C.1 给出了恒星的演化过程。一旦恒星从分子云中产生，其演化过程在很大程度上取决于其初始质量的大小。低质量（或者说小）恒星，特别是那些质量小于 $8\ M_{\odot}$ 的恒星，会变成红巨星，再变成行星状星云，最后演变为一颗白矮星。而高质量（或者说大）恒星则会演变为红超巨星，再变为超新星，最后终结为一颗中子星或者黑洞。恒星在这些演变过程中的很多细节还不清楚，尤其是高质量恒星的演化过程。目前只是知道它们发生在团簇状的天体物理环境中。本文的讨论重点是低质量的恒星的诞生和死亡过程中的分子的化学性质。天文学家们对这个领域有着比较成熟的理解。

低质量的恒星的形成可分为几个不同的演化阶段。从坍缩的暗云形成星核到形成行星状星云，再到可以形成行星系统的含有盘系统的早期主序星阶段，大致需要几百万年的时间。最终，盘系统也会消失，只留下一颗年轻的恒星，它的周围残留着很小一部分的宇宙尘埃。我们的太阳系已经经历了这个过程。目前，太阳系的寿命已经有四十六

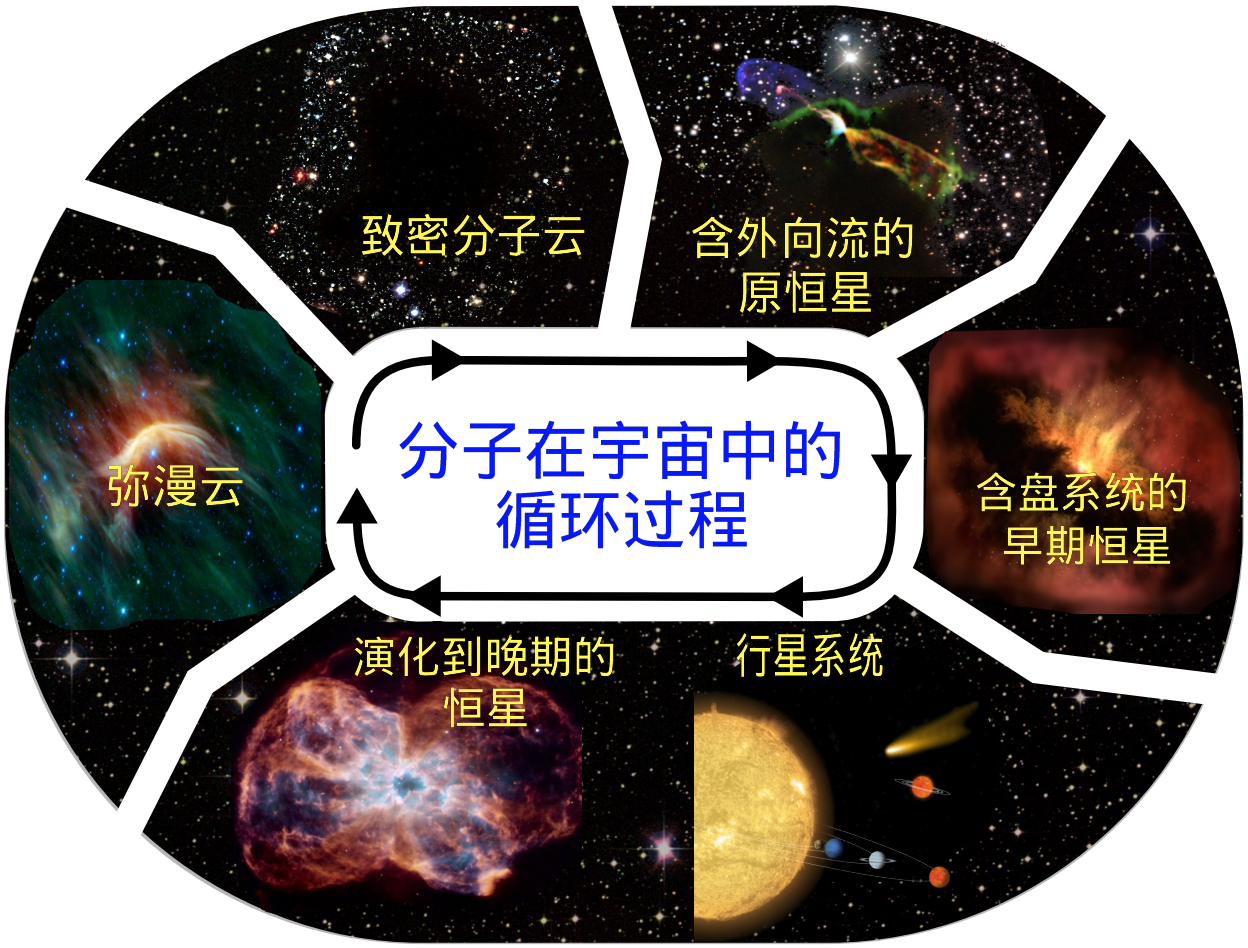

图 **C.2** — 分子在宇宙中的循环过程。该图是 M. Persson 博士为 van Dishoeck (2014) 的综述文章所设计的插图，原图的示例文字采用的是英文。本人对该图进行了改进，并翻译成了荷兰文和中文两个版本。

亿年了，却任带有它最初从分子云中形成时的印记。

宇宙中分子云的引力坍缩释放热量，增加原恒星的温度，诱导氘核聚变。之后发生的是氢核聚变。氢核聚变让恒星长期稳定的处于主序星阶段。当核聚变耗尽燃料之后，低质量的恒星最终会变成白矮星。恒星演化后期，最重要的阶段之一是渐近巨星分支（AGB）阶段。天文学家对 AGB 恒星尤为感兴趣。这是因为，这种恒星不断向其周围喷射气体分子和宇宙尘埃，于是形成了一个温暖而致密的包层（CSE）。这个过程包含了复杂的物理化学反应，能生成新的分子，而且将星际气体和尘埃返还给星际介质（ISM），从而导致新的分子云的产生，而这些分子云将重新孕育新的恒星，从而进入下一轮恒星的演化过程。如此，周而复始，不断循环，见示意图 C.2。

C.4 该博士毕业论文的主要内容及展望

本毕业论文探讨了在恒星形成和死亡过程中，星际分子和恒星包层中的分子的化学性质。论文主体用英语写成，主要结论翻译成了中文和荷兰文。该论文的第一章是研究综述，包含研究背景和主要结论。第二到第五章则是各个子课题的研究细节。这里，我们概括一下本论文最主要的工作和发现。从化学物理或者物理化学的角度来看，该论文

最重要的贡献在于，我们首次精确研究了两个重要的化学反应速率：一个是 N_2 的光解速率。为了这个目标，物理化学家和天文学家已经合力奋斗了二十年左右。现在终于得以实现。另一个是 H 原子与 OH 分子的反应，本文精确计算了态 -态反应速率以及热速率常数。从天文学的角度来看，我们发展了新的、精确的计算分子屏蔽函数的方法，解决了红巨星包层模拟中一个存在了很久的问题。使用新的模型和算法，我们模拟了两颗典型的红巨星包层中的分子的分布。这些结果是目前为止该领域最精确的数据。它们为未来的天文观测提供了直接的依据。

在第二章中，我们研究得到了 N_2 分子在星际中的精确光解速率。氮是宇宙中含量最高的元素之一。N 原子与 N_2 之间的相互转化，控制着更为复杂的含 N 元素的分子的形成过程。在任何有强 UV 光子的星际区域中，光解是 N_2 分子最主要的解离过程。基于分子的高精度光谱，使用我们的天体化学模型，以及精确的 H 和 H_2 分子的高精度光谱，我们计算了不同辐射场、不同温度、不同宇宙环境中的精确的 N_2 分子的光解速率以及屏蔽函数。同时，使用不同的天体化学 $N \rightarrow N_2$ 在光解占主导的区域以及其它天体物理环境中的转化过程。这样，我们发现了一些非常有趣的现象。比如，我们发现以前所报道的探测到的 N_2 分子的吸收光谱可能是不可靠的 (他们的结果是发表在《自然》杂志上的)。

在第三章中，我们将第二章中所计算得到精确的 N_2 光解速率应用到了一个富含碳的红巨星（IRC+10216）模型中，重新研究了这颗恒星周围的气体分子的分布和化学性质。这颗星是离地球最近的渐近巨星分支恒星，它是远红外波段天空中最亮的物体，并且也是所含分子种类最丰富的天体对象之一。根据对天体化学模型中用到的庞大的化学网络的敏感性分析，氮分子的光解过程，即 $N_2 + h\nu \rightarrow N + N$，是整个化学网络中最重要的反应之一。然而，该反应从来没有被正确研究过。本文中，我们除了采用了最新报道的 N_2 和 CO 的光解速率以及屏蔽函数，还发展了一种全新的采用分子屏蔽函数的方法。这种方法在各向异性的星际辐射场中，考虑来自各个方向的光子对光解速率的影响。也就是说，是完全三维的处理方法。同时，我们还采用了最新发布的化学网络的数据库，即 RATE12 气相反应网络。做了这些改进之后，我们发现，很多含 N 和含 C 的分子的丰度和化学反应都和以前有所不同。我们把最新的结果与天文观测得到的数据进行了比较。

在第四章中，我们采用与第三章类似的模型，研究了一颗富含氧的红巨星。具体而言，我们研究的恒星是 IK Tau。近年来，关于这颗恒星的高精度天文观测已经有很多报道，但是模拟方面所能参考的数据却是二十年以前的，很不准确。本文研究中，我们遴选了目前为止最精确的天文观测方面的数据，以及各种理论研究的核心结论，辅以我们所开发的全新的模型，最大程度上准确研究了这颗恒星包层中子分子的形成和解离过程，并找出了丰度最高的子分子。这项研究对以后的天文观测非常有用。与第三章不同的是，这里丰度最高的分子是含氧元素的分子，比如H_2O, OH, 和 NO。某些子分子的丰度与它们的母分子的丰度是紧密相关的，因此我们能够根据子分子的丰度来间接研究母分子的丰度。

在第五章，我们计算了实验上很难研究的基元反应 $H + OH \longrightarrow O + H_2$ 的态 –态分辨速率系数。这个反应的逆向反应 $O(^3P) + H_2$ 已经被研究了超过半个世纪，这是因为这个过程不仅属于燃烧化学，而且在高温的星际气体中，如激流、强紫外辐射场中的星际云、以及原恒星的盘系统区域中，都起着一个非常重要的作用。尽管理论和实验对

$O(^3P) + H_2$ 的研究颇多, 却鲜有关于其正向反应，$H + OH\ (v, j) \rightarrow O + H_2$ 的研究。天文学家在研究离解的激流和盘系统中，必须用到该反应的态 –态反应速率。然而，这些数据却从未被报道。在本章中，我们基于高精度的从头算（*ab initio*）势能面，用准经典轨线方法和各种过渡态理论方法研究得到了这些必须的数据。我们首先计算了不同碰撞能下的振转激发态的态 –态反应截面，然后推导出了态 –态反应速率以及热速率常数。

本论文的主要结果概括如下：

- 第二章：计算了 N_2 分子的精确的光解速率，误差被控制在 10% 以内，该误差比以前所使用的数据的误差减小了一个数量级。对 N_2 分子而言，自我屏蔽（self-shielding）、星际尘埃屏蔽、以及 H_2 分子的屏蔽作用远比 H 原子和 CO 分子的屏蔽更有效。在星际云中，$N \rightarrow N_2$ 与 $C^+ \rightarrow C \rightarrow CO$ 的转化几乎发生在同一深度。

- 第三章：提出了一种精确计算分子自我屏蔽以及多重屏蔽函数的方法，并采用这种方法研究了一颗富含碳的红巨星包层中分子的分布。对于 N_2 和 CO 分子在红巨星包层边缘的丰度而言，新模型预示的结果比以前的预示结果高出很多。对于 IRC +10216 这颗红巨星而言，我们所采用的对分子光解速率的精确求解过程，导致了某些分子（例如，C_nN 和 C_nN^- 碳链）的柱密度和峰值半径的显著变化（十倍左右）。这些新的结果可以通过未来的 ALMA 的观测直接加以证实。

- 第四章：对于富含氧的红巨星 IK Tau，我们识别、量化和分析了丰度最高的子分子，包括所有含 C-，N，O，Si，P，S, Cl, 和 F 的分子。这些分子最有可能在未来的天文观测中被识别出来。富含氧的红巨星包层中，最关键的分子反应过程是光电离和光解，离子 -分子反应，和分离性重组（dissociative recombination）。CH_4 有可能是一个母分子。在模拟中，我们根据 CH_4 的两个子分子（C_2H 和 CH_3OH）在天文观测上的上限，获得了其丰度上限，为 $< 2.5 \times 10^{-6}$。如果将来能够观测和识别出 NS 和 N_2H^+，我们就能间接模拟出它们的母分子（S 和 N_2）的丰度。最后，恒星的质量亏损速率是很难从天文观测中直接获得的。然而，它在模拟分子的丰度的过程中有着很重要的作用。

- 第五章：基元反应 $H + OH \rightarrow O + H_2$ 的振动激发和转动激发的速率常数比其热速率常数高出好几个数量级。这在天体化学模型中需要被考虑进去。低能碰撞 (< 0.6 eV) 的情况下，转动激发可能导致该体系产生了一个有效势垒。

毫无疑问，天体化学领域的前景是一片光明的。这是因为，天文观测技术与物理化学（理论和实验）领域的迅速发展，为复杂的天体化学模型提供了必要的支持。本文试图涵盖天体化学在这些方面所取得的成就。随着更多观测结果的出现，以及人们对天体对象的理解的不断加深，一定会有新的问题浮现出来。同时，不断改进的天体化学模型，能帮助我们理解一部分新出现的问题。但是，解释新的观测结果，无疑会需要物理化学家们做出更多的努力，提供天体化学研究中所必须的精确的反应速率系数。

对于未来，我们必须努力看得更远。再次拿罗塞塔号（Rosetta）机器人空间探测器计划为例来说明。30 年之前制定的这个计划，不但有助于研究和理解许多有趣的天体化学方面的问题，而且也证明了（几乎）任何事情都是有可能发生的——从长远的角度来说！对人类唯一的限制就是我们的想象力——这种说法是非常有道理的，尤其是在

迅速发展的天体化学领域。

Bibliography

Abgrall, H., Roueff, E., Launay, F., Roncin, J. Y., & Subtil, J. L. 1993a, A&AS, 101, 273

Abgrall, H., Roueff, E., Launay, F., Roncin, J. Y., & Subtil, J. L. 1993b, A&AS, 101, 323

Agúndez, M. & Cernicharo, J. 2006, ApJ, 650, 374

Agúndez, M., Cernicharo, J., & Goicoechea, J. R. 2008a, Astron. Astrophys., 483, 831

Agúndez, M., Cernicharo, J., & Guélin, M. 2010a, ApJ, 724, L133

Agúndez, M., Cernicharo, J., Guélin, M., et al. 2010b, A&A, 517, L2

Agúndez, M., Fonfría, J. P., Cernicharo, J., et al. 2012, A&A, 543, A48

Agúndez, M., Fonfría, J. P., Cernicharo, J., Pardo, J. R., & Guélin, M. 2008b, A&A, 479, 493

Agúndez, M. & Wakelam, V. 2013, Chemical Reviews, 113, 8710

Aikawa, Y., van Zadelhoff, G. J., van Dishoeck, E. F., & Herbst, E. 2002, A&A, 386, 622

Aikawa, Y., Wakelam, V., Garrod, R. T., & Herbst, E. 2008, ApJ, 674, 984

Ajello, J. M., James, G. K., Franklin, B. O., & Shemansky, D. E. 1989, Phys. Rev. A, 40, 3524

André, M. K., Oliveira, C. M., Howk, J. C., et al. 2003, ApJ, 591, 1000

Asplund, M., Grevesse, N., Sauval, A. J., & Scott, P. 2009, ARA&A, 47, 481

Atahan, S., Alexander, M. H., & Rackham, E. J. 2005, J. Chem. Phys., 123, 204306

Atahan, S., Klos, J., Zuchowski, P. S., & Alexander, M. H. 2006, Phys. Chem. Chem. Phys., 8, 4420

Balakrishnan, N. 2003, J. Chem. Phys., 119, 195

Balakrishnan, N. 2004, J. Chem. Phys., 121, 6346

Baulch, D. L., Bowman, C. T., Cobos, C. J., et al. 2005, Journal of Physical and Chemical Reference Data, 34, 757

Baulch, D. L., Cobos, C. J., Cox, R. A., et al. 1992, J. Phys. Chem. Ref. Data, 21, 411

Baulch, D. L., Cobos, C. J., Cox, R. A., et al. 1994, J. Phys. Chem. Ref. Data, 23, 847

Bergin, E. A., Aikawa, Y., Blake, G. A., & van Dishoeck, E. F. 2007, Protostars and Planets V, 751

Bergin, E. A., Alves, J., Huard, T., & Lada, C. J. 2002, ApJ, 570, L101

Bethell, T. & Bergin, E. 2009, Science, 326, 1675

Bettens, R. P. A., Lee, H.-H., & Herbst, E. 1995, ApJ, 443, 664

Bieging, J. H. & Rieu, N.-Q. 1988, ApJ, 329, L107

Black, J. H. & van Dishoeck, E. F. 1987, ApJ, 322, 412

Boersma, C., Hony, S., & Tielens, A. G. G. M. 2006, A&A, 447, 213

Bohlin, R. C., Savage, B. D., & Drake, J. F. 1978, ApJ, 224, 132

Bowman, J. M., Wagner, A. F., Walch, S. P., & Thom. H. Dunning, J. 1984, J. Chem. Phys., 81, 1739

Brandão, J., Mogo, C., & Silva, B. C. 2004, J. Chem. Phys., 121, 8861

Braunstein, M., Adler-Golden, S., Maiti, B., & Schatz, G. C. 2004, J. Chem. Phys., 120, 4316

Cernicharo, J., Guélin, M., Agúndez, M., McCarthy, M. C., & Thaddeus, P. 2008, ApJ, 688, L83

Cernicharo, J., Guélin, M., & Kahane, C. 2000, A&AS, 142, 181

Cernicharo, J., Waters, L. B. F. M., Decin, L., et al. 2010, A&A, 521, L8

Chatfield, D. C., Friedman, R. S., Lynch,

G. C., Truhlar, D. G., & Schwenke, D. W. 1993, J. Chem. Phys., 98, 342
Cherchneff, I. 2006, A&A, 456, 1001
Cherchneff, I. 2011, in EAS Publications Series, ed. C. Joblin & A. G. G. M. Tielens, Vol. 46, 177–189
Cherchneff, I. 2012, A&A, 545, A12
Cho, S.-H. & Ukita, N. 1998, AJ, 116, 2495
Chu, T.-S., Zhang, X., & Han, K.-L. 2005, J. Chem. Phys., 122, 214301
Chu, T. S., Zhang, Y., & Han, K. L. 2006, Int. Rev. Phys.Chem., 25, 201
Codella, C., Viti, S., Ceccarelli, C., et al. 2013, ApJ, 776, 52
Cohen, N. & Westberg, K. R. 1983, J. Phys. Chem. Ref. Data, 12, 531
Cordiner, M. A. & Millar, T. J. 2009, ApJ, 697, 68
Crapsi, A., Caselli, P., Walmsley, C. M., et al. 2005, ApJ, 619, 379
D'Alessio, P., Calvet, N., Hartmann, L., Lizano, S., & Cantó, J. 1999, ApJ, 527, 893
Dalgarno, A. 2008, ARA&A, 46, 1
Danilovich, T., Bergman, P., Justtanont, K., et al. 2014, A&A, 569, A76
Daranlot, J., Hincelin, U., Bergeat, A., et al. 2012, Pro. Natl. Acad. Sci., 109, 10233
De Beck, E., Decin, L., de Koter, A., et al. 2010, A&A, 523, A18
De Beck, E., Kamiński, T., Patel, N. A., et al. 2013, A&A, 558, A132
De Beck, E., Lombaert, R., Agúndez, M., et al. 2012, A&A, 539, A108
de Graauw, T., Helmich, F. P., Phillips, T. G., et al. 2010, A&A, 518, L6
De Luca, M., Gupta, H., Neufeld, D., et al. 2012, ApJ, 751, L37
Decin, L. 2012, Advances in Space Research, 50, 843
Decin, L., Agúndez, M., Barlow, M. J., et al. 2010, Nature, 467, 64
Decin, L., Cherchneff, I., Hony, S., et al. 2008, A&A, 480, 431
Decin, L., De Beck, E., Brünken, S., et al. 2010a, A&A, 516, A69
Decin, L., Justtanont, K., De Beck, E., et al. 2010b, A&A, 521, L4
Dinh-V-Trung & Lim, J. 2008, ApJ, 678, 303
Draine, B. T. 1978, ApJ, 36, 595
Duari, D., Cherchneff, I., & Willacy, K. 1999, A&A, 341, L47
Dunne, L. J. & Murrell, J. N. 1983, Mol. Phys., 50, 635
Dutrey, A., Henning, T., Guilloteau, S., et al. 2007, A&A, 464, 615
Eichelberger, B., Snow, T. P., Barckholtz, C., & Bierbaum, V. M. 2007, ApJ, 667, 1283
Evans, II, N. J., Dunham, M. M., Jørgensen, J. K., et al. 2009, ApJ, 181, 321
Fernandez-Ramos, A., Ellingson, B. A., Garrett, B. C., & Truhlar, D. G. 2007, POLYRATE-9.7
Fernandez-Ramos, A., Ellingson, B. A., Garrett, B. C., & Truhlar, D. G. 2013, NIST Chemical Kinetics Database Nist., `http://kinetics.nist.gov/kinetics/index.jsp`
Fong, D., Meixner, M., & Shah, R. Y. 2003, ApJ, 582, L39
Fong, D., Meixner, M., Sutton, E. C., Zalucha, A., & Welch, W. J. 2006, ApJ, 652, 1626
Fontani, F., Palau, A., Caselli, P., et al. 2011, A&A, 529, L7
Fuchs, G. W., Cuppen, H. M., Ioppolo, S., et al. 2009, A&A, 505, 629
Garashchuk, S., Rassolov, V. A., & Schatz, G. C. 2006, J. Chem. Phys., 124, 244307
Garrod, R. T. & Herbst, E. 2006, A&A, 457, 927
Garton, D. J., Brunsvold, A. L., Minton, T. K., et al. 2006, J. Phys. Chem. A, 6, *110* , 1327
Garton, D. J., Minton, T. K., Maiti, B., Troya, D., & Schatz, G. C. 2003, J. Chem. Phys., 118, 1585
Geppert, W. D., Hamberg, M., Thomas, R. D., et al. 2006, Faraday Discuss., 133, 177
Gerin, M., de Luca, M., Black, J., et al. 2010, A&A, 518, L110
Gerin, M., de Luca, M., Lis, D. C., et al. 2013,

J. Phys. Chem. A, 117, 10018
Gielen, C., Cami, J., Bouwman, J., Peeters, E., & Min, M. 2011, A&A, 536, A54
Glassgold, A. E. 1996, ARA&A, 34, 241
Gobrecht, D., Cherchneff, I., Sarangi, A., Plane, J. M. C., & Bromley, S. T. 2014, A&A, submitted
Gondhalekar, P. M., Phillips, A. P., & Wilson, R. 1980, A&A, 85, 272
Graff, M. M. & Dalgarno, A. 1987, Astrophys. J., 317, 432
Guélin, M. 2011, in EPJ Web of Conferences, 18, 1002
Guélin, M., Neininger, N., & Cernicharo, J. 1998, A&A, 335, L1
Guélin, M., Neininger, N., Lucas, R., & Cernicharo, J. 1999, in The Physics and Chemistry of the Interstellar Medium, ed. V. Ossenkopf, J. Stutzki, & G. Winnewisser, 326
Habing, H. J. 1968, Bull. Astron. Inst. Netherlands, 19, 421
Han, B. & Zheng, Y. 2011, J. Comput. Chem., 32, 3520
Hase, W. L., Duchovic, R. J., Hu, X., et al. 1996, Quantum Chem. Progr. Exch., 16, 671
Haverd, V. E., Lewis, B. R., Gibson, S. T., & Stark, G. 2005, J. Chem. Phys., 123, 214304
Heays, A. N. 2011, PhD thesis, The Australian National University
Heays, A. N., Dickenson, G. D., Salumbides, E. J., et al. 2011, J. Chem. Phys., 135
Heays, A. N., Lewis, B. R., Stark, G., et al. 2009, J. Chem. Phys., 131, 194308
Heays, A. N., Visser, R., Gredel, R., et al. 2014, A&A, 562, A61
Helm, H., Hazell, I., & Bjerre, N. 1993, Phys. Rev. A, 48, 2762
Henning, T. & Semenov, D. 2013, Chemical Reviews, 113, 9016
Herbst, E., Green, S., Thaddeus, P., & Klemperer, W. 1977, ApJ, 215, 503
Herbst, E. & Klemperer, W. 1973, ApJ, 185, 505
Herbst, E. & Osamura, Y. 2008, ApJ, 679, 1670
Herbst, E. & Yates, Jr., J. T. 2013, Chemical Reviews, 113, 8707
Herwig, F. 2005, ARA&A, 43, 435
Hoffmann, M. R. & Schatz, G. C. 2000, J. Chem. Phys., 113, 9456
Hollenbach, D. J. & Tielens, A. G. G. M. 1997, ARA&A, 35, 179
Howard, M. J. & Smith, I. W. M. 1982, J. Chem. Soc. Faraday Trans. 2 Mol. Chem. Phys., 78, 1403
Howard, R. E., McLean, A. D., & W. A. Lester, J. 1979, J. Chem. Phys., 71, 2412
Huber, K. P. & Herzberg, G. 1979, Molecular spectra and molecular structure IV: Constants of diatomic molecules (Van Nostrand, New York)
Huggins, P. J., Olofsson, H., & Johansson, L. E. B. 1988, ApJ, 332, 1009
Iben, Jr., I. & Renzini, A. 1983, ARA&A, 21, 271
Jansen, D. J., Spaans, M., Hogerheijde, M. R., & van Dishoeck, E. F. 1995a, A&A, 303, 541
Jansen, D. J., van Dishoeck, E. F., Black, J. H., Spaans, M., & Sosin, C. 1995b, A&A, 302, 223
Johnson, B. R. & Winter, N. W. 1977, J. Chem. Phys., 66, 4116
Joseph, T., Truhlar, D. G., & Garrett, B. C. 1988, J. Chem. Phys., 88, 6982
Ju, L. P., Han, K. L., & Zhang, J. Z. H. 2009, J. Comput. Chem., 30, 305
Jura, M. & Morris, M. 1981, ApJ, 251, 181
Justtanont, K., Khouri, T., Maercker, M., et al. 2012, A&A, 537, A144
Karplus, M., Porter, R. N., & Sharma, R. D. 1965, J. Chem. Phys., 43, 3259
Kim, H., Wyrowski, F., Menten, K. M., & Decin, L. 2010, A&A, 516, A68
Knauth, D. C., Andersson, B.-G., McCandliss, S. R., & Warren Moos, H. 2004, Nature, 429, 636
Kumar, S. S., Hauser, D., Jindra, R., et al. 2013, ApJ, 776, 25
Kwon, Y.-J. & Suh, K.-W. 2012, J. Korean.

Astron. Soc., 45, 139
Langer, W. D. & Graedel, T. E. 1989, ApJ, 69, 241
Le Bertre, T. 1997, Lecture Notes in Physics, Vol. 497, Stellar Atmospheres: Theory and Observations, ed. J. P. Greve, R. Blomme, & H. Hensberge (Berlin, Heidelberg: Springer Berlin Heidelberg), 133
Le Petit, F., Nehmé, C., Le Bourlot, J., & Roueff, E. 2006, ApJ, 164, 506
Lee, H.-H., Herbst, E., Pineau des Forets, G., Roueff, E., & Le Bourlot, J. 1996, A&A, 311, 690
Lefebvre-Brion, H. & Field, R. W. 2004, The spectra and dynamics of diatomic molecules (Elsevier)
Lewis, B. R., Baldwin, K. G. H., Heays, A. N., et al. 2008a, J. Chem. Phys., 129, 204303
Lewis, B. R., Baldwin, K. G. H., Sprengers, J. P., et al. 2008b, J. Chem. Phys., 129, 164305
Lewis, B. R., Gibson, S. T., Sprengers, J. P., et al. 2005a, J. Chem. Phys., 123, 236101
Lewis, B. R., Gibson, S. T., Zhang, W., Lefebvre-Brion, H., & Robbe, J.-M. 2005b, J. Chem. Phys., 122, 144302
Lewis, B. R., Heays, A. N., Gibson, S. T., Lefebvre-Brion, H., & Lefebvre, R. 2008c, J. Chem. Phys., 129, 164306
Li, B. & Han, K.-L. 2009, J. Phys. Chem. A, 113, 10189
Li, X., Heays, A. N., Visser, R., et al. 2013, A&A, 555, A14
Li, X., Millar, T. J., Walsh, C., Heays, A. N., & van Dishoeck, E. F. 2014, A&A, 568, A111
Liang, M.-C., Heays, A. N., Lewis, B. R., Gibson, S. T., & Yung, Y. L. 2007, ApJ, 664, L115
Light, G. C. 1978, J. Chem. Phys., 68, 2831
Lis, D. C., Phillips, T. G., Goldsmith, P. F., et al. 2010, A&A, 521, L26
Liu, S. & Shi, Y. 2010, Chinese J. Chem. Phys., 23, 649
Liu, X., Shemansky, D. E., Malone, C. P., et al. 2008, J. Geophys. Res., 113, A02304
Liu, X.-L., Wang, J.-J., & Xu, J.-L. 2013, MNRAS, 431, 27
Lucas, R., Guélin, M., Kahane, C., Audinos, P., & Cernicharo, J. 1995, Ap&SS, 224, 293
Lutz, B. L., Snow, Jr., T. P., & Owen, T. 1979, ApJ, 227, 159
Lyons, J. R. 2009, Meteoritics and Planetary Science Supplement, 72, 5437
Lyons, J. R. 2010, Meteoritics and Planetary Science Supplement, 73, 5424
Lyons, J. R. & Young, E. D. 2003, Geochimica et Cosmochimica Acta Supplement, 67, 263
MacKay, D. D. S. & Charnley, S. B. 2001, MNRAS, 325, 545
Maercker, M., Mohamed, S., Vlemmings, W. H. T., et al. 2012, Nature, 490, 232
Maercker, M., Schöier, F. L., Olofsson, H., et al. 2009, A&A, 494, 243
Maercker, M., Schöier, F. L., Olofsson, H., Bergman, P., & Ramstedt, S. 2008, A&A, 479, 779
Maillard, J. P., Chauville, J., & Mantz, A. W. 1976, J. Mol. Spectrosc., 63, 120
Maiti, B. & Schatz, G. C. 2003, J. Chem. Phys., 119, 12360
Mandell, A. M., Bast, J., Dishoeck, E. F. v., et al. 2012, Astrophys. J., 747, 92
Maret, S., Bergin, E. A., & Lada, C. J. 2006, Nature, 442, 425
Margitan, J. J., Kaufman, F., & Anderson, J. G. 1975, Chem. Phys. Lett., 34, 485
Marvel, K. B. 2005, AJ, 130, 261
Mathis, J. S., Mezger, P. G., & Panagia, N. 1983, A&A, 128, 212
Mauersberger, R. & Henkel, C. 1991, A&A, 245, 457
Mauron, N. & Huggins, P. J. 1999, A&A, 349, 203
McElroy, D., Walsh, C., Markwick, A. J., et al. 2013, A&A, 550, A36
McKee, C. F. & Hollenbach, D. J. 1980, ARA&A, 18, 219
Meier, D. S. & Turner, J. L. 2005, ApJ, 618, 259
Meier, R. R., Samson, J. A. R., Chung, Y.,

Lee, E.-M., & He, Z.-X. 1991, Planet. Space Sci., 39, 1197

Melnick, G. J., Neufeld, D. A., Ford, K. E. S., Hollenbach, D. J., & Ashby, M. L. N. 2001, Nature, 412, 160

Menten, K. M., Wyrowski, F., Alcolea, J., et al. 2010, A&A, 521, L7

Milam, S. N., Apponi, A. J., Woolf, N. J., & Ziurys, L. M. 2007, ApJ, 668, L131

Milam, S. N., Halfen, D. T., Tenenbaum, E. D., et al. 2008, ApJ, 684, 618

Millar, T. J., Herbst, E., & Bettens, R. P. A. 2000, MNRAS, 316, 195

Morris, M. 1975, ApJ, 197, 603

Morris, M. & Jura, M. 1983, ApJ, 264, 546

Muller, S., Beelen, A., Guélin, M., et al. 2011, A&A, 535, A103

Ndome, H., Hochlaf, M., Lewis, B. R., et al. 2008, J. Chem. Phys., 129, 164307

Nejad, L. A. M. & Millar, T. J. 1987, A&A, 183, 279

Neufeld, D. A. & Dalgarno, A. 1989, ApJ, 340, 869

Neufeld, D. A., Roueff, E., Snell, R. L., et al. 2012, ApJ, 748, 37

Öberg, K. I., Qi, C., Fogel, J. K. J., et al. 2010, ApJ, 720, 480

Ohishi, M., McGonagle, D., Irvine, W. M., Yamamoto, S., & Saito, S. 1994, ApJ, 427, L51

Pascucci, I., Apai, D., Luhman, K., et al. 2009, ApJ, 696, 143

Pettey, L. R. & Wyatt, R. E. 2008, J. Phys. Chem. A, 112, 13335

Pilbratt, G. L., Riedinger, J. R., Passvogel, T., et al. 2010, A&A, 518, L1

Polehampton, E. T., Menten, K. M., van der Tak, F. F. S., & White, G. J. 2010, A&A, 510, A80

Pontoppidan, K. M., Salyk, C., Blake, G. A., et al. 2010, Astrophys. J., 720, 887

Prasad, S. S. & Huntress, Jr., W. T. 1980, ApJ, 43, 1

Pulliam, R. L., Edwards, J. L., & Ziurys, L. M. 2011, ApJ, 743, 36

Qi, C., Öberg, K. I., & Wilner, D. J. 2013, ApJ, 765, 34

Quan, D., Herbst, E., Osamura, Y., & Roueff, E. 2010, ApJ, 725, 2101

Rachford, B. L., Snow, T. P., Destree, J. D., et al. 2009, ApJ, 180, 125

Radenovic, D. C., van Roij, A. J. A., Chestakov, D. A., et al. 2003, J. Chem. Phys., 119, 9341

Ramstedt, S., Maercker, M., Olofsson, G., Olofsson, H., & Schöier, F. L. 2011, A&A, 531, A148

Ramstedt, S., Schöier, F. L., & Olofsson, H. 2009, A&A, 499, 515

Ramstedt, S., Schöier, F. L., Olofsson, H., & Lundgren, A. A. 2006, A&A, 454, L103

Reynard, L. M. & Donaldson, D. J. 2001, Geophys. Res. Lett., 28, 2157

Roberge, W. G., Dalgarno, A., & Flannery, B. P. 1981, ApJ, 243, 817

Roberge, W. G., Jones, D., Lepp, S., & Dalgarno, A. 1991, ApJ, 77, 287

Robie, D. C., Arepalli, S., Presser, N., Kitsopoulos, T., & Gordon, R. J. 1987, Chem. Phys. Lett., 134, 579

Robitaille, T. P., Whitney, B. A., Indebetouw, R., Wood, K., & Denzmore, P. 2006, ApJ, 167, 256

Rogers, S., Wang, D., Kuppermann, A., & Walch, S. 2000a, J. Phys. Chem. A, 104, 2308

Rogers, S., Wang, D., Kuppermann, A., & Walch, S. 2000b, The Journal of Physical Chemistry A, 104, 2308

Salyk, C., Pontoppidan, K. M., Blake, G. A., et al. 2008, Astrophys. J. Lett., 676, L49

Sasselov, D. D. & Lecar, M. 2000, ApJ, 528, 995

Savage, B. D., Bohlin, R. C., Drake, J. F., & Budich, W. 1977, ApJ, 216, 291

Savage, B. D. & Mathis, J. S. 1979, ARA&A, 17, 73

Schatz, G. C. 1985, J. Chem. Phys., 83, 5677

Schatz, G. C., Wagner, A. F., Walch, S. P., & Bowman, J. M. 1981, J. Chem. Phys., 74, 4984

Schöier, F. L., Bast, J., Olofsson, H., &

Lindqvist, M. 2007, A&A, 473, 871
Schöier, F. L., Maercker, M., Justtanont, K., et al. 2011, A&A, 530, A83
Schöier, F. L., Ramstedt, S., Olofsson, H., et al. 2013, A&A, 550, A78
Sheffer, Y., Rogers, M., Federman, S. R., et al. 2008, ApJ, 687, 1075
Smith, I. W. M. 2011, ARA&A, 49, 29
Spelsberg, D. & Meyer, W. 2001, J. Chem. Phys., 115, 6438
Sprengers, J. P., Reinhold, E., Ubachs, W., Baldwin, K. G. H., & Lewis, B. R. 2005, J. Chem. Phys., 123, 144315
Sprengers, J. P., Ubachs, W., Baldwin, K. G. H., Lewis, B. R., & Tchang-Brillet, W.-Ü. L. 2003, J. Chem. Phys., 119, 3160
Sprengers, J. P., Ubachs, W., Johansson, A., et al. 2004, J. Chem. Phys., 120, 8973
Stark, G., Lewis, B. R., Heays, A. N., et al. 2008, J. Chem. Phys., 128, 114302
Sternberg, A. & Dalgarno, A. 1995, ApJ, 99, 565
Sternberg, A. & Dalgarno, A. 1995, Astrophys. J. Suppl., 99, 565
Strobel, D. F. 1982, Origins of Life, 12, 244
Sultanov, R. A. & Balakrishnan, N. 2004, J. Chem. Phys., 121, 11038
Szczerba, R., Schmidt, M. R., & Pulecka, M. 2007, Baltic Astronomy, 16, 134
Tappe, A., Lada, C. J., Black, J. H., & Muench, A. A. 2008, Astrophys. J. Lett., 680, L117
Tenenbaum, E. D., Dodd, J. L., Milam, S. N., Woolf, N. J., & Ziurys, L. M. 2010, ApJ, 720, L102
Tenenbaum, E. D. & Ziurys, L. M. 2010, ApJ, 712, L93
Thaddeus, P., Cummins, S. E., & Linke, R. A. 1984, ApJ, 283, L45
Thaddeus, P., Gottlieb, C. A., Gupta, H., et al. 2008, ApJ, 677, 1132
Tielens, A. G. G. M. 2013, Reviews of Modern Physics, 85, 1021
Tobin, J. J., Hartmann, L., Bergin, E., et al. 2012, ApJ, 748, 16
Truhlar, D. G. & Garrett, B. C. 1984, Annual Review of Physical Chemistry, 35, 159
Truhlar, D. G. & Garrett, B. C. 1984, Annu. Rev. Phys. Chem., 35, 159
Tsang, W. & Hampson, R. F. 1986, J. Phys. Chem. Ref. Data, 15, 1087
Turner, B. E. 1974, Ap&SS, 29, 247
van Dishoeck, E. F. 1988, in Rate Coefficients in Astrochemistry, ed. T. J. Millar, and D. A. Williams, Kluwer Academic Publishers, Dordrecht, 49
van Dishoeck, E. F. 1998, The Molecular Astrophysics of Stars and Galaxies, edited by Thomas W. Hartquist and David A. Williams. Clarendon Press, Oxford, 1998., p.53, 4, 53
van Dishoeck, E. F. 2014, Faraday Discuss., 168, 9
van Dishoeck, E. F. & Black, J. H. 1988, ApJ, 334, 771
van Dishoeck, E. F. & Dalgarno, A. 1984, ApJ, 277, 576
van Dishoeck, E. F., Herbst, E., & Neufeld, D. A. 2013, Chemical Reviews, 113, 9043
van Dishoeck, E. F., Jonkheid, B., & van Hemert, M. C. 2006, Faraday Discuss., 303, 231
van Dishoeck, E. F., van Hemert, M. C., Allison, A. C., & Dalgarno, A. 1984, ApJ, 81, 5709
van Dishoeck, E. F. & Visser, R. 2011, ArXiv e-prints
Varandas, A. J. C., Voronin, A. I., Riganelli, A., & Caridade, P. J. S. B. 1997, Chem. Phys. Lett., 278, 325
Viala, Y. P., Letzelter, C., Eidelsberg, M., & Rostas, F. 1988, A&A, 193, 265
Visser, R., Geers, V. C., Dullemond, C. P., et al. 2007, A&A, 466, 229
Visser, R., van Dishoeck, E. F., & Black, J. H. 2009, A&A, 503, 323
Vlemmings, W. H. T., Ramstedt, S., Rao, R., & Maercker, M. 2012, A&A, 540, L3
Wakelam, V., Herbst, E., Loison, J.-C., et al. 2012, ApJ, 199, 21
Wakelam, V., Smith, I. W. M., Herbst, E., et al. 2010, Space Sci. Rev., 156, 13

Wakelam, V., Smith, I. W. M., Loison, J.-C., et al. 2013, ArXiv e-prints

Walch, S. P., Wagner, A. F., Thom. H. Dunning, J., & Schatz, G. C. 1980, J. Chem. Phys., 72, 2894

Walsh, C., Harada, N., Herbst, E., & Millar, T. J. 2009, ApJ, 700, 752

Walter, C. W., Cosby, P., & Helm, H. 1993, J. Chem. Phys., 99, 3553

Wang, W., Rosa, C., & Brandao, J. 2006, Chem. Phys. Lett., 418, 250

Watanabe, N. & Kouchi, A. 2002, ApJ, 571, L173

Wayne, R. P. 2000, Chemistry of Atmospheres (Oxford University Press)

Weck, P. F., Balakrishnan, N., ao, B., Rosa, C., & Wang, W. 2006, J. Chem. Phys., 124, 74308

Wei, Q., Li, X., & Li, T. 2010, Chem. Phys., 368, 58

Westenberg, A. A. & Haas, N. d. A. 1967, J. Chem. Phys., 47, 4241

Willacy, K. & Millar, T. J. 1997, A&A, 324, 237

Willems, F. J. & de Jong, T. 1986, ApJ, 309, L39

Woodall, J., Agúndez, M., Markwick-Kemper, A. J., & Millar, T. J. 2007, A&A, 466, 1197

Woods, P. M., Schöier, F. L., Nyman, L.-Å., & Olofsson, H. 2003, A&A, 402, 617

Wu, C. Y. R., Judge, D. L., Tsai, M.-H., et al. 2012, J. Chem. Phys., 136, 044301

Wu, M. & Fehlner, T. 1975, Chem. Phys. Lett., 36, 114

Zack, L. N., Halfen, D. T., & Ziurys, L. M. 2011, ApJ, 733, L36

Zhai, H., Zhang, P., & Zhou, P. 2012, Comput. Theor. Chem., 986, 25

Ziurys, L. M. 2006, Pro. Natl. Acad. Sci., 103, 12274

Ziurys, L. M., Milam, S. N., Apponi, A. J., & Woolf, N. J. 2007, Nature, 447, 1094

Ziurys, L. M., Tenenbaum, E. D., Pulliam, R. L., Woolf, N. J., & Milam, S. N. 2009, ApJ, 695, 1604

Publications

Refereed publications

My major publications are listed as follows, among which the latest three (items 1, 2, and 3) are my favourite papers.

In item 3, accurate N_2 photodissociation rate and shielding functions were calculated. The results are very useful in many astrophysical fields. Both chemists and astronomers worked hard for this aim for decades. In item 2, a new method for accurately calculating molecular shielding functions in full 3D radiation field was proposed, and was employed to give new predictions for molecule distributions in a C-rich AGB star, IRC +10216. In item 1, a detailed discussion on the chemistry in O-rich AGB stars was carefully conducted based on the latest progress from both observations and simulations. By far, the results are the most accurate ones, and can be directly compared to the future observations.

1. **Xiaohu Li**, Tom J. Millar, Alan N. Heays, Catherine Walsh, Ewine F. van Dishoeck, and Isabelle Cherchneff, *The chemistry and distribution of daughter species in the circumstellar envelopes of O-rich AGB stars*, Submitted to A&A, 2015 (18 pages, Impact factor 5.084)

2. **Xiaohu Li**, Tom J. Millar, Catherine Walsh, Alan N. Heays, and Ewine F. van Dishoeck, *Photodissociation and chemistry of N_2 in the circumstellar envelope of carbon-rich AGB stars*, A&A, 2014, 568, A111 (13 pages, Impact factor 5.084, citation: 1)

3. **Xiaohu Li**, Alan N. Heays, Wim Ubachs, Brenton R. Lewis, Ruud Visser, and Ewine F. van Dishoeck, *Photodissociation of interstellar N_2*, A&A, 2013, 555, A14 (18 pages, citation: 9, Impact factor 5.084)

4. **Xiaohu Li**, Ewine F. van Dishoeck, Marc C. van Hemert, and Carina Arasa, *Effects of reagent rotation and vibration on H + OH(v, j) → O + H_2*, JPC-A, 2013, 117, 12889 (8 pages, Impact factor 2.775, citation 1)

5. **Xiaohu Li**, Meishan Wang, Ilaria Pino, Chuanlu Yang, and Lingzhi Ma, *The stereodynamics of the two reactions: H + LiH^+(v=0, j=0) → H_2 + Li^+ and H^+ + LiH(v=0, j=0) → H_2^+ + Li*, Phys. Chem. Chem. Phys., 2009, 11, 10438 (8 pages, Impact factor 4.198, citation: 39)

6. **Xiaohu Li**, Meishan Wang, Ilaria Pino, Chuanlu Yang, and Jicheng Wu, *The isotopic effects on stereodynamics for the two reactions: H + LiH^+(v=0, j=0) → H_2 + Li^+ and H^+ + LiH(v=0, j=0) → H_2^+ + Li*, Phys. Chem. Chem. Phys., 2010, 12, 7942 (8 pages, Impact factor 4.198, citation: 9)

7. **Xiaohu Li**, Meishan Wang, Chuanlu Yang, Lingzhi Ma, Ning Ma, and Jicheng Wu, *The polarization dependent differential cross sections of the reactions: H + LiH^+ (v=0, j=0) → H_2 + Li^+ and H^+ + LiH(v=0, j=0) → H_2^+ + Li*, Chin. Chem. Lett. 2010, 21, 376

8. Jicheng Wu, Meishan Wang, Chuanlu Yang, **Xiaohu Li**, and Xiaoqiong Chen, *Theoretical Study of the Stereodynamics of the Reaction C(^3P) + CH($X^2\Pi$) and Its Isotopic Variants*, Chin. Phys. Lett., 2011, 28, 063401

9. Lingzhi Ma, Meishan Wang, Chuanlu Yang, Chunyan Xia, **Xiaohu Li**, and Ning Ma, *Influence of reagent rotation on the integral cross sections of the collision (He, HD^+)*, J. At. Mol. Phys., 2009, 26, 3

10. Lingzhi Ma, Meishan Wang, Chuanlu Yang, Chunyan Xia, and **Xiaohu Li**, *The Stereodynamics Study on the Reactions of He + H_2^+ (HD^+, DH^+)*, Ludong University Journal (Natural Science Edition), 2008, 4, 13

11. Ning Ma, Meishan Wang, Chuanlu Yang, Xiongde Lin, **Xiaohu Li**, and Xiaoguang Ma, *Theoretical study of the influence of laser intensity on the population of the NO molecule electronic states*, Acta Phys. Sin., 2010, 59, 251

Conference proceedings

1. **Xiaohu Li**, Ewine F. van Dishoeck, Marc C. van Hemert, and Carina Arasa, *Effects of reagent rotation and vibration on H + OH(v, j) → O + H_2* , The Molecular Universe, Posters from the proceedings of the 280th Symposium of the International Astronomical Union held in Toledo, Spain, May 30-June 3, 2011.

Curriculum vitae

I was born in the center of Jingning County, Pingliang city, Gansu Province, the People's Republic of China. There are quite a few interesting places there. For instance, 3 km away from my home, there is a small library together with the majestic Fu Xi Temple. Fu Xi is one of the cultural heroes in Chinese legend and mythology, and he is thought to be the "original human". In particular, it is said that he created the *BaGua*, which are eight trigrams used in *Taoist* cosmology. Importantly, the *BaGua* consists of only two fundamental elements: *Yin* and *Yang*, which are also the basis of *Taichi* ("Supreme Ultimate" state). The *BaGua* and *Taichi* may represent the best wisdom of Chinese philosophy over its long history.

Here is a simple route of my education. My first school was the No. 1 Kindergarten in Jingning. There I did very well and got my current name, Xiaohu, which means 'small tiger'. I got this name because my teacher told my father that I looked like a lovely little tiger. Two years later, I was sent to a primary school. At the beginning, I refused to go to that school, because the teachers there always gave lots of home work. After an impressive beat from my mother, I finally agreed to take classes and eventually became the top student. Then I entered into middle school. Quickly, I became the class leader in my class, and had some other 'important' tasks as a student leader. I obtained the best scores and also helped some other students to make progress. Afterwards, I entered into the best middle school, called "No. 1 middle school" in my county, where I met some 'genius' and we became very good friends. After the graduation, we took a terrible exam, called 'Gao Kao', which is the entrance examination to the university. Unfortunately, I did not make a good score, which made me spent my next 4 years in Hexi university.

The good thing was that I was in the physics department. Again, I became the students leader and organized lots of student activities. I built the first 'English Corner' for the physics department, and invited many foreigner teachers to tell us something about their countries and culture. After I got my Bachelor degree, I passed the entrance examination of a 3-year master program of Ludong University, and my research was fully financed. In the very beautiful seaside city, Yantai, I started my master studies under the supervision of Prof. Meishan Wang. Quickly, I became the class leader in my class, though there were only 6 students in total, and we were divided into 3 different fields, including pure theory, numerical simulations, and experiments. My research topic was atomic and molecular physics, specifically working on molecular reactions. Because we were only 6 classmates, to make our teachers feel better, all of us attended all of the courses in three different fields, and took the examinations. An important thing for my life was that I met Miss Changchun Song in that university, and quickly, she became my girlfriend. One and a half years later, she became my wife, and now, she is still my wife.

After I got my master degree with the best record in Ludong University, I went to Dalian Institute of Chemical Physics (DICP), Chinese Academy of Science, work as a staff member in Prof. Keli Han's group. I would say that DICP is the best chemical-physics institution in China. One of my idols, Prof. Can Li, is also working there. There I learnt basic techniques and theory about experiments on femtosecond ultrafast dynamics from Prof. Jianyong Liu. By that time I only had a master degree, to get a better position I must obtain a PhD degree, either at DICP or other places. I had a few options. Suddenly, I noticed that Prof. Ewine van Dishoeck was looking for a PhD student. After a Skype interview, I got the position quickly, within 2 hours. Before coming to Leiden, I did not take any astronomy courses. But two years later, when I

started to do a project on astrochemistry, I started to step into this field very quickly, partly because the project was much more interesting than any other projects that I have ever done before, and partly because I had no time to wait. So, 'quickly', is a good word during my study. Nowadays, it becomes important to determine things fast and take actions.

A few more words about my life and study in Leiden, a university city since 1575. Leiden is a small, quiet, beautiful, friendly, and very interesting city, but looks quite modern, especially Leiden Observatory where I have been working/studying for 4 years. Here, I met and talked with many very nice, smart, and distinguished people. I attended a lot of interesting and impressive conferences, including most of the astrochemistry seminars and theoretical chemistry group-meetings organized by the Astrochemistry Group in Leiden Observatory and the Institute of Theoretical Chemistry of Leiden University. I selectively attended some of the Sterrewacht Colloquia, "This week's discoveries", and especially some workshops held in the Lorentz Center. I gave talks or presented posters at a number of international meetings, e.g., IAU280 "The Molecular Universe" Symposium in Toledo (Spain, 2011), the annual Dutch Astrochemistry Network (DAN) network meetings, NOVA Network II meetings, Faraday Discussion 168 meeting (2014, Leiden), etc. In particular, I was selected to attend the Onsala Space Observatory summer school "Molecules in space", with applications from PhD students and postdoctoral researchers all over the world with only 15% chance of success. There I made my first real observations towards the molecular cloud CB 17 using the Onsala 20m mm-telescope, and my report achieved the top score.

I got many honours and awards during my 26 years of studies, mostly due to helping other students, organizing student activities, and hard-work, sometimes due to competitions. Eventually I understood that it is not important how excellent/distinguished a person is, but that it is important to what extent one can help/influence other people. Contributions and mercy are very important to be a good scientist. Meanwhile, life is short, and sometimes life is hard to many people. I mention this here because one of my very good friends, one of my 'genius' classmates during my middle school, died in May of 2014 in Beijing, partly due to lots of hard work. Moreover, some other 'successful' people have died at a very young age. Therefore, enjoying one's own work, having fun, and being happy are much more important than so-called 'success'. Good attitudes are very important to human beings, including scientists.

I would like to close this section with an interesting story of my own. In China, there was a very traditional question: what do you want to be when you grow up? Many of my classmates wanted to be a teacher, a policeman, an engineer, a scientist, etc. And many of them forgot their original aims when they grew up. My answer to that question was, "I want to be an Astronaut" (I was like 8 years old at that time), and I also forgot my words for a long time. When I started to write this section, suddenly I realized that now I am very closing to my original dream: rather than an "Astronaut", I am on my way to be an "Astronomer", which suits me even better. Just like an interesting saying, "Everybody should have a dream, what if that dream comes true?!".

Acknowledgements

It is not easy to obtain a PhD degree, which is probably one of the reasons why most PhD students want one. So, we came, we conquered, and we gained. The degree is useful, but what is more important is how we got there and what we learnt during this process. Meanwhile, the "new" faces we meet and communicated with, together with the "old" faces that always exist in our memory can give us power to move forward, overcome difficulties, feel love, feel friendship, remember our responsibilities, and motivate us to do our best to perform better and better. Because of them, we always cherish our good luck and appreciate the beauty of this planet, and in turn try to help others and make the world a little bit better. These people include our families, friends, teachers, collaborators, students, and also some distinguished opponents. It is hard to mention all of them here, but never mind, I don't really wish to, and couldn't fully express the thanks from the bottom of my heart with words. Instead, I will always remember the good times we spent together and try to keep in touch if it is possible. I will miss them. These memories are mine and will stay with me forever. So, just a few sentences and a simple list of the names for those people I can remember at the moment.

According to Leiden tradition, Leiden professors are not acknowledged in this section. I appreciate the spirit but I must mention that we have quite a few very distinguished professors at Leiden University, especially in the Leiden Observatory. Many of our professors are very well-known in the world. To some extent it is really these professors who work very hard day-by-day and continue the glory of the University, and benefit the students generation-by-generation. Any small piece of work from us students contains lots of contributions from our supervisors, in addition to valuable discussions with other professors during various seminars, a simple drop by, lunch, or any other connection. Some of these professors are my very good friends, shared me with their knowledge, wisdom, favourite music, poems, interesting stories, 'paper cakes', cookies, and delicious home-made food. So, my deepest thanks!

Then, a few names that guided me, and closely interacted with me. Alan, my co-promoter plus brother, it is so great to have you involved in all of my projects, you are such a nice, helpful, patient, and considerate guy! Carina, a very nice person who, always smiles and very patiently, taught me quite a few things, even including how to make movies of molecular reactions. Ruud, you taught me my first astrochemical modeling, and then continued to help me with various details. Catherine, one of my office mates, trained me with dark cloud models and then brought me into my favourite field, AGB envelopes. Well, a big name, Tom Millar! Every time I meet you, including the first time, made me feel very happy. You shared with me your wisdom, many stories, and hosted me with very delicious food every summer during my visit to your group in Queen's University Belfast in the past two years. Our friendship will last forever. Lars, I cannot appreciate your spirit too much, I miss the time when you were in our office. You are the person I can always rely on. Jiancheng, Dongfeng, Junfeng, Feijia, and Ko-ju, only with you can I discuss the scientific questions in another language, it is such a pleasure to meet you guys here! Oh wait, also with Gleb, a smart guy who can even play Chinese chess and Pingpang with me! Our very international astrochemistry group members, we spent many Friday mornings together, shared ideas, discussed progress, learnt from the same materials, celebrated many achievements, in addition to preparing talks and posters for many international conferences. We had lots of parties together, including our annual retreats, with various nice dinners. We are belonging to a special "family", lead by our "Queen". I will miss you guys soon, especially the first Friday

after I leave Leiden. OK, no more words are needed, I believe you guys understand that I cannot express the feeling, no matter how hard I try. So, just list your names: Lars, Ruud, Isa, Jeanette, Carina, Geoff, Catherine, Mihkel, Anna, Alan, Umut, Daniel, Agata, Magnus, Joe, Irene, Nienke, Kenji, Niels, Maria, Paola, Simon, Davide, Nadia, Christian, John, Andreas, and Vianney. In the past 4 years, I am staying in one office, 503. My office mates used to be Lars, Jeanette, Remco, Geoff, Jaya; Currently, are: Mihkel, Anna, and Catherine. Basically, everyone comes from a different country, but the daily greetings, the funny chat, the smile/laughing, the care, the help, the warm words, and understanding, are the same. I remember many of you guys' favourite sayings and words, e.g., "Yes and No!", "Think differently!", "Don't be childish, stick to our plan!", etc., also "Could be better, could be worse" . You guys are so smart, funny, and considerable! It was/is my great pleasure to be your office mate, wish you every success and good luck in the future!

A special thanks goes to Nienke. Not only because you translated the Dutch summary for my thesis during the New Year holiday time, but more importantly, during my 4 years of living in your country, whenever I needed your help you were always there. You are among one of the most lucky Ph.D. students since your first first-author paper has been published in Science.

The computer staff, Erik, David, Aart, and Niels, in addition to secretaries, Liesbeth, Anita, and Jacqueline, amongst others in our department, and at the Graduate School, are just excellent and very efficient. Without any of your help the process of this thesis would take a much longer time. I am also very grateful to Evelijn Gerstel and Eveline Castermans for lots of kind help and support.

I am very grateful to my co-workers, who made this thesis excellent, in addition to the reading committee of this thesis, for instance, Prof. Leen Decin, who provided some detailed comments. I enjoyed lots of stimulating discussions during my presence of Dutch Astrochemical Network meetings, for example, with Wim Ubachs and David Parker. I had a great time during my visits to Tom's Astrophysics group in Queen's University Belfast where I also met some good friends and distinguished researchers, for instance, Stephen Smartt, Wanting, and Paul Woods.

At Leiden Observatory, some of my colleagues and friends were not directly involved in my scientific work, but shared with me friendships, in particular, Carl, Daniel Caputo, Sergio, Mateo, Emanuele, Francisco, Daniel Paardekooper, Leen, Heather, Michiko Fuji, Steven, Shuro, Edith, Anton, Nicola, Olmo, Silvia, Olivera, Steven, Kalle, Rafael, Kuo-Song, Thanja, David, Pablo, Edwin, Sebastiaan, Carmen, Marissa, Tiffany, Gilles, Berenice, Alexander, Marco, Alessandra, Grainne, Jean-Baptiste, Tim, Luke, Silvia, Markus, Isabel, and Pamela. Sascha, Alex, and Josha, you three gave me and my visitors tours to the old observatories, introduced the history and telescopes there to us, and guided us to observe the beautiful stars. I still remember the feeling of sitting on Albert Einstein's favourite chair, and the exciting moment when I saw a clear surface of the Moon, the Jupiter with moons, also Saturn, Titan, and Mars. Wish you all the best in the future and good luck for your thesis! Surprisingly and happily, I met an excellent Pingpang opponent here- Walter Jaffe, who used to be a member in a Pingpang club for more than 10 years. Walter, let's cheers for our friendship and wish you and Lexa every happiness!

I would like to acknowledge the friendship from my friends in the Netherlands outside my working place as well. Qiang Ge and Da Jie, together with Shushu, Ayi, Jiawen and Jiacheng, you like my families. We celebrated many important events together, including every New Year during the past four years. I do believe the Chinese restaurant (Kwangtung Restaurant) you run is the best one in Leiden. Leo and Majella, I will miss you, wish you every happiness. Victory, Fumi, and Clara, thanks for visiting me twice from Taiwan. It is hard to mention everything, so, a list of the names that I can immediately remember: cr; Pq; Fastq; Liang Zhang, Xinyi, Lei Song, Mingli, Xiaoshuang, Shengfa, Yuli, Wen Pan, Changsheng, Chengjun, Jianqiang, Qiang Wang,

Jun Hao, Chuangjuan, Zhongxiao, Yingchun, Qinggang, Hao Qiu, Erkai, Guiling, Ancong, Jiali, Jiayuan, Jing Shi, Na An, Meiliang, Wenjie, Dapeng, Haojun, Jin Wang, Bo Chen, Zhao Zhou, Alan Chow, Mushi Zhou, Kuan Yan, Ying Shi, Maggie, Qiushi, Qiuye, Chunli, and Lei Xia. I am pretty sure some of you guys will miss me very soon as well.

Help and inspiration from Profs. Can Li, Keli Han, Meishan Wang, Guihua Sun, De Wang, Aigen Li, Xueming Yang, and Lei Jiang, together with my friends Ilaria Pino, Wenzheng, Kuijie, Ning Ma, and Liang Shi, made me who I am today. Without any of them, this thesis may not happen. In addition, I can always get help and support from my previous work/study places, especially DICP, many thanks!

Baba, Mama, Xiaoliang, and Xifeng, together with my wife's families: I've been away so far from home for a long time, I know sometimes it is hard for you. The love and understanding from you make me always feel that I am very important. Because of you, I can overcome any difficulties. I will see you soon, which is better than words. My sweet wife, Changchun, you have been with me for more than 5 years, life couldn't be easier and happier when we are together. In my eyes, you are the best girl in this planet! My other family members, previous teachers, friends, and students in China, your care, understanding, kind words, and friendship always warm my heart.

During my application of 2015 East Asian Core Observatories Association (EACOA) fellowship, I got the fullest support from Prof. Gang Zhao, who is the leading scientist in the National Astronomical Observatories, Chinese Academy of Sciences, and Dr. Ciska Kemper at the Academia Sinica Institue of Astronomy and Astrophysics, in addition to some of my very good friends and guiders. I passed the first round of selection, and just had my interview. I will know the final results after this thesis being printed. All of your efforts and valuable suggestions are highly appreciated from the bottom of my heart!

Last but not the least, thanks to my friends that I forgot to mention here, and thanks to the Netherlands Organisation for Scientific Research (NWO) for financing my research!

From left: Xiaohu, Nadia, Kenji, Agata, Irene, Andreas, Ewine, Joe, Anna, Daniel, Catherine, Mihkel, Paola, Alan, Maria, Nienke, Magnus, Niels, Davide, Simon, Ko-ju.

"Two roads diverged in a wood, and I-

I took the one less travelled by,

And that has made all the difference."

– Robert Frost